Lehrstuhl für Aerodynamik und Strömungsmechanik
Technische Universität München

Nonlinear Aerodynamic Reduced-Order Modeling Using Neuro-Fuzzy Approaches

Maximilian Winter

Vollständiger Abdruck der von der Fakultät für Luftfahrt, Raumfahrt und Geodäsie der Technischen Universität München zur Erlangung des akademischen Grades eines

Doktor-Ingenieurs

genehmigten Dissertation.

Vorsitzender: Prof. Dr.-Ing. Manfred Hajek
Prüfer der Dissertation:
1. apl. Prof. Dr.-Ing. Christian W. M. Breitsamter
2. Prof. Dr. Stefan Görtz

Die Dissertation wurde am 06.07.2020 bei der Technischen Universität München eingereicht und durch die Fakultät für Luftfahrt, Raumfahrt und Geodäsie am 09.02.2021 angenommen.

© Maximilian Winter 2021

All rights reserved. No part of this publication may be reproduced, modified, re-written, or distributed in any form or by any means, without the prior written permission of the author.

Typesetting: LaTeX

Acknowledgments

The present thesis was written during and after my work as a research associate at the Chair of Aerodynamics and Fluid Mechanics of the Technical University of Munich. At this point, I would like to take the opportunity to sincerely thank all who have accompanied me during this time and who have paved the way to the success of this work.

First of all, I would like to express my deep gratitude to my advisor and first examiner Prof. Dr. Christian W. M. Breitsamter for giving me the opportunity to conduct my research in a highly interesting, inspiring, and trendsetting topic as well as for the excellent support he offered me over the years. I very much appreciated his accessibility, his constructive criticism, his always open ear, and his continuous support in attending national and international workshops and conferences. The associated experiences and technical discussions have contributed significantly to the success of this work.

Furthermore, I would like to thank Prof. Dr. Stefan Görtz for assuming the function of the second examiner as well as for providing very valuable feedback over many years. I would also like to thank Prof. Dr. Manfred Hajek for chairing the examination.

Moreover, I am very grateful to the current and former members of the Chair of Aerodynamics and Fluid Mechanics. They made the research very pleasant and supported me wherever possible. Special thanks go to my friends Vladislav Rosov, Marco Stuhlpfarrer, Florian M. Heckmeier, Dr. Florian Knoth, Dr. Julie Piquee, Dr. Alexander N. Pechloff, Andrei Buzica, Dr. Anja Kölzsch, and Dr. Mark Förster. With their help, profound questions, and inspiring discussions which also went far beyond the actual work, they essentially contributed to this research and the working atmosphere. I wish all of them great success in their future endeavors. Besides, I would like to express my gratitude to Cyrille Vidy, Dr. Dietmar Fleischer, and Dr. Michail Iatrou for the pleasant project-related cooperation and the associated fruitful technical discussions. Not least, I want to acknowledge the Bavarian Research Foundation (BFS) and the German Research Foundation (DFG) for providing the funding that allowed me to undertake this research.

Finally, I wholeheartedly thank my family, particularly my parents Gabriele and Peter as well as my brother Matthias and my grandparents, for their love, their support and their continuous encouragement; my friends, who have been there for me; and my wife Rosa de los Angeles for her love and the permanent support she offered me also in difficult times. Without all of them, this work would hardly have been possible.

Munich, March 2021 Maximilian Winter

Abstract

For further increasing the performance and safety characteristics of aircraft, it is necessary to accurately predict the static and dynamic interactions between the structural-elastic, inertial, and aerodynamically-induced forces. In the context of the associated aeroelastic investigations, efficient linear potential flow methods have been mainly applied to model the unsteady aerodynamic loads. However, these methods do not fully meet today's accuracy requirements, especially in terms of transonic flow problems that are governed by nonlinear effects. In contrast, the time-varying aerodynamic forces can be determined with sufficient precision using computational fluid dynamics (CFD) approaches. Since the latter methods require extensive computing capacities, their industrial use for multidisciplinary analyses is still limited.

Motivated by this bottleneck, model-order reduction methods based on recurrent neuro-fuzzy models are developed in the present thesis in order to efficiently reproduce the unsteady aerodynamic characteristics. Therefore, the time-domain reduced-order models (ROMs) exploit modern system identification principles, which allow the prediction of nonlinear flow phenomena. Consequently, the aerodynamic ROM reflects the essential dynamics of the underlying CFD system in a resource-saving manner and is capable, inter alia, of modeling the flight behavior across varying freestream conditions, pronounced shock motions, and structural vibrations. Based on the proposed methodology, integral motion-induced forces and moments or, in combination with the proper orthogonal decomposition, locally-distributed aerodynamic loads can be computed in an accurate and robust way. Hence, a significant efficiency enhancement of the CFD-based numerical analysis is achieved, which allows the assessment of the aircraft aeroelastic behavior at an earlier stage in the development process. The proposed methods are comprehensively tested and validated by considering four test cases of variable complexity. In this regard, the computational efficiency as well as the fidelity of the ROMs is assessed relative to the full-order simulation procedure.

Zusammenfassung

Zur Steigerung der Effizienz und Sicherheit von Luftfahrzeugen ist es notwendig, die statischen und dynamischen Wechselwirkungen zwischen struktur-elastischen Kräften, Trägheitskräften sowie aerodynamischen Kräften präzise vorherzusagen. Im Kontext solcher aeroelastischer Untersuchungen wurden zur Modellierung der instationären Aerodynamik bisher hauptsächlich lineare Potenzialverfahren eingesetzt, welche jedoch die heutigen Genauigkeitsanforderungen speziell im transsonischen Strömungsbereich nicht in vollem Umfang erfüllen. Im Gegensatz dazu lassen sich die Luftkräfte mithilfe von Computational Fluid Dynamics-Ansätzen (CFD) mit hinreichender Präzision ermitteln. Allerdings setzen letztere Verfahren enorme Rechenkapazitäten voraus, was deren industriellen Einsatz für multidisziplinäre Analysen stark limitiert.

Motiviert durch diese Problemstellung werden in der vorliegenden Arbeit Modellreduktionsverfahren basierend auf rekurrenten Neuro-Fuzzy Modellen entwickelt, welche die instationären aerodynamischen Zusammenhänge auf effiziente Weise reproduzieren. Diese adaptiven, im Zeitbereich formulierten Ansätze werden anhand von modernen Systemidentifikationsverfahren hergeleitet, was die Vorhersage von strömungsmechanisch-nichtlinearen Phänomenen erlaubt. Die auf diese Weise erhaltenen vereinfachten Aerodynamikmodelle geben die dominante Charakteristik des CFD-Systems ressourcensparend wieder und eignen sich u.a. zur Modellierung des Flugverhaltens bei unterschiedlichen Anströmbedingungen, ausgeprägten Stoßwanderungen sowie strukturellbedingten Vibrationen. Basierend auf dieser Vorgehensweise können integrale Luftkräfte bzw. in Kombination mit der Hauptkomponentenanalyse auch lokale strömungsinduzierte Lasten auf präzise und robuste Weise ermittelt werden. Dadurch wird eine deutliche Effizienzsteigerung des CFD-basierten numerischen Analyseprozesses erzielt, was eine Beurteilung des aeroelastischen Verhaltens von Luftfahrzeugstrukturen zu einem früheren Zeitpunkt im Entwicklungsprozess ermöglicht. Die vorgestellten Verfahren werden anhand von vier Testfällen variierender Komplexität erprobt und umfassend validiert, wobei sowohl die Rechenzeiten als auch die Genauigkeit relativ zur CFD-Referenzlösung bewertet werden.

Contents

List of Figures

List of Tables

Nomenclature

Roman Symbols	**Denotation**
$\mathbf{A}$	time-averaged snapshot vector
AR	aspect ratio
a	speed of sound
$\mathbf{B}$	matrix of POD coefficients
$\mathbf{b}$	POD coefficient vector
b	wing span
$\mathbf{C}$	damping matrix
$\mathbf{C}_f$	skin friction coefficient vector
$\mathbf{C}_{gen}$	generalized damping matrix
$\mathbf{C}_i$	aerodynamic force coefficient vector for surface element i
$\mathbf{C}_{i,p}$	pressure-induced force coefficient vector for surface element i
$\mathbf{C}_{i,f}$	shear-stress-induced force coefficient vector for surface element i
$\mathbf{C}_{m,i}$	aerodynamic moment coefficient vector for surface element i
C_D, C_L, C_Y	drag, lift, side-force coefficients
C_{M_x}, C_{M_y}, C_{M_z}	rolling-, pitching-, yawing-moment coefficients
$C_{M_x,b}$, $C_{M_y,b}$, $C_{M_z,b}$	moment coefficients about body-fixed axes
$C_{X,b}$, $C_{Y,b}$, $C_{Z,b}$	longitudinal, lateral, normal force coefficients (body-fixed coordinate system)
C_p	pressure coefficient
C_p^*	critical pressure coefficient
$\mathbf{c}_j$	center vector corresponding to LLM j
c_p	heat capacity at constant pressure
c_r	root chord
c_{ref}	reference length for k_{red} calculation
c_t	tip chord
c_v	heat capacity at constant volume
$d\mathbf{S}$	surface element vector
E	Young's modulus
$\mathbf{e}$	model error
e	specific energy
$\mathbf{F}$, $\mathbf{G}$, $\mathbf{H}$	convective fluxes in curvilinear coordinates
$\mathbf{F_v}$, $\mathbf{G_v}$, $\mathbf{H_v}$	viscous fluxes in curvilinear coordinates
FSI	flutter speed index
FR	frequency ratio

Roman Symbols	**Denotation**
$\mathbf{f}$	time-domain external forces vector
$\mathbf{f}$, $\mathbf{g}$, $\mathbf{h}$	convective fluxes in Cartesian coordinates
$\mathbf{f}_{gen}$	time-domain generalized aerodynamic forces vector
$\mathbf{f_v}$, $\mathbf{g_v}$, $\mathbf{h_v}$	viscous fluxes in Cartesian coordinates
f	frequency
$f_{gen,i}$	time-domain generalized aerodynamic force vector element i
$f_{gen,ij}$	time-domain generalized aerodynamic force vector element i caused by an excitation of mode j
$\mathbf{G}$	system operator
$\mathbf{G}^L$, $\mathbf{G}^N$	linear and nonlinear weights of the MLP neural network
$\mathbf{GAF}$	frequency domain generalized aerodynamic forces matrix
G	shear modulus
$\mathbf{g}$	gradient of the model error
g	aeroelastic damping
$\mathbf{H}$	Hessian matrix
h	heave displacement degree of freedom
$\mathbf{I}$	identity matrix
$\mathrm{Im}\, x$	imaginary part of x
I_j	local loss function for LLM j
i, j, k	grid index system
$\mathbf{J}$	Jacobian matrix of the model error $\mathbf{e}$ with respect to the parameter vector $\boldsymbol{\theta}$
J	Jacobian determinant of the coordinate transformation
$\mathbf{K}$	stiffness matrix
$\mathbf{K}_{gen}$	generalized stiffness matrix
k	discrete time increment
k_{red}	reduced frequency
k_σ	basis function width scaling factor
l_μ	mean aerodynamic chord
l_{ref}	grid reference length
$\mathbf{M}$	mass matrix
$\mathbf{M}_{gen}$	generalized mass matrix
M	number of local linear models of the NFM
M_{MLP}	number of neurons of the MLP neural network
M_{POD}	number of POD modes

Roman Symbols	**Denotation**
Ma	Mach number
m	mass
m, n	input and output dynamic delay-orders
N_{DOF}	number of structural model degrees of freedom
N_{FC}	number of training freestream conditions
N_M	number of considered structural eigenmodes
N_{MC}	number of Monte-Carlo samples
N_{Nodes}	number of finite element model nodes
N_S	number of samples
N_{SE}	number of surface elements
N_T	number of training samples
N_τ	number of time steps per cycle
N_V	number of validation samples
n_f	dimension of the GAF vector
n_q	dimension of the generalized coordinates vector
n_u	system input vector dimension
n_y	system output vector dimension
o_h	heuristic parameter of the input/output delay optimization
Pr	Prandtl number
p	static pressure
p	nondimensional Laplace variable
p	dimension of the neuro-fuzzy model input vector
$\mathbf{Q}$	conservative variables vector in curvilinear coordinates
$\mathbf{Q}$	generalized aerodynamic forces matrix, time domain
Q	fit factor
$\mathbf{q}$	generalized coordinates vector
$\mathbf{q}$	conservative variables solution vector
q	dynamic pressure
q	generalized coordinate
$q_i^d(l)$	lth largest Lipschitz index for a d-dimensional model input vector (formed with model output i)
q_x, q_y, q_z	thermal fluxes in Cartesian coordinates
R	specific gas constant
Re	Reynolds number
$\mathrm{Re}\, x$	real part of x

Roman Symbols	**Denotation**
RIC	relative information content criterion
S_{ref}	reference area
SF	scaling factor for modal deflections
s	semi-span
s	Laplace variable
T	temperature
T	nondimensional period length
t	time
t/c	relative thickness (airfoil)
$\mathbf{U}$, $\mathbf{V}$	unitary matrices resulting from the SVD
U	absolute velocity
$\mathbf{u}$	system input vector
u, v, w	velocity components in Cartesian coordinates
$\mathbf{v}$	input vector of the MLP neural network
$\mathbf{W}_i$	snapshot vector at time instant i
$\hat{\mathbf{W}}_i$	centered snapshot vector (time instant i)
$\mathbf{w}_j$	vector containing the weights for the jth LLM
w_{j0}	input-independent offset for the jth LLM
$\mathbf{x}$	position/displacement vector
$\mathbf{x}$	model input vector
x, y, z	Cartesian coordinates
$\mathbf{Y}$	snapshot matrix
$\mathbf{y}$	system output vector
$\hat{\mathbf{y}}$	model output vector
y^+	nondimensional wall distance
$\hat{y}$	scalar neuro-fuzzy model output (MISO)

Greek Symbols	**Denotation**
α	angle of attack
β	angle of sideslip
γ	heat capacity ratio
Δ_{jl}	input space extension in dimension l related to the jth LLM
$\Delta\tau$	nondimensional time step size

Greek Symbols	**Denotation**
ε	user-defined threshold for *RIC* criterion
η	nondimensional spanwise coordinate
η	step increment (nonlinear LM optimization)
Θ	normalized excitation amplitude
$\boldsymbol{\theta}$	parameters of the MLP neural network
θ	pitch angle degree of freedom
λ	thermal conductivity
λ	wing taper ratio
$\boldsymbol{\mu}$	mean of the Monte-Carlo responses
μ	dynamic viscosity
μ	blending factor (nonlinear LM optimization)
$\overline{\mu}$	mass ratio
μ_j	basis function operator (LLM j)
ν	Poisson's ratio
$\boldsymbol{\Xi}$	time-invariant parameter vector
ξ, η, ζ	curvilinear coordinates
ρ	density
$\boldsymbol{\Sigma}$	rectangular diagonal matrix resulting from the SVD
$\boldsymbol{\Sigma}_j$	matrix containing the basis function widths (LLM j)
$\boldsymbol{\sigma}$	standard deviation of the Monte-Carlo responses
σ	singular value
σ	standard deviation
σ	basis function width
$\boldsymbol{\tau}$	shear stress tensor
$\boldsymbol{\tau}_w$	wall shear stress vector
τ	nondimensional time
τ_s	problem-related nondimensional time
$\boldsymbol{\Phi}$	modal matrix
$\boldsymbol{\phi}$	structural eigenmode
$\boldsymbol{\varphi}$	POD mode
Φ_j	activation function related to MLP neuron j
φ	wing sweep angle
Ψ_j	fuzzy membership/validity function corresponding to LLM j
ω	angular frequency
ω_α	angular frequency of the first uncoupled torsion mode

Subscripts	**Denotation**
b	body-fixed coordinate system
def	deformed state
f	flutter onset
gen	generalized/modal quantity
LE	leading edge
max	maximum
min	minimum
Nyq	Nyquist frequency
$Pred$	one-step prediction
ref	reference state
Sim	application/generalization
std	standardized quantity
TE	trailing edge
Trn	training
t	tangential components
w	wall
∞	freestream value

Superscripts	**Denotation**
d	dimension of the model input vector
L	linear influence
N	nonlinear influence
1, 2	first, second harmonic
$*$	scaling factor for nondimensionalization
$\top$	transpose

Modifier	**Denotation**
$\bar{\bullet}$	dimensionful variable
$\bullet^{\circ 2}$	Hadamard power
$\hat{\bullet}$, $\tilde{\bullet}$	neural-network-based approximation

Abbreviations and Acronyms

AER	Chair of Aerodynamics and Fluid Mechanics, TUM
AGARD	Advisory Group for Aerospace Research and Development
AIAA	American Institute of Aeronautics and Astronautics
ANFIS	adaptive-network-based fuzzy inference system
ANN	artificial neural network
APRBS	amplitude-modulated pseudo-random binary signal
ARMA	auto-regressive moving average model
ARX	auto-regressive model with exogenous inputs
BC	boundary condition
CFD	computational fluid dynamics
CGAN	conditional generative adversarial network
CNN	convolutional neural network
CPU	central processing unit
CRM	common research model
CT	computational test
DPW	drag prediction workshop
ERA	eigensystem realization algorithm
FEM	finite element method
FERMAT	flutter reduced-order model assessment
FFT	fast Fourier transform
FVM	finite volume method
FWGN	filtered white Gaussian noise
GAF	generalized aerodynamic forces
GRNN	general regression neural network
HB	harmonic balance
HIRENASD	high Reynolds number aero-structural dynamics (test case)
LANN	Lockheed-Georgia, Air Force Flight Dynamics Laboratory, NASA-Langley, NLR (test case)
LCO	limit-cycle oscillation
LLM	local linear model
LM	Levenberg-Marquardt (algorithm)
LOLIMOT	local linear model tree (algorithm)
LRZ	Leibniz Supercomputing Center (Leibniz Rechenzentrum)
LSTM	long short-term memory (neural network)
LTI	linear time-invariant
LU-SSOR	lower-upper symmetric successive over-relaxation

MC	Monte-Carlo
MIMO	multiple-input multiple-output
MISO	multiple-input single-output
MLP	multilayer perceptron (neural network)
MTOW	maximum take-off weight
MUSCL	monotonic upstream-centered schemes for conservation laws
MZFW	maximum zero fuel weight
NACA	National Advisory Committee for Aeronautics
NARMAX	nonlinear auto-regressive moving average model with exogenous inputs
NARX	nonlinear auto-regressive model with exogenous inputs
NASA	National Aeronautics and Space Administration
NFM	neuro-fuzzy model
NLR	Netherlands Aerospace Center (Nationaal Lucht- en Ruimtevaartlaboratorium)
NN	neural network
NOE	nonlinear output error model
NSI	nonlinear system identification
POD	proper orthogonal decomposition
PRBS	pseudo-random binary signal
RANS	Reynolds-averaged Navier-Stokes
RBF	radial basis function
ROM	reduced-order model
SA, MA, LA	small, medium, large amplitude cases
SAPRBS	smoothed amplitude-modulated pseudo-random binary signal
SD	small disturbance
SISO	single-input single-output
SVD	singular value decomposition
TDNN	time-delay neural networks
TFI	transfinite interpolation
TPS	thin-plate spline
TVD	total variation diminishing
TUM	Technical University of Munich
URANS	unsteady Reynolds-averaged Navier-Stokes
VT	vertical tail
WBT	wing/body/horizontal-tail configuration

1 Introduction

For the design, analysis, and certification of aircraft, the efficient and accurate determination of the flight envelope boundaries is a task of paramount importance. Therefore, the interplay of aerodynamic, structural-elastic, and inertial forces and moments acting on the airframe must be investigated, which is embodied by the discipline of aeroelasticity. Consequently, a multidisciplinary simulation approach is required in order to predict the static and dynamic phenomena that are caused by the aeroelastic coupling. Associated to this challenging task, the analysis of unsteady aerodynamic loads plays a decisive role for the industrial development of both civil and military aircraft.

This chapter provides the motivation for the conducted research including an introduction to the topic. Subsequently, the established methods as well as the current state of research is discussed by means of a literature review. Finally, the objectives and the structure of this thesis are outlined.

1.1 Motivation

Besides aerodynamic- and engine-related restrictions, aeroelastic stability and response problems typically limit the flight envelope of aircraft. According to Collars' well-known triangle of forces, the coupling of aerodynamic, elastic, and inertial forces can lead to often undesired phenomena [11]. Considering for example static aeroelastic effects, which arise due to the mutual reaction of the quasi-steady flow-induced forces with the elastic structure, the divergence of the lift-generating surfaces or the control surface reversal are interdisciplinary consequences that need to be prevented. However, even moderate flight-load-induced deformations have a non-negligible impact on the performance and, therefore, must be taken into account within the design process [40]. Since a reduction of the structural weight is of particular interest for the overall aircraft design, a compromise has to be realized between the structural mass and stiffness distribution and the resulting aeroelastic behavior. Nevertheless, it is also possible to consciously exploit aeroelastic deformations in order to optimize the properties of highly-flexible aircraft. For example, the structural deformation can be passively controlled in a beneficial manner by means of smartly placed fiber composite materials, leading to the so-called aeroelastic tailoring concept [29].

The focus in this work, however, is laid on unsteady aerodynamic as well as dynamic aeroelastic effects. Dynamic aeroelastic phenomena can be categorized into stability and response problems. The stability problem, referred to as flutter, is generally defined as a self-excited vibration of the wing or tail structure [15]. Due to phase shifts between the structural motion and the aerodynamic force response, the structure extracts energy from the flow under certain conditions. Ultimately, severe damage up to an explosive failure of the affected parts of the aircraft occurs. Thereby, the critical flutter speed marks the condition at which any disturbance-induced vibration becomes invariantly damped. Consequently, the flutter phenomenon places high demands on the design and construction of aircraft structures. In fact, various manifestations of flutter are addressed in the literature, e.g., the classical bending-torsion flutter, propeller-whirl flutter, panel flutter, control surface flutter, and body-freedom flutter [11, 29].

Besides the gust- or maneuver-induced dynamics, aeroelastic response problems are, inter alia, associated to aerodynamic buffet, control surface buzz, and limit-cycle oscillations [119, 132]. In particular, aeroelastic buffeting is a nonlinear effect that involves the presence of locally separated flow [197]. In the low speed regime, buffeting is usually caused by high-lift-related flow separation that occurs for example at the leading edge of the wing or the canard. The turbulent pressure fluctuations of the wake then interact with the downstream-located structure, e.g., the vertical tail plane. At transonic conditions, buffet is triggered by shock-boundary-layer interactions leading to self-sustained shock motions and associated oscillating flow-separations. Another dynamic aeroelastic phenomenon is the control surface buzz, which can arise at transonic and low supersonic conditions. Thereby, the flow-inherent nonlinearities lead to high-frequency oscillations of the control surface, while a single motion degree of freedom is involved [15, 160]. Last but not least, aeroelastic limit-cycle oscillations (LCOs) are characterized by an initially increasing or decreasing vibration amplitude of the affected structural parts [168]. In contrast to the stability problem, however, the self-sustained motion of a LCO is limited at a single or even multiple amplitude levels due to the presence of a nonlinearity [142]. In order to avoid a deterioration in passenger/pilot comfort as well as fatigue issues associated to the aforementioned phenomena, the multidisciplinary prediction of aeroelastic nonlinearities is of crucial importance.

Although the theoretical fundamentals of dynamic aeroelasticity are to a large extent understood, challenges still exist with respect to the numerically-driven aircraft design and analysis process and the treatment of off-design conditions [101]. For example, the aeroelastic behavior of natural laminar flow wings is subject to recent research [166]. The high-speed stall occurring at transonic conditions, that is caused by three-dimensional aerodynamic buffet, is another research topic of present interest. In general, nonlinear aeroelastic effects require special attention as they cannot be simulated using the well-established and efficient linear potential flow methods [30].

Within the scope of this work, aeroelastic nonlinearities refer, on the one hand, to a nonlinear relationship between the structural deflection and the associated aerodynamic loads. On the other hand, also a freestream condition variation can result in a nonlinear behavior regarding the aerodynamic force and, consequently, the aeroelastic response. For example, it has been shown that the compressibility of the flow affects the unsteady aerodynamic loads such that the flutter speed in the transonic flight regime is reduced. This well-known characteristic is commonly referred to as the transonic dip of the flutter boundary [4]. It is important to emphasize that a nonlinear dependency can be introduced into the coupled system by every sub-discipline, i.e., the structure can also exhibit a nonlinear behavior due to material laws, play, or geometric nonlinearities resulting from large elastic deflections [41]. In the present work, however, only aerodynamic nonlinearities are further taken into account.

Focusing on the industrial aircraft development process, the unsteady flow-induced loads have been mainly modeled using the highly-efficient potential-flow-theory-based methods [29,101], e.g., the doublet-lattice method [1] or the transonic-small-disturbance equations [5]. More complex approaches are typically used only for selective investigations in a later development phase. However, the classical methods are limited in their fidelity if aerodynamic nonlinearities such as strong shocks or distinct flow separations are present [8]. In contrast to the established linear methods, modern computational fluid dynamics (CFD) solvers are able to reproduce the inviscid and viscous flow-induced loads with significantly higher accuracy, capturing the aforementioned nonlinear characteristics [13, 59]. Nevertheless, it is well-known that the use of CFD-based methods is accompanied with a drastically increased computational effort. The problem of costly individual simulations is aggravated by the large parameter space that needs to be investigated for aircraft aeroelastic applications. Considering exemplarily the effort of a typical flutter analysis, unsteady aerodynamic computations must be conducted for the design space spanned by many structural eigenmodes, freestream conditions, excitation frequencies, control surface positions, etc. in order to determine the flutter boundary [23]. Today, the long turnaround times are still limiting the widespread use of unsteady CFD methods with respect to the preliminary aircraft design phase [103, 107].

As a remedy to the aforementioned CFD-related efficiency bottleneck, various linear and nonlinear aerodynamic reduced-order modeling (ROM) approaches have been developed in recent years. The objective of these auxiliary models is the reduction of the full-order problem to a computationally less costly and simpler system description under the premise that the essential static and dynamic characteristics of the underlying aerodynamic system are preserved. According to Lucia et al. [103], a model order reduction can be interpreted as a projection of the full-order problem characterized by a large number of degrees of freedom onto a much smaller subspace that encapsulates the fundamental dynamics. Within the present work, a ROM is considered as a mathematical model that is conditioned by high-fidelity CFD data in order to fulfill a specified simulation task. Once the ROM is available, the simulations of interest can be carried out within a fraction of the computational cost compared to the full-order system. A literature review of the recently-developed unsteady aerodynamic ROM methodologies is given below.

1.2 State of Research

A priori to a more detailed discussion of the published ROM approaches, the broad variety of methodologies requires a fundamental classification. First, the aerodynamic model-order reduction methods can be categorized according to their resulting output, i.e., whether the approach allows the computation of the entire flow field (or surface distribution) or the prediction of integral quantities only. Second, a distinction is advisable with regard to the mathematical equations: Based on the specific ansatz, the reduced-order models might be limited to the treatment of linear problems, whereas more complex approaches are suited to address nonlinearities as well. Third, the methods can be grouped into time-domain- and frequency-domain-based formulations. Finally, it must be distinguished between methodologies that are generally based on a modification or approximation of the underlying fluid dynamic equations (e.g., via linearization) in contrast to system-identification-based methods that are employed virtually as a CFD post-processing tool. Since a recapitulation of all ROM classes is beyond the scope of this work, only the context-relevant approaches that inspired the present research are further taken into account. In particular, the time-domain modeling of motion-induced aerodynamic loads by means of nonlinear system identification principles is of primary interest in the following.

The review articles of Lucia et al. [103], Dowell and Hall [31], and Ghoreyshi et al. [45] provide a comprehensive overview of several ROM concepts, for example, the Volterra theory, the harmonic balance method, and the proper orthogonal decomposition (POD), while their application to unsteady aerodynamic as well as aeroelastic test cases is presented. Volterra-series methods are based on the generalization of the convolutional integral or indicial response approach in order to allow the identification of nonlinear systems. In contrast to the indicial method [6], which is applicable to linear dynamics only, the Volterra theory states that a nonlinear time-invariant system can be described by an infinite sum of convolutional integrals [148]. Therefore, the so-called kernel serves as the multidimensional transfer function, while higher-order kernel elements allow the representation of aerodynamic nonlinearities. For problems with many degrees of freedom or a distinctly nonlinear behavior, however, the estimation of the kernel becomes an exhaustive task that is strongly connected with the fidelity of the resulting ROM. Nevertheless, Silva [147–149] and Raveh [134] demonstrated the successful application of Volterra-theory-based ROMs to weakly-nonlinear unsteady aerodynamic problems. The recent work of de Paula et al. [24] pointed out that a neural network can be employed for the identification of the higher-order kernel components.

The harmonic balance method has been originally developed within the electrical engineering community to model electrical circuits. As the approach is valid for the treatment of nonlinear differential equation systems in general, the methodology has been adopted for fluid dynamic model-order reduction purposes. By assuming periodically unsteady flows, the state of each physical quantity in a finite volume cell is therefore approximated using a Fourier-series-based ansatz. Depending on the order of the considered Fourier coefficients, nonlinear aerodynamic effects can be generally respected. However, both the computational effort and the memory requirements become considerably higher with an increasing order of the Fourier approximation. Initially applied by Hall et al. [53] for turbomachinery-related simulations, the harmonic balance method has been adapted to external aerodynamic problems by Thomas et al. [164]. A similar approach is also followed by the small disturbance or linear frequency domain CFD methods. In contrast to the harmonic balance methodology, the small disturbance solvers are based on the assumption that the unsteady flow perturbations about an aerodynamic reference state can be considered as entirely linear. Based on this hypothesis, the time-linearized Euler equations have been derived by Hall and Crawley [52] with respect to turbomachinery applications. A posteriori, the method has been generalized by Kreiselmaier [86] to external aerodynamic test cases and extended to time-linearized Navier-Stokes formulations by Iatrou [66], Pechloff [127], and Thormann and Widhalm [165].

Furthermore, the proper orthogonal decomposition, which is also known as the principal component analysis or Karhunen-Loève decomposition, is a popular dimensionality reduction technique for a variety of engineering disciplines. In the present context, the basic idea of the POD is the representation of the flow by means of a comparatively small set of representative modes. In this way, it is possible to significantly reduce the number of degrees of freedom with respect to the underlying problem, while capturing the dominant, high-energy structures of the flow. Hence, there is an analogy between the modal transformation applied within the structural dynamics community and the POD usage in terms of aerodynamic ROMs. In general, the POD can be used to treat linear as well as nonlinear problems, which is underpinned by several publications [3,70,103]. For example, the POD modes obtained from a set of steady-state results can be employed to span the possible solution space for a range of freestream conditions. Then, the conservation equations can be re-formulated by means of the available POD subspace as suggested by Zimmermann and Görtz [203]. Though, the focus in this work is on the utilization of the proper orthogonal decomposition as a CFD post-processing tool, which leads to the so-called snapshot method introduced by Sirovich [154]. For unsteady aerodynamic considerations, the flow field or surface distribution must be therefore provided at several time instants, while the grouped data at a certain time step constitutes a snapshot. Subsequently, the available snapshots are used to compute the complete set of potential POD modes. Since the magnitude of the resulting singular values related to each mode indicates the relative importance of the corresponding POD mode, a reduced number of modes can be selected that inherits the essential flow characteristics. The application examples vary from steady to unsteady two- and three-dimensional flow field decompositions. Without claim to completeness, the POD has been applied by Hall et al. [54], Lucia et al. [104], Willcox and Peraire [181], Farhat and Amsallem [36], and

Iuliano and Quagliarella [70] for instance. For the modeling of linear dynamic systems, a frequency domain POD methodology has been proposed by Kim [76] and Kim and Bussoletti [78].

Concurrently, several unsteady aerodynamic reduced-order models originating from linear and nonlinear system identification techniques evolved. It is important at this point to highlight the general difference between system identification and model-order reduction. Traditionally, the system identification methodologies are used to obtain a model of an unknown system by means of available input/output data. In the ROM context, however, a system that has been a priori described by first-order principles such as physical conservation laws is taken into consideration. Thus, the identification methods are used to obtain a model from selected full-order solutions with the aim of an efficiency enhancement. For a more detailed discussion of the system identification terminology, refer to Chapter 3.

A well-known linear aerodynamic identification approach is based on the eigensystem realization algorithm (ERA, [74]) that has been employed by Silva and Bartels [152] to obtain a linear time-invariant state-space model. Thereby, the focus is on the time-domain prediction of integral aerodynamic loads caused by structural excitations [151]. For a further gain in computational efficiency, this method has been extended by various researchers in order to allow the excitation of several structural eigenmodes within a single unsteady CFD simulation [39, 77, 150]. Moreover, linear aerodynamic input/output models have been derived from the recurrence framework approach, which is an established system identification concept [102]. Examples for this class are the auto-regressive moving-average (ARMA) model devised by Cowan et al. [22], Raveh [135], and Won et al. [191] as well as the auto-regressive with exogenous input (ARX) model developed by Zhang and Ye [201].

The referred linear identification approaches can adequately capture the linear dynamic characteristics around a fixed aerodynamic reference state. However, the associated ROMs are exclusively valid for a specific freestream condition and are not suited to describe nonlinear dynamic effects induced by large shock motions or separated flows. With respect to the latter modeling tasks, sophisticated approaches based on nonlinear system identification principles have been developed. Because of their mathematical foundation, these ROMs can be applied to model the nonlinear aerodynamic response, e.g., caused by large-amplitude motions in transonic flow. However, the identification of nonlinear systems is a challenging and often non-robust task [9, 121]. As the homogeneity and additivity principles do not apply in general, the response becomes amplitude-dependent which may lead to bifurcations [8], limit-cycle oscillations [28, 169], or even a chaotic behavior of the system [9]. Furthermore, instability of the identified nonlinear models is frequently encountered for time-marching simulations due to error accumulations as a consequence of the model output feedback [102, 121]. For many applications, the ROM may be also expected to reproduce both linear and nonlinear system characteristics depending on the operating regime and amplitude range. Hence, a variety of algorithms and approaches have been developed to cope with those difficulties.

In the context of unsteady aerodynamic modeling, Faller and Schreck [34,35] proposed the application of a recurrent multilayer perceptron (MLP) neural network [57, 140] for the identification of experimentally-recorded aerodynamic coefficient time series. Marques and Anderson [112] used a feedforward multi-layer neural network to predict the unsteady flow-induced forces acting on the NACA 0012 airfoil. Denegri and Johnson [27] developed a static MLP neural network for interpolating the flutter and LCO characteristics with respect to varying external store configurations. Pitt and Haudrich [129] used a non-recurrent artificial neural network of MLP-type to investigate the influence of distributed non-structural weights on the flutter characteristic of a generic wing. Consequently, Voitcu and Wong [173] demonstrated the capability of artificial neural networks for modeling the dynamic behavior of aeroelastic systems. For that purpose, a two-layer feedforward neural network has been combined with a wavelet decomposition regarding the input/output signals. Furthermore, Rampurawala et al. [133] employed a non-recurrent MLP neural network to model the aeroelastic behavior of the Goland wing. In order to capture dynamic effects using the aforementioned quasi-steady model framework, temporal derivatives of the excitation signal have been added to the input vector of the neural network. Subsequently, Mannarino and Mantegazza [109, 110] further developed those ideas by using a recurrent MLP neural network to approximate the lift and pitching moment coefficients of the NACA 64A010 airfoil.

Besides MLP-based identification approaches, the radial basis function (RBF) neural network [16] is a nonlinear function approximation method that has been utilized in various publications. For instance, Won et al. [191] employed a RBF neural network to predict the motion-induced forces related to the AGARD 445.6 wing. Similarly, Yao and Liou [193] used a RBF approach to model the unsteady aerodynamics of a generic wing/body configuration. Moreover, Zhang et al. [200] employed a recurrent RBF neural network to investigate the LCO behavior of the NACA 64A010 airfoil at transonic flow conditions. For that purpose, randomly-selected centers have been chosen prior to the linear optimization of the basis function widths. Consequently, Winter and Breitsamter [182] utilized a recurrent RBF neural network trained by the orthogonal least-squares algorithm [21] to simulate transient aerodynamic force and moment responses induced by prescribed motions. A different training approach has been followed by Zhang et al. [199] who applied the proper orthogonal decomposition for selecting the RBF centers. With respect to the subsequent basis function width determination, a particle swarm optimization has been carried out. Recently, Kou and Zhang [82] generalized their RBF neural network formulation to allow the incorporation of asymmetric wavelet kernels.

In addition, reduced-order models based on the Kriging interpolation technique [88] have shown the ability for accurate aerodynamic response prediction purposes. For example, Glaz et al. [46, 47] formulated a surrogate model for rotorcraft applications using the external dynamic filter approach linked with a Kriging-based interpolator. Liu et al. [100] simulated the dynamic stall behavior of wind turbine airfoils using a Kriging approximation of the nonlinear response surface. Furthermore, a nonlinear state-space identification methodology has been suggested by Mannarino and Dowell [108] to model unsteady aerodynamic responses. Therefore, the matrices related to the linear part of the state-space model are initially determined by a subspace projection method, while the nonlinear parameters are a posteriori computed using a nonlinear output error optimization.

Another class of ROMs is based on the fuzzy logic theory, which has been originally inspired by neuro-biological processes and human thought patterns. The core element of the fuzzy logic theory, from a mathematical point of view, is the existence of fuzzy sets. In contrast to the well-known binary logic, fuzzy sets allow the assignment of intermediate states of validity/membership, i.e., states between true and false. In this regard, Huang et al. [63] proposed the use of a fuzzified eigensystem realization algorithm to identify the steady aerodynamic characteristics of a small unmanned aerial vehicle. The fuzzified ERA can be considered as a nonlinear generalization of the methodology suggested in Reference [74]. A further application of fuzzy-logic-based decision rules is shown in the work of Kouba et al. [85], who modeled the F/A-18 overall aircraft characteristics from flight test data using a Sugeno approach [14]. Similarly, Wang et al. [177] predicted aerodynamic coefficients for the F-16XL configuration using a Takagi-Sugeno fuzzy model [161] trained by forced-oscillation test data.

In contrast to the methodologies introduced beforehand, only a few approaches have been published that account for variable flow conditions using a monolithic reduced-order model. Though, a single aerodynamic model that is valid across a broad range of freestream conditions or even the entire flight envelope is highly desirable for efficient simulation and control purposes. In 2005, Lind et al. [94] proposed a Volterra-theory-based approach to model the aerodynamics of a generic pitch-plunge system. In particular, the authors employed a first-order parameter-varying approximation with respect to the Volterra model to account for different freestream velocities. Subsequently, Prazenica et al. [131] computed first- and second-order Volterra kernels as a function of a user-defined freestream parameter to obtain results for non-trained flight conditions. An extension of the aforementioned method has been proposed by Omran and Newman [123], who applied a nonlinear parameter-varying approach with respect to the locally-estimated Volterra models. In this way, the approach can deal with a larger range of freestream conditions comprising stronger nonlinear characteristics compared to the linear parameter-varying ansatz. Furthermore, a surrogate-based recurrence framework has been devised by Glaz et al. [47] to model the unsteady aerodynamic forces acting on rotor blades. For capturing the prevailing physical effects, harmonic Mach number variations have been taken into consideration, while a Kriging algorithm is employed to train the nonlinear characteristics. Similarly, Liu et al. [99] utilized a Kriging surrogate model for the prediction of the unsteady aerodynamics of the NACA 64A010 airfoil undergoing a combined pitch and plunge motion, while the freestream condition has been treated as an additional model input. Moreover, Skujins and Cesnik [155] developed a method that unites a linear convolutional method with a nonlinear correction factor approach and the so-called method-of-segments to model the aerodynamics of the AGARD 445.6 wing across multiple Mach regimes. Recently, Kou and Zhang [83] applied a recurrent RBF-neural-network-based ROM to predict integral aerodynamic responses for variable freestream conditions. To challenge the model, they considered the NACA 64A010 airfoil test case undergoing harmonic excitations at transonic flow conditions.

In the previous paragraphs, the POD-based model-order reduction approaches have been discussed independently from the respective linear and nonlinear system identification methodologies. Nevertheless, some combinations of these methods have been proposed for the efficient treatment of aerodynamic and aeroelastic problems. For instance, Park et al. [126] linked a set of POD modes with a single-layer neural network in order to construct static flow fields for efficient wing design optimization purposes. Furthermore, a successful combination of a non-recurrent RBF-based nonlinear system identification approach with the proper orthogonal decomposition has been suggested by Lindhorst et al. [96–98] to study the aeroelastic behavior of the HIRENASD wing-fuselage configuration [136]. By taking many previous input states into account, unsteady problems can be modeled as long as no strong dynamic nonlinearities are present. Consequently, this methodology allows the computation of time-varying surface pressure distributions in a time-efficient manner.

The nonlinear models that are based for example on MLP or RBF neural networks show generally promising results for unsteady aerodynamic model-order reduction applications. The aforementioned approaches exhibit a high precision with respect to the one-step prediction task; see Section 3.3.2 for a detailed discussion. However, multi-step ahead predictions, which characterize the relevant modus operandi for time-marching simulations, often become unstable due to the feedback of the model outputs [9, 84]. Another drawback, from a practical point of view, is the limited capability of the ROMs if both linear and nonlinear dynamics need to be captured with a monolithic model. In order to address these issues, block-oriented models such as Wiener and Hammerstein models or their respective permutations have been widely employed by numerous authors in the system and control theory community [9]. These models are characterized by a linear dynamic block that is followed or preceded by a nonlinear static function approximation block. In the present context, Kou et al. [84] suggested the use of Wiener-type models to obtain an aerodynamic ROM that is valid for small and large amplitude motions. Therefore, the ARX model is utilized to form the linear dynamic block, whereas the static nonlinearities are represented by a RBF neural network. Kou and Zhang [81] further developed this idea by implementing a layered ROM. In this regard, the linear ARX model is independently constructed by exploiting a small-amplitude, linear-dynamic training dataset, while the RBF neural network is conditioned by large-amplitude-motion-based data covering the nonlinear system behavior. Finally, the results provided by the two parallel models are superimposed in order to yield the overall model prediction. Nevertheless, despite the diversity of approaches, some drawbacks are still maintained. Either the state-of-the-art methods are limited to linear dynamic effects by means of a restricted model structure, or the models are non-robust for practical purposes.

1.3 Objectives and Thesis Outline

In order to address the efficiency bottleneck of modern aircraft aeroelastic investigations, a novel unsteady aerodynamic model-order reduction framework based on recurrent local linear neuro-fuzzy models is proposed in this thesis. The focus is on the cost-efficient simulation of aerodynamic loads subject to structural or rigid body excitations. Thus, the main objective is the development of a reliable and accurate system-identification-based methodology capable of predicting nonlinear aerodynamic effects due to freestream parameter variations, arbitrary deflection amplitude signals, and pronounced shock motions. Conditioned by selected full-order CFD solutions, the time-domain ROMs reflect the essential dynamics of the underlying physical equations. Consequently, a significant acceleration of CFD-based multidisciplinary investigations is envisioned, which may allow the assessment of the aircraft aeroelastic behavior at an earlier stage in the development process. Specifically, the following technical problems are approached within the scope of this work:

- Prediction of motion-induced aerodynamic forces and moments across varying freestream conditions using a monolithic model
- Efficient simulation of unsteady surface pressure fluctuations caused by prescribed excitations
- Reduced-order modeling for aerodynamic systems involving both linear and strongly-nonlinear characteristics

For demonstration and validation purposes, several well-established test cases are considered, ranging from a basic two-dimensional airfoil case to a full-scale transport-aircraft-type configuration. Due to the prevailing nonlinear physics, transonic flow conditions are of primary interest in this work, although the methods are applicable to the subsonic and supersonic flight regimes as well. Particular attention is paid to a transparent model training procedure, input/output interface formulation, and error quantification. For a comprehensive assessment of the derived models, the computational efficiency as well as the fidelity of the ROMs is evaluated relative to the full-order CFD simulation procedure.

The present thesis is organized as follows: Chapter 2 discusses the fundamental relationships of the fluid mechanical modeling. In particular, the in-house CFD methods as well as the calculation of aerodynamic forces and moments are dealt with. Moreover, the context-relevant aeroelastic modeling concepts and approaches are introduced. In Chapter 3, the theoretical background of the utilized nonlinear system identification approaches is recapitulated. The focus is laid on the presentation of the recurrence framework followed by a detailed discussion of the neuro-fuzzy-model-based approximation of nonlinear functions. Moreover, application-oriented remarks regarding the reproducibility of the results, error quantification, and training signal design are provided. Subsequently, the unsteady aerodynamic ROM approaches, which have been developed within the scope of this work, are outlined in Chapter 4. Specifically, the approach valid across variable freestream conditions, the surrogate modeling procedure for simulating motion-induced unsteady surface pressure fluctuations, and the methodology for the prediction of strongly-nonlinear aerodynamic characteristics are discussed. In Chapter 5, the neuro-fuzzy-model-based ROM is applied for the modeling of generalized aerodynamic forces induced by structural eigenmode-based excitations. Considering the AGARD 445.6 wing test case, a monolithic model is trained to simulate the motion-induced aerodynamics across subsonic, transonic, and supersonic freestream conditions, while the results are additionally exploited to compute the flutter boundary. Consequently, Chapter 6 demonstrates the application of the proposed surrogate model with respect to the efficient prediction of unsteady pressure distributions. The approach, which is based on a combination of the recurrent neuro-fuzzy model with the proper orthogonal decomposition, is evaluated for the LANN wing undergoing a pitching motion. Furthermore, the performance of the suggested connected neural network approach for modeling strongly nonlinear excitation/response relationships is addressed in Chapter 7. In this regard, small and large amplitude pitch and plunge motions of the NLR 7301 airfoil are investigated using the novel ROM approach. It is shown that the combined model consisting of the recurrent local linear neuro-fuzzy model and the MLP neural network reproduces the essential linear and nonlinear aerodynamic characteristics with high accuracy. In order to evaluate the robustness and validity of the methods in terms of realistic aircraft configurations, the ROMs are further applied in Chapter 8 to the common research model, which is featured by an increased level of complexity relative to the previously studied basic test cases. In this way, the potential of the neuro-fuzzy modeling approach for industrial purposes is indicated. Finally, a summary of the results and findings is given, which is concluded by an outlook on future ROM developments.

2 Aerodynamic and Aeroelastic Simulation Methodology

In this chapter, the unsteady aerodynamic and aeroelastic modeling fundamentals, that are particularly relevant for the research presented in this work, are highlighted. Therefore, the equations of fluid motion, namely the Euler and Navier-Stokes equations, are recapitulated since they form the basis for the conducted flow simulations. Concerning the utilized computational fluid dynamics (CFD) solver framework, the numerical discretization and solution concepts as well as the boundary condition treatment are briefly discussed. In addition, the calculation of flow-induced force and moment coefficients is approached.

Besides the discussion of the aerodynamic computation methodology, the finite element method (FEM) is roughly outlined with respect to the structural dynamic modeling. In this regard, the focus is particularly on the modal reduction of an already available finite-element model. Furthermore, to establish the link between the aerodynamic and the structural modeling frameworks, the concept of generalized aerodynamic forces is introduced. Finally, the application of aeroelastically-coupled models to the simulation of aircraft stability problems is discussed. The present chapter is essentially based on the previous dissertations of Kreiselmaier [86], Iatrou [66], Fleischer [38], Förster [41], and Pechloff [127], all of whom paved the way for the in-house aeroelastic modeling tool chain.

2.1 Computational Fluid Dynamics Framework

For aircraft aeroelastic investigations, the unsteady flow-induced forces and moments acting on the airframe must be determined. Focusing on transonic freestream conditions in particular, the Navier-Stokes equations describe the governing physical relations with respect to the occurrence of both shock-induced nonlinearities as well as viscosity- and flow-separation-related effects. For practical applications, however, the consideration of viscous effects is often omitted to facilitate a first approximation [172,192]. If the viscous fluxes are not taken into account, the Euler equations are obtained as a special case of the Navier-Stokes equations.

Within the scope of this work, the Euler-equations-based solver AER-Eu and the Reynolds-averaged Navier-Stokes solver AER-NS, which have been developed at the Chair of Aerodynamics and Fluid Mechanics of the Technical University of Munich, are used to provide the reduced-order models with training, validation, and test data for the steady and unsteady aerodynamic loads. Moreover, the aforementioned CFD solvers are employed for intermethod comparisons in order to assess the accuracy and fidelity of the proposed reduced-order modeling approaches.

2.1.1 Navier-Stokes and Euler Equations

The Navier-Stokes equations form a nonlinear coupled system of second-order partial differential equations. According to Hoffmann and Chiang [60–62] and Hirsch [59], the mass, momentum, and energy conservation equations can be written for a discrete fluid element without acting volume forces as:

$$\frac{\partial \boldsymbol{q}}{\partial t} + \frac{\partial \boldsymbol{f}}{\partial x} + \frac{\partial \boldsymbol{g}}{\partial y} + \frac{\partial \boldsymbol{h}}{\partial z} = \frac{\partial \boldsymbol{f_v}}{\partial x} + \frac{\partial \boldsymbol{g_v}}{\partial y} + \frac{\partial \boldsymbol{h_v}}{\partial z} \tag{2.1}$$

In Equation (2.1), the solution vector is denoted by $\mathbf{q}$, whereas the respective convective fluxes ($\mathbf{f}$, $\mathbf{g}$, $\mathbf{h}$) and viscous fluxes ($\mathbf{f_v}$, $\mathbf{g_v}$, $\mathbf{h_v}$) are given as:

$$\mathbf{q} = [\rho, \quad \rho u, \quad \rho v, \quad \rho w, \quad \rho e]^\top \tag{2.2}$$

$$\begin{aligned}
\mathbf{f} &= [\rho u, \quad \rho u^2 + p, \quad \rho u v, \quad \rho u w, \quad u(\rho e + p)]^\top \\
\mathbf{g} &= [\rho v, \quad \rho u v, \quad \rho v^2 + p, \quad \rho v w, \quad v(\rho e + p)]^\top \\
\mathbf{h} &= [\rho w, \quad \rho u w, \quad \rho v w, \quad \rho w^2 + p, \quad w(\rho e + p)]^\top
\end{aligned} \tag{2.3}$$

$$\begin{aligned}
\mathbf{f_v} &= [0, \quad \tau_{xx}, \quad \tau_{xy}, \quad \tau_{xz}, \quad u\tau_{xx} + v\tau_{xy} + w\tau_{xz} - q_x]^\top \\
\mathbf{g_v} &= [0, \quad \tau_{yx}, \quad \tau_{yy}, \quad \tau_{yz}, \quad u\tau_{yx} + v\tau_{yy} + w\tau_{yz} - q_y]^\top \\
\mathbf{h_v} &= [0, \quad \tau_{zx}, \quad \tau_{zy}, \quad \tau_{zz}, \quad u\tau_{zx} + v\tau_{zy} + w\tau_{zz} - q_z]^\top
\end{aligned} \tag{2.4}$$

In Equations (2.2)-(2.4), ρ and p denote the fluid's density and pressure, while u, v, w refer to the velocities in x, y, and z direction, respectively. By introducing the heat capacity at constant volume c_v and the temperature T, the specific energy can be generalized to:

$$e = c_v \cdot T + \frac{u^2 + v^2 + w^2}{2} \tag{2.5}$$

Originating from Stokes' hypothesis for a Newtonian fluid, the viscous shear stress tensor elements can be computed based on the formulas presented in Equation (2.6).

$$\begin{aligned}
\tau_{xx} &= \mu\left(2\frac{\partial u}{\partial x} - \frac{2}{3}\left[\frac{\partial u}{\partial x} + \frac{\partial v}{\partial y} + \frac{\partial w}{\partial z}\right]\right), & \tau_{xy} = \tau_{yx} &= \mu\left(\frac{\partial u}{\partial y} + \frac{\partial v}{\partial x}\right) \\
\tau_{yy} &= \mu\left(2\frac{\partial v}{\partial y} - \frac{2}{3}\left[\frac{\partial u}{\partial x} + \frac{\partial v}{\partial y} + \frac{\partial w}{\partial z}\right]\right), & \tau_{xz} = \tau_{zx} &= \mu\left(\frac{\partial u}{\partial z} + \frac{\partial w}{\partial x}\right) \\
\tau_{zz} &= \mu\left(2\frac{\partial w}{\partial z} - \frac{2}{3}\left[\frac{\partial u}{\partial x} + \frac{\partial v}{\partial y} + \frac{\partial w}{\partial z}\right]\right), & \tau_{yz} = \tau_{zy} &= \mu\left(\frac{\partial v}{\partial z} + \frac{\partial w}{\partial y}\right)
\end{aligned} \tag{2.6}$$

Within the present work, air is exclusively considered as the fluid medium. Therefore, the dynamic viscosity μ occurring in Equation (2.6) can be evaluated by employing Sutherlands's law [159]:

$$\mu = \mu_{ref} \left(\frac{T}{T_{ref}}\right)^{\frac{3}{2}} \frac{T_{ref} + 110\ K}{T + 110\ K} \quad \text{with} \ \mu_{ref} = 1.716 \cdot 10^{-5}\ \frac{kg}{m \cdot s},\ T_{ref} = 273.15\ K \tag{2.7}$$

Moreover, the thermal fluxes are summarized in Equation (2.8). In this regard, the thermal conductivity k is calculated using a Prandtl number of $Pr = 0.72$, a heat capacity ratio of $\gamma = c_p/c_v = 1.4$, and a specific gas constant of $R = c_p - c_v = 287.06\ J/(kg \cdot K)$.

$$q_x = -k \cdot \frac{\partial T}{\partial x}, \quad q_y = -k \cdot \frac{\partial T}{\partial y}, \quad q_z = -k \cdot \frac{\partial T}{\partial z} \quad \text{with} \ k = \frac{\mu}{Pr} \cdot \frac{\gamma R}{\gamma - 1} \tag{2.8}$$

Additionally, the equation of state for ideal gases is employed in order to close the system of equations. Based on $p = \rho R T$, the following relation can be derived for the pressure:

$$p = (\gamma - 1) \left[\rho e - \frac{1}{2\rho}\Big((\rho u)^2 + (\rho v)^2 + (\rho w)^2\Big)\right] \tag{2.9}$$

The Euler equations form a special case of the Navier-Stokes equations. Specifically, the viscous fluxes $\mathbf{f_v}$, $\mathbf{g_v}$, $\mathbf{h_v}$ are omitted from Equation (2.1) resulting in a purely hyperbolic partial differential equation system:

$$\frac{\partial \mathbf{q}}{\partial t} + \frac{\partial \mathbf{f}}{\partial x} + \frac{\partial \mathbf{g}}{\partial y} + \frac{\partial \mathbf{h}}{\partial z} = 0 \tag{2.10}$$

2.1.2 Nondimensionalization of the Flow Variables

In the context of the employed CFD solvers AER-Eu and AER-NS, the equations introduced in the previous section are formulated and solved in nondimensional form [66, 86, 127]. The nondimensionalization offers advantages for the comparison of different flow problems and also leads to a reduction of the number of problem-describing variables. Below, the transformation between dimensionful and nondimensional flow quantities is briefly recapitulated.

Following the notation of Reference [86], a dimensionful variable is marked with an overbar, whereas the scaling factor between the nondimensional and the dimensionful quantity is indicated by an asterisk. For an arbitrary variable ϕ, the nondimensional value is therefore obtained by:

$$\phi = \frac{\bar{\phi}}{\phi^*} \tag{2.11}$$

As it has been defined in References [66, 86], the scaling factors ϕ^* are expressed exclusively by means of the grid reference length $\bar{l}_{ref}$, the freestream density $\bar{\rho}_\infty$, the freestream temperature $\bar{T}_\infty$, and the freestream pressure $\bar{p}_\infty$:

$$l^* = \bar{l}_{ref} \qquad \Rightarrow x = \frac{\bar{x}}{l^*},\ y = \frac{\bar{y}}{l^*},\ z = \frac{\bar{z}}{l^*} \tag{2.12}$$

$$\rho^* = \bar{\rho}_\infty \qquad \Rightarrow \rho = \frac{\bar{\rho}}{\rho^*} \tag{2.13}$$

$$T^* = \bar{T}_\infty \qquad \Rightarrow T = \frac{\bar{T}}{T^*} \tag{2.14}$$

$$p^* = \bar{p}_\infty \qquad \Rightarrow p = \frac{\bar{p}}{p^*} \tag{2.15}$$

Based on the four scaling factors shown in Equations (2.12)-(2.15), the reference values for the time t, the dynamic viscosity μ, and the velocity components u, v, w are exemplarily given in Equation (2.16). Analogously, the remaining physical quantities can be transformed into their nondimensional counterpart using the basic definitions for l^*, ρ^*, T^*, and p^*.

$$t^* = \bar{l}_{ref}\sqrt{\frac{\bar{\rho}_\infty}{\bar{p}_\infty}} \qquad \Rightarrow t = \frac{\bar{t}}{t^*} \tag{2.16}$$

$$\mu^* = \bar{l}_{ref}\bar{\rho}_\infty\sqrt{\frac{\bar{p}_\infty}{\bar{\rho}_\infty}} \qquad \Rightarrow \mu = \frac{\bar{\mu}}{\mu^*} \tag{2.17}$$

$$u^* = \sqrt{\frac{\bar{p}_\infty}{\bar{\rho}_\infty}} \qquad \Rightarrow u = \frac{\bar{u}}{u^*},\ v = \frac{\bar{v}}{u^*},\ w = \frac{\bar{w}}{u^*} \tag{2.18}$$

For steady aerodynamic investigations, it is sufficient in most cases to fulfill the geometrical similarity laws along with the Mach number and Reynolds number similarity. Consequently, the wind tunnel test conditions or the CFD simulation set-up must feature the same Mach and Reynolds numbers compared to the respective flight conditions. The freestream Mach number Ma_∞ is given in Equation (2.19), whereas the Reynolds number Re_∞ is defined in Equation (2.20).

$$Ma_\infty = \frac{\bar{U}_\infty}{\bar{a}_\infty} = \frac{\bar{U}_\infty}{\sqrt{\gamma}} \cdot \sqrt{\frac{\bar{\rho}_\infty}{\bar{p}_\infty}} \tag{2.19}$$

$$Re_\infty = \frac{\bar{\rho}_\infty \cdot \bar{U}_\infty \cdot \bar{c}_{Re}}{\bar{\mu}_\infty} \tag{2.20}$$

In Equation (2.20), $\bar{c}_{Re}$ denotes the geometric reference length for the evaluation of the Reynolds number, which is typically chosen as the mean aerodynamic chord of the wing or the root chord. However, for the investigation of unsteady aerodynamic phenomena, additional similarity parameters must be respected, namely the problem-related nondimensional time τ_s and the reduced frequency k_{red} [15]. The aforementioned parameters are introduced in Equations (2.21)-(2.22), while $\bar{c}_{ref}$ represents the dimensionful reference length for the calculation of the reduced frequency.

$$\tau_s = \frac{\bar{U}_\infty}{\bar{l}_{ref}} \cdot \bar{t} = \frac{Ma_\infty \sqrt{\gamma}}{\bar{l}_{ref}} \cdot \sqrt{\frac{\bar{p}_\infty}{\bar{\rho}_\infty}} \cdot \bar{t} \tag{2.21}$$

$$k_{red} = \frac{\bar{l}_{ref}}{\bar{U}_\infty} \cdot \frac{\bar{c}_{ref}}{\bar{l}_{ref}} \cdot \bar{\omega} = \frac{\bar{l}_{ref}}{Ma_\infty \sqrt{\gamma}} \cdot \sqrt{\frac{\bar{\rho}_\infty}{\bar{p}_\infty}} \cdot \frac{\bar{c}_{ref}}{\bar{l}_{ref}} \cdot 2\pi \bar{f} \tag{2.22}$$

If the nondimensional quantities are substituted into the Euler and Navier-Stokes equations, the dimensionless equations can be derived. For further information, refer to References [66, 86, 127, 179].

2.1.3 Equations in Curvilinear Coordinates

In order to allow a CFD-based analysis of arbitrarily shaped geometries based on body-fitted structured grids, the nondimensionalized Euler and Navier-Stokes equations are further transformed into curvilinear coordinates. In this way, the formulation of the boundary conditions is considerably simplified [59]. Prior to the numerical discretization, Equations (2.1) and (2.11) are therefore transformed from the physical space (x,y,z) into curvilinear, body-fitted coordinates. The respective temporal and spacial coordinates of the auxiliary computational space are $\tau = t$ and $\xi(x,y,z,t)$, $\eta(x,y,z,t)$, $\zeta(x,y,z,t)$. Based on References [66, 127], the fluid dynamic equations in curvilinear coordinates can be written as:

$$\text{Navier-Stokes:} \quad \frac{\partial \mathbf{Q}}{\partial \tau} + \frac{\partial \mathbf{F}}{\partial \xi} + \frac{\partial \mathbf{G}}{\partial \eta} + \frac{\partial \mathbf{H}}{\partial \zeta} = \frac{\partial \mathbf{F_v}}{\partial \xi} + \frac{\partial \mathbf{G_v}}{\partial \eta} + \frac{\partial \mathbf{H_v}}{\partial \zeta} \tag{2.23}$$

$$\text{Euler:} \quad \frac{\partial \mathbf{Q}}{\partial \tau} + \frac{\partial \mathbf{F}}{\partial \xi} + \frac{\partial \mathbf{G}}{\partial \eta} + \frac{\partial \mathbf{H}}{\partial \zeta} = 0 \tag{2.24}$$

In Equations (2.23)-(2.24), the transformed solution vector is denoted by $\mathbf{Q}$, whereas the respective convective fluxes ($\mathbf{F}$, $\mathbf{G}$, $\mathbf{H}$) and viscous fluxes ($\mathbf{F_v}$, $\mathbf{G_v}$, $\mathbf{H_v}$) formulated in ξ-, η-, and ζ-direction can be expressed as:

$$\mathbf{Q} = J\mathbf{q} \tag{2.25}$$

$$\begin{aligned}\mathbf{F} &= J\xi_t\mathbf{q} + J\xi_x\mathbf{f} + J\xi_y\mathbf{g} + J\xi_z\mathbf{h}\\ \mathbf{G} &= J\eta_t\mathbf{q} + J\eta_x\mathbf{f} + J\eta_y\mathbf{g} + J\eta_z\mathbf{h}\\ \mathbf{H} &= J\zeta_t\mathbf{q} + J\zeta_x\mathbf{f} + J\zeta_y\mathbf{g} + J\zeta_z\mathbf{h}\end{aligned} \tag{2.26}$$

$$\begin{aligned}\mathbf{F_v} &= J\xi_x\mathbf{f}_v + J\xi_y\mathbf{g}_v + J\xi_z\mathbf{h}_v\\ \mathbf{G_v} &= J\eta_x\mathbf{f}_v + J\eta_y\mathbf{g}_v + J\eta_z\mathbf{h}_v\\ \mathbf{H_v} &= J\zeta_x\mathbf{f}_v + J\zeta_y\mathbf{g}_v + J\zeta_z\mathbf{h}_v\end{aligned} \tag{2.27}$$

The Jacobian determinant of the coordinate transformation J, which is explained in Equation (2.28), can be interpreted as the cell volume in physical space. Moreover, the terms $J\psi_x$, $J\psi_y$, $J\psi_z$ ($\psi \in [\xi, \eta, \zeta]$) refer to the the cell face areas, whereas the expressions $J\xi_t$, $J\eta_t$, $J\zeta_t$ correspond to the velocities of the cell faces in the case of present grid motions.

$$J = \det\left[\frac{\partial(x,y,z,t)}{\partial(\xi,\eta,\zeta,\tau)}\right], \quad \psi_x = \frac{\partial\psi}{\partial x}, \quad \psi_y = \frac{\partial\psi}{\partial y}, \quad \psi_z = \frac{\partial\psi}{\partial z} \quad \text{with } \psi \in [\xi, \eta, \zeta] \tag{2.28}$$

Further details regarding the computation of the metric terms shown in Equation (2.28) as well as the derivation of the curvilinear equations are provided in References [86,146].

2.1.4 Turbulence Modeling

Due to the circumstance that the direct numerical simulation of the Navier-Stokes equations is practically not feasible for aircraft aerodynamic applications using the currently available computing resources [37], additional simplifications and assumptions have been incorporated within the AER-NS solver. Specifically, the flow variables are split into their temporal mean and their turbulent fluctuation part as it has been suggested by Reynolds. By inserting the two splitted parts for each quantity into Equation (2.23) and performing an ensemble averaging operation for the entire equation system, this basic idea leads to the so-called Reynolds-averaged Navier Stokes (RANS) equations [127,143]. Consequently, any flow-inherent turbulent unsteadiness is suppressed, whereas other time-variant flow phenomena are still captured. Nevertheless, due to the nonlinear nature of the Navier-Stokes equations, terms representing turbulent fluctuations still appear in the RANS equations. For these terms – referred to as Reynolds stresses – an additional turbulence modeling is required in order to close the RANS equations. Within the AER-NS solver, the Reynolds stress tensor is approximated by applying the Boussinesq hypothesis, whereas the Spalart-Allmaras turbulence model is employed to model the turbulent eddy viscosity [158]. As the Spalart-Allmaras turbulence model is a one-equation model, an additional transport equation for the eddy viscosity must be solved. Besides, it should be noted that the AER-NS code does not explicitly treat or predict the laminar-turbulent transition. Consequently, the entire flow field including the boundary layer is assumed to be fully-turbulent within the scope of this work if the AER-NS solver is utilized.

2.1.5 Discretization and Numerical Solution

Based on the previously discussed fundamentals, this subsection addresses the discretization and numerical solution methodologies with respect to the Euler and Navier-Stokes equations. In this regard, the focus here is exclusively on the employed CFD solvers, namely AER-Eu and AER-NS.

For the discretization of Equations (2.23)-(2.27), the cell-centered finite volume method (FVM) is applied. Since the FVM exploits the conservation form of the fluid dynamic equations, discontinuous solutions such as shocks are already part of the solution and do not have to be artificially enforced [167]. Due to the aforementioned property, the underlying density-based CFD solvers are especially suited to simulate transonic, compressible flows.

Within the scope of the discretization, the considered flow domain must be divided by means of small hexahedral finite-volume cells, which in total form the computational grid. The CFD solvers AER-Eu and AER-NS support exclusively structured multiblock grids. As the steady or unsteady solution strongly depends on the quality of the underlying grid, the mesh generation is of particular importance for the aerodynamic modeling. On the one hand, the use of structured computational grids leads to an increased manual meshing effort and thus higher overall costs. On the other hand, body-fitted structured grids usually exhibit better grid quality properties compared to unstructured grids, which positively affects the CFD solution fidelity [41, 59]. Since the fluxes are evaluated for each of the six cell faces, the following spatial discretization is obtained for a specific finite volume:

$$\begin{aligned}\frac{\partial \mathbf{Q}_{i,j,k}}{\tau} + \frac{\mathbf{F}_{i+\frac{1}{2},j,k} - \mathbf{F}_{i-\frac{1}{2},j,k}}{\Delta\xi} + \frac{\mathbf{G}_{i,j+\frac{1}{2},k} - \mathbf{G}_{i,j-\frac{1}{2},k}}{\Delta\eta} + \frac{\mathbf{H}_{i,j,k+\frac{1}{2}} - \mathbf{H}_{i,j,k-\frac{1}{2}}}{\Delta\zeta} = \\ \frac{\mathbf{F_v}_{i+\frac{1}{2},j,k} - \mathbf{F_v}_{i-\frac{1}{2},j,k}}{\Delta\xi} + \frac{\mathbf{G_v}_{i,j+\frac{1}{2},k} - \mathbf{G_v}_{i,j-\frac{1}{2},k}}{\Delta\eta} + \frac{\mathbf{H_v}_{i,j,k+\frac{1}{2}} - \mathbf{H_v}_{i,j,k-\frac{1}{2}}}{\Delta\zeta}\end{aligned} \tag{2.29}$$

The discretization of the convective fluxes is based on the upwind flux-difference-splitting procedure developed by Roe [138]. In this regard, a Riemann problem is approximately solved at each cell face to respect the wave propagation characteristics of the solution. Moreover, the second-order spatial discretization accuracy is retained by applying the so-called MUSCL (monotonic upstream-centered schemes for conservation laws) extrapolation [13]. In order to guarantee the total variation diminishing (TVD) property, suitable flux limiters have been implemented [127]. In this way, unphysical oscillations in the vicinity of discontinuities are prevented. With respect to the discretization of the viscous fluxes, the method proposed by Chakravarthy [18] is employed within the AER-NS solver [66].

The second-order accurate temporal integration is performed with the implicit dual-time stepping scheme [13], whereas the embedded pseudo-time solution is computed using the lower-upper symmetric successive over-relaxation (LU-SSOR), [12, 72]. For steady-state simulations, the solution is advanced exclusively by means of the pseudo-time-stepping procedure. Furthermore, a deforming mesh approach is available within the AER-Eu/NS CFD framework. Therefore, predefined and user-defined time laws can be applied to perform a linear interpolation between the reference grid and one or various amplitude grids [38]. The deformed grids are created on the basis of the reference grid by using the methods implemented in the work of Förster [41]. In this context, arbitrary deflections can be interpolated onto the CFD surface grid using the thin-plate spline (TPS) method [32]. A posteriori, the transfinite interpolation (TFI) is used to update the block-internal grid points [49]. Consequently, the unsteady aerodynamic response due to user-defined rigid body or structural-eigenmode-based deflections can be simulated.

2.1.6 Boundary Conditions and Initial Value Problem

With respect to the solution of the Euler and Reynolds-averaged Navier Stokes equations, an adequate boundary treatment is required to formulate a well-posed problem of engineering interest. The following boundary conditions (BCs) are of particular importance for the present work:

- Wall BC: According to Hirsch [59], the conservative variables are linearly extrapolated to the boundary, whereas the resulting velocities are corrected with the kinematic boundary condition. The kinematic boundary condition enforces that the wall-normal velocity of the flow is identical with the surface normal velocity for impermeable bodies. In terms of the AER-NS solver, the applied no-slip condition additionally leads to zero tangential flow velocities relative to the wall. Consequently, all velocity components at the wall are zero for the viscous modeling if no grid motion is taken into account. Besides the no-slip condition, the temperature or the heat flux at the wall must be set for the RANS-based modeling. Within the scope of this work, an adiabatic wall is assumed for all investigations.

- Farfield BC: At the farfield boundary, the inflow conditions characterized for example by the freestream Mach number and the angle of attack are specified. According to Whitfield and Janus [180], the characteristic variables are therefore prescribed under the assumption of a one-dimensional flow propagation according to the characteristic propagation direction. The non-reflecting boundary condition is used in both the AER-Eu and the AER-NS solver. In order to simulate the conditions of an undisturbed external flow, the farfield is placed sufficiently distant from the body to be investigated.

- Symmetry BC: Along the symmetry boundary, the fictitious states of the ghost cells are adapted such that the velocity component normal to the plane of symmetry vanishes.
- Block-cut BC: The block-cut boundary condition ensures the information exchange between adjacent blocks of a structured multi-block grid.

Besides the treatment of the domain boundaries, the flow quantities must be initialized. For steady-state simulations, on the one hand, the solution vector **Q** of each finite-volume cell center is set to the corresponding farfield values. On the other hand, an a priori computed steady solution is commonly imported as the starting point for unsteady CFD simulations.

2.1.7 Aerodynamic Force and Moment Calculation

In this subsection, the computation of the aerodynamic force and moment coefficients is outlined based on Reference [38]. The flow-induced loads acting on the aircraft result mainly from the static pressure distribution. Besides, also the shear stresses have an impact on the aerodynamic loads, especially on the drag component. However, care must be taken that the wall shear stresses are considered exclusively in the case of a viscous CFD simulation.

In the following, the pressure coefficient and the skin friction coefficient are introduced in order to incorporate both effects. For clarity, Equation (2.30) defines the pressure coefficient by employing the nondimensionalized variables discussed in Section 2.1.2.

$$C_p = \frac{\bar{p} - \bar{p}_\infty}{\frac{\bar{\rho}_\infty}{2} \cdot \bar{U}_\infty^2} = \frac{2}{\gamma \cdot Ma_\infty^2}(p-1) \tag{2.30}$$

As a prerequisite for defining the skin friction coefficient, the wall shear stress vector is given in Equation (2.31), while a Newtonian fluid is implicitly assumed. For the computation of $\boldsymbol{\tau}_w$, the gradient of the tangential components of the velocity vector $\mathbf{u}_t = [u_t, v_t, w_t]^\top$ is determined with respect to the wall-normal direction. The index w denotes that the gradient is evaluated at the wall.

$$\boldsymbol{\tau}_w = \mu \left(\frac{\partial \mathbf{u}_t}{\partial s} \right)_w \tag{2.31}$$

Using the definition of the wall shear stress, the skin friction coefficient vector can be computed according to Equation (2.32):

$$\mathbf{C}_f = \frac{\boldsymbol{\tau}_w}{\frac{\bar{\rho}_\infty}{2} \cdot \bar{U}_\infty^2} = \frac{2\boldsymbol{\tau}_w}{\gamma \cdot Ma_\infty^2} \tag{2.32}$$

With the respective surface element vector components in x, y, z direction, namely $dS_{x,i}$, $dS_{y,i}$, $dS_{z,i}$, the pressure-induced force coefficient on surface element i is calculated as follows:

$$\mathbf{C}_{i,p} = \begin{pmatrix} C_{x,i,p} \\ C_{y,i,p} \\ C_{z,i,p} \end{pmatrix} = C_{p,i} \cdot d\mathbf{S}_i = C_{p,i} \cdot \begin{pmatrix} dS_{x,i} \\ dS_{y,i} \\ dS_{z,i} \end{pmatrix} \tag{2.33}$$

Analogously, the shear-stress-induced force coefficient acting on surface element i can be written as:

$$\mathbf{C}_{i,f} = \begin{pmatrix} C_{x,i,f} \\ C_{y,i,f} \\ C_{z,i,f} \end{pmatrix} = \frac{2\mu}{\gamma Ma_\infty^2} \cdot \sqrt{dS_{x,i}^2 + dS_{y,i}^2 + dS_{z,i}^2} \cdot \begin{pmatrix} \left(\frac{\partial u_t}{\partial s}\right)_w \\ \left(\frac{\partial v_t}{\partial s}\right)_w \\ \left(\frac{\partial w_t}{\partial s}\right)_w \end{pmatrix} \tag{2.34}$$

By adding the previously shown pressure- and friction-based force components, the respective aerodynamic force and moment coefficient vectors acting at surface element i are given in body-fixed coordinates as:

$$\mathbf{C}_i = \begin{pmatrix} C_{x,i} \\ C_{y,i} \\ C_{z,i} \end{pmatrix} = \begin{pmatrix} C_{x,i,p} + C_{x,i,f} \\ C_{y,i,p} + C_{y,i,f} \\ C_{z,i,p} + C_{z,i,f} \end{pmatrix} \qquad \text{(Forces)} \tag{2.35}$$

$$\mathbf{C}_{m,i} = \begin{pmatrix} C_{mx,i} \\ C_{my,i} \\ C_{mz,i} \end{pmatrix} = \begin{pmatrix} (x_i - x_{ref}) \cdot C_{x,i} \\ (y_i - y_{ref}) \cdot C_{y,i} \\ (z_i - z_{ref}) \cdot C_{z,i} \end{pmatrix} \qquad \text{(Moments)} \tag{2.36}$$

In Equation (2.36), $\mathbf{x}_{ref} = (x_{ref}, y_{ref}, z_{ref})^\top$ characterizes the user-defined moment reference point. Under consideration of the reference area S_{ref}, the lateral reference length s, and the longitudinal reference length l_μ, the aerodynamic force and moment coefficients in body-fixed coordinates (index b) are obtained via numerical integration over all N_{SE} surface elements:

$$C_{X,b} = \frac{1}{S_{ref}} \sum_{i=1}^{N_{SE}} C_{x,i} \tag{2.37}$$

$$C_{Y,b} = \frac{1}{S_{ref}} \sum_{i=1}^{N_{SE}} C_{y,i} \tag{2.38}$$

$$C_{Z,b} = \frac{1}{S_{ref}} \sum_{i=1}^{N_{SE}} C_{z,i} \tag{2.39}$$

$$C_{M_x,b} = \frac{1}{S_{ref} \cdot s} \sum_{i=1}^{N_{SE}} C_{mx,i} \tag{2.40}$$

$$C_{M_y,b} = \frac{1}{S_{ref} \cdot l_\mu} \sum_{i=1}^{N_{SE}} C_{my,i} \tag{2.41}$$

$$C_{M_z,b} = \frac{1}{S_{ref} \cdot s} \sum_{i=1}^{N_{SE}} C_{mz,i} \tag{2.42}$$

Finally, a coordinate transformation is necessary to obtain the force and moment coefficients in the aerodynamic coordinate system. The transformation from the body-fixed to the aerodynamic reference system for a given angle of attack α and sideslip angle β reads:

$$\begin{pmatrix} C_D \\ C_Y \\ C_L \end{pmatrix} = \begin{bmatrix} \cos\beta & -\sin\beta & 0 \\ \sin\beta & \cos\beta & 0 \\ 0 & 0 & 1 \end{bmatrix} \begin{bmatrix} \cos\alpha & 0 & \sin\alpha \\ 0 & 1 & 0 \\ -\sin\alpha & 0 & \cos\alpha \end{bmatrix} \begin{pmatrix} C_{X,b} \\ C_{Y,b} \\ C_{Z,b} \end{pmatrix} \tag{2.43}$$

$$\begin{pmatrix} C_{M_x} \\ C_{M_y} \\ C_{M_z} \end{pmatrix} = \begin{bmatrix} \cos\beta & -\sin\beta & 0 \\ \sin\beta & \cos\beta & 0 \\ 0 & 0 & 1 \end{bmatrix} \begin{bmatrix} \cos\alpha & 0 & \sin\alpha \\ 0 & 1 & 0 \\ -\sin\alpha & 0 & \cos\alpha \end{bmatrix} \begin{pmatrix} C_{M_x,b} \\ C_{M_y,b} \\ C_{M_z,b} \end{pmatrix} \tag{2.44}$$

In Equations (2.43)-(2.44), C_D, C_Y, and C_L denote the respective drag, side-force, and lift coefficients, whereas C_{M_x}, C_{M_y}, and C_{M_z} symbolize the moment coefficients with respect to the x, y, and z axes of the aerodynamic coordinate system [105].

2.2 Structural Dynamic and Aeroelastic Modeling

In this section, the modeling of the structural dynamics is outlined with respect to the conducted aeroelastic investigations. For structural analysis, solvers based on the finite element method (FEM) are mainly used today. The FEM is a discretization methodology for the approximate solution of partial differential equations and has long since become the standard for structural dynamic computations, but also for thermal and electrodynamic simulations [176]. The content of this section is roughly based on the structural dynamics review given in Reference [38].

In the present context, the basic idea of the FEM is to discretize the structure with finite elements that are interconnected by means of their nodes. However, in contrast to the finite volume method discussed in Section 2.1, also one- and two-dimensional elements such as shells, plates, and beams can be used for modeling purposes besides 3D elements. Across each element, the displacement of the nodes is expressed by a linear combination of so-called shape functions. If the formulation for the displacement is combined with known mechanical relationships and material properties, the elasto-dynamic characteristics can be approximated [44]. Finally, by combining various elements and applying problem-specific boundary conditions, a thin-banded system of algebraic equations is obtained, which can be solved using established numerical methods. Within the scope of this work, already existing structural models or results derived therefrom have been utilized. For this reason, only an introductory overview is given to this topic.

Further information related to the finite-element method and the structural dynamics theoretical background can be found in References [25, 41, 125].

2.2.1 Equations of Motion

Based on Hamilton's principle applied to a mass-spring oscillator, the fundamental structural dynamics equations can be derived [192]. With the displacement vector $\mathbf{x}(t) \in \mathbb{R}^{N_{DOF}}$, the external forces vector $\mathbf{f}(\mathbf{x},t) \in \mathbb{R}^{N_{DOF}}$, and the mass, damping, and stiffness matrices, respectively, $\mathbf{M}$, $\mathbf{C}$, $\mathbf{K} \in \mathbb{R}^{N_{DOF} \times N_{DOF}}$, the equations of motion for a N_{DOF} degree-of-freedom system can be written as:

$$\mathbf{M}\ddot{\mathbf{x}}(t) + \mathbf{C}\dot{\mathbf{x}}(t) + \mathbf{K}\mathbf{x}(t) = \mathbf{f}(\mathbf{x},t) \tag{2.45}$$

A FEM-based structural analysis provides the mass and stiffness matrices, whereas the damping matrix is typically constructed by semi-empirical approaches such as Rayleigh's proportional damping method [192].

The displacement vector $\mathbf{x}(t)$ incorporates up to six degrees of freedom per node, depending on the employed element type and the specific element formulation [125]. In this regard, the three spatial coordinates and, optionally, the three rotational degrees of freedom are represented for each node of the FEM model. In the following, however, it is defined for simplicity that the displacement vector contains only the node's spatial coordinates. Consequently, the number of nodes of the FE model can be expressed as $N_{Nodes} = N_{DOF}/3$. For all considerations presented in this work, it is further assumed that the structure is affected by external aerodynamic forces only. Based on this assumption in combination with the aerodynamic force definitions given in Section 2.1.7, the external forces vector acting at node i of the discrete structure can be expressed in the following way:

$$\mathbf{f}_i = \bar{q}_\infty \cdot \mathbf{C}_i = \frac{\bar{\rho}_\infty}{2} \bar{U}_\infty^2 \cdot \mathbf{C}_i, \qquad \mathbf{f}_i \in \mathbb{R}^{N_{Nodes}} \tag{2.46}$$

For the sake of a clear presentation, Equation (2.46) is based on two implicit assumptions: First, it is presupposed that the centers of the CFD surface elements coincide with the nodes of the FE model. Second, it is assumed that both the aerodynamic and the structural modeling are based on the same body-fixed coordinate system. For practical purposes, however, an interpolation between the aerodynamic and the structural grids is generally required [41, 42]. The overall external forces vector $\mathbf{f}(\mathbf{x},t)$ is obtained by assemblying the nodal forces given in Equation (2.46) across all nodes.

Keeping in mind that the aerodynamic forces are affected by static and dynamic structural deflections, i.e., $\mathbf{f} = f(\mathbf{x}(t))$, Equation (2.45) describes an aeroelastically coupled system. Thereby, the structural system properties are represented by the left hand side of Equation (2.45), whereas the aerodynamic modeling enters the equation by means of the external forces on the right hand side.

2.2.2 Modal Analysis and Transformation to Modal Coordinates

Since complex aerospace structures involve a large number of elements, the FE model in physical space, which is expressed by means of Equation (2.45), is commonly transferred into generalized coordinates in order to reduce the computational effort. Therefore, a modal analysis must be carried out to obtain the structural eigenmodes as well as the natural frequencies. For that purpose, a harmonic motion ansatz is chosen for the displacement vector [192]:

$$\mathbf{x}(t) = \mathbf{x}_0 \cdot e^{\mathrm{i}\omega t} \tag{2.47}$$

By substituting Equation (2.47) into the homogeneous part of Equation (2.45) and neglecting the damping term, the following equations can be derived:

$$\left[-\omega^2\mathbf{M} + \mathbf{K}\right]\mathbf{x}_0 = 0 \quad \xrightarrow{\lambda := \omega^2} \quad \left[-\lambda\mathbf{M} + \mathbf{K}\right]\mathbf{x}_0 = 0 \;\; \Rightarrow \det\left[-\lambda\mathbf{M} + \mathbf{K}\right] \overset{!}{=} 0 \tag{2.48}$$

Equation (2.48) denotes a classical eigenvalue problem, which can be solved for the eigenvalues λ_i by established methods such as the Lanczos algorithm [65]. Once the eigenvalues are known, the natural frequencies f_i can be calculated as:

$$f_i = \frac{\omega_i}{2\pi} = \frac{\sqrt{\lambda_i}}{2\pi} \tag{2.49}$$

Linked to the respective eigenvalues λ_i, the computed eigenvectors $\boldsymbol{\phi}_i \in \mathbb{R}^{N_{DOF}}$ (with $i = 1, \ldots, N_{DOF}$) form the complete set of possible structural modes for the given problem. Nonetheless, if the expected structural deflections can be considered as geometrically linear and if also a linear elastic material behavior is prevailing, the first N_M low-frequency eigenmodes determine the structural dynamic characteristic of the underlying system, whereas higher-order modes can be disregarded [192]. Consequently, the eigenmodes $\boldsymbol{\phi}_i$ can be arranged in form of the so-called modal matrix $\boldsymbol{\Phi} \in \mathbb{R}^{N_{DOF} \times N_M}$, which is illustrated by means of Equation 2.50.

$$\boldsymbol{\Phi} = [\boldsymbol{\phi}_1, \boldsymbol{\phi}_2, \ldots, \boldsymbol{\phi}_{N_M}] \quad \text{with } \lambda_1 \leq \lambda_2 \leq \ldots \leq \lambda_{N_M} \tag{2.50}$$

Since the eigenvectors are scalable by an arbitrary factor, it has become common practice in the structural dynamics community to normalize the modal matrix such that the generalized mass matrix $\mathbf{M}_{gen}$ becomes the identity matrix; see Equation (2.51). Originating from the aforementioned scaling of $\boldsymbol{\Phi}$, the generalized stiffness matrix $\mathbf{K}_{gen}$ can be expressed exclusively by means of the eigenvalues:

$$\mathbf{M}_{gen} = \boldsymbol{\Phi}^\top\mathbf{M}\boldsymbol{\Phi} \overset{!}{=} \mathbf{I} \in \mathbb{R}^{N_M \times N_M} \qquad \Rightarrow \qquad \mathbf{K}_{gen} = \boldsymbol{\Phi}^\top\mathbf{K}\boldsymbol{\Phi} = \mathrm{diag}(\lambda_i) \in \mathbb{R}^{N_M \times N_M} \tag{2.51}$$

For a given set of structural eigenmodes, the Rayleigh-Ritz approach [192] can be used to express the displacement vector by means of the modal matrix and the generalized coordinate vector $\mathbf{q}(t) \in \mathbb{R}^{N_M}$:

$$\mathbf{x}(t) = \mathbf{\Phi} \cdot \mathbf{q}(t) \tag{2.52}$$

Thus, the displacement is approximated by the superposition of N_M structural eigenmodes, whereas the generalized coordinate q_i serves as the scaling factor corresponding to the ith mode. By inserting Equation (2.52) into Equation (2.45) and performing a subsequent left-hand multiplication with $\mathbf{\Phi}^\top$, the basic structural dynamic equation system in modal/generalized form is obtained:

$$\underbrace{\mathbf{\Phi}^\top \mathbf{M} \mathbf{\Phi}}_{\mathbf{M}_{gen}} \ddot{\mathbf{q}}(t) + \underbrace{\mathbf{\Phi}^\top \mathbf{C} \mathbf{\Phi}}_{\mathbf{C}_{gen}} \dot{\mathbf{q}}(t) + \underbrace{\mathbf{\Phi}^\top \mathbf{K} \mathbf{\Phi}}_{\mathbf{K}_{gen}} \mathbf{q}(t) = \underbrace{\mathbf{\Phi}^\top \mathbf{f}(\mathbf{q},t)}_{\breve{\mathbf{f}}_{gen}} \tag{2.53}$$

In Equation (2.53), the respective generalized mass, damping, and stiffness matrices, $\mathbf{M}_{gen}$, $\mathbf{C}_{gen}$, $\mathbf{K}_{gen}$, are mathematically connected with the generalized coordinates $\mathbf{q}(t)$ as well as the generalized (aerodynamic) forces $\breve{\mathbf{f}}_{gen} \in \mathbb{R}^{N_M}$. Although Equation (2.53) describes the basic aeroelastic relations in the time domain for both motion- and gust-induced aerodynamic forces, the focus in this work is exclusively laid on the consideration of motion-induced unsteady aerodynamic loads. In the latter context, Equation (2.53) is also referred to as the time-domain flutter equation.

2.2.3 Computation of Generalized Aerodynamic Forces

In the following, the computation of the time-domain generalized aerodynamic forces (GAFs) is discussed. Within the scope of the present work, the GAFs represent the link between the CFD-based aerodynamic and the structural dynamic modeling.

Starting from the generalized external forces vector $\breve{\mathbf{f}}_{gen} = \mathbf{\Phi}^\top \mathbf{f}$ according to Equation (2.53) and inserting the knowledge about the flow-induced forces as it is shown in Equation (2.46), the mth generalized aerodynamic force vector element $\breve{f}_{gen,m,i}$ acting at surface element i can be written as:

$$\breve{f}_{gen,m,i}(t) = \bar{q}_\infty \cdot \mathbf{C}_i(t) \cdot \boldsymbol{\phi}_{m,i} \qquad \text{with } m = 1, \ldots, N_M \tag{2.54}$$

In Equation (2.54), $\mathbf{C}_i(t)$ denotes the nondimensional aerodynamic force vector introduced in Section 2.1.7, whereas $\bar{q}_\infty$ refers to the dimensionful dynamic pressure. If inviscid flow-induced loads are investigated, the corresponding GAF formula is obtained by replacing $\mathbf{C}_i(t)$ with $\mathbf{C}_{i,p}(t)$ in Equation (2.54). Based on the assumption that only the translational degrees of freedom of the FE nodes are taken into account, $\boldsymbol{\phi}_{m,i} \in \mathbb{R}^3$ denotes a subset of the eigenmode vector $\boldsymbol{\phi}$ that represents the x-, y-, and z-components of the modal deflection of surface element i. In terms of the employed CFD solvers AER-Eu and AER-NS, N_M additional deformed grids representing the mode shapes $\boldsymbol{\phi}_m$ are imported prior to the simulation run in order to carry out the GAF computation within each time step. Analogously to the aerodynamic coefficient computation methodology, a summation is performed to obtain the mth element of the integral generalized aerodynamic forces vector:

$$\breve{f}_{gen,m}(t) = \bar{q}_\infty \cdot \sum_{i=1}^{N_{SE}} \mathbf{C}_i(t) \cdot \boldsymbol{\phi}_{m,i} \tag{2.55}$$

For consistency reasons with respect to the nondimensional flow solver framework, the generalized aerodynamic forces are shown in this work in nondimensional form unless otherwise specified. According to Reference [38], the nondimensional time-domain GAF $\mathbf{f}_{gen}(t)$ is given as:

$$\mathbf{f}_{gen}(t) = \frac{\breve{\mathbf{f}}_{gen}(t)}{\bar{q}_\infty \cdot \left(\bar{l}_{ref}\right)^3} \tag{2.56}$$

Here, the employed computational grids are always scaled such that a grid-internal length of 1 represents 1 m in physical space. Hence, the reference length is given as $\bar{l}_{ref} \equiv 1\ m$ according to Equation (2.12).

2.2.4 Time-Domain Aeroelastic Solution

In order to solve the generalized equations of motion represented by Equation (2.53), the different models and methods described beforehand must be coupled in an interdisciplinary way.

For illustration purposes, it is initially assumed that the inhomogeneous part of Equation (2.53), i.e., the generalized aerodynamic forces vector, is a known input to the structural solver. Therefore, based on available generalized mass, damping, and stiffness matrices as well as eigenmodes, a temporal integration of the second-order differential equation system can be performed. Starting from given initial conditions, the Newmark-β approach is commonly employed to iteratively obtain the time-marching structural solution [41]. Alternatively, Equation (2.53) can be transferred into the state-space representation. The resulting first-order differential equation system can be integrated by the Runge-Kutta method or a multi-step approach such as the Adams-Moulten predictor-corrector scheme [33, 198]. The output of the structural solver framework is the generalized coordinates vector, which is caused by the present aerodynamic, inertial, and elastic forces. Additionally, the generalized coordinates can be directly translated to the prevailing structural displacements using the a priori known eigenmodes.

Taking the aerodynamic solver into account, the deformation of the aircraft's external surfaces is required as an input to the CFD method in order to compute the aerodynamic loads for the altered structural state. Since different computational grids are generally used for the structural dynamic and the aerodynamic modeling, grid and load interpolation methods are employed to ensure that the corresponding model inputs and outputs are compatible. In this regard, it is of particular importance that the total energy is maintained in the coupled system. Otherwise energy is introduced or artificially extracted across the interfaces by means of numerical errors, which can falsify the overall stability properties of the aeroelastic system [118]. Besides the spatial coupling of the solvers, the temporal coupling also affects the quality and stability of the solution. In the literature, a basic distinction is made between so-called loosely-coupled and strongly-coupled approaches, which differ in the way in which information is exchanged between the two solvers [41,192]. As a result of the aerodynamic modeling, the flow solver yields the generalized aerodynamic forces for the provided deformation state. After the GAFs have been transferred to the structural solver, the fluid-structure interaction cycle is repeated until a user-defined termination criterion is fulfilled.

As it has been already indicated in the introduction of this work, the investigated multidisciplinary computations are computationally very demanding. In particular, the CFD solver is by far the largest cost driver for the addressed applications. The situation is further aggravated by the fact that a large parameter space must be considered in terms of the aircraft analysis process. Inter alia, simulations for various flight altitudes, freestream Mach numbers, and angles of attack must be undertaken. Consequently, the number of cases is unmanageable even without considering configurational changes. For this reason, an aeroelastic analysis in the time domain, as described for example in Reference [41], can be conducted in an acedemic environment or for selected simulation cases. However, today's computing resources are still limited to allow comprehensive fully-coupled aeroelastic simulations in an industrial context.

As a remedy to the aforementioned computational cost restrictions, the developed reduced-order models that are discussed in Chapter 4 can be utilized to considerably reduce the simulation effort for aeroelastic and multidisciplinary investigations. For this purpose, the ROM must be conditioned to receive the generalized coordinates as the model input, whereas the generalized aerodynamic forces correspond to the output of the model; see Chapter 5 for instance. In this way, the trained ROM can be used to replace the CFD solver within the coupled solution process, leading to a significant simulation acceleration.

2.2.5 Frequency-Domain Flutter Problem

For the investigation of the aeroelastic stability behavior, also referred to as the flutter problem, small structural perturbations around a given reference state are assumed.

According to Bisplinghoff et al. [11], the aforementioned restriction leads to a linear relation between the structural deflection and the motion-induced unsteady aerodynamic loads if sufficiently small amplitudes are considered. Hence, the time-domain generalized aerodynamic forces vector $\breve{\mathbf{f}}_{gen}(t)$ can be expressed by the convolutional integral involving the generalized-coordinate-based excitation $\mathbf{q}(t)$ and the impulse response transfer function of the aerodynamic system [204]:

$$\breve{\mathbf{f}}_{gen}(t) = q_\infty \cdot \int_0^t \mathbf{Q}(t-\tau) \cdot \mathbf{q}(\tau) d\tau \tag{2.57}$$

In Equation (2.57), $\mathbf{Q}$ symbolizes the generalized aerodynamic forces transfer matrix in the time domain, containing the GAF responses due to impulsive deflections with respect to the structural mode shapes. The relationship shown in Equation (2.57) can be exploited to transform the generalized equations of motion into the frequency-domain since the evaluation of the convolutional integral is simplified in the Laplace domain to a basic multiplication. By combining Equations (2.53) and (2.57), the system of equations can be expressed in the Laplace domain as:

$$\left[\mathbf{M}_{gen}\, s^2 + \mathbf{C}_{gen}\, s + \mathbf{K}_{gen} - q_\infty \cdot \mathbf{Q}(s)\right] \mathbf{q}_0 = \mathbf{0} \tag{2.58}$$

Based on Equation (2.58) formulated for the Laplace operator s, the frequency-domain flutter equation can be derived according to Irwin and Guyett [68] and Hassig [56]; see Equation (2.59). The frequency-domain flutter representation is a well-accepted means for studying the stability characteristics of the aeroelastically-coupled system [11, 192, 204].

$$\left[\frac{\bar{U}_\infty^2}{\bar{c}_{ref}^2}\mathbf{M}_{gen}\, p^2 + \frac{\bar{U}_\infty}{\bar{c}_{ref}}\mathbf{C}_{gen}\, p + \mathbf{K}_{gen} - \bar{q}_\infty \cdot \mathbf{GAF}(k_{red}, Ma_\infty)\right] \mathbf{q}_0 = \mathbf{0} \tag{2.59}$$

$$\text{with } p = \frac{\bar{c}_{ref} \cdot s}{\bar{U}_\infty} = g + \mathrm{i} \cdot k_{red}, \quad k_{red} = \frac{\bar{c}_{ref} \cdot \omega}{\bar{U}_\infty}$$

In Equation (2.59), p denotes the nondimensional Laplace parameter, k_{red} is the reduced frequency analog to the nondimensional quantity introduced in Section 2.1.2, and $\mathbf{GAF}(k_{red}, Ma_\infty) \in \mathbb{C}^{N_M \times N_M}$ symbolizes the complex-valued generalized aerodynamic forces transfer matrix in the frequency domain. The complex matrix element GAF_{ij} represents the contribution of the ith generalized aerodynamic force due to a harmonic motion in eigenmode j. As it is indicated in Equation (2.59), the aerodynamic transfer function depends on the reduced frequency as well as the freestream Mach number. In this work, the **GAF** matrix is computed, on the one hand, using the dynamically fully-nonlinear CFD solver and, on the other hand, by means of the developed time-domain ROM approaches. For this purpose, each structural degree of freedom is harmonically excited for a selected set of reduced frequencies at given freestream conditions. Subsequently, a Fourier analysis is conducted with respect to the time series of the GAF response leading to the frequency-domain transfer function [38]. Within the scope of this work, the **GAF** matrix is used for comparison and verification purposes, i.e., the ROM-based matrix elements are juxtaposed to the respective CFD-based results.

Additionally, a stability analysis is carried out based on Equation 2.59 using the well-established p-k method [56,68] for linear frequency-domain flutter investigations. Starting from a set of tabulated **GAF** matrices for several k_{red}-Ma_{∞}-combinations, Equation (2.59) describes a quadratic eigenvalue problem with respect to the nondimensional Laplace parameter p. For a given dynamic pressure and user-defined discrete velocities, the p-k method is used to solve the eigenvalue problem by iteratively matching the reduced frequency k_{red} with the imaginary part of p for every structural eigenmode [204]. The velocity at which the damping of the entire system (structural and aerodynamic damping) is zero is referred to as the flutter speed V_f.

3 System Identification and Neuro-Fuzzy Approaches

In this chapter, the fundamentals of the employed nonlinear system identification approaches are introduced. The focus is laid on the presentation of the recurrence framework, the clarification of prediction versus simulation operation, as well as a detailed discussion of the neuro-fuzzy modeling approach. The chapter is concluded by application-oriented remarks regarding the reproducibility of the results, error quantification, and training signal design. To some extent, the underlying theory has been already discussed in pre-publications of the author; see References [184, 185, 187, 189, 190].

3.1 Properties of Linear and Nonlinear Systems

Prior to the selection of a suitable identification algorithm, it is of paramount importance to understand and characterize the main properties of the system under investigation. The term *system* describes any process that produces an output signal $y(t)$ in response to an input signal $u(t)$, [156]. By definition, a general dynamic system $\mathbf{G}$ shown in Figure 3.1 maps the inputs $\mathbf{u}(t) = [u_1(t), u_2(t), \dots, u_{n_u}(t)]^\top$ to the outputs $\mathbf{y}(t) = [y_1(t), y_2(t), \dots, y_{n_y}(t)]^\top$. In this regard, n_u denotes the dimension of the input vector, whereas n_y refers to the output vector dimension. Introducing the symbol "$\circ$" to describe the dynamic connection between the input vector $\mathbf{u}(t)$ and the output vector $\mathbf{y}(t)$ via the system operator $\mathbf{G}$, the relation can be generalized to [71, 106]:

$$\mathbf{y}(t) = \mathbf{G} \circ \mathbf{u}(t) \tag{3.1}$$

Based on Smith [156], a linear system is governed by two mathematical principles:

- Homogeneity: Once the system's response $\mathbf{y}(t)$ for a certain input signal $\mathbf{u}(t)$ is known, the output caused by a linearly scaled input is given as:

$$\mathbf{G} \circ \big(k \cdot \mathbf{u}(t)\big) = k \cdot \big(\mathbf{G} \circ \mathbf{u}(t)\big) \tag{3.2}$$

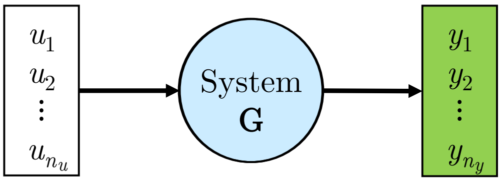

Figure 3.1: General representation of a dynamic system with n_u system inputs and n_y system outputs.

- Additivity: The result obtained by a superposition of arbitrary input signals and their corresponding responses also represents a valid solution to the system. Assuming the two inputs $\mathbf{u}_1(t)$ and $\mathbf{u}_2(t)$, this relation can be stated algebraically as:
$$\mathbf{G} \circ \big(\mathbf{u}_1(t) + \mathbf{u}_2(t)\big) = \mathbf{G} \circ \mathbf{u}_1(t) + \mathbf{G} \circ \mathbf{u}_2(t) \tag{3.3}$$

If it is shown that the system conforms with the homogeneity and the additivity property, the investigated dynamic problem is proven to behave in a linear way [156]. On the contrary, the system is nonlinear if at least one of the aforementioned principles is violated. In the latter case, nonlinear dynamic phenomena such as bifurcations, limit-cycle oscillations, or even a chaotic behavior of the system could be encountered [90], making the modeling task generally more cumbersome. Hence, it is mandatory to perform a linearity test [51] if the mathematical nature of the problem is unclear.

Within the scope of this work, unsteady aerodynamic and aeroelastic test cases are investigated, while the focus is on modeling motion-induced forces and loads. For that purpose, the system is represented by the CFD solver or, from a physical point of view, the discretized Euler and Reynolds-averaged Navier-Stokes equations. As it has been discussed in Section 2.1.1, both of the aforementioned equation systems are nonlinear. Consequently, it can be expected that the system also responds in a nonlinear manner. Indeed, the input/output characteristics of a CFD solver are generally nonlinear except from special cases.

Considering aeroelastic applications in particular, the system inputs are the modal displacements and/or rigid-body deflections, whereas the system response is represented by the corresponding pressure distribution, generalized aerodynamic forces, or aerodynamic coefficients. Chapter 4 gives an approach-dependent definition for the mentioned problems. Provided that the reference state given for example by the freestream conditions can be considered constant, small elastic or rigid-body disturbances lead to a linear variation in the pressure distribution and, consequently, the forces and moments [15, 86, 192]. The linear system characteristics have been shown to be valid for the subsonic, supersonic, and transonic flow regimes, although the steady reference state might be governed by discontinuities such as shocks. Nonetheless, the maximum amplitude to retain the linear relation between the perturbation and the aerodynamic loads is highly case-dependent and must be verified prior to further investigations.

For larger excitation amplitudes, the aerodynamic response becomes no longer linearly related to the displacement amplitude, especially, if transonic flow conditions with distinct shock motion or separation effects occur [8, 174]. Hence, only a nonlinear modeling approach is suited to adequately capture the system behavior for large amplitude motions. Furthermore, the special case of linearity due to small disturbances does not apply across various reference states, e.g., variable freestream Mach numbers. If a single model is intended to be applied for a range of flow conditions, a nonlinear approach must be employed as well [185]. In conclusion, the selection of the model architecture is strongly connected with the specific problem and the question, whether the system outputs depend linearly or nonlinearly on the respective inputs.

3.2 System Identification - General Methodology

System identification approaches are used to obtain a model by means of experimentally or computationally gathered input/output datasets, which characterize the investigated process. In contrast to a white-box modeling procedure, where the model is built by exploiting first principles, i.e., via the numerical discretization of physically-motivated conservation laws, system identification methods require no knowledge about the internal system dynamics [121]. Consequently, the term *black-box* modeling is often used in this context; see Figure 3.2. However, prior knowledge is always advantageous and can be exploited in various ways, leading to so-called *grey-box* models. For instance, if the dynamic order, the presence of time delays, or the existence of a linear operating regime is already known, suitable methods and identification parameters can be selected a priori [9]. By decreasing the model complexity, the computational effort for parameter identification is reduced. Concurrently, a more robust model might be obtained since undesired model characteristics are excluded.

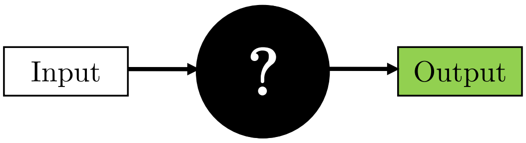

Figure 3.2: Black-box modeling using system identification methods. Known input/output relations are exploited to construct the model.

The general methodology of data-driven model construction has been originally developed within the system and control theory communities. According to Billings [9], system identification can be seen as the complement of the simulation task. Nowadays, identification approaches are widely applied, e.g., for industrial processes, control systems, economic/financial systems, medical systems, and social systems [9]. As the models built via identification are often compact and efficient to simulate, black-box or grey-box system identification can be also applied to realize a model-order reduction [31, 103, 130]. In the literature, many different identification techniques exist with respect to linear as well as nonlinear processes for both the time and the frequency domain. Due to the large variety of different approaches, the recapitulation and classification of available system identification methods is beyond the scope of this work. However, comprehensive overviews of the most popular approaches are given in Ljung [102], Nelles [121], Tangirala [163], Bishop [10], and Billings [9]. In the remainder of this chapter, the focus lies on the presentation of the theoretical fundamentals which form the basis for the author's investigations.

In the last decades, linear systems as well as their identification have been extensively studied and can be considered as well understood [102]. Thereby, it is important to highlight that the use of linear identification does not always imply that the underlying process is intrinsically linear [196]. For practical purposes, the system dynamics can be often considered linear in the vicinity of a specific operating point. For unsteady aerodynamic applications, this property has been exploited by several authors for fixed freestream conditions and small excitation amplitudes, for which a linear model is adequate in most instances [87, 134, 152].

In contrast, the analysis and identification of nonlinear dynamic systems still remains a challenging task [9, 10]. It is important to highlight that nonlinear identification approaches should be only applied if the underlying system is in fact governed by nonlinearities. Otherwise, the use of linear identification techniques is more robust and accurate. Moreover, if no detailed knowledge about the system is available, linear approaches should be initially considered. Beyond the question whether the method must cover linear or nonlinear dynamics (see Section 3.1), further aspects have to be taken into account before and during an identification process [121]:

- Definition of the relevant system inputs and outputs
- Design of training excitation signals and training data acquisition
- Selection of the identification approach
- Choice of the dynamic model order
- Definition of the number of terms/submodels (complexity)
- Estimation of unknown model parameters
- Validation and error quantification

Prior to the discussion of the identification fundamentals, the difference between the system/process input and the respective model input is emphasized in the following. For example, a system may be characterized by n_u inputs and a single output. In contrast, the model input corresponding to this process commonly involves more than n_u input quantities to capture memory effects such as time lags or phase shifts; see Section 3.3 for further information. Hence, dynamic models usually possess a larger input space compared to the corresponding process. Accordingly, three model architectures exist, which are shown in Figure 3.3: First, a single-input single-output (SISO) model defines the basic case where only one degree of freedom influences the scalar model output. Second, a multiple-input single-output (MISO) model maps several inputs to a scalar output quantity. Finally, using a multiple-input multiple-output (MIMO) model, every element of the model input vector is internally coupled with all output vector elements. Consequently, a variation in a single input may affect all model responses. For general applications, the MIMO model architecture is the most frequently encountered case. Nevertheless, many parallel MISO models can be employed for practical purposes to realize a MIMO model.

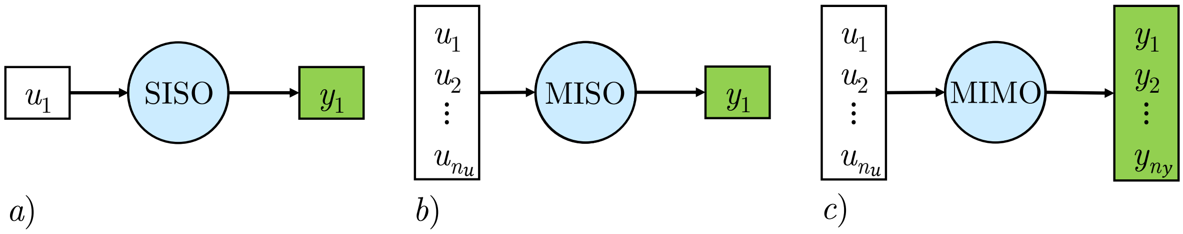

Figure 3.3: Schematic presentation of a single-input single-output (SISO) model (a), multiple-input single-output (MISO) model (b), and multiple-input multiple-output (MIMO) model (c).

Regardless of the model architecture being employed, care must be taken that all inputs, which have a significant influence on the process response, are taken into account. Otherwise, changes in the output quantities can not be traced back to a specific external excitation during the identification. As a consequence, the performance of the resulting model deteriorates drastically.

3.3 Recurrence Framework

The recurrence framework or external dynamics approach is a widely applied concept for nonlinear identification. The basic idea is to compose the nonlinear dynamic model out of two parts [102, 121]:

- External dynamic filter
- Nonlinear multivariate static function

Therefore, the model input vector comprises not only the system inputs, but also previous, time-delayed input and/or output quantities to account for time-dependencies and dynamic effects. A posteriori, the nonlinear function maps the model input vector to the model responses. It is important to emphasize that the nonlinear approximator becomes a static function due to the input/output formulation of the external dynamic model.

3.3.1 External Dynamic Filtering

Based upon the time-discrete recurrence framework approach, which has been originally developed for linear identification and control purposes [9, 102], the response of a general dynamic system can be approximated as a nonlinear function $\mathcal{N}(\cdot)$ of the instantaneous system inputs in combination with a finite series of previous/time-delayed system inputs and previous outputs. The aforementioned principle is well-known as the nonlinear auto-regressive with exogenous input (NARX) modeling architecture. In the following, the system inputs are denoted by $\mathbf{u} \in \mathbb{R}^{n_u}$, whereas the system outputs are characterized by $\mathbf{y} \in \mathbb{R}^{n_y}$. In contrast to the system response, the approximated model output is denoted as $\hat{\mathbf{y}}$. Defining k as the currently considered discrete time increment, i.e., $t_{k+1} = t_k + \Delta t$, $\Delta t = \mathit{const.}$, the one-step prediction problem for a NARX-based model can be generalized to:

$$\begin{aligned} \hat{\mathbf{y}}(k) &= \mathcal{N}\big[\boldsymbol{\Xi}^\top, \mathbf{u}^\top(k),\, \mathbf{u}^\top(k-1), \ldots,\, \mathbf{u}^\top(k-m), \\ &\qquad \mathbf{y}^\top(k-1), \mathbf{y}^\top(k-2), \ldots, \mathbf{y}^\top(k-n)\big] \\ \hat{\mathbf{y}}(k) &= \mathcal{N}\big[\mathbf{x}_{\mathit{Pred}}\big],\ \mathbf{x}_{\mathit{Pred}} \in \mathbb{R}^d \end{aligned} \tag{3.4}$$

In Equation (3.4), $m \in \mathbb{N}$ and $n \in \mathbb{N}^+$ characterize the respective maximum dynamic delay-orders for the input and output quantities, which have to be chosen by the user or, alternatively, via a data-based approach as discussed in Section 3.3.3. Moreover, $\boldsymbol{\Xi}$ defines a non-delayed parameter vector. The latter quantity can be used to incorporate different static equilibrium conditions or operating points such as varying freestream conditions [185], which are not considered as a function of time. Moreover, the consideration of the element $\mathbf{u}^\top(k)$ in Equation (3.4) is optional, because an input might not lead to an instantaneous response. In the present work, the relations expressed by the right hand side of Equation (3.4) are exploited during the training process. Thus, the system response $\mathbf{y}$ known from the training dataset is used for estimating $\mathcal{N}(\cdot)$.

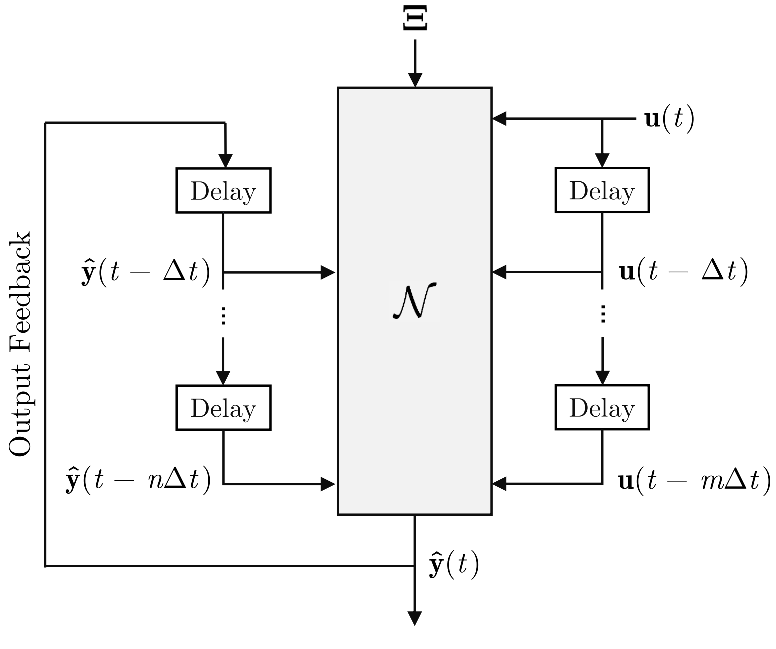

Figure 3.4: Schematic of the recurrence framework methodology. For application purposes, the previously computed, time-delayed model output enters the model input vector (feedback).

However, if the system-identification-based model is applied in recurrent mode for performing a simulation, the recently obtained model outputs have to be fed back iteratively by means of the model input vector as it is shown in Figure 3.4. Hence, $\mathbf{y}$ on the right hand side of Equation (3.4) has to be substituted by $\hat{\mathbf{y}}$ to describe the relationship for the application process of the recurrent model:

$$\begin{aligned} \hat{\mathbf{y}}(k) &= \mathcal{N}\big[\Xi^\top, \mathbf{u}^\top(k),\ \mathbf{u}^\top(k-1), \ldots,\ \mathbf{u}^\top(k-m), \\ &\qquad \hat{\mathbf{y}}^\top(k-1), \hat{\mathbf{y}}^\top(k-2), \ldots, \hat{\mathbf{y}}^\top(k-n)\big] \\ \hat{\mathbf{y}}(k) &= \mathcal{N}\big[\mathbf{x}_{Sim}\big],\ \mathbf{x}_{Sim} \in \mathbb{R}^d \end{aligned} \tag{3.5}$$

If the nonlinear function $\mathcal{N}(\cdot)$, however, is trained according to the relations given by Equation (3.5), the resulting model is referred to as a nonlinear output error (NOE) model. Since the training of a NOE model becomes computationally quite demanding as $\hat{\mathbf{y}}$ changes with the function $\mathcal{N}(\cdot)$ itself, this modeling framework is not further considered in this work.

Keeping in mind that $\mathcal{N}(\cdot)$ is an approximated function, it becomes evident that the model output $\hat{\mathbf{y}}$ is not equal to the system response $\mathbf{y}$. Hence, an error measure $\mathbf{e}$ can be defined in the following way:

$$\mathbf{e}(k) = \mathbf{y}(k) - \hat{\mathbf{y}}(k) \tag{3.6}$$

Presupposing that the error given by Equation (3.6) can be modeled or computed, another recurrence framework becomes promising, namely the nonlinear auto-regressive moving average model with exogenous inputs (NARMAX) architecture [9]. Thereby, information about $\mathbf{e}$ is utilized to increase the prediction quality of the resulting model. Mathematically, a NARMAX model can be written as:

$$\begin{aligned} \hat{\mathbf{y}}(k) &= \mathcal{N}\big[\Xi^\top, \mathbf{u}^\top(k),\ \mathbf{u}^\top(k-1), \ldots,\ \mathbf{u}^\top(k-m), \\ &\qquad \mathbf{y}^\top(k-1), \mathbf{y}^\top(k-2), \ldots, \mathbf{y}^\top(k-n), \\ &\qquad \mathbf{e}^\top(k-1), \mathbf{e}^\top(k-2), \ldots, \mathbf{e}^\top(k-n)\big] \end{aligned} \tag{3.7}$$

In Equation (3.7), it is assumed for convenience that the maximum delay-order of the error term is identical with the maximum output delay-order. In general, a different delay-order can be prescribed for each input, output, and error vector element. The methodology of combining a recurrent with a static neural network, which is outlined in Section 4.3, can be considered to belong to the NARMAX model class.

As the function $\mathcal{N}(\cdot)$ occurring in Equations (3.4), (3.5), and (3.7) is typically unknown, a static multi-dimensional input/output mapping has to be realized based on given training data. For that purpose, any nonlinear function approximation approach can be applied. Within the scope of this work, a neuro-fuzzy model as well as a neural network is employed for this task; see Section 3.4 for further information. Methodologies which combine a recurrence framework with a neural network are referred to as *time-delay neural networks* (TDNN) in the literature [145]. Before introducing the nonlinear function approximation techniques, the difference between the prediction and the simulation modus operandi is clarified.

3.3.2 Prediction Versus Simulation

Given the NARX framework expressed by Equation (3.4), the nonlinear function $\mathcal{N}(\cdot)$ is calibrated during the training process such that the one-step prediction error is minimized in a user-defined sense using the available training samples. Thus, based on the known values for the current and previous system inputs as well as the previous system responses, $\mathcal{N}(\cdot)$ is trained to yield an optimal prediction of the current system output. Thereby, no model output can be found on the right hand side of Equation (3.4). Consequently, the prediction can be only applied if the system response is known. Defining a time series with $k = 1, \ldots, N_S$ samples, it becomes evident from Equation (3.4) that for the initial samples, i.e., $k = 1, \ldots, \max(m,n)$, the prediction cannot be evaluated since the delayed-values of the previous inputs and/or outputs needed for the NARX approximation are not completely defined. In contrast, the one-step ahead prediction can be computed for the remaining samples ($k = \max[m,n] + 1, \ldots, N_S$) assuming that $\mathcal{N}(\cdot)$ is already known. The predicted output does not exactly coincide with the system response due to the approximative character of $\mathcal{N}(\cdot)$ as well as numerical round-off errors. Nonetheless, the prediction can be a valuable indicator for the model performance since a poor prediction quality with respect to the training data usually implies a poor simulation capability as well [10]. If the prediction of the training case does not yield an adequate agreement with the training data, either relevant inputs are missing in the model input vector $\mathbf{x}_{Pred}$ or the chosen model structure and parameters, which are implicitly contained in $\mathcal{N}(\cdot)$, cause a mismatch of the predicted model response and the system output.

For the intended use of the identified model as a reduced-order model, the simulation mode (also known as the recurrent feedback operation) depicted in Figure 3.4 is of primary interest in this work. Therefore, multiple consecutively-executed one-step predictions must be carried out in order to realize a time-marching simulation. Contrary to the prediction operation, the model output itself enters the model input vector $\mathbf{x}_{Sim}$ as it is shown in Equation (3.5). Hence, the model input vector cannot be directly determined prior to the model application and must be adapted within each discrete time step. Thereby, the previously obtained model outputs are iteratively fed back to the model input vector. In this way, the model can be employed for cases where the input excitation is known but the system response is unknown.

Since the one-step prediction produces an error compared to the response of the original process, the output feedback in terms of a multi-step ahead time series prediction can lead to an accumulation of these errors. At worst, instability of the identified models is encountered [84, 102], which must be avoided for practical purposes. Analog to the prediction mode, the initial values $k = 1, \ldots, \max[m,n]$ are also not available with respect to the simulation mode. Moreover, neither the system nor the model response is known. Hence, an adequate simulation initialization regarding the inputs and outputs must be defined, which is typically problem-dependent; see Chapter 4 for a detailed discussion.

3.3.3 Input/Output Delay-Order Optimization

In previous research related to system-identification-based models for aerodynamic and aeroelastic applications, the dynamic delay-orders m and n arising for example in Equation (3.4) are commonly defined by the user; see [96, 135, 201] for instance. Hence, those model parameters are in general not optimally fitted to the underlying problem unless extensive and time-consuming trial and error attempts are undertaken. As suggested by He and Asada [58], the model orders can be alternatively identified by exploiting the training data itself. The application of their methodology towards unsteady aerodynamic reduced-order modeling has been demonstrated in a prior publication of the author [184]. Considering for example the ith output vector element y_i, the Lipschitz quotients for a d-dimensional model input vector $\mathbf{x}_i \in \mathbb{R}^d$ can be evaluated based on N_S training samples according to Equation (3.8), whereas $\mathbf{x}_i$ is defined in Equation (3.9). The input vector may contain the current and time-delayed inputs as well as previous system outputs according to the NARX approach. However, $\mathbf{x}_i$ has to be considered as an unknown since the aim of this method is to find the optimal composition and dimension of the model input vector. After computing the Lipschitz quotients based on Equation (3.8), the so-called Lipschitz index q_i^d can be determined by applying Equation (3.10); see also Reference [58].

$$q_{jk,i}^d = \frac{|y_i(j) - y_i(k)|}{\sqrt{\sum\limits_{l=1}^{d} \Big(x_{l,i}(j) - x_{l,i}(k)\Big)^2}} \qquad \begin{cases} j = \max(m,n) + 1, \ldots, N_S \\ k = \max(m,n) + 1, \ldots, N_S \\ j \neq k \end{cases} \tag{3.8}$$

$$\begin{aligned} \mathbf{x}_i = \big[&\mathbf{u}^\top(k), \mathbf{u}^\top(k-1), \ldots, \mathbf{u}^\top(k-m), \boldsymbol{\Xi}^\top, \\ &y_i(k-1), y_i(k-2), \ldots, y_i(k-n)\big]^\top \end{aligned} \tag{3.9}$$

$$q_i^d = \left(\prod_{l=1}^{o_h} \sqrt{d} \cdot q_i^d(l) \right)^{1/o_h} \qquad \text{with } o_h = \lceil N_S/100 \rceil \tag{3.10}$$

With respect to Equation (3.8), $x_{l,i}(k)$ represents the lth element of the model input vector $\mathbf{x}_i$ evaluated at time step k. Moreover, $q_i^d(l)$ denotes the lth largest Lipschitz quotient $q_{jk,i}^d$.

For practical purposes, the determination of m and n based on the Lipschitz index starts with a maximum input delay of $m = 0$, whereas no time-delayed outputs are considered [184]. Based on this information, the initial model input vector can be constructed, which yields $\mathbf{x}_i = [\mathbf{u}^\top(k), \Xi^\top]^\top$. With each further iteration, the maximum input delay-order m is increased by one. If the Lipschitz index q_i^d evaluated with the adapted input vector $\mathbf{x}_i$ is not further decreased for more input vector dimensions d, the maximum input delay order has been selected adequately. Subsequent to the input delay optimization, the same procedure is repeated in order to specify the output delay order. Thereby, the previously obtained input delay m is retained and the initial output delay-order is set to $n = 1$. Analogously, n is increased by one within each iteration until the termination criterion is satisfied. Here, the iteration process for both the input and output delays is stopped if the relative change of the Lipschitz index q_i^d over one iteration reaches a value below the defined threshold of 1% [184].

3.4 Nonlinear Function Approximation

In the following, the employed neural network and neuro-fuzzy-model approaches are outlined, which serve for the data-driven approximation of the nonlinear function $\mathcal{N}(\cdot)$. Therefore, the fundamental ideas of neural networks, fuzzy logic, and neuro-fuzzy modeling are briefly discussed. Besides, the training procedure as well as the model's strengths and weaknesses are highlighted.

3.4.1 Introduction to Neural Networks and Fuzzy Logic

As an example of bionics, the research on artificial neural networks (ANNs) was originally motivated by the natural structures and capabilities of the human brain. According to the biological counterpart, neural networks were found to be well-suited and effective for complex tasks such as information linking and processing, perception, pattern recognition, learning, and adaption [57, 121]. During the past decades, investigations were initiated to apply the observed functionalities and principles for the solution of engineering problems. Starting with the rediscovery of the back-propagation algorithm in 1986, the development and application of neural networks received increased attention [140, 145]. Moreover, due to the recent advances in computer architectures, high-performance computing capabilities, and programming languages, the success of neural networks still continues. Historically, the application of ANNs such as the MLP neural network or the radial basis function neural network for identification, control, and time series prediction problems was proposed in the 1990s by Chen et al. [19, 20] and Narendra and Parthasarathy [120]. Subsequently, also neuro-fuzzy approaches [17, 121] and a variety of other neural network methodologies have been developed and applied to engineering problems [9].

For convenience, the term *neural network* (NN) is used as a synonym for ANN in the following because no biological issues are considered within the scope of this work. In fact, many research efforts in the field of artificial neural networks are no longer related to the biological example, but require a broad knowledge with respect to mathematics, statistics, signal processing, optimization, and computer science [121]. Hence, the methods are developed for specific purposes and do not necessarily mimic the neural networks occurring in nature. Nowadays, neural-network-based approaches are widely applied for classification, function fitting, nonlinear identification, time-series forecasting, and control purposes [9].

Neural networks can be generally characterized by a large number of simple processing units, called neurons, which are strongly interconnected with each other. Hence, a NN is robust against the failure of single neurons and able to adapt its parameters and structural composition by exploiting a set of training data [121].

Following the terminology accepted in the neural network community, the network depicted in Figure 3.5 can be subdivided into three layers [10, 57, 182]: Initially, the input layer distributes all input vector elements to the first hidden layer. Within the hidden layer, linear or nonlinear computations are carried out depending on the network architecture and the user-defined activation function. The resulting information is weighted and passed to the next hidden layer in the case of a deep neural network or, alternatively, the output layer. Finally, each output layer neuron receives the weighted signals of the previous layer and commonly performs a linear operation in order to yield the output quantity. Although a single neuron enables only simple algebraic operations, the synergistic interaction of many neurons makes the neural network powerful for the aforementioned purposes [121].

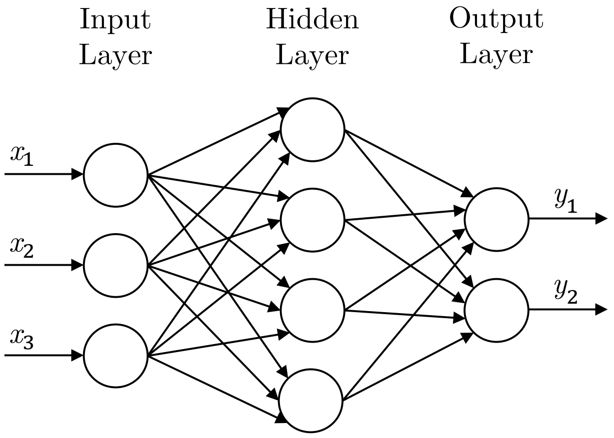

Figure 3.5: Schematic of a neural network with a single hidden layer connecting three input quantities with a two-dimensional output vector.

According to Schröder [145], many neural network approaches have become established for research and industrial applications. For example, the radial basis function (RBF) neural network and the general regression neural network (GRNN) achieve their approximation capability by the weighted superposition of basis functions. Other network architectures, such as the popular multilayer-perceptron (MLP) neural network, use the ridge construction mechanism in order to approximate the target function.

Given a multilayer feedforward neural network, i.e., a neural network with one or more hidden layers such as the MLP neural network discussed in Section 3.4.3, the input signals are propagated and processed layer by layer to obtain the network's response [9]. In contrast to a feedforward NN, where the information is only transferred unidirectionally, a recurrent network is characterized by the feedback of the NN's output to the hidden layer neurons or the input layer. Applying the relations introduced in Section 3.3, most of the models considered in this investigation belong by definition to the class of recurrent neural networks.

Since the focus in this work is laid on system identification and nonlinear function approximation, the so-called supervised training methodology is always applied here[1]. Hence, the network structure and the unknown parameters are calibrated according to a known dataset via an approach-dependent learning strategy. During the training procedure, the weights defining the connection strength between different neurons are modified in order to represent the training data optimal in a user-defined statistical sense [9].

Parallel to the advances in the artificial neural network community, identification approaches based on fuzzy logic have been devised. In general, fuzzy logic can be considered as an extension of the classical Boolean logic, in which only the integers 0 (*false*) and 1 (*true*) are permitted to characterize a variable's state. Originally proposed by Zadeh in the 1960s, a fuzzy set can contain any real value in the closed interval of $[0, 1]$ to describe a quantity's degree of truth [195]. This development has been motivated by the fact that humans often communicate and think in an uncertain or imprecise manner [121].

By employing methods based on fuzzy logic theory, vague statements or observations are treated in order to interpret their validity in an algebraic manner. Consequently, models can be derived which allow the application of reasoning mechanisms in form of rules using fuzzy inputs and outputs [121]. For practical purposes, the well-known linguistic, singleton, Mamdani, and Takagi-Sugeno fuzzy systems are of particular importance [113]. The first step, referred to as *fuzzification*, is the definition of so-called membership or validity functions. Validity functions realize the translation process from uncertain information towards data that is assessable by computers. As a consequence, all uncertain interrelations are described via membership functions, which are mathematically defined for the entire input or output space. For example, an input A may be either *low* or *high*, whereas an output B can be assigned with the three fuzzy states

---

[1] Unsupervised training methods are typically applied for data classification.

slow, *medium*, and *fast*. The fuzzification process connects these fuzzy states with value ranges, for example, with respect to the altitude or the speed. After the considered inputs and outputs have been fuzzyfied, rules can be applied to logically connect the fuzzy inputs to the respective output functions. The rules reflect the vaguely formulated dependencies and can be defined, along with the membership functions, either by expert knowledge or, alternatively, via a data-driven learning algorithm. For instance, a possible rule could be as follows: if input A is *high* or input B is fast then output O is *poor*. The operator for the logical connection, i.e., the *or* in the previous example, is realized by algebraic functions or min/max operators. Finally, the fuzzy outputs must be *defuzzified* to obtain the overall model outputs of interest. Based on this roughly depicted methodology, models can be constructed to facilitate decisions or approximate nonlinear multivariate functions. The reader is advised to References [14,89,113,121,195] for further information about the fundamentals of fuzzy logic.

As already indicated, fuzzy models can be partly or even completely constructed via a training procedure in combination with a given set of training data. This leads to so-called *neuro-fuzzy networks* (NFMs), while the terminology indicates the link between fuzzy modeling and the training techniques known from the neural network community. Nonetheless, the learning procedures for neuro-fuzzy models must not necessarily be adapted from classical neural networks. Representative approaches for the class of NFMs are the adaptive-network-based fuzzy inference system (ANFIS) of Jang [73] and the local linear neuro-fuzzy model. The latter nonlinear function approximation technique is discussed in more detail below.

3.4.2 Local Linear Neuro-Fuzzy Models

Neuro-fuzzy models consolidate fundamental ideas from the research areas of neural networks and fuzzy logic [121, 145]. Concerning the local linear NFM in particular, the basic idea is to piecewisely approximate a nonlinear multivariate function via the superposition of several linear submodels. Thereby, each local linear model (LLM) is valid only within certain bounds of the model input space. The assignment of the LLM's activation region is implemented by means of fuzzy membership functions, i.e., the local linear model is always linked with a corresponding validity function. Consequently, the overall model output becomes a blended superposition of the individual LLM responses.

Analog to the general network schematic discussed in Section 3.4.1, the local linear neuro-fuzzy model can be composed of three layers as it is shown in Figure 3.6: The input layer distributes the input vector information $\mathbf{x}$ to the M neurons contained in the hidden layer. Within each neuron, the received data are processed in order to yield, on the one hand, the output of the local linear model. On the other hand, the corresponding degree of validity is computed based on the current input. Subsequently, both information, namely the LLM output and the activation level, are consolidated to obtain the output of the neuron. Finally, the data gathered from all neurons contained in the hidden layer are linearly combined to produce the overall model output.

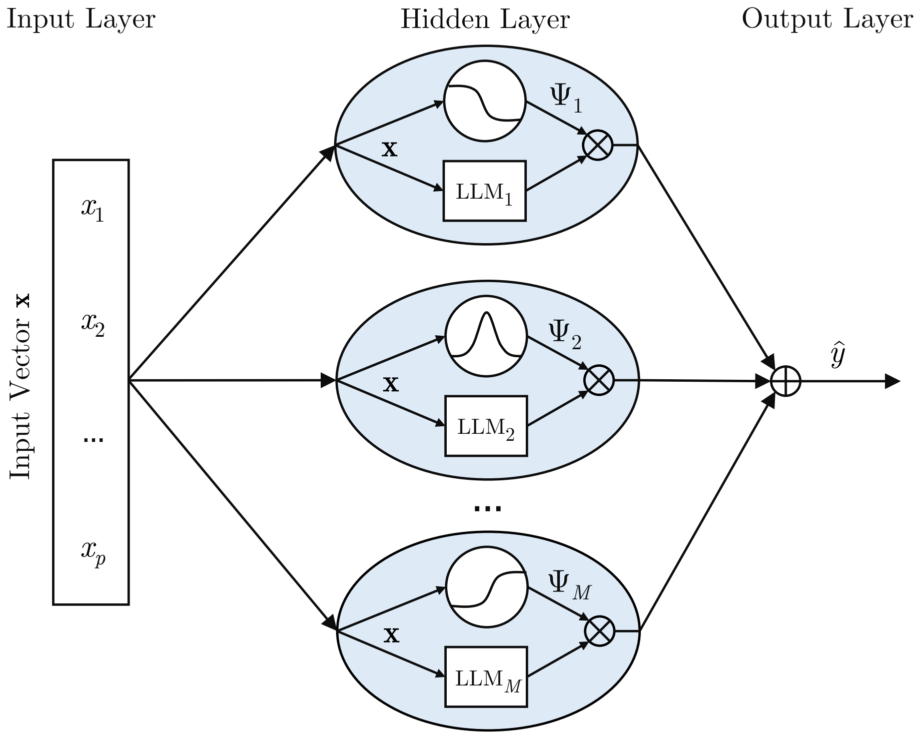

Figure 3.6: Schematic representation of the local linear neuro-fuzzy model according to Reference [121].

Concerning the training of the local linear NFM based on given input/output samples, the local linear model tree (LOLIMOT) algorithm has been selected in this work. Using this training strategy, both the structure of the model as well as the unknown parameters are optimized. For the given local linear NFM, the structural optimization refers to the specific placement of the local linear models in the parameter space as well as the determination of the number of neurons. The LOLIMOT procedure published by Nelles in 1999 has been utilized by various authors for modeling and identification purposes [121]. For instance, it has been employed for pH control [141], the identification of a Diesel engine turbocharger [121], flight control [55], and the modeling of self-excited thermo-acoustic oscillations [71]. Here, the NFM is used to approximate the unknown nonlinear function $\mathcal{N}(\cdot)$ introduced in Equation (3.4) in order to model unsteady aerodynamic characteristics. Below, the mathematical basics of the model as well as the training procedure are discussed.

3.4.2.1 Basis Function Formulation

A local linear neuro-fuzzy model with M local linear sub-models can be written as:

$$\begin{aligned}\hat{y} &= \sum_{j=1}^{M} \Big[w_{j0} + \mathbf{w}_j^\top \cdot (\mathbf{x} - \mathbf{c}_j) \Big] \cdot \Psi_j(\mathbf{x}, \mathbf{c}_j, \mathbf{\Sigma}_j) \\ &= \sum_{j=1}^{M} \Big[w_{j0} + w_{j1} \cdot (x_1 - c_{j1}) + \ldots + w_{jp} \cdot (x_p - c_{jp}) \Big] \cdot \Psi_j(\mathbf{x}, \mathbf{c}_j, \mathbf{\Sigma}_j)\end{aligned} \tag{3.11}$$

In Equation (3.11), $\mathbf{x} \in \mathbb{R}^p$ characterizes the NFM input vector that is related to the scalar output quantity $\hat{y}$ by means of the local linear neuro-fuzzy model. The respective weights w_{j0} and $\mathbf{w}_j \in \mathbb{R}^p$ refer to the offset/bias and the linear model parameters of the jth LLM. Each local linear model spans a hyperplane in the p-dimensional input space defined by $\mathbf{x}$. Moreover, Ψ_j denotes the fuzzy membership function that is linked with the jth local linear model. It is composed of Gaussians evaluated with the Euclidean distance from the input vector to the center $\mathbf{c}_j$ of the jth neuron. As the validity functions are normalized similar to the procedure known from normalized radial basis function (NRBF) neural networks, the sum of all membership functions evaluated at any point of the model input space is one. This property, referred to as the partition of unity, can be mathematically written as $\sum_{j=1}^{M} \Psi_j(\mathbf{x}, \mathbf{c}_j, \mathbf{\Sigma}_j) = 1$. This characteristic is ensured by the following equation:

$$\Psi_j(\mathbf{x}, \mathbf{c}_j, \mathbf{\Sigma}_j) = \frac{\mu_j(\mathbf{x}, \mathbf{c}_j, \mathbf{\Sigma}_j)}{\sum_{k=1}^{M} \mu_k(\mathbf{x}, \mathbf{c}_j, \mathbf{\Sigma}_j)}, \qquad \mathbf{\Sigma}_j = \begin{bmatrix} \frac{1}{\sigma_{j1}^2} & 0 & 0 & 0 \\ 0 & \frac{1}{\sigma_{j2}^2} & 0 & 0 \\ \vdots & \vdots & \ddots & \vdots \\ 0 & 0 & 0 & \frac{1}{\sigma_{jp}^2} \end{bmatrix} \in \mathbb{R}^{p \times p} \tag{3.12}$$

In this context, the employed validity functions evaluated with the respective centers $\mathbf{c}_j \in \mathbb{R}^p$ and basis function widths $\mathbf{\Sigma}_j$ are described by Equation (3.13).

$$\begin{aligned}\mu_j(\mathbf{x}, \mathbf{c}_j, \mathbf{\Sigma}_j) &= \exp\left[-\frac{1}{2} \Big((\mathbf{x} - \mathbf{c}_j)^\top \mathbf{\Sigma}_j (\mathbf{x} - \mathbf{c}_j) \Big) \right] \\ &= \exp\left[-\frac{1}{2} \left(\frac{(x_1 - c_{j1})^2}{\sigma_{j1}^2} + \ldots + \frac{(x_p - c_{jp})^2}{\sigma_{jp}^2} \right) \right]\end{aligned} \tag{3.13}$$

Equations (3.11)-(3.13) define the general structure of the NFM. Keeping in mind that only a set of associated input and output information is available for the identification purpose, many unknowns must be determined to obtain the desired model. Those unknowns are the weights w_{j0} and $\mathbf{w}_j$, the centers $\mathbf{c}_j$, and the basis function widths

$\boldsymbol{\sigma}_j \in \mathbb{R}^p$ contained in $\boldsymbol{\Sigma}_j$ ($j = 1, \ldots, M$). Besides, also the model complexity M is typically not known a priori and, therefore, must be adapted to the problem as well. Given the aforementioned tasks, the LOLIMOT algorithm is a well-suited procedure to train the neuro-fuzzy model. Since the underlying methodology is of particular interest for this work, the essential training steps are further highlighted in the following.

3.4.2.2 Training Procedure: LOLIMOT Algorithm

The local linear model tree algorithm constitutes an iterative training strategy starting with the estimation of a global linear model. Subsequently, the model is continuously refined via axis-orthogonal splits with regard to the p input dimensions. Thus, local linear model partitions are added to regions with predominant nonlinearities such that the model complexity is gradually increased within each iteration. As a consequence, an incrementally expanding tree structure is obtained as it can be seen in Figure 3.7. Due to these properties, some inputs may linearly influence the model output while others contribute nonlinearly to the overall response.

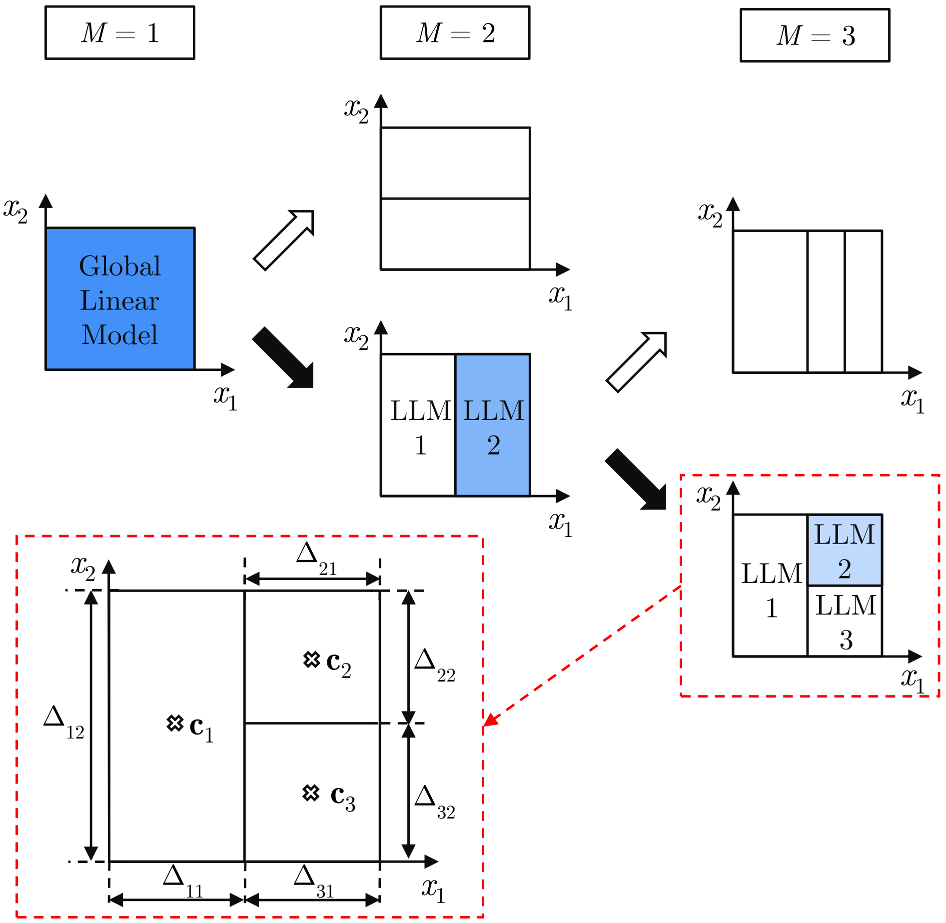

Figure 3.7: Structure selection mechanism based on the LOLIMOT algorithm. An example case with two input dimensions is shown for the first three iterations.

Considering a MISO model, the LOLIMOT training strategy can be recapitulated by the following steps [121, 185, 189]:

1) Initialization: As the starting point, a global linear model ($\Psi_1 = 1$, $M = 1$) is computed by estimating the weights w_{j0} and $\mathbf{w}_j$ for $j = 1$ using linear least-squares optimization. Since the model output depends linearly on the aforementioned parameters, a linear method is sufficient to calculate the weighting factors. For estimating the weights within the LOLIMOT procedure, the training dataset containing $i = 1, \ldots, N_T$ samples is employed. The training dataset is a subset of the available process data. A detailed discussion regarding the important distinction between training, validation, and test data is provided in Section 3.5. Defining the center of the global linear model as shown in Equation (3.14), the linear parameters can be estimated according to Equations (3.15) and (3.16).

$$c_{1i} = \frac{\max_{1 \leq k \leq N_T} \Big(x_i(k)\Big) - \min_{1 \leq k \leq N_T} \Big(x_i(k)\Big)}{2} \quad \text{for } i = 1, 2, \ldots, p \tag{3.14}$$

$$\mathbf{X} = \begin{bmatrix} 1 & \Big(x_1(1) - c_{11}\Big) & \Big(x_2(1) - c_{11}\Big) & \cdots & \Big(x_p(1) - c_{11}\Big) \\ 1 & \Big(x_1(2) - c_{12}\Big) & \Big(x_2(2) - c_{12}\Big) & \cdots & \Big(x_p(2) - c_{12}\Big) \\ \vdots & \vdots & \vdots & \ddots & \vdots \\ 1 & \Big(x_1(N_T) - c_{1p}\Big) & \Big(x_2(N_T) - c_{1p}\Big) & \cdots & \Big(x_p(N_T) - c_{1p}\Big) \end{bmatrix} \tag{3.15}$$

$$\begin{bmatrix} w_{10} \\ \mathbf{w}_1 \end{bmatrix} = \left(\mathbf{X}^\top \mathbf{X}\right)^{-1} \mathbf{X}^\top \overline{\mathbf{y}} \tag{3.16}$$

In Equation (3.16), $\overline{\mathbf{y}} \in \mathbb{R}^{N_T}$ denotes the scalar outputs assembled in a vector for all training samples ($k = 1, 2, \ldots, N_T$):

$$\overline{\mathbf{y}} = [y(1), y(2), \ldots, y(N_T)]^\top \tag{3.17}$$

2) Local error estimation: The next step consists in finding the worst performing local linear model. Therefore, a locally-defined loss function is evaluated for all existing LLMs ($j = 1, 2, \ldots, M$):

$$I_j = \sum_{i=1}^{N_T} \Psi_j\Big(\mathbf{x}(i), \mathbf{c}_j, \mathbf{\Sigma}_j\Big) \cdot \Big(y(i) - \hat{y}(i)\Big)^2 \tag{3.18}$$

The local linear model which exhibits the highest error I_j is selected for the splitting procedure discussed in the third step. If only the global linear model initialized within the first step is present, it is automatically chosen. In Figure 3.7, bluish-colored models refer to the LLMs that yield the highest local error within the corresponding iteration.

3) Model refinement: The previously detected, worst-performing LLM is split in each input dimension with a ratio of 1:1 resulting in p temporary models. As a consequence of this partitioning process, the centers, widths, and linear weights have to be updated with respect to the p potential models and their local linear sub-models. Therefore, the following substeps need to be performed: On the one hand, the unknowns $\mathbf{c}_j$ are determined as the geometric center of the corresponding jth hyperrectangle; see Figure 3.7 for a two-dimensional visualization. On the other hand, the basis function widths $\boldsymbol{\sigma}_j$ are given as the input space extensions of the respective local linear sub-model scaled by the user-defined constant k_σ. According to the schematic depicted in Figure 3.7, the width can be written as $\sigma_{jl} = k_\sigma \cdot \Delta_{jl}$. Thereby, Δ_{jl} denotes the extension in dimension l related to the jth LLM. For all considerations in this work, the scaling factor is chosen to $k_\sigma = 1/3$ as suggested in Reference [121]. Since the nonlinearly-acting parameters are known once the centers and widths are determined for the given model structure, the weights can be computed by linear methods again. Therefore, the local weighted least-squares technique is carried out according to Equations (3.19), (3.20), and (3.21) in order to calculate the weights w_{j0} and $\mathbf{w}_j$. It is important to emphasize that a weighted least-squares technique must be employed to correctly consider the influence of the validity functions.

$$\mathbf{X}_j = \begin{bmatrix} 1 & \Big(x_1(1) - c_{j1}\Big) & \Big(x_2(1) - c_{j1}\Big) & \cdots & \Big(x_p(1) - c_{j1}\Big) \\ 1 & \Big(x_1(2) - c_{j2}\Big) & \Big(x_2(2) - c_{j2}\Big) & \cdots & \Big(x_p(2) - c_{j2}\Big) \\ \vdots & \vdots & \vdots & \ddots & \vdots \\ 1 & \Big(x_1(N_T) - c_{jp}\Big) & \Big(x_2(N_T) - c_{jp}\Big) & \cdots & \Big(x_p(N_T) - c_{jp}\Big) \end{bmatrix} \tag{3.19}$$

$$\begin{aligned} \mathbf{Q}_j &= \begin{bmatrix} \Psi_j\Big(\mathbf{x}(1), \mathbf{c}_j, \mathbf{\Sigma}_j\Big) & 0 & \cdots & 0 \\ 0 & \Psi_j\Big(\mathbf{x}(2), \mathbf{c}_j, \mathbf{\Sigma}_j\Big) & \cdots & 0 \\ \vdots & \vdots & \ddots & \vdots \\ 0 & 0 & \cdots & \Psi_j\Big(\mathbf{x}(N_T), \mathbf{c}_j, \mathbf{\Sigma}_j\Big) \end{bmatrix} \\ &= \operatorname{diag}\Big[\Psi_j\Big(\mathbf{x}(1), \mathbf{c}_j, \mathbf{\Sigma}_j\Big), \ \ldots, \Psi_j\Big(\mathbf{x}(N_T), \mathbf{c}_j, \mathbf{\Sigma}_j\Big)\Big] \end{aligned} \tag{3.20}$$

$$\begin{bmatrix} w_{j0} \\ \mathbf{w}_j \end{bmatrix} = \arg\min\{I_j\} = \left(\mathbf{X}_j^\top \mathbf{Q}_j \mathbf{X}_j\right)^{-1} \mathbf{X}_j^\top \mathbf{Q}_j \bar{\mathbf{y}} \quad \text{for } j = 1, 2, \ldots, M \tag{3.21}$$

The matrices in Equations (3.19) and (3.20) have the respective dimensions $\mathbf{X}_j \in \mathbb{R}^{N_T \times (p+1)}$ and $\mathbf{Q}_j \in \mathbb{R}^{N_T \times N_T}$. Analog to the model initialization, the definition of $\overline{\mathbf{y}}$ is given in Equation (3.17).

4) Error evaluation: The squared error e expressed by Equation (3.22) is evaluated for the previously generated p temporary models in order to detect the best splitting configuration. For this purpose, the validation dataset is employed, which contains N_V data samples that have not been used for the aforementioned weighting factor estimation. Hence, the p models are evaluated yielding a set of outputs $\hat{y}$ that can be compared to the reference outputs y by means of Equation (3.22).

$$e = \sum_{i=1}^{N_V} \Big(y(i) - \hat{y}(i) \Big)^2 \tag{3.22}$$

Based on this error measure, the partition-setup with the minimum squared error e is selected for further processing.

5) Termination criterion: Steps two, three, and four are repeated until the relative change of the optimal e (compared to the previous iteration) becomes smaller than a user-defined threshold. Within this work, an error threshold of 1% is chosen. Alternatively, the model complexity can be limited by prescribing a maximum number of LLMs (M_{max}).

Besides, it is beneficial to include a validation check criterion such that the splitting process is continued although the squared error described by Equation (3.22) is not always reduced compared to the previous iteration. Practical experience showed that the algorithm can further decrease the squared error for many cases. Hence, a criterion has been implemented that the iterative process is aborted once the error is not decreased within four consecutive iterations. Finally, the least complex model with the optimal squared error is selected.

Below, the properties of the local linear neuro-fuzzy model trained by the LOLIMOT algorithm are discussed. This discussion also illustrates the motivation why this method has been chosen in this work.

3.4.2.3 LOLIMOT Properties

Besides the excellent numerical efficiency due to the extensive use of linear optimization techniques, local linear neuro-fuzzy models trained by the LOLIMOT algorithm offer several advantages for nonlinear function approximation, especially, in the context of nonlinear identification. Without claiming completeness, the following properties are of particular importance within the scope of this work:

1. The model complexity must not be constrained a priori. By means of the LOLIMOT training procedure, the number of unknowns is gradually increased within each iteration. The algorithm performs the structural refinement starting from a linear model. In the further course, only input regimes with a distinct nonlinear characteristic are refined. Consequently, the complexity of the finally obtained model is kept as low as possible under the given constraints, reducing the likelihood of dynamic instabilities which are often encountered during multiple one-step-ahead predictions [102]. In contrast, many methods such as the conventional MLP neural network approach described in Section 3.4.3 require the specification of the model structure in advance. Since no information with respect to the necessary number of parameters is available for general applications, the model structure is commonly not optimally fitted to the underlying problem. For the aforementioned case, realizing an adequate structure selection is a computationally demanding task. As the optimization of the model structure is already performed by the LOLIMOT algorithm, no further processing is needed to choose the degree of complexity of the final model.

2. The user can incorporate prior knowledge about the investigated problem in order to control the model refinement. For example, if the system is known to depend linear from most of the inputs with the exception of a single input parameter, the splitting procedure can be restricted to that input which is anticipated to have a nonlinear impact on the overall model response. Thus, the user can assure whether specified inputs act with a linear or a nonlinear characteristic. Moreover, the training speed can be significantly increased since the dimensionality of the problem is virtually decreased. Besides, the local linear neuro-fuzzy model can be employed to realize a linearization around several operating points. Thereby, inputs defining the operating point or the environmental conditions may have a nonlinear effect whereas the remaining parameters are linearly connected with the model response. This property is of particular interest for the ROM approach discussed in Section 4.1.

3. The computational effort of the LOLIMOT training procedure is of the order $\mathcal{O}\left(2Mp^4\right)$ [121]. Hence, the training cost increases only linearly with the number of incorporated LLMs. As a consequence, the algorithm is well-suited for constructing complex models incorporating high-dimensional mappings. This property is crucial for the identification of nonlinear dynamic systems since the model input vector dimension p is commonly very high; see Equation (3.4). Additionally, the number of linear weights to be optimized for a given model structure is $M(p+1)$. This circumstance in combination with the use of deterministic linear optimization approaches yields a highly-efficient parameter determination.

4. The extrapolation behavior of the local linear neuro-fuzzy model is favorable for many regression applications. As the validity functions in conjunction with the partition of unity property lead to a superposition of the constructed local linear models, a certain linear model or a blending between adjacent LLMs becomes active also outside of the trained input regime. Hence, a generally linear extrapolation is ascertained, which is beneficial for identification purposes in contrast to a constant or polynomial extrapolation characteristic [9, 57].

Due to these advantages, the local linear neuro-fuzzy model architecture trained by the LOLIMOT algorithm has been implemented in this work in order to identify nonlinear aerodynamic systems. Nonetheless, the chosen NFM also exhibits some drawbacks. For example, the axis-orthogonal splitting is not always optimal with respect to the underlying function to be estimated. This leads to an increased model complexity compared to a NFM architecture with axis-oblique partitions such as the hinging hyperplane model [121]. Furthermore, if strong nonlinear dependencies must be captured, the selected modeling approach is adversarial since the nonlinearity can be approximated solely by overlaying many linear models. However, the increased efficiency and the overall robust model employment were decisive for the local linear neuro-fuzzy model. It is therefore always used as the baseline model in this work.

3.4.3 Multilayer Perceptron (MLP) Neural Networks

Besides the local linear neuro-fuzzy model, another approach belonging to the class of neural networks, namely the multilayer perceptron feedforward neural network, is employed in this work. In Section 4.3, the combination of both the NFM and the MLP neural network is further motivated. The multilayer perceptron neural network, which is often regarded as the *classical* artificial neural network approach in the literature, is characterized by its favorable approximation capabilities regarding highly nonlinear functions [10, 57]. Referring to the introductory part in Section 3.4.1, each processing unit of the MLP feedforward neural network collects the weighted signals distributed by preceding input or hidden layer neurons. Subsequently, a typically nonlinear activation function is applied to translate the received scalar input into the output of the neuron. Finally, the response of each unit is passed to the output layer or consequent hidden layer neurons. Mathematically, the relationship between the overall model output $\hat{\mathbf{y}} \in \mathbb{R}^{n_y}$ and the input vector $\mathbf{v} \in \mathbb{R}^{q+1}$ is shown in Equation (3.23) for a MLP neural network with a single hidden layer [114, 121]:

$$\hat{y}_i = \sum_{j=0}^{M_{MLP}} G_{ij}^{L} \cdot \Phi_j \left(\sum_{k=0}^{q} G_{jk}^{N} v_k \right), \quad v_0 = 1, \quad i = 1, \ldots, n_y \tag{3.23}$$

$$\Phi_j(\varkappa) = \begin{cases} \tanh(\varkappa) = \frac{1-\exp(-2\varkappa)}{1+\exp(-2\varkappa)} & \text{for } j > 0 \\ 1 & \text{for } j = 0 \end{cases} \tag{3.24}$$

For clarification, M_{MLP} introduced in Equation (3.23) denotes the number of neurons contained in the hidden layer, whereas v_k symbolizes the kth element of the input vector $\mathbf{v}$. The hyperbolic tangent has been chosen as the activation function Φ_j that is applied to the scalar $\varkappa$; see Equation (3.24). The latter auxiliary variable is obtained via ridge construction, i.e., by summing up the weights G^N_{jk} multiplied by the respective v_k for all input vector dimensions $k = 0, \ldots, q$. The case $j = 0$ in combination with the input vector element v_0 introduces an offset to the neural network, which was shown to improve the model's function fitting performance [121]. In the neural network community, this offset is often termed as bias value [57, 114]. Due to the nonlinear nature of the selected activation function for $j \neq 0$, the corresponding weights as well as the input vector elements contained in the parenthesis of Equation (3.23) are in general nonlinearly connected to the output of the MLP neural network. It is important to emphasize that the weighting factors G^N_{jk} are, therefore, denominated as nonlinear weights in contrast to the linearly acting weights G^L_{ij}.

Using a set of training data composed of the linked input/output information with regard to the function to be approximated, the respective linear and nonlinear weights of the MLP, namely $\mathbf{G}^L \in \mathbb{R}^{n_y \times (M_{MLP}+1)}$ and $\mathbf{G}^N \in \mathbb{R}^{(M_{MLP}+1) \times (q+1)}$, are computed. For this purpose, the error back-propagation methodology in combination with the nonlinear Levenberg-Marquardt (LM) optimization [57,111] is employed. Consequently, a cost function is minimized in order to achieve a high model performance for nonlinear static approximations. Here, the cost function is defined as the mean squared error between the MLP output and the reference training output. In the course of this investigation, the algorithms implemented within MATLAB's Neural Network Toolbox [114] have been used in order to train the MLP feed-forward neural network. The fundamentals of the back-propagation procedure as well as the LM algorithm are addressed in the following.

3.4.3.1 Weight Initialization

Prior to the iterative training process, a suitable initialization of the weights must be provided as a starting point for the nonlinear optimization. Therefore, the well-established Nguyen-Widrow algorithm is used to achieve advantageous convergence properties [122]. According to Reference [114], the aforementioned algorithm determines the initial weights and offsets such that the neuron's active regions are uniformly distributed over the input space. However, it is important to emphasize that almost all initialization strategies including the Nguyen-Widrow algorithm incorporate random processes and are, therefore, non-deterministic. Consequently, a different neural network is obtained for every training process, even if the same training data composition is provided. A more detailed discussion about the challenges and consequences of non-deterministic learning procedures is given in Section 3.6.

3.4.3.2 Error Back-Propagation Procedure

In the following, the basic idea of the back-propagation procedure is illustrated, which has been proposed by Rumelhart et al. [140] in the 1980s.

It is well known that nonlinear optimization tasks can be performed either globally or locally. Due to the usually faster convergence of nonlinear local optimization techniques, they are commonly used for MLP neural network training, although the finally obtained parameters represent at best a good local optimum but not a global optimum. Since the local optimization starts from an initially chosen point and proceeds by searching in the neighborhood of the current point, further information about the variation of the objective function with respect to the parameter vector is needed. Hence, first-order and, depending on the specific approach, also second-order derivatives of the objective function must be provided. In the present context, the derivatives of the ith model output $\hat{y}_i$ with respect to the linear and nonlinear weights are required within the optimization process. At this point, the choice of the activation function defined by Equation (3.24) becomes particularly important. Considering the single hidden layer model described by Equation (3.23), the derivative according to the linear weight $\partial \hat{y}_i / \partial G_{ij}^L$ can be written as:

$$\frac{\partial \hat{y}_i}{\partial G_{ij}^L} = \Phi_j(\varkappa) \tag{3.25}$$

The activation function given in Equation (3.24) has the special property that its gradient can be expressed by the function itself:

$$\frac{\partial \Phi_j(\varkappa)}{\partial \varkappa} = 1 - \Phi_j^2(\varkappa) \quad \text{for } j > 0 \tag{3.26}$$

By exploiting this knowledge, the derivative of the model output with respect to the nonlinearly acting hidden layer weights is obtained for $j > 0$ as shown in Equation (3.27).

$$\frac{\partial \hat{y}_i}{\partial G_{jk}^N} = G_{ij}^L \frac{\partial \Phi_j(\varkappa)}{\partial \varkappa} v_k = G_{ij}^L \left(1 - \Phi_j^2\right) v_k \tag{3.27}$$

Consequently, the derivatives can be efficiently evaluated by utilizing already computed quantities. Moreover, due to the analytical gradient calculation, both the accuracy and the training speed are increased. As the output error of the model can be traced back layer by layer starting from the output layer, this principle is referred to as error back-propagation. The extension of the aforementioned principles towards MLP neural networks with two or more hidden layers is straightforward [57].

3.4.3.3 Nonlinear Parameter Optimization

Given the relationship between the MLP output and the parameter vector as described in Section 3.4.3.2, a nonlinear optimization algorithm is utilized to determine the weights. Here, the widely employed Levenberg-Marquardt approach for nonlinear least-squares optimization is used to minimize the mean squared error performance function depicted in Equation (3.28).

$$\mathbf{e}(\boldsymbol{\theta}) = \frac{1}{N_T} \sum_{i=1}^{N_T} \Big(\mathbf{y}(i) - \hat{\mathbf{y}}(i,\boldsymbol{\theta})\Big)^2 \tag{3.28}$$

$$\boldsymbol{\theta} = \operatorname{vec}(\mathbf{G}^L,\mathbf{G}^N) \tag{3.29}$$

In Equation (3.29), $\operatorname{vec}(\cdot)$ denotes the operator that reorders a matrix into a column vector. It is important to note that the system output $\mathbf{y}$ is not dependent on the neural network parameters contained in $\boldsymbol{\theta}$. Following the aforementioned argumentation, the error $\mathbf{e}(\boldsymbol{\theta})$ and its gradient according to the neural network weights can be expressed using Equations (3.25) and (3.27).

Within the framework of the Levenberg-Marquardt optimization, the Hessian matrix is approximated to achieve nearly second-order training speed [114]. Defining $\mathbf{J}(\boldsymbol{\theta}) = \partial \mathbf{e}(\boldsymbol{\theta})/\partial \boldsymbol{\theta}$ as the Jacobian containing the first-order derivatives of the model errors with respect to the parameter vector $\boldsymbol{\theta}$, the Hessian can be approximated as $\mathbf{H}(\boldsymbol{\theta}) = \mathbf{J}^\top(\boldsymbol{\theta})\mathbf{J}(\boldsymbol{\theta})$. Furthermore, the gradient $\mathbf{g}(\boldsymbol{\theta})$ can be calculated via $\mathbf{g}(\boldsymbol{\theta}) = \mathbf{J}^\top(\boldsymbol{\theta})\mathbf{e}(\boldsymbol{\theta})$. Given the Hessian and the gradient at iteration $k-1$, the LM procedure performs the following update for the parameter vector $\boldsymbol{\theta}_k$ containing all linear and nonlinear MLP weights [111, 114]:

$$\boldsymbol{\theta}_k = \boldsymbol{\theta}_{k-1} - \eta_{k-1}\big[\mathbf{H}(\boldsymbol{\theta}_{k-1}) + \mu\mathbf{I}\big]\mathbf{g}(\boldsymbol{\theta}_{k-1}) \tag{3.30}$$

In Equation (3.30), $\mathbf{I}$ and η denote the identity matrix and a step increment, respectively, whereas μ is a scalar which blends between the Gauss-Newton method for small μ and the steepest descent method for large values of μ. For further remarks on the Levenberg-Marquardt algorithm, the reader is referred to References [111, 114].

3.4.3.4 MLP Neural Network Properties

In comparison to the local linear neuro-fuzzy model introduced in Section 3.4.2 the multilayer perceptron neural network offers some advantages but also distinct drawbacks, which are highlighted in the following according to the discussion in Reference [121]:

- The MLP neural network can generally achieve a very high accuracy in terms of nonlinear multivariate approximations. Due to the ridge construction mechanism in combination with the nonlinear parameter optimization, the aforementioned neural network is a powerful universal function approximator. Since no linear submodels are incorporated within the multilayer perceptron formulation compared to the local linear NFM, the attainable one-step prediction accuracy is higher for the MLP neural network. This is particularly evident in the case of highly nonlinear problems. The MLP neural network also requires fewer processing units as well as model parameters in contrast to RBF neural networks or local linear neuro-fuzzy models to yield a comparable approximation quality. Consequently, the multilayer perceptron neural network can be considered to offer a high data reduction performance.

- The smoothness of the function approximated by the MLP neural network is typically very high. The reason for this property is the neural networks monotonic interpolation tendency which is driven by the hyperbolic tangent activation function.

- The extrapolation behavior of the MLP neural network is essentially constant if the considered input vector exhibits a sufficiently large distance from the trained input regime. Nonetheless, the shape of the hyperbolic tangent leads to a differing extrapolation characteristic in the short range. This is a major disadvantage of the MLP neural network, especially, related to the recurrent modus operandi of the model.

- As the parameter determination is realized via nonlinear optimization methodologies, the training process is computationally demanding. Moreover, an adequate structure selection, namely the determination of the number of neurons M_{MLP} or the number of layers (and neurons per layer), is challenging and requires many trial and error attempts or sophisticated pruning and growing algorithms. The aforementioned options need user-interaction or extensive computing resources. Therefore, the structure selection concerning MLP neural networks is a complex and expensive task. Although this training cost might be almost negligible within the scope of this work as the CFD simulations yielding the training data are computationally much more expensive, this is still a significant disadvantage of the MLP neural network in comparison to the local linear neuro-fuzzy model trained by the LOLIMOT algorithm. The latter already provides a structure selection strategy combined with the very fast parameter estimation procedure outlined in Section 3.4.2.2.

- Numerical experiments and practical experience showed that the MLP neural network is more susceptible to simulation instabilities. This holds especially true if the multi-step ahead prediction performance is directly compared to the simulation result of the local linear NFM. As a consequence, the MLP neural network will not be employed in recurrent operation, i.e., with output feedback, in this work to avoid numerically unstable solutions.

The intended use of the multilayer perceptron neural network as a nonlinear static, non-recurrent function approximator is explained in more detail in Section 4.3. Below, the splitting of the available process data into training, validation, and test data is motivated.

3.5 Data Preprocessing – Concept of Training, Validation, and Test Data

As already indicated in previous sections, not the entire system-representing data are used for calibrating the unknown parameters of the MLP neural network or the NFM. It is important to keep in mind that the main goal of the identified models is to achieve a good generalization ability [145]. A model with a favorable generalization behavior provides meaningful output values for unknown, non-trained inputs. However, the latter property cannot be verified with the training data since the model has been already conditioned with this information. Therefore, further data samples must be provided to ensure a desired generalization behavior. Besides, overfitting and underfitting must be prevented [10]. Consequently, three datasets are typically employed for model construction [10, 80, 121]:

1. Training data: In the present work, the weights, centers, and widths of the local linear neuro-fuzzy model as well as the linear and nonlinear weights of the multilayer perceptron neural network are determined based on the training dataset by means of supervised learning methodologies. If the model is a posteriori applied to predict the output of the training case, the model should be able to reproduce the trained information. Otherwise, the model structure offers too few parameters and is, therefore, not complex enough to adequately describe the problem. This effect is referred to as underfitting. However, the training dataset should not be used to optimize the model's structural complexity, as this would increase the risk of overfitting.

2. Validation data: Based on the validation dataset, the problem-dependent optimal model complexity is determined, i.e., the number of local linear models or the number of hidden layer neurons. Concurrently, the validation data are also used to avoid overfitting. Given only the training data, the introduced training strategies lead to an almost arbitrary reduction of the selected error criterion with an increased number of training steps [48]. Hence, the definition of a termination condition would be difficult and the model often becomes over-adapted to the training data (overfitting). In contrast, if the mean squared error as an exemplary error measure is also evaluated for the validation data during the training process, the model quality does not necessarily improve with more training iterations. Hence, the model with the minimum validation error is commonly selected and the training process is terminated. However, in this way the validation data is indirectly included in the model. Consequently, it should be avoided to utilize the validation data for assessing the model's generalization capability.

3. Test data: The test dataset contains information of the underlying system that was neither used for model structure determination nor for parameter calibration.

Thus, this dataset allows a non-biased evaluation of the generalization behavior as well as the overall model performance.

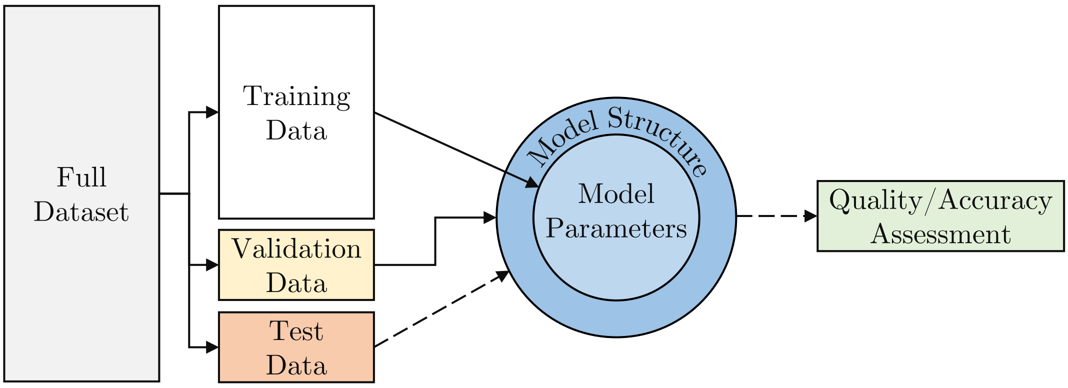

Figure 3.8: Schematic of the data splitting procedure to obtain training, validation, and test samples.

Nevertheless, it must be ensured that the three introduced datasets are representative for the investigated system. If some operating regimes are not covered by the training data, the identified model cannot be expected to provide reasonable outputs under these conditions.

Within the scope of this work, the full dataset stemming from the CFD solver is divided into training, validation, and test datasets according to Figure 3.8. Nonetheless, prior to this segmentation procedure, the input and output signals are preprocessed. It was shown by Sola and Sevilla [157] that not only the training speed but also the numerical robustness and the prediction performance of the resulting model can be significantly improved by normalizing the inputs and outputs. In this regard, the standardization, also referred to as the standard score transformation, is applied for all input and output features unless otherwise specified. The standard score normalization is a widely employed technique in the neural network and machine learning community [50] leading to signals that are statistically characterized by a zero mean and unit variance [117]. With the mathematical operators of the Hadamard power $\mathbf{A}^{\circ 2} = A_{ij}^2$ and the Hadamard division $\mathbf{A} \oslash \mathbf{B} = A_{ij}/B_{ij}$, the standardization of the inputs and outputs can be generalized to:

$$\bar{\mathbf{u}} = \frac{1}{N_S} \sum_{k=1}^{N_S} \mathbf{u}(k), \qquad \boldsymbol{\sigma}_u = \sqrt{\frac{1}{N_S - 1} \sum_{k=1}^{N_S} \Big(\mathbf{u}(k) - \bar{\mathbf{u}}\Big)^{\circ 2}} \tag{3.31}$$

$$\bar{\mathbf{y}} = \frac{1}{N_S} \sum_{k=1}^{N_S} \mathbf{y}(k), \qquad \boldsymbol{\sigma}_y = \sqrt{\frac{1}{N_S - 1} \sum_{k=1}^{N_S} \Big(\mathbf{y}(k) - \bar{\mathbf{y}}\Big)^{\circ 2}} \tag{3.32}$$

$$\mathbf{u}_{std}(k) = \Big(\mathbf{u}(k) - \bar{\mathbf{u}}\Big) \oslash \boldsymbol{\sigma}_u \tag{3.33}$$

$$\mathbf{y}_{std}(k) = \Big(\mathbf{y}(k) - \bar{\mathbf{y}}\Big) \oslash \boldsymbol{\sigma}_y \tag{3.34}$$

In Equations (3.31) and (3.32), $\bar{\mathbf{u}}$ and $\bar{\mathbf{y}}$ denote the respective mean of the system input and output vector. Moreover, the standard deviations of the input and output vectors are, respectively, $\boldsymbol{\sigma}_u$ and $\boldsymbol{\sigma}_y$. Using the previously introduced quantities, the resulting standardized input vector at time increment k is symbolized by $\mathbf{u}_{std}(k)$ according to Equation 3.33. Correspondingly, $\mathbf{y}_{std}(k)$ refers to the standardized system output.

Subsequent to the standardization, the normalized dataset $\mathbf{u}_{std}(k) \rightarrow \mathbf{y}_{std}(k), k = 1, \ldots, N_S$ is arranged according to the external dynamic filtering approach discussed in Section 3.3.1. As the final preprocessing step, the data is then partitioned into separate datasets as it is shown in Figure 3.8. Thereby, random sampling (without replacement) is employed to select, on the one hand, 70% of the available samples for the training dataset. On the other hand, the remaining data samples are equally divided into validation and test datasets. Care must be taken that the same random order is applied to both the input and the output vector in order to ensure the correct linkage of these data. It is worth to note that the random sampling strategy leads to a loss of the temporal sequence between the succeeding model input vectors $[\mathbf{x}(i-1), \mathbf{x}(i), \mathbf{x}(i+1)]$. However, due to the external-dynamics-based re-ordering the relevant information about the temporal connection is still preserved within each model input vector $\mathbf{x}(i)$. On the contrary, the random sample order offers some advantages for the training algorithms by avoiding ill-conditioned matrices [48,114]. Thus, after conducting the discussed preprocessing procedure, the multilayer perceptron neural network, the local linear neuro-fuzzy model, or any other function approximator can be employed to map the preprocessed inputs to the preprocessed outputs.

Owing to the standardization, it should be noted for completeness that the final model output must be re-normalized in order to obtain consistent output values. With the definition of the Hadamard product $\mathbf{A} \circ \mathbf{B} = A_{ij} \cdot B_{ij}$, the non-normalized output can be computed according to Equation (3.35).

$$\mathbf{y}(k) = \bar{\mathbf{y}} + \mathbf{y}_{std}(k) \circ \boldsymbol{\sigma}_y \tag{3.35}$$

3.6 Monte-Carlo-Based Training and Application Framework

The quality of models that have been obtained by system identification techniques is very sensitive to the training data as well as the parameter initialization prior to the learning process [9]. Specifically, the training excitation signal discussed in Section 3.7, the random data composition described beforehand, and the optimization starting point can have a crucial influence on the finally obtained model. If varying training signals are excluded from the following considerations, the modeling is still subject to uncertainties due to the randomly sorted training data as well as the random parameter initialization in the case of MLP neural networks. Consequently, it is unclear whether the response of the model is reproducible with high probability or only an outlier in comparison to the output of many trained models. Exemplarily, two scenarios can be considered concerning this issue [187]: On the one hand, a good performance might be ascertained for a specific model, whereas models trained by other data compositions or initial settings yield a comparatively poor agreement with the reference data. On the other hand, it is possible that a given model performs not satisfactorily, although all representative and necessary information about the underlying system have been provided within the training dataset. Both cases are undesired since they hide the true potential of the identification approach.

In order to make the previously explained model uncertainties measurable, a Monte-Carlo-based training and application strategy is employed. Within the scope of unsteady aerodynamic and aeroelastic reduced-order modeling, the Monte-Carlo framework has been first introduced by the author in References [187] and [189]. By estimating statistical deviations due to the model construction process, it can be ensured that the results of the identified models become both reproducible and comparable. Since the Monte-Carlo framework is independent from the specific identification algorithm, the methodology also leads to an increased transparency between results that have been obtained by different identification-driven reduced-order modeling techniques.

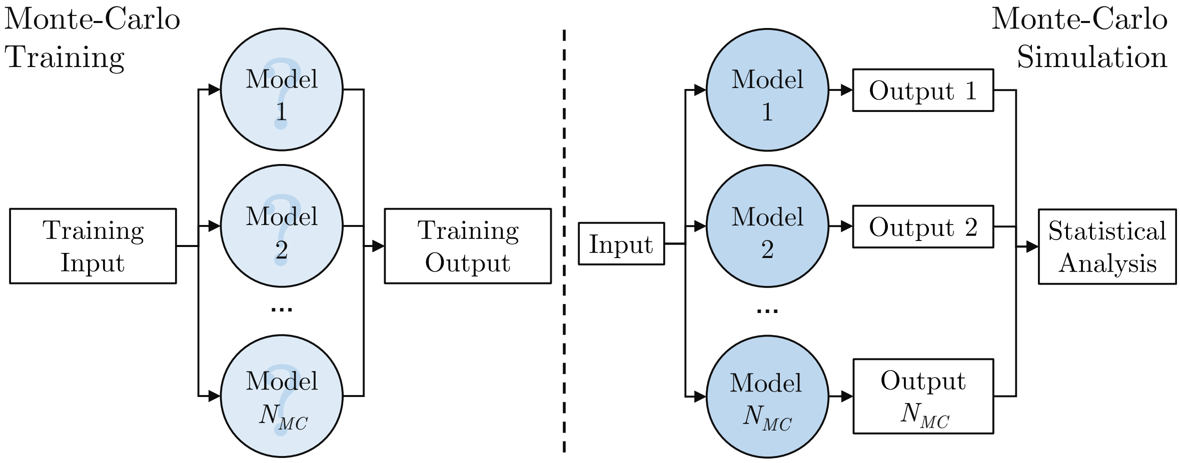

Figure 3.9: Monte-Carlo training (left) and application procedure (right) for identification-based modeling.

Generally, Monte-Carlo approaches are characterized by repeated numerical simulations that are initialized by random processes [116]. Here, N_{MC} independent models are trained in parallel, while all identification settings are kept constant. A schematic showing the general method is presented in Figure 3.9. Due to the random data segmentation process, which is performed autonomously for each of the N_{MC} models, the finally obtained models differ from each other. Consequently, they will not produce the same response for a given input signal. However, it is important to emphasize that the underlying full dataset containing the training, validation, and test data is the same across all training instances.

After the N_{MC} models have been trained, they can be employed for the intended purpose to simulate the response caused by unknown inputs. According to Figure 3.9, the same user-defined input signals are fed into each model resulting in N_{MC} different output vector time series. Given those responses, statistical methods can be applied to analyze the data. In the present work, the mean of the response $\boldsymbol{\mu}$ as well as the standard deviation $\boldsymbol{\sigma}$ is computed for comparison and classification purposes. Defining $\mathbf{y}_j(k)$ as the output vector at time step k produced by model j, the following equations are evaluated:

$$\boldsymbol{\mu}(k) = \frac{1}{N_{MC}} \sum_{j=1}^{N_{MC}} \hat{\mathbf{y}}_j(k) \tag{3.36}$$

$$\boldsymbol{\sigma}(k) = \sqrt{\frac{1}{N_{MC}-1} \sum_{j=1}^{N_{MC}} \left(\hat{\mathbf{y}}_j(k) - \boldsymbol{\mu}(k)\right)^{\circ 2}} \tag{3.37}$$

As the CFD simulation yielding the training data is the main computational cost driver for system-identification-based unsteady aerodynamic reduced-order modeling, the slightly increased numerical effort of the suggested Monte-Carlo procedure is justified by the additional insights about the models.

3.7 Excitation Signal Design

A decisive, highly problem-dependent task within the reduced-order modeling process is the design of suitable excitation signals in order to obtain training datasets that are representative for the investigated system. This step is even more important for nonlinear systems than for the linear counterpart [10]. Referring to the discussion in Section 3.1, the homogeneity and additivity principles are not valid for nonlinear systems. Hence, the data exploited by nonlinear identification techniques must contain considerably more information compared to the respective linear case. Regardless of the chosen identification strategy and the specific approximation approach, the quality and information content of the excitation signal in combination with the respective system response determines an upper limit for the achievable accuracy of the model. In summary, the following questions must be addressed for the design of adequate excitation signals:

- What is the purpose of the model?
- Is the system behavior linear or nonlinear?
- What amplitude range of each input parameter should the model cover?

- Are there different operating points in which a dynamically linear behavior is encountered?
- Which frequency range should be described by the model?
- How many samples are needed?
- Which discrete time step is adequate for the underlying problem?
- Does an equilibrium or static offset exist with respect to the input parameters?
- Is it possible to feed the user-defined signal(s) into the system to obtain its response?

Taking the aforementioned aspects into account, it becomes obvious that prior knowledge about the investigated system is highly beneficial for excitation signal generation. In the context of this work, a deep understanding of the unsteady aerodynamic and aeroelastic phenomena is therefore necessary to create a problem-tailored excitation signal [124].

Regarding linear systems, the response induced by an impulsive deflection [38, 106] or step excitation [69] contains sufficient information to identify a precise and stable model [102]. Besides the static or equilibrium amplitude, the respective signal types depicted in Figures 3.10a and 3.10b are represented by a single amplitude level for each degree of freedom, while the induced output incorporates all frequencies limited only by the resolution of the discrete temporal sampling. Moreover, the pseudo-random binary signal (PRBS) shown in Figure 3.10c is often employed for linear identification purposes [9]. If multiple inputs are present, the Walsh functions can be employed as it was shown in the work of Silva [150] and Fleischer [38]. Nonetheless, in order to avoid large gradients and abrupt changes within the training signal, e.g., due to limitations of the numerical method, further signals have been developed. Exemplarily, the so-called pulse excitation signal introduced by Kaiser et al. [75] can be employed for linear system identification. The pulse signal visualized in Figure 3.10d can be regarded as an asymmetrically smoothed step function. Although it does not excite the resolved frequency bandwidth equally well, it can be designed such that the frequencies of interest are adequately captured.

Considering the application of unsteady aerodynamic reduced-order models across varying freestream conditions (refer to Section 4.1 for a thorough discussion), the aerodynamic system for a given operating point can be regarded to respond in a linear way as long as the excitation amplitudes are small [185]. Although the overall system exhibits a nonlinear behavior due to the influence of the operating condition, the dynamic linearity for fixed freestream parameters allows the use of excitation signals known from linear identification theory. Therefore, the signals shown exemplarily in Figure 3.10 have to be applied independently for each operating point. Finally, the data originating from the considered training freestream conditions are merged to a single dataset in order to train the nonlinear model. With respect to the modeling presented in Chapter 5, the pulse signal has been utilized for the robust and efficient training data generation.

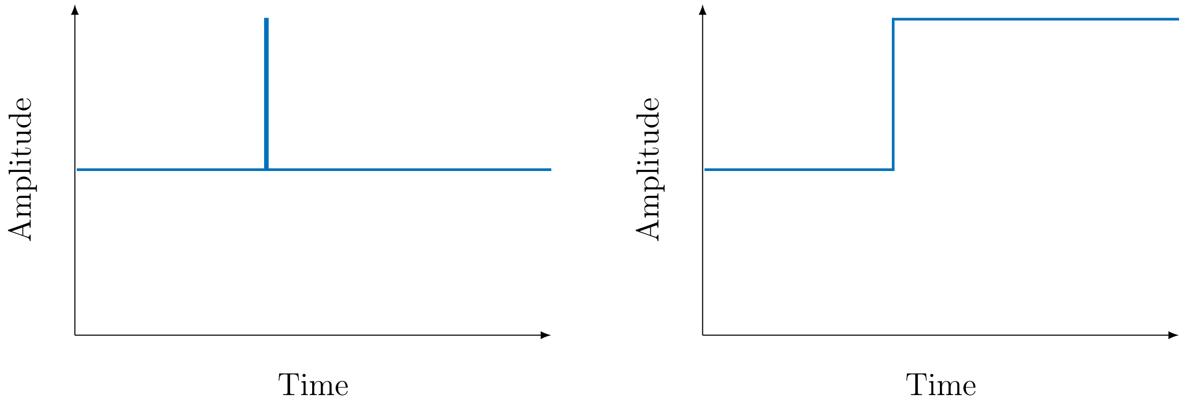

(a) Impulse signal (b) Step signal

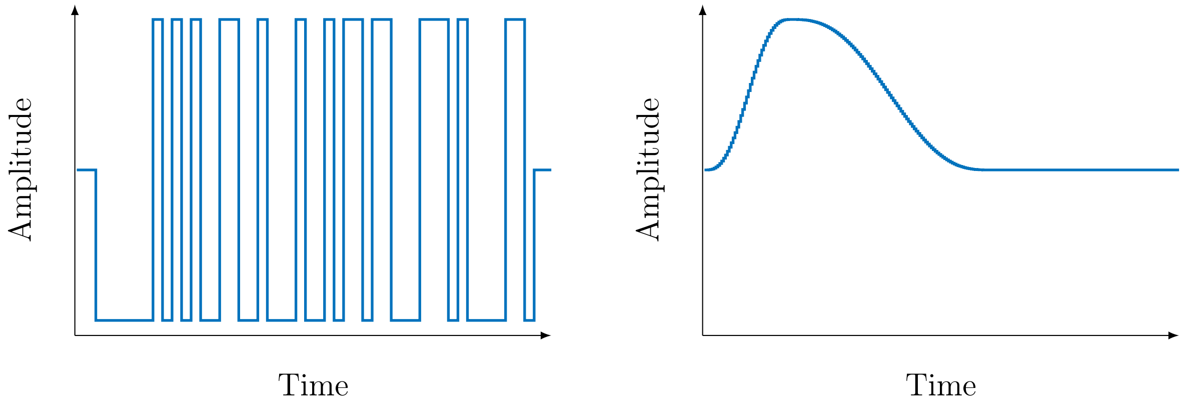

(c) Pseudo-random binary signal (PRBS) (d) Pulse signal [75]

Figure 3.10: Selected excitation signals for linear system identification.

If the system, however, cannot be thought of to be dynamically linear, further information about the underlying system is required to train the reduced-order model. In case of the approaches presented in Sections 4.2 and 4.3, the signal(s) must excite the relevant amplitude and frequency characteristics of the nonlinear aerodynamic system. In fact, the definition of adequate excitation signals is strongly correlated with the kind of system under investigation as well as the intended usage of the model. As the superposition principle does not apply, it is not sufficient to prescribe the amplitude in the way that only a maximum, a minimum, and a static level is reached. In contrast, numerous intermediate values between the maximum and minimum amplitudes must be considered for each input parameter. Concurrently, the effort associated to the training data generation must be limited in order to retain the computational advantages of the reduced-order modeling approaches. Moreover, to capture possible nonlinear interactions and interference effects between the excitation of multiple degrees of freedom, the system must be simultaneously excited with respect to all considered input dimensions.

One possible solution is the use of a random signal [69] shown in Figure 3.11a for the excitation of the nonlinear system. Mannarino [107] showed that random-like signals yield reasonable identification results of the unsteady aerodynamics with inherent nonlinear characteristics. Nonetheless, the use of random signals results in computationally demanding CFD simulations since each considerable jump within the excitation signal incorporates more iterations of the fluid solver to reach the specified density residuum convergence limit. Furthermore, the filtered white Gaussian noise (FWGN) signal depicted in Figure 3.11b, which is employed for example by Kou and Zhang [80], yields promising nonlinear-identification-based models in the context of transonic aerodynamics and aeroelasticity.

Nevertheless, the signal type, which is mainly applied in this work, is the amplitude-modulated pseudo-random binary signal (APRBS, [121]). This signal can be generated from the well-known PRBS (see Figure 3.10c) by assigning random amplitudes to each plateau. In this way, a square-wave signal with pseudo-randomly varying duty cycle and amplitude is obtained as it can be seen in Figure 3.11c. The main advantage of the APRBS compared to other well-known signals such as dc-chirps or multisine Schroeder sweeps [124] is the high information content per signal length in combination with the large spectrum of excited frequencies and amplitudes. The former aspect is especially important with respect to computational cost limitations. For practical purposes, the user can define the maximum and minimum amplitudes as well as the equilibrium amplitude, which must not be equidistant to the amplitude extrema. Moreover, the minimum hold time of the signal can be varied by the user in order to shape the frequency characteristics of the signal. Extensive simulation campaigns with a fixed number of excitation signal samples pointed out that the APRBS-based CFD computation converges faster compared to simulations employing the random signal. The reason for the cost reduction is the presence of regimes in which the APRBS does not undergo any change. Hence, fewer iterations of the CFD solver are required within each time step on average to reach a user-defined residuum. The utilization of the APRBS for nonlinear aerodynamic identification was first suggested by the author in Reference [182]. Moreover, to mitigate large gradients occurring in the original APRBS, a smoothed variant of this signal, referred to as the smoothed amplitude-modulated pseudo-random binary signal (SAPRBS) has been developed within the scope of this work [188]; see also Figure 3.11d. For the excitation of more than a single degree of freedom, several APRBS can be simultaneously applied for each input channel.

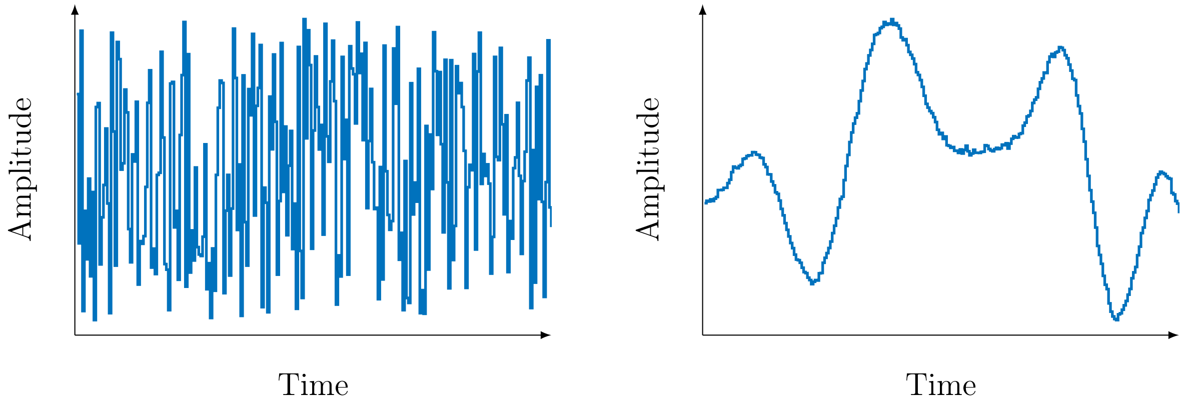

(a) Random signal

(b) Filtered white Gaussian noise (FWGN)

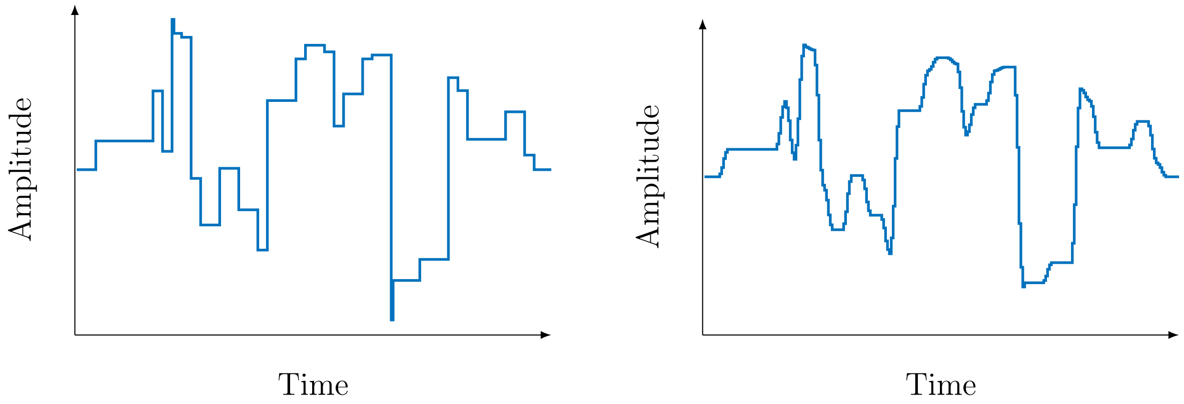

(c) Amplitude-modulated pseudo-random binary signal (APRBS)

(d) Smoothed amplitude-modulated pseudo-random binary signal (SAPRBS)

Figure 3.11: Excitation signals for nonlinear identification purposes.

In the next chapter, the introduced fundamental approaches are consolidated in order to yield powerful methods for unsteady aerodynamic and aeroelastic reduced-order modeling.

4 Developed Aerodynamic Reduced-Order Models

This chapter presents the unsteady aerodynamic reduced-order modeling approaches, which have been developed within the scope of this work. The content is structured as follows: First, Section 4.1 deals with the model-order reduction methodology for computing generalized aerodynamic forces with respect to multiple inflow conditions. In contrast to established approaches, a monolithic reduced-order model is trained to capture the motion-induced unsteady aerodynamic forces for different freestream Mach numbers or incidence angles. Subsequently, Section 4.2 discusses an approach which allows the efficient modeling of entire flow fields or surface distributions of specified physical quantities. Based on the interconnection of the local linear neuro-fuzzy model and the proper orthogonal decomposition (POD), it becomes feasible to predict the time-varying aerodynamic load distribution. Finally, in Section 4.3 a combination of the neuro-fuzzy model and the multilayer perceptron neural network is presented in order to model strongly nonlinear characteristics. Consequently, the aerodynamics due to large structural deflections or rigid body excitations can be accurately reproduced with the developed method. This chapter includes key findings that have already been documented in pre-publications of the author; see References [183–185, 188, 189].

4.1 Variation of Freestream Parameters

As it has been discussed in the introduction, only a few unsteady aerodynamic ROM approaches can be found in the literature that account for variable freestream conditions. Though, an efficient and reliable aerodynamic model that is valid across a range of inflow conditions or even for the entire flight envelope is highly desirable for numerous industrial applications. Hence, an unsteady aerodynamic reduced-order modeling methodology is developed that can be applied across freestream parameter variations; see also Reference [185]. Based on the recurrent local linear neuro-fuzzy model, it is possible to predict the motion-induced integral aerodynamic loads (forces, moments, generalized aerodynamic forces) across a range of freestream conditions.

Supported by Figure 4.1, the methods and theories described in Chapters 2 and 3 are consolidated to obtain the overall model-order reduction procedure. Since the approach is based on the nonlinear identification principles explained in Section 3.2, the model parameters must first be trained before a ROM-based simulation can be carried out. For this purpose, sets of training, validation, and test data representing the underlying system are required. Here, the investigated system is constituted by the unsteady CFD solver, which allows a user-defined deformation of the surface geometry and delivers the resulting aerodynamic forces and moments within each physical time step due to the prescribed motion. It is important to highlight that the workflow shown in Figure 4.1 involves *white-box* methods, e.g., the CFD solver derived from the Euler or Navier-Stokes equations, as well as *black-box* methods. By generating the training data using a white-box method, the physical relationships of the aerodynamic system are implicitly embedded in this dataset. Thus, the physics and in particular the characteristic dynamic relations between the inputs and outputs can be reproduced by the ROM within the limits defined by the training data. However, only the range of deflection amplitudes and frequencies which has been excited during the training CFD simulation(s) can be reproduced adequately by the ROM; see the discussion in Section 3.7. The same applies to the freestream condition range. As a consequence, the more nonlinear the inter-dependencies between the model output and the inflow parameters are, the more training inflow conditions must be provided to yield reliable results. For example, if the surface pressure distribution is nonlinearly related to the variation in the Mach number, additional training conditions must be considered compared to a case where a linear characteristic predominates. However, this strongly depends on the investigated configuration and flight regime. Although a ROM-based extrapolation aside from the trained system behavior is possible from a methodological point of view, it should be avoided since the accuracy of the model output becomes questionable.

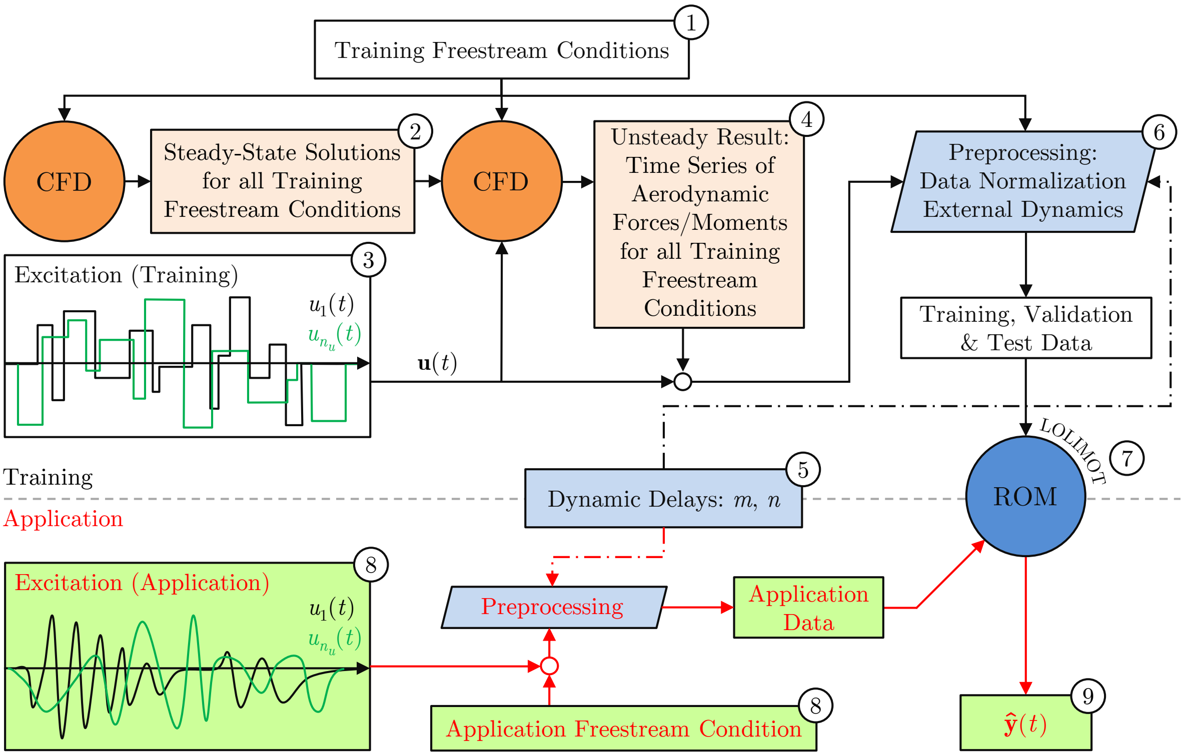

Figure 4.1: Schematic showing the developed unsteady aerodynamic ROM approach that can be employed across varying freestream conditions.

Considering the step-by-step overview provided by Figure 4.1, training freestream conditions must be initially chosen by the user (1), keeping in mind the previously discussed constraints. In this regard, a set of training freestream Mach numbers Ma_{Trn}, training incidence angles α_{Trn}, or any other parameter, which enters the CFD solver in a time-invariant manner, is defined. Besides, it is also feasible to vary more than a single freestream parameter within the ROM procedure. Consequently, corresponding sets for all flow condition variables must be defined prior to the training process. Nonetheless, the overall computational effort increases drastically with an increased number of different freestream parameters as the entire input space must be adequately resolved. For convenience, the following discussion is based on the assumption that only a single freestream parameter is varied. Hence, the parameter vector introduced in Equation (3.4) essentially becomes a scalar ($\boldsymbol{\Xi} \rightarrow \Xi$).

Related to the number of chosen training freestream conditions defined as N_{FC}, steady-state flow solutions have to be computed in step (2) using the CFD solver. Before performing the unsteady simulations, the excitation signal(s) for the structural and/or rigid body degrees of freedom must be defined (3). Depending on the amplitudes and frequencies of interest as well as the expected dynamic characteristics, i.e., a linear dynamic behavior due to small disturbances, the excitation signals must be generated according to the training signal design guidelines discussed in Section 3.7. Consequently, a unique excitation signal is assigned to each structural and/or rigid body mode to realize prescribed motions of the aerodynamic shapes within the CFD framework. At each time increment, the instantaneous geometry is formed by the undeflected reference shape in combination with a superposition of all considered mode shapes (see Section 2.2) scaled by their respective excitation signal value. Depending on the specific training signal design, the degrees of freedom can be excited either simultaneously or independently from each other.

Subsequently, the unsteady CFD simulations are carried out for the selected N_{FC} training freestream conditions as it is depicted in Figure 4.1 by means of step (4). As a result, time-series of the aerodynamic coefficients or generalized aerodynamic forces induced by the forced excitation are obtained. As all structural/rigid body degrees of freedom can be excited within a single CFD computation, the numerical effort is approximately proportional to the number of training freestream conditions N_{FC}. Depending on the purpose of the model, the definition of the model output is undertaken at this point. If, on the one hand, the model is intended to provide the overall force and moment characteristics, the output can be defined by the integral aerodynamic coefficients of interest, e.g., $\mathbf{y}(t) \equiv [C_L(t), C_{M_y}(t)]^\top$ considering the lift and pitching moment coefficients. On the other hand, if the model is intended to be used for aeroelastic investigations, the generalized aerodynamic forces may serve as the model output $\mathbf{y}(t) \equiv \mathbf{f}_{gen}(t)$. Generally, all data from the unsteady CFD runs such as local pressures or velocities can be extracted from the simulations in order to be modeled by the ROM, making this framework universally applicable.

By linking the excitation inputs $\mathbf{u}(t)$ with the CFD-based outputs $\mathbf{y}(t)$ for all available training freestream conditions, the merged dataset can be employed to calibrate the neuro-fuzzy-model-based ROM. Nevertheless, some data preprocessing is required prior to the execution of the LOLIMOT training algorithm. In this regard, the maximum input/output delays introduced in Equation (3.4) must be determined in step (5) according to the explanations given in Section 3.3. Additionally, the data is normalized with respect to the mean and standard deviation in order to improve the numerical robustness of the training procedure. Finally, the random distribution of the available data into training, validation, and test data is conducted (see Section 3.5). After the preprocessing step (6) is completed, the data can be utilized to train the unknown parameters of the local linear neuro-fuzzy model using the LOLIMOT algorithm (7); see Section 3.4.2.2 for a detailed discussion. In order to make the approach-inherent uncertainties assessable, the Monte-Carlo-based training strategy can be optionally employed according to Section 3.6.

Once the model error evaluation with respect to the test dataset yields acceptable results, the calibrated ROM can be used for the intended unsteady aerodynamic simulations. Generally, arbitrary excitation signals and application freestream conditions can be defined by the user as it is depicted in step (8) of Figure 4.1. However, the quality of the model output deteriorates if the signal's amplitudes and frequencies are not covered by the training signal(s). Analogously, the application freestream conditions should be in the range of the chosen N_{FC} training conditions. As the ROM framework is based on the discrete time formulation shown in Equation (3.4), the (nondimensional) time step size embedded in the training data has become a fixed model-inherent constant. Consequently, the application signals must be always sampled with the same time step size.

A posteriori to the preprocessing of the application data, the ROM can be used for the efficient simulation of the aerodynamic system's response (9). For this purpose, multiple one-step-ahead prediction operations are carried out, while the model output is fed back iteratively by means of the model input vector following the discussion in Section 3.3.1. Since initial input and output states are required for starting a ROM-based simulation (see Section 3.3.2), the model outputs can be initialized by their corresponding steady-state values, whereas the excitation can be defined as non-existent. If no steady-state information is available for the unknown freestream parameters, this data can be generated by interpolating between the known CFD results. Practical experience has shown that a precise initialization of the outputs is not crucial for the quality of the ROM results.

In case the Monte-Carlo procedure is employed, the ROM simulation is performed for each of the trained N_{MC} neuro-fuzzy models. Subsequently, a statistical analysis of the N_{MC} ROM outputs yields the final results as it is indicated in Section 3.6. In this way, the aerodynamic response $\hat{\mathbf{y}}$ due to user-defined structural and/or rigid body excitations can be obtained for various freestream conditions.

4.2 Prediction of Unsteady Surface Pressure Distributions

In this section, a surrogate modeling framework for the prediction of motion-induced surface pressure fluctuations is presented; see also Reference [184]. The motivation for this approach is that aircraft design and analysis applications often require detailed knowledge about the flow-induced load distribution in addition to integral aerodynamic coefficients. Hence, the method proposed in this section aims at the efficient prediction of aerodynamic load distributions. Similar to the procedure described in Section 4.1, the model construction is based on forced-motion unsteady CFD simulations. However, before applying methods from the nonlinear system identification domain the result is processed via the proper orthogonal decomposition (POD) in order to reduce the dimensionality of the problem. In this way, the predominant *modes* are obtained with respect to the flow field or surface distribution of user-defined physical quantities. Subsequently, the identification task is performed using the recurrent neuro-fuzzy model approach. In this regard, the model is conditioned to output the scaling coefficients corresponding to the computed POD modes. After a reconstruction step, entire field or surface data can be efficiently computed by means of this methodology. As soon as the surrogate model is trained, it can substitute the flow solver within unsteady aerodynamic or aeroelastic simulation frameworks.

Before the unsteady aerodynamic reduced-order modeling procedure is discussed in further detail, the proper orthogonal decomposition known from the literature is recapitulated.

4.2.1 Proper Orthogonal Decomposition (POD)

According to Iuliano and Quagliarella [70], the POD is a mathematical procedure that can be employed to decompose a large multi-dimensional dataset into a comparatively small number of representative modes. In this way, a condensed system description with a considerably reduced number of degrees of freedom is obtained. In the present context, the so-called POD snapshot method introduced by Sirovich [154] is applied for this purpose.

Therefore, the user must initially define the physical quantity of interest in order to apply the snapshot POD. Moreover, it is important to specify whether 3D field data, e.g., from finite volume cells, or data from surface elements shall be considered within the modeling process. In this regard, a unique mapping between the field or surface information and the so-called snapshot vector $\mathbf{W}_i$ must be defined. Consequently, it becomes feasible to transform surface or field data into snapshot vectors and vice versa without loosing information.

Anticipating the application of the POD presented in Chapter 6, the local pressure coefficient C_p can be exemplarily selected as the investigated aerodynamic quantity if the pressure-induced loads acting on the body are of primary interest. Hence, the C_p values of all CFD surface elements are arranged as a vector by means of a prescribed mapping yielding the snapshot vector $\mathbf{W}_i$. Thereby, the index i refers to the time instant of the snapshot. Assuming that an available unsteady training dataset consists of N_S samples, the full-order snapshot matrix $\mathbf{Y}$ can be written as

$$\mathbf{Y} = \left[\hat{\mathbf{W}}_1, \hat{\mathbf{W}}_2, \ldots, \hat{\mathbf{W}}_{N_S}\right] \in \mathbb{R}^{N_{SE} \times N_S}, \qquad \hat{\mathbf{W}}_i = \mathbf{W}_i - \mathbf{A}, \qquad \mathbf{A} = \frac{1}{N_S} \sum_{i=1}^{N_S} \mathbf{W}_i \tag{4.1}$$

In Equation (4.1), N_{SE} denotes the number of considered finite volume cells or surface elements, whereas $\hat{\mathbf{W}}_i$ symbolizes the ith centered snapshot vector. Moreover, $\mathbf{A} \in \mathbb{R}^{N_{SE}}$ represents the mean snapshot vector that has been averaged over the available N_S time steps. Given the snapshot matrix $\mathbf{Y}$, the aim of the proper orthogonal decomposition is to find $M_{POD} \ll N_S$ orthogonal basis vectors under the premise that these *modes* approximate $\mathbf{Y}$ optimally in the least-squares sense. For this purpose, the singular value decomposition (SVD) is computed with respect to the snapshot matrix [70], leading to

$$\mathbf{Y} = \mathbf{U}\mathbf{\Sigma}\mathbf{V}^\top = \mathbf{U} \begin{bmatrix} \sigma_1 & \cdots & 0 \\ \vdots & \ddots & \vdots \\ 0 & \cdots & \sigma_{N_S} \\ 0 & \cdots & 0 \end{bmatrix} \mathbf{V}^\top \tag{4.2}$$

Considering Equation (4.2), the SVD provides, inter alia, the unitary matrix $\mathbf{U} \in \mathbb{R}^{N_{SE} \times N_{SE}}$ and the rectangular diagonal matrix $\mathbf{\Sigma} \in \mathbb{R}^{N_{SE} \times N_S}$. It is important to emphasize that the first N_S column vectors of $\mathbf{U}$ correspond to the full set of possible POD modes. Hence, using the basis vectors contained in $\mathbf{U}$, the snapshot matrix $\mathbf{Y}$ can be exactly reconstructed apart from round-off errors. However, since the singular values σ_i are ordered such that $\sigma_1 \geq \sigma_2 \geq \ldots \geq \sigma_{N_S} \geq 0$, the singular values with larger subscripts become comparatively small for practical applications [70]. As the singular value is a measure of the mode's relative significance, the basis modes corresponding to singular values with higher subscripts $(\sigma_{M_{POD}+1}, \ldots, \sigma_{N_S})$ can be neglected in order to reduce the number of degrees of freedom. Nonetheless, the dominant system characteristics are maintained by considering the first M_{POD} modes. In Equation (4.2), it is implicitly assumed that the number of volume cells or surface panels is larger than the number of samples, i.e., $N_{SE} > N_S$. In the opposite, less-frequent case, the highest occurring index related to the singular values changes to N_{SE}.

Based on the matrices $\mathbf{U}$ and $\mathbf{\Sigma}$ obtained via the SVD, the number of relevant modes M_{POD} is still not uniquely determined. For this task, the relative information content (RIC) criterion can be evaluated [70, 96]:

$$RIC = \frac{\sum_{i=1}^{M_{POD}} \sigma_i^2}{\sum_{j=1}^{N_S} \sigma_j^2} \geq \varepsilon \tag{4.3}$$

In Equation (4.3), ε is a user-defined threshold which should be set to 0.99 in order to preserve 99% of the information contained in the original dataset [70]. By continuously increasing the value of M_{POD}, it can be ensured that the RIC criterion is satisfied. As the SVD has to be computed only once, the selection of the number of POD modes is numerically not expensive. The resulting POD modes $\boldsymbol{\varphi} \in \mathbb{R}^{N_{SE} \times M_{POD}}$ are determined as a subset of matrix $\mathbf{U}$ in terms of the first M_{POD} column vectors. Consequently, the full-order snapshot vector at time step k can be approximated by the relation

$$\mathbf{W}(k) \cong \mathbf{A} + \sum_{i=1}^{M_{POD}} b_i(k)\, \boldsymbol{\varphi}_i \tag{4.4}$$

considering the M_{POD} dominant basis vectors. In order to construct a reduced-order model, the time-dependent POD coefficients $b_i(k)$ have to be determined based on the training dataset for all modes $i = 1, \ldots, M_{POD}$ and time steps $k = 1, \ldots, N_S$. For this purpose, a least-squares optimization is performed in this work with respect to the snapshot matrix $\mathbf{Y}$ and the POD modes $\boldsymbol{\varphi}$. Alternatively, the POD coefficients can be computed by further exploiting the matrix $\mathbf{V}^\top$ resulting from the SVD. In this way, the matrix of POD coefficients $\mathbf{B} = [\mathbf{b}(t_1), \mathbf{b}(t_2), \ldots, \mathbf{b}(t_{N_S})]$ is obtained.

Following the aforementioned POD snapshot procedure, the existing training dataset ($\mathbf{Y} \in \mathbb{R}^{N_{SE} \times N_S}$) can be considerably compressed by means of the basis vectors ($\boldsymbol{\varphi} \in \mathbb{R}^{N_{SE} \times M_{POD}}$) and the corresponding time-dependent coefficients ($\mathbf{B} \in \mathbb{R}^{M_{POD} \times N_S}$). Since the POD modes can be regarded as time-invariant [3], the modeling task is shifted to the treatment of the POD coefficients $\mathbf{b}(k)$.

4.2.2 POD-Based Aerodynamic Reduced-Order Model

Based on the combination of the proper orthogonal decomposition with the recurrent neuro-fuzzy approach that has been discussed in Chapter 3, a surrogate model is devised for the prediction of motion-induced unsteady aerodynamic field, slice, or surface quantities. In particular, the POD leads to a dimensionality reduction in the first step, whereas the nonlinear system identification methodology is applied as a second step to allow efficient aerodynamic computations. This basic strategy is similar to the approach proposed by Lindhorst et al. [96]. In contrast to previous research, however, the methodology presented here employs a recurrent neural network which incorporates the feedback of the network outputs to realize a highly-efficient, low-dimensional reduced-order model. Considering the exemplary applications of the POD-ROM presented in Chapters 6 and 8, the focus is laid on the modeling of surface pressure fluctuations that are caused by structural and/or rigid body excitations. Besides applications in the context of aeroelasticity or loads estimation, however, the method is generally applicable to any user-defined physical quantity as well as arbitrary two- and three-dimensional data distributions. The only prerequisite is that a unique mapping between the data from the CFD domain and the snapshot vector introduced in Equation (4.1) exists. Thus, also 3D field information or unsteady variations within defined slices through the domain can be taken into account with the model. Supported by the schematic presented in Figure 4.2, an application-oriented overview of the training procedure as well as the POD-ROM utilization is given in the following.

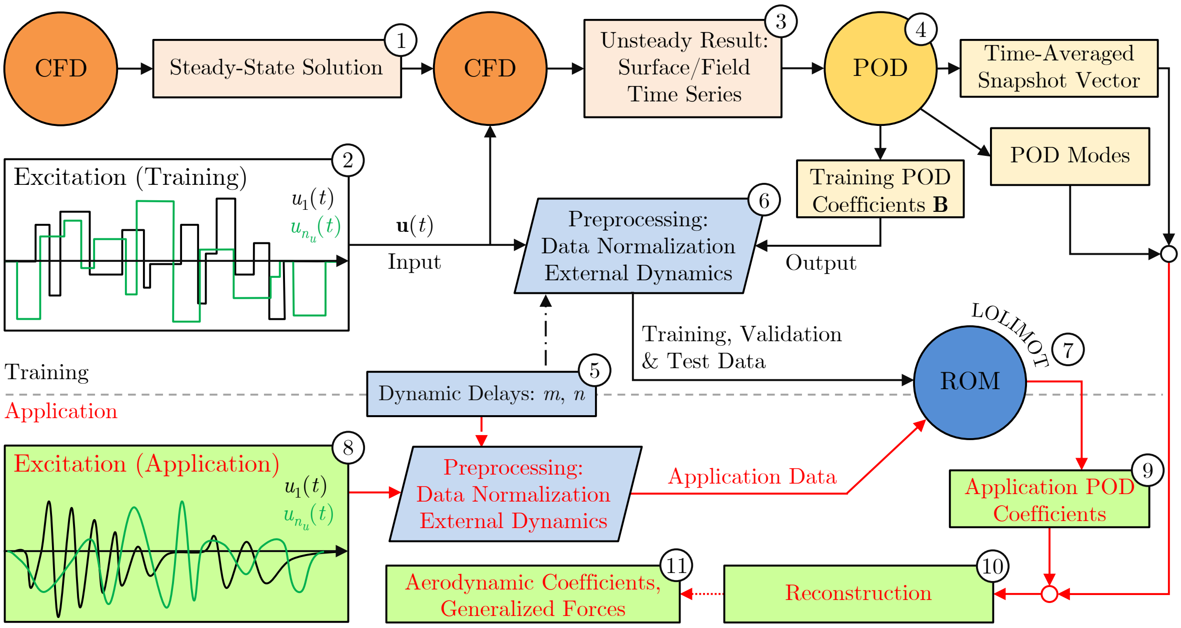

Figure 4.2: Process chart of the surrogate modeling approach based on the proper orthogonal decomposition and recurrent neuro-fuzzy models.

In contrast to the process chain discussed in Section 4.1, the POD-ROM procedure does not involve the feature to capture various freestream conditions. An extension of the present methodology towards freestream parameter variations should be feasible, but requires future research. Hence, step (1) depicted in Figure 4.2 refers to the conduction of a steady-state CFD simulation for a user-defined freestream condition and given configuration. As the POD-ROM approach is also based on nonlinear identification principles, an adequate input/output dataset characterizing the underlying CFD system must be generated. Note that the CFD solver can be either an Euler or a RANS solver, without changing the general ROM procedure. However, the user must be aware that depending on the employed CFD set-up (set of equations, turbulence model, boundary conditions, grid, etc.), the degree of dynamic nonlinearity between the CFD-based inputs and outputs can vary substantially. Hence, the identification task of the system can become more or less challenging.

Step (2) shown in Figure 4.2 comprises the definition of the excitation signal(s) for the considered structural and/or rigid body degrees of freedom. According to the discussion in Chapter 3, only those excitation amplitudes and frequencies, which have been excited during the training CFD simulation, can be reproduced subsequently by the ROM. Furthermore, the type of the excitation signal(s) depends on the expected system dynamics; see the remarks in Section 3.7. In the context of unsteady aerodynamic investigations, the magnitude of the deflection is typically the main driver with regard to a linear or a nonlinear input/output characteristic.

For each structural or rigid body degree of freedom taken into account, a specific excitation signal is generated and assigned. Thus, the aerodynamic body is formed by the reference shape and the superposition of the investigated mode shapes multiplied by their excitation signal values corresponding to the currently considered time step. In this way, all degrees of freedom can be excited simultaneously, i.e., within a single CFD computation. Based on the steady simulation and the defined excitation signal(s), the unsteady forced-motion CFD computation is performed in step (3). The output of the CFD solver is a time-series of the field or surface distribution of the aerodynamic quantities, e.g., the pressure coefficient or the local velocity. Since nonlinear aerodynamic phenomena are taken into account using Euler- or RANS-based CFD solvers, the nonlinearity is incorporated in the field or surface distribution that forms the basis for the ROM calibration. Consequently, nonlinear effects can be generally reproduced by the surrogate model.

Once the unsteady CFD result is available, the mapping between the field or surface distribution and the snapshot vector must be defined in order to construct the snapshot matrix $\mathbf{Y}$. For example, the pressure coefficients C_p across all surface elements can be arranged in a structured manner to form the snapshot vector. Following the POD procedure (4) discussed in Section 4.2.1, the singular value decomposition in combination with a subsequent least-squares optimization provides the relevant POD modes $\boldsymbol{\varphi}_i$ $(i = 1, \ldots, M_{POD})$ and the corresponding POD coefficient matrix $\mathbf{B}$ related to the training dataset. In this way, the high-dimensional training dataset governed by the number of volume or surface elements has been drastically compressed by means of the POD modes. As a consequence, it is sufficient to identify the influence of the structural excitation on the POD coefficients since the volume or surface information can be finally reconstructed using the available POD modes.

Combining the user-defined excitation signals with the time-series of the POD coefficients, the merged dataset can be used to calibrate the recurrent local linear neuro-fuzzy model. Analog to the explanations given in Section 3.3, the maximum dynamic delays (m, n) must be determined in step (5) to allow a reordering of the data with respect to the recurrence framework methodology. Moreover, various preprocessing steps such as data normalization and random data partitioning have to be carried out in step (6) prior to the actual training procedure. Subsequently, the unknown parameters and the structure of the local linear neuro-fuzzy model are optimized by applying the LOLIMOT algorithm (7); cf. Section 3.4.2.2. Optionally, the model training can be performed according to the Monte-Carlo methodology introduced in Section 3.6, resulting in N_{MC} neuro-fuzzy models for the prediction of the POD coefficients.

If the model error evaluation based on the test dataset (see Section 3.5) provides reasonable results, the POD-ROM can be used for time-marching aerodynamic simulations. By performing multiple one-step-ahead predictions including a feedback of the model outputs, the recurrent neuro-fuzzy model is applied to deliver the POD coefficients due to prescribed structural or rigid body excitations. In this regard, arbitrary excitation signals (8), that should be generally covered by the training data range with respect to the amplitude and frequency spectrum, are preprocessed and fed into the neuro-fuzzy model as it is depicted in Figure 4.2. Since initial conditions are required for starting a ROM-based simulation, the POD coefficients corresponding to the steady-state can be used, on the one hand, for the output initialization. For the inputs, on the other hand, it can be defined that no excitation is initially present. In contrast to the training process, the model outputs, i.e., the estimated POD coefficients, have to be fed back to the neural network input vector within each iteration; see Equation (3.5). As it has been already indicated in Section 4.1, the discrete time step size embedded in the training dataset is also fixed for the POD-ROM approach and, therefore, has to be utilized for all intended simulations.

Resulting from the application of the neuro-fuzzy model, the POD coefficients induced by the user-defined excitation become available (9). By applying Equation (4.4) using the known POD modes, the time-averaged snapshot vector, and the NFM-based time-series of the POD coefficients, the snapshot matrix can be reconstructed with respect to the application case (10). Furthermore, using the predefined mapping between the snapshot vector and the investigated surface or field distribution, the quantities of interest such as the surface pressure distribution can be computed. If not only the distribution is sought-after but also integral quantities, arbitrary calculations can be performed based on the reconstructed information (11). For example, based on available surface pressures the aerodynamic coefficients or generalized aerodynamic forces can be computed. Due to these properties, the constructed ROM can be easily coupled with a structural and/or flight mechanics solver in order to realize a highly-efficient multi-physics framework.

4.3 Modeling of Strongly-Nonlinear Aerodynamic Characteristics

The third unsteady aerodynamic model-order reduction strategy developed in this work addresses the prediction of distinctly-nonlinear system dynamics. A more pronounced nonlinear aerodynamic behavior occurs, inter alia, when increasing deflection amplitudes are considered [8]. For example, in contrast to the analysis of the flutter onset, the investigation of limit-cycle oscillations requires the simulation of larger excitation amplitudes that can lead to an aerodynamically-driven nonlinear behavior. Besides, also certain freestream conditions, especially within the transonic flight regime, can cause noticeable nonlinear dependencies of the flow-induced response, e.g., if transonic buffet or flow-separation occurs [7, 43, 67]. The methodologies discussed in Sections 4.1 and 4.2 are based on a neuro-fuzzy model, which has been shown to be well-suited for capturing weak aerodynamic nonlinearities as well as small perturbation flow characteristics across nonlinearly-acting freestream parameters [184, 185]. The beneficial properties in this context can be attributed to the use of local linear sub-models making the NFM less prone to simulation instabilities compared to MLP or RBF neural networks [121]. However, as the degree of nonlinearity increases, it becomes more difficult to identify the unknown input/output relation exclusively by means of the superposition of linear shape functions. Furthermore, the state-of-the-art ROM methods have their limits if they are applied for the modeling of both linear and nonlinear system characteristics [84]. In particular, established methods fail to accurately predict aerodynamic responses for small excitation amplitudes if they are trained for large amplitude cases.

4.3.1 Connected Neural Network Approach

As a remedy to the previously outlined issues, a novel identification strategy is suggested for aerodynamic reduced-order modeling; see also Reference [189]. The approach is based on a series connection of the recurrent local linear neuro-fuzzy model and the multilayer perceptron neural network. Specifically, the neuro-fuzzy model is used for multi-step ahead predictions, whereas the MLP neural network is a posteriori employed to perform a nonlinear correction of the NFM's time-series response. It is important to highlight that the MLP does not feature a direct feedback. Thus, an overall robust model characteristic is retained unless the NFM becomes unstable. In the following, the nonlinear identification procedure is explained based on the theoretical foundations of recurrent NFMs and MLP neural networks; cf. Chapter 3. According to the schematic depicted in Figure 4.3, the identification strategy involves three sequential training steps [189]:

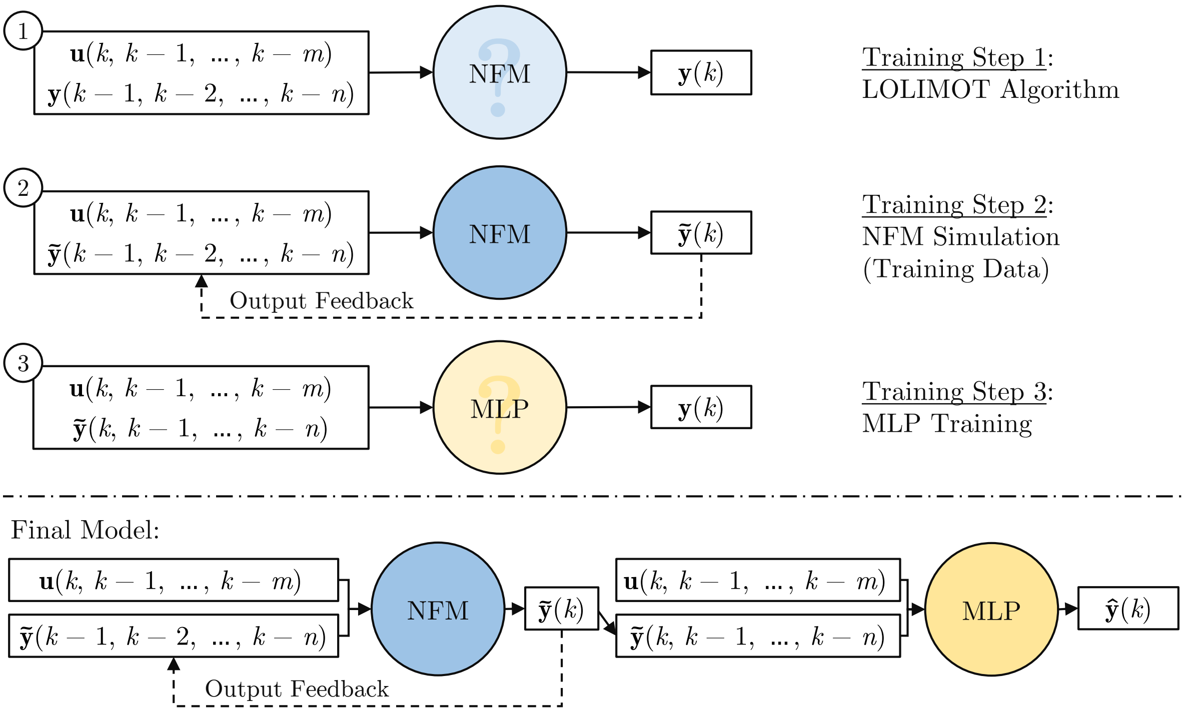

Figure 4.3: Schematic showing the sequential three-stage training procedure (top) and the application of the connected neural network approach (bottom). For convenience, the time-independent parameter vector $\boldsymbol{\Xi}$ has been omitted within the model input vectors.

1) Initially, the neuro-fuzzy model is trained by means of the LOLIMOT algorithm according to the explanations given in Section 3.4.2.2. For this purpose, the NFM input vector consists of the (time-delayed) system input and system output quantities. Presuming the notation introduced in Section 3.3.1, the following function approximation problem is addressed by means of the NFM:

$$\left[\boldsymbol{\Xi}^\top, \mathbf{u}^\top(k), \ldots, \mathbf{u}^\top(k-m), \mathbf{y}^\top(k-1), \ldots, \mathbf{y}^\top(k-n)\right]^\top \xrightarrow{\mathcal{N}_1 ?} \mathbf{y}(k) \tag{4.5}$$

   In Equation (4.5), $\mathcal{N}_1$ refers to the unknown functional that will be constituted by the neuro-fuzzy model. It is important to emphasize that the system outputs $\mathbf{y}(k)$ known from the provided training dataset are used to calibrate the unknown parameters as well as the structure of the NFM. Thus, no iterative feedback is considered during the training of the neuro-fuzzy model. Detailed information related to the first identification step can be found in Section 3.4.2.

2) After the neuro-fuzzy model has been obtained, the second stage of the training procedure is carried out. According to Figure 4.3, a simulation must be performed with the NFM for the given training data. Related to this step, the outputs of the neuro-fuzzy model $\tilde{\mathbf{y}}$ are fed back by means of the NFM input vector. Hence, the NFM is applied within each discrete time step to generate the subsequent model response:

$$\left[\boldsymbol{\Xi}^\top, \mathbf{u}^\top(k), \ldots, \mathbf{u}^\top(k-m), \tilde{\mathbf{y}}^\top(k-1), \ldots, \tilde{\mathbf{y}}^\top(k-n)\right]^\top \xrightarrow{\mathcal{N}_1} \tilde{\mathbf{y}}(k) \tag{4.6}$$

Since local linear neuro-fuzzy models are comparatively robust regarding multi-step ahead predictions, they are well-suited for the simulations in the present context. Henceforth, two output time-series are available for the training dataset, namely the original training response $\mathbf{y}(k)$ and the result generated by the recurrent NFM $\tilde{\mathbf{y}}(k)$.

3) Beyond the previously outlined procedure for a LOLIMOT-based nonlinear identification, the MLP neural network discussed in Section 3.4.3 is a posteriori employed to considerably improve the fidelity of the resulting coupled model. For this third step, the MLP input vector comprises the (time-delayed) system inputs and the recently obtained (time-delayed) NFM outputs $\tilde{\mathbf{y}}(k)$ as it is indicated in Equation (4.7). Thereby, the functional mapping denoted by $\mathcal{N}_2$ is realized using the MLP neural network.

$$\left[\boldsymbol{\Xi}^\top, \mathbf{u}^\top(k), \ldots, \mathbf{u}^\top(k-m), \tilde{\mathbf{y}}^\top(k), \ldots, \tilde{\mathbf{y}}^\top(k-n)\right]^\top \xrightarrow{\mathcal{N}_2?} \mathbf{y}(k) \tag{4.7}$$

Since the complete NFM-based output time-series is already available, also the current discrete time step information $\tilde{\mathbf{y}}(k)$ can be considered within the MLP input vector. Thus, the MLP input vector shown on the left hand side of Equation (4.7) comprises only known quantities. In the case that the model is generalized to new datasets (application process), the aforementioned property also applies. Nonetheless, the MLP neural network is still trained to minimize the mean squared error with respect to the training information $\mathbf{y}(k)$ using the Levenberg-Marquardt optimization algorithm. Once the MLP neural network has been trained, the overall model output $\hat{\mathbf{y}}$ can be obtained via

$$\left[\boldsymbol{\Xi}^\top, \mathbf{u}^\top(k), \ldots, \mathbf{u}^\top(k-m), \tilde{\mathbf{y}}^\top(k), \ldots, \tilde{\mathbf{y}}^\top(k-n)\right]^\top \xrightarrow{\mathcal{N}_2} \hat{\mathbf{y}}(k) \tag{4.8}$$

In Equation (4.8), it is assumed that the LOLIMOT simulation result ($\tilde{\mathbf{y}}$) has been computed a priori.

Because of the serial model structure shown in Figure 4.4, the MLP neural network cannot produce a dynamically unstable response since it is not operated in a recurrent modus operandi. For clarity, the outputs of the overall model are fed back neither to the MLP nor to the NFM input vector. In fact, the MLP neural network can be considered to perform a nonlinear quasi-static correction of the neuro-fuzzy model outputs. As the error of the NFM is further processed by means of the MLP neural network, the overall model structure can be considered to belong to the nonlinear auto-regressive moving-average with exogenous inputs (NARMAX) class [9] according to Equation (3.7).

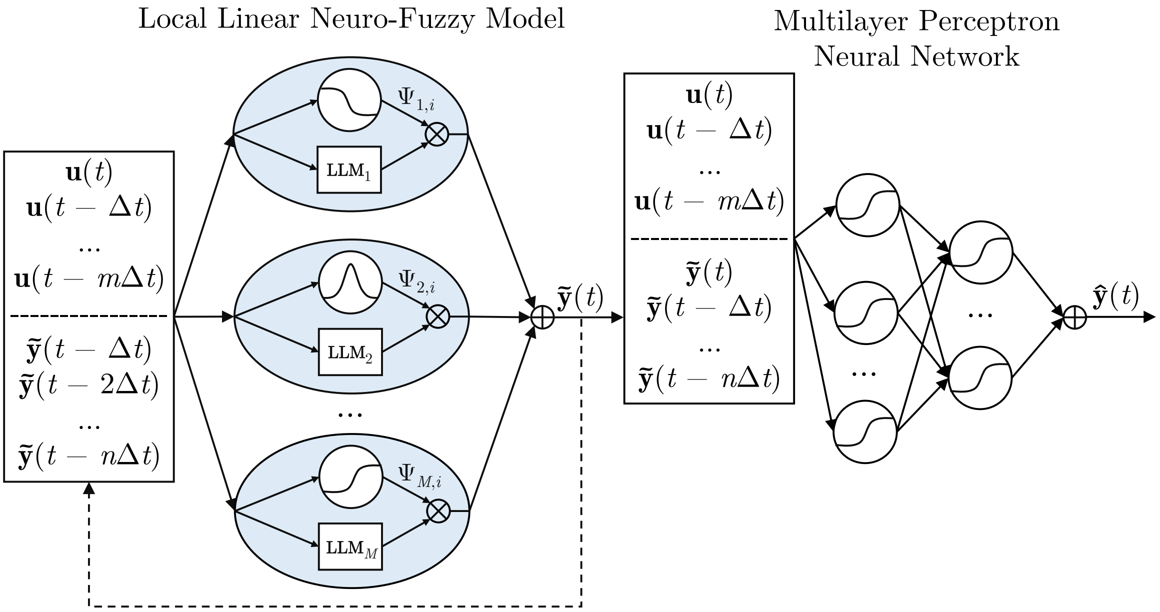

Figure 4.4: Visualization of the connected neural network approach including the recurrent local linear neuro-fuzzy model as well as the multilayer perceptron neural network.

Another interesting feature of the novel aerodynamic reduced-order modeling strategy is revealed if the NFM's number of local linear models is artificially restricted to $M = 1$. Then, the neuro-fuzzy model becomes a dynamically linear model and, from a global point of view, a nonlinear Wiener-type model (dynamic linear model in series with a static nonlinear model) is obtained as a special case. Hence, the user can incorporate prior knowledge to select a problem-fitted model structure depending on the intended application. For example, the overall model complexity can be adapted ranging from a global linear model to a dynamically nonlinear model with a nonlinear static correction. Besides its robustness and flexibility, the resulting identification framework yields a high simulation accuracy as well as generalization capability, which is demonstrated in Chapter 7.

As it has been already noted in Section 3.3, initial conditions must be prescribed for the input and output quantities due to the existence of delayed elements within the model input vectors. The number of time steps that must be defined a priori is equal to the maximum delay-order, i.e., $\max(m,n)$. Commonly, the initial values are set to zero or to values representing the system's static equilibrium. This procedure may lead to initial conditions which are not strictly consistent with the physics of the underlying system. However, practical experience showed that initialization errors are not crucial unless the transient response at the simulation start is of primary interest. With increasing simulation time, the error due to inaccurate starting conditions usually vanishes. Nevertheless, if the system is governed by bifurcations or chaotic characteristics, initialization errors may be not tolerable. In the following, the application of the NFM-MLP-based nonlinear identification strategy for efficient unsteady aerodynamic modeling is outlined.

4.3.2 NFM-MLP Network for Aerodynamic Modeling

Since the aerodynamic reduced-order modeling procedure based on the NFM-MLP approach is generally similar to the workflow discussed in Section 4.1, only the highlights and noteworthy differences within the training and application process are explained in the following.

In contrast to the ROM procedure depicted in Figure 4.1, the methodology for simulating strongly-nonlinear aerodynamic characteristics does not necessarily involve freestream parameter variations. Considering both motion- and freestream-parameter-caused nonlinearities at the same time places high demands on the training data information content and, therefore, may drastically increase the ROM construction effort. Besides, the increased input/output model complexity leads to additional challenges with respect to the nonlinear identification task. However, according to the set of equations provided in Section 4.3, it is feasible to incorporate static model input parameters as well. Consequently, the workflow given by Figure 4.1 can be analogously applied such that variable freestream conditions are taken into account. The only difference is that the neuro-fuzzy model has to be substituted by the coupled NFM-MLP model during the system identification process. Thus, the steps and remarks given in Section 4.3.1 must be considered in order to train and apply the connected network. Furthermore, the NFM-MLP neural network can also replace the neuro-fuzzy model in the context of the POD-ROM procedure discussed in Section 4.2 if a more dominant nonlinear behavior is encountered for the POD coefficients.

For the following discussion of Figure 4.5, it is presumed for convenience that aerodynamic force or moment coefficients, which depend distinctly nonlinear on the investigated structural excitation, are intended to be modeled. Hence, the use of the NFM-MLP model should be preferred for improved simulation fidelity compared to the use of the neuro-fuzzy model only. For practical applications, however, it is recommended to verify first whether the system is governed by a linear or a nonlinear behavior keeping in mind the aims of the model as well as the application regimes of interest; see the remarks in Section 3.1.

Based on Figure 4.5, a training dataset containing the representative system features is needed for ROM calibration similar to the procedures discussed in Sections 4.1 and 4.2. Therefore, user-defined excitation signals must be generated for all considered structural or rigid body degrees of freedom; cf. Section 3.7. Subsequently, an unsteady forced-motion CFD simulation is computed with respect to a chosen freestream condition. The

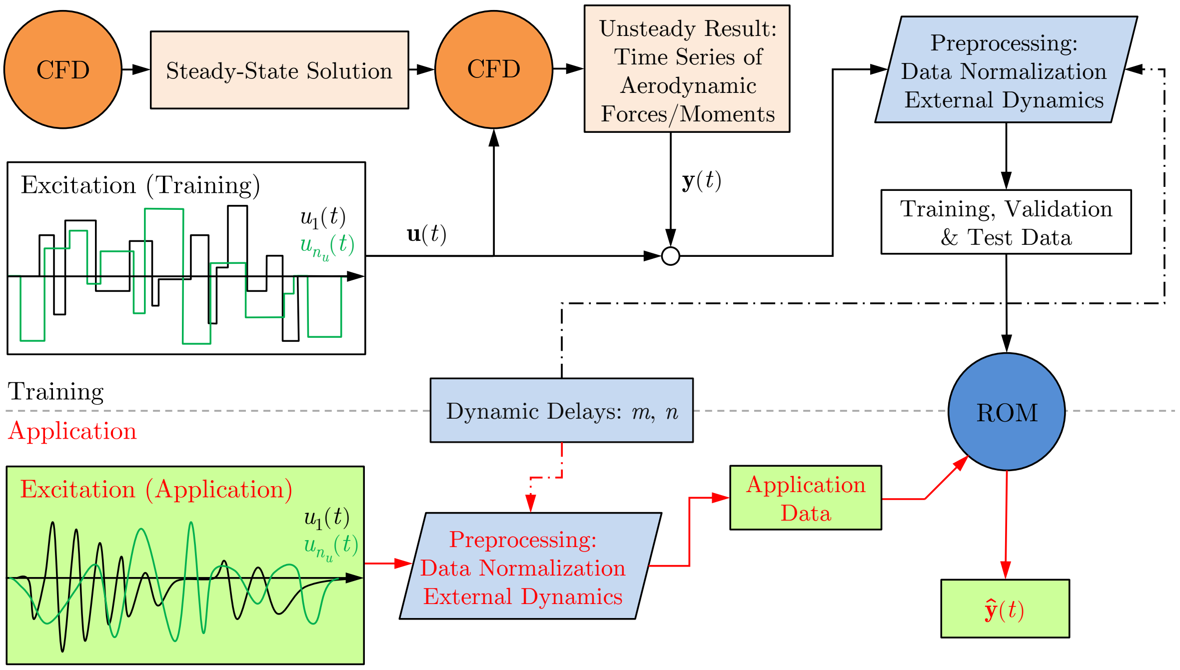

Figure 4.5: Reduced-order modeling procedure for predicting strongly-nonlinear, motion-induced aerodynamic characteristics using the NFM-MLP approach. Variable freestream conditions are excluded in the chart to limit the problem's complexity.

output of the CFD solver is a time-series of the forces and moments acting on the investigated aerodynamic body. Provided that the employed solver reproduces nonlinear phenomena such as shock motions or flow separation, a nonlinear relation between the degrees of freedom of the prescribed motion and the aerodynamic response is obtained for sufficiently large deflections.

Once the input/output training database characterizing the underlying system has become available, the procedure explained in Section 4.3 can be followed. Thus, the connected network consisting of the recurrent local linear neuro-fuzzy model and the multilayer perceptron neural network is trained. It should be noted for completeness that the methodology is also compatible with the Monte-Carlo strategy presented in Section 3.6; see also [189]. Thus, several NFM-MLP models can be independently trained and applied to estimate the influence of random initialization and data composition on the ROM solution quality. After the connected neural network yields satisfying simulation results based on the test dataset, the resulting reduced-order model can be applied for simulating the aerodynamic response due to user-defined structural motions analogously to the description given in Section 4.1. In this way, the conduction of computationally-demanding unsteady CFD simulations can be transferred to ROM, leading to a significant acceleration of the associated aerodynamic investigations.

5 Analysis of Freestream Parameter Variations

In this chapter, the neuro-fuzzy-model-based ROM approach discussed in Section 4.1 is applied for the prediction of generalized aerodynamic forces induced by structural eigenmode-based excitations to demonstrate the efficiency and accuracy of the freestream-parameter-adaptive methodology. The content is largely based on the author's pre-publication, Reference [185]. However, in contrast to the previous outcomes where the Euler equations solver AER-Eu had been employed, the results presented herein originate from the Reynolds-averaged Navier-Stokes solver AER-NS. In this way, it is shown that the method is generally applicable to different CFD solvers and degrees of fluid-dynamic modeling.

In order to illustrate the application of the ROM procedure for aeroelastic investigations, the AGARD 445.6 test case has been selected. The aeroelastic test case along with the aerodynamic and structural modeling is presented in detail in Section 5.1. Concerning the ROM training, steady and unsteady CFD solutions at six training freestream Mach numbers are computed and utilized for the NFM calibration. Subsequently, the trained ROM is employed to obtain motion-induced aerodynamic responses at various freestream Mach numbers, which are not contained explicitly in the training dataset. The aforementioned model generalization towards new freestream conditions is explained in Section 5.3. It is important to highlight that the ROM results are always juxtaposed to results of the respective reference system, which is the AER-NS solver in the present chapter.

Due to the fact that the first harmonic of the aerodynamic loads is of particular importance for linear flutter analysis, a further comparison of the frequency domain **GAF** matrix elements is conducted. In Section 5.4, the ROM and CFD responses due to harmonic excitations in each generalized coordinate are therefore transformed into the frequency domain via Fourier analysis, whereas higher-order terms are neglected. Additionally, a frequency-domain flutter analysis is carried out in Section 5.5 using the p-k method [56, 68] to evaluate the ROM performance by means of the flutter speed index and the frequency ratio.

5.1 Test Case: AGARD 445.6 Wing

In the present study, the AGARD 445.6 wing has been selected for applying the neuro-fuzzy model approach. This test case is well-suited for the verification of unsteady aerodynamic models, especially, if the focus is on predicting a wide range of freestream conditions including subsonic, transonic, and supersonic flows. The aeroelastic characteristics of this wing have been thoroughly investigated. In this regard, it is worth to emphasize that the AGARD 445.6 wing has been studied experimentally in the 1960s by means of wind tunnel flutter tests at the NASA Langley Transonic Dynamics Tunnel [194] using air and Freon-12. The aim of these experiments was, on the one hand, to provide a validation database for numerical simulation tools and, on the other hand, to contribute to a better understanding of flutter and transonic aeroelastic effects including the transonic dip [194]. The experimental flutter results are available in terms of flutter speed indices (FSI) and frequency ratios (FR) for the freestream Mach numbers $Ma_\infty = [0.499, 0.678, 0.901, 0.954, 1.072, 1.141]$; see also Section 5.5 for the definition of FSI and FR. The corresponding angle of attack has been fixed to $\alpha = 0°$ in order to avoid static aeroelastic deformations. Besides, the AGARD 445.6 wing has been extensively used for numerical investigations including CFD solver validation, ROM testing, and aeroelastic studies; see Lee-Rausch and Batina [92, 93], Silva et al. [153], and Förster [41] for exemplary computational results. In the following, only the so-called weakened model 3 configuration in combination with air as the fluid medium is taken into account to evaluate the neuro-fuzzy-model-based reduced-order model.

5.1.1 Aerodynamic and Structural Modeling

The AGARD 445.6 configuration is geometrically represented by a swept semi-span wing with low aspect ratio as it is shown in Figure 5.1a. The weakened model 3 exhibits a quarter-chord sweep angle of $\varphi_{0.25} = 45°$, a taper ratio of $\lambda = 0.66$, and a semi-span of $s = 0.762\ m$. The wing's cross-section is further characterized by the NACA 65A004 airfoil exhibiting a relative thickness of $t/c = 4\%$.

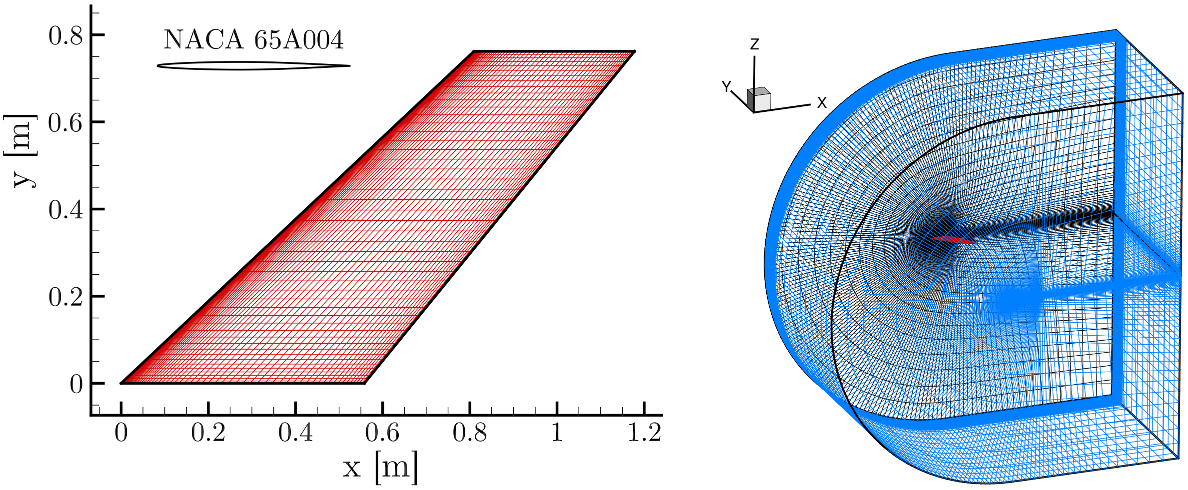

(a) Planform of the AGARD 445.6 wing (b) Computational grid

Figure 5.1: Planform and reference CFD grid of the AGARD 445.6 weakened model 3. The wing is marked red, whereas the blue and black faces illustrate the farfield and symmetry boundary conditions, respectively.

Moreover, the root chord of the AGARD 445.6 wing is given as $c_r = 0.558\ m$. With respect to the experiments summarized in Yates [194], the semi-span model was attached directly to the wind tunnel wall, i.e., no peniche had been utilized to mimic a fuselage. The important geometric properties, that are needed to define the aerodynamic shape, are recapitulated in Table 5.1.

Table 5.1: Geometric properties of the AGARD 445.6 wing [194].

Quantity	**Symbol**	**Value**
Root chord	c_r	$0.558\ m$
Reference area	S_{ref}	$0.353\ m^2$
Semi-span	s	$0.762\ m\ (2.5\ ft)$
Aspect ratio	AR	1.65
Taper ratio	λ	0.66
Sweep angle	$\varphi_{0.25}$	45°
Reference length (k_{red})	c_{ref}	0.558 m

As a prerequisite for conducting steady and unsteady CFD computations, the fluid domain has been discretized by a two-block C-H-topology. The structured computational grid was generated in the work of Fleischer [38] using ANSYS ICEMCFD [2]. Thereby, the grid dimensions have been scaled such that the grid reference length for the nondimensional flow solver equals one. The Spalart-Allmaras turbulence model is used for all (U)RANS computations within this chapter. Thus, it is assumed for all simulations that the flow can be considered as fully turbulent, although the transition was not fixed within the original experiments [194]. Using the Spalart-Allmaras turbulence model [158], it is recommended that the dimensionless wall distance satisfies $y^+ < 5$. In this way, at least one wall-attached cell is located in the viscous sub-layer of the turbulent boundary layer. In order to achieve the aforementioned resolution of the boundary layer, the grid was refined towards the wall by an off-body distance of $5 \cdot 10^{-5}\ c_r$ with respect to the first cell height. A further preprocessing of the grid with the in-house Poisson-equation mesh smoother [26] led to grid lines that are virtually orthogonal to the block boundaries. A grid sensitivity study was conducted in the work of Fleischer [38] to ensure independence of the solution from the grid resolution. In Figure 5.1b, the employed non-deformed reference grid containing 450,560 cells is shown, while the wing itself is represented by 6,912 surface elements.

The weakened model 3 used for the wind tunnel flutter experiments is made of laminated mahogany wood. In order to reduce the stiffness of the wing and, thereby, its flutter velocity, circular holes were drilled into the wood. Subsequently the holes were closed

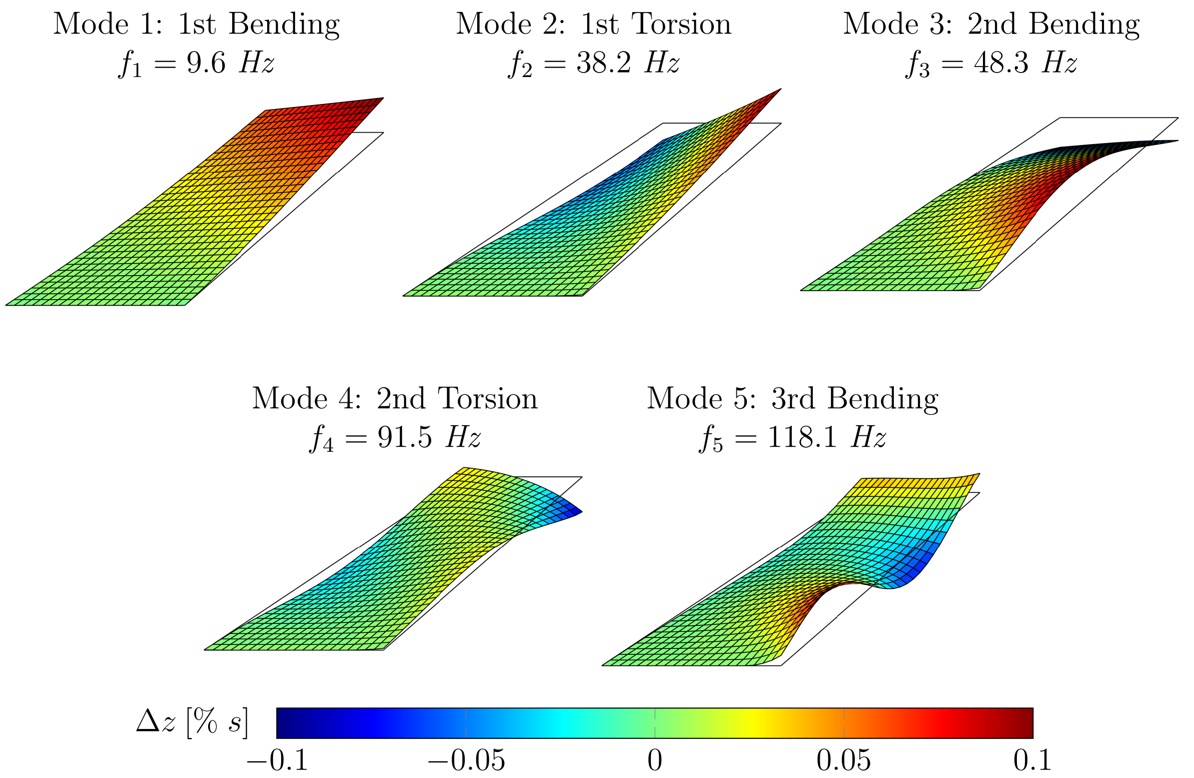

Figure 5.2: Exaggerated deflections (factor 200) normal to the wing midplane regarding the first five eigenmodes of the AGARD 445.6 weakened model 3. The natural frequencies and mode shapes are taken from Yates [194].

with a filler to restore the wing surface. The name weakened model 3 can be derived from this procedure. According to Yates [194], the AGARD 445.6 wing is structurally characterized by an E-modulus of $E = 3.245\ GPa$, a shear modulus of $G = 0.412\ GPa$, a Poisson's ratio of $\nu = 0.31$, and a total mass of $m = 1.86\ kg$. On the basis of a FEM analysis, the first five structural eigenmode shapes and natural frequencies are provided by Yates' technical report [194]. Thus, the modes visualized in Figure 5.2 are considered for the structural dynamic modeling of the wing.

5.1.2 Deformed Grids and Modal Scaling

The eigenmode-based deformations have been scaled to small maximum amplitudes in order to take only nonlinear dependencies due to varying freestream conditions into account, whereas the motion-induced aerodynamics is governed by a linear characteristic. In this regard, a deflection amplitude study has been carried out to ensure dynamic linearity with respect to the structural perturbations. The resulting scaling factors for the considered eigenmodes are summarized in Table 5.2. Although a nonlinear influence of the structural inputs can be modeled with the presented approach as well, the ROM process for both sources of nonlinearity, namely changing freestream conditions and large amplitude motions, is still challenging.

Table 5.2: Scaling factors for the first five mode shapes to ensure $|\Delta z_{max}| = 0.1\%\ s$.

	Mode 1	Mode 2	Mode 3	Mode 4	Mode 5
Scaling factor SF $[10^{-3}]$	1.767	1.025	1.569	0.614	0.922

The interpolation of the scaled modal deflections onto the CFD surface grid has been realized by means of the thin-plate spline (TPS) method [32] using the non-deformed CFD and CSD grids as well as the FEM-based mode shape grids. Subsequently, the arc-length-based transfinite interpolation (TFI) is applied to update the block-internal grid points within the CFD domain [49]. As a consequence of the mode scaling procedure, the generalized aerodynamic forces provided by the CFD solver must be rescaled prior to an aeroelastic analysis to represent the correct relationship between the structural model and the flow-induced forces.

5.1.3 Steady Results and Flow Characterization

Prior to discussing the ROM training and application procedure, selected steady-state CFD results of the AGARD 445.6 wing are presented in order to verify the simulation set-up. To allow a comparison of the AER-NS results with reference data from the literature, the freestream Mach numbers $Ma_\infty = 0.96$ and $Ma_\infty = 1.141$ have been chosen, whereas the corresponding angle of attack is always defined to $\alpha = 0°$. The aforementioned freestream conditions were investigated during the original wind tunnel tests. For clarity, the relevant flow parameters and experimental data extracted from Reference [194] are recapitulated in Table 5.3. Considering the $Ma_\infty = 0.96$ and $Ma_\infty = 1.141$ cases, the numerical results presented by Lee-Rausch and Batina [91] can be used for comparative purposes. It should be noted that the freestream temperatures and Reynolds numbers presented in Table 5.3 are only implicitly given in Yates' technical report. Specifically, T_∞ has been computed based on the freestream Mach number and the flutter velocity via $T_\infty = V_f^2/(Ma_\infty^2 \cdot \gamma R)$. Moreover, the Reynolds numbers have been determined by applying Sutherland's law with respect to the dynamic viscosity.

On the basis of several RANS solutions with a fixed Reynolds number of $Re_{c_r} = 10^6$ for the AGARD 445.6 wing at zero angle of attack, the flow regime is categorized as subsonic up to $Ma_\infty \approx 0.93$. A further increase in the freestream Mach number leads to transonic flow conditions characterized by the coexistence of subsonic and supersonic regions in the vicinity of the investigated body. Thereby, a shock is formed near the wing inboard section. With a further increase of Ma_∞, the shock propagates towards the wing tip. This change in the flow topology affects the pressure distribution and, as a consequence, the forces and moments. Although the flow across the AGARD 445.6 wing is not governed by strong transonic effects according to Silva et al. [153], neither the steady nor

Table 5.3: Selected test conditions and experimental results sorted by the freestream Mach number on the basis of Yates' technical report [194].

Freestream Mach number Ma_∞	0.499	0.678	0.901	0.954	0.960	1.072	1.141
Freestream density $\rho_\infty[\frac{kg}{m^3}]$	0.428	0.208	0.100	0.063	0.063	0.055	0.078
Freestream temperature $T_\infty[K]$	297.3	289.8	269.9	258.3	257.8	257.4	253.7
Reynolds number $Re_{c_r}[10^6]$	2.245	1.495	0.968	0.662	0.655	0.648	0.984
Flutter velocity $V_f[\frac{m}{s}]$	172.46	231.37	296.69	307.36	309.01	344.73	364.33
Flutter frequency $f_f[Hz]$	20.39	17.98	16.09	14.50	13.89	13.80	17.49

the unsteady aerodynamic loads depend linearly on the freestream Mach number due to the influence of compressibility. For freestream Mach numbers of $Ma_\infty > 1.07$, the flow can be regarded as entirely supersonic.

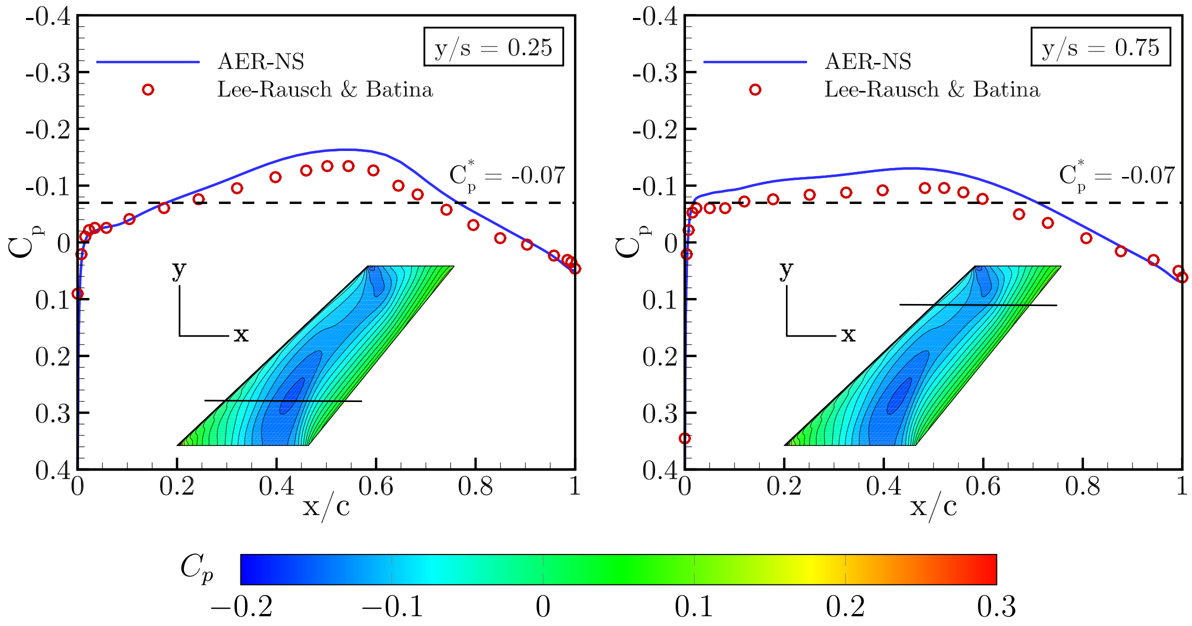

Figure 5.3: Steady-state pressure coefficient distribution for $Ma_\infty = 0.96$ computed with AER-NS. The results are shown for the sections $y/s = 0.25$ and $y/s = 0.75$. AGARD 445.6 configuration, $\alpha = 0°$, $Re_{c_r} = 0.655 \cdot 10^6$, $T_\infty = 257.8\ K$.

In Figure 5.3, the chordwise steady-state pressure coefficient distribution is shown for the $Ma_\infty = 0.96$ test case at two spanwise sections ($y/s = 0.25$ and $y/s = 0.75$), while both the AER-NS solution and the reference result from Lee-Rausch and Batina [91] are depicted. Since the NACA 65A004 airfoil is symmetric with respect to the chord, the C_p distribution is identical for the upper and lower wing surface. Therefore, only the upper surface is shown for convenience. The critical pressure coefficient $C_p^* = -0.07$ computed by Equation (5.1) has been added to Figure 5.3 for classification purposes.

When the pressure coefficient falls below C_p^*, the local Mach number becomes greater than one. As this is the case for the $Ma_\infty = 0.96$ case, local subsonic and supersonic regions coexist on the wing surface. Comparing the AER-NS result with the data provided by Lee-Rausch and Batina [91], the trend of the pressure distribution is very similar. However, the suction amplitude is slightly overpredicted by the AER-NS solver, leading to an offset between the diagrammed C_p curves between $0.3 \leq x/c \leq 0.7$. Nonetheless, an equivalent deviation has been also noted by Zhao et al. [202].

$$C_p^* = -\frac{2}{\gamma Ma_\infty^2}\left(1-\left(\frac{2}{\gamma+1}+\frac{\gamma-1}{\gamma+1}Ma_\infty^2\right)^{\frac{\gamma}{\gamma-1}}\right) \tag{5.1}$$

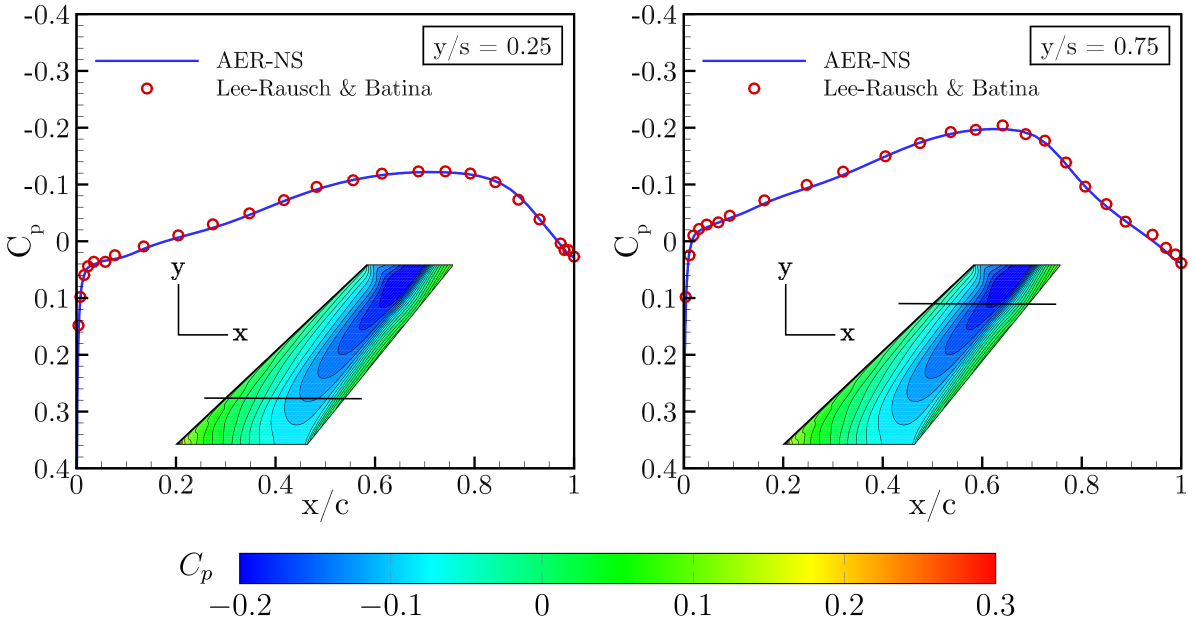

Figure 5.4: Steady-state pressure coefficient distribution for $Ma_\infty = 1.141$ computed with AER-NS. The results are shown for the sections $y/s = 0.25$ and $y/s = 0.75$. AGARD 445.6 configuration, $\alpha = 0°$, $Re_{c_r} = 0.984 \cdot 10^6$, $T_\infty = 253.7\ K$.

Furthermore, Figure 5.4, shows the chordwise steady C_p distribution for the $Ma_\infty = 1.141$ case; see Table 5.3 for an overview of the experimental test conditions. In contrast to the transonic case depicted in Figure 5.3, the flow at $Ma_\infty = 1.141$ can be characterized as supersonic. As it can be seen, the AER-NS solution agrees very well with the result obtained by Lee-Rausch and Batina [91]. Given the steady-state CFD solutions in Figures 5.3 and 5.4, it is concluded that the aerodynamic modeling of the AGARD 445.6 configuration is sufficiently accurate with respect to the subsequent ROM analyses.

5.2 Training Data Acquisition and ROM Construction

Based on the ROM procedure depicted in Figure 4.1, six training freestream conditions have been defined ranging from the subsonic to the supersonic flow regime in order to construct the reduced-order model. In particular, the freestream Mach numbers $Ma_{\infty,Trn} = [0.5, 0.7, 0.9, 1.0, 1.1, 1.2]$ have been selected for training the ROM, whereas the remaining freestream parameters are kept constant at $\alpha = 0°$, $Re_{c_r} = 10^6$, and $T_\infty = 270\ K$ throughout the following considerations. The selected $N_{FC} = 6$ freestream Mach numbers reflect the experimental test condition range outlined in Table 5.3. For an impression how the flight regime affects the flow on the wing, the steady-state pressure coefficient distribution for selected subsonic, transonic, and supersonic training conditions is shown in Figure 5.5.

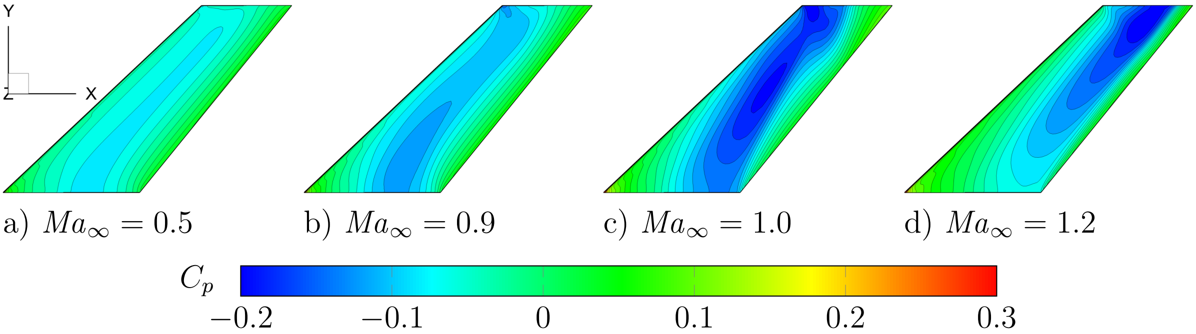

a) $Ma_\infty = 0.5$ b) $Ma_\infty = 0.9$ c) $Ma_\infty = 1.0$ d) $Ma_\infty = 1.2$

Figure 5.5: Steady-state pressure coefficient distribution of the AGARD 445.6 weakened model 3 configuration for selected training Mach numbers at $\alpha = 0°$, $T_\infty = 270\ K$, and $Re_{c_r} = 10^6$ (AER-NS).

As the variation of multiple freestream parameters at the same time leads to a drastically increased training data acquisition effort, fixed values have been assigned to the angle of attack, the Reynolds number, and the freestream temperature within the scope of this work. With respect to the zero angle of attack, the chosen state is in accordance with the experimental test conditions [194]. For the Reynolds number and the freestream temperature, however, an intermediate value within the respective variables' range has been chosen. Thus, the considered set-up is not strictly consistent with the test cases summarized in Table 5.3, as the Reynolds number and the freestream temperature depend on Ma_∞ in the original experiments. This fact must be taken into account when comparing the present results with experimental data. Nonetheless, the CFD-based reference data for evaluating the ROM performance have been generated with the same set-up ($Re_{c_r} = 10^6$ and $T_\infty = 270\ K$), which legitimizes the subsequent comparisons.

It is worth to emphasize that the CFD simulations as well as the ROM training and application presented in this chapter have been computed on the Linux cluster of the Leibniz Supercomputing Center (LRZ) which is equipped with Intel Xeon E5-2697 v3 2.6 GHz CPUs. In order to ensure comparability regarding the efficiency considerations discussed in Section 5.6, the computation jobs have been processed in serial operation (serial/parallel farming). Moreover, the steady and unsteady AER-NS simulations have been terminated if the Euclidean norm applied for the density normalized with the respective value after the first iteration falls below 1.0×10^{-5}.

Following the discussion of the ROM procedure in Section 4.1, problem-dependent inputs and outputs must be defined prior to the training data generation step. Due to the fact that the AGARD 445.6 configuration is commonly investigated in terms of aeroelastic flutter investigations, the ROM is also conditioned here to provide the generalized aerodynamic forces induced by structural, eigenmode-based excitations. Thus, the system inputs and outputs as well as the time-independent parameter vector introduced in Section 3.3 can be defined to:

$$\mathbf{u}(t) = \begin{pmatrix} q_1(t) \\ q_2(t) \\ \vdots \\ q_{n_q}(t) \end{pmatrix} \in \mathbb{R}^{n_q}, \qquad \mathbf{y}(t) = \begin{pmatrix} f_{gen,1}(t) \\ f_{gen,2}(t) \\ \vdots \\ f_{gen,n_f}(t) \end{pmatrix} \in \mathbb{R}^{n_f}, \qquad \Xi = (Ma_\infty) \in \mathbb{R} \tag{5.2}$$

In Equation (5.2), the ith modal coordinate is denoted by q_i, whereas the time-domain generalized aerodynamic forces vector element j is symbolized by $f_{gen,j}$; see Section 2.2 for a discussion of the variables. Referring to Section 5.1, five modes are considered for the AGARD 445.6 wing. Thus, the dimension of the vectors $\mathbf{u}$ and $\mathbf{y}$ is $n_q = n_f = 5$.

Starting from the steady-state solutions exemplarily shown in Figure 5.5, the aerodynamic responses induced by forced structural deflections have been computed using the AER-NS solver to obtain the training data for the freestream-condition-adaptive neuro-fuzzy model. Since small structural disturbances are considered in the context of the flutter modeling, which is in accordance with the modal scaling procedure shown in Section 5.1.2, the deformation influences the aerodynamic response in a linear way. Consequently, a signal for linear identification purposes is sufficient to excite the motion degrees of freedom. In this regard, the excitation signals are chosen to be of pulse type; see Figure 3.10d. The length of the pulse has been specified to 150 discrete time steps, whereas the maximum deflection amplitudes for the five considered mode shapes coincide with the corresponding scaling factors *SF* presented in Table 5.2. The aforementioned factors have been obtained by scaling the FEM-based mode shapes under the constraint that the deformation normal to the wing midplane must not exceed $|\Delta z_{max}| = 0.1\%\ s$, fulfilling the requirement of small perturbations. Hence, an excitation of the first mode by the generalized coordinate $q_1 = 1.767\times10^{-3}$ results in a maximum deflection of $0.1\%\ s$.

In order to clearly distinguish the influence of each generalized coordinate on the aerodynamic response and, at the same time, incorporate all modal degrees of freedom within a single CFD computation, the five mode shapes are consecutively excited by their corresponding pulse signal. Therefore, the pulse of the subsequently excited mode is applied if 1,000 time steps have elapsed since the end of the previous pulse excitation. The pulse signals depicted in Figure 5.6 are used for the $N_{FC} = 6$ time-marching simulations, while

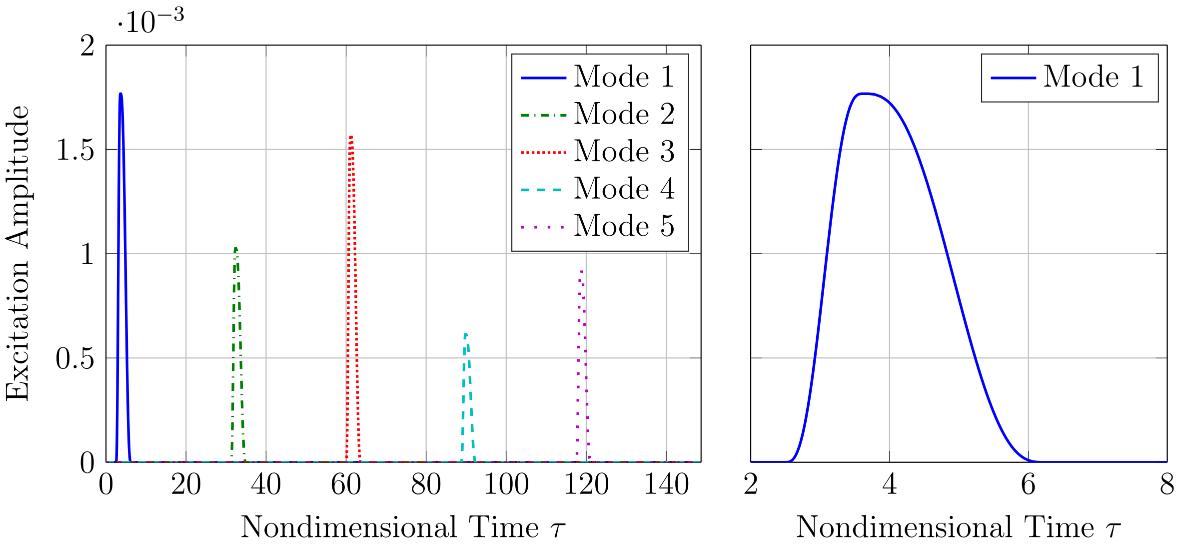

a) Excitation signals for all modes b) Detailed view of the first pulse

Figure 5.6: Discrete-time pulse signals for the forced-motion excitation of the first five modal degrees of freedom (AGARD 445.6 configuration, $\Delta\tau$=0.025).

the freestream Mach number is kept constant within each unsteady CFD run. Since a nondimensional time step size of $\Delta\tau = 0.025$ has been defined, the nondimensional time interval from 0 to 148.725 is taken into account. Thus, 5,950 × N_{Ma} input-output training samples are provided by the URANS-equation-based computations.

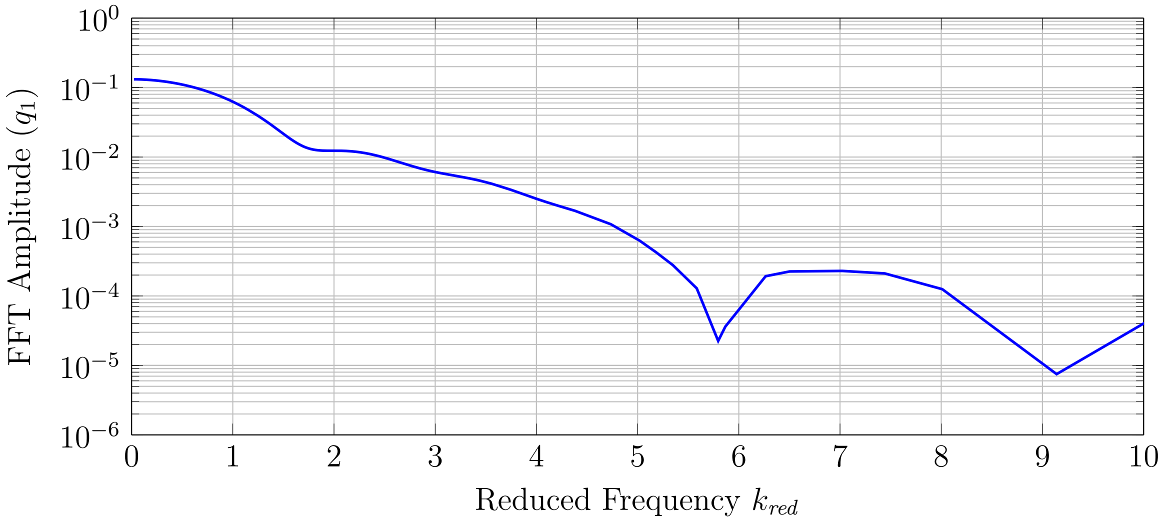

Figure 5.7: Frequency spectrum of the pulse excitation signal. FFT denotes the fast Fourier transform.

Additionally, the frequency spectrum of the applied pulse signal is depicted in Figure 5.7. As the reduced frequency ($k_{red} = c_{ref} \cdot \omega / U_\infty$ with $c_{ref} = c_r = 0.558\ m$) does not depend on the Mach number owing to the nondimensional time formulation of the AER-NS code, the frequency spectrum of the signal is also not Ma_∞-dependent. Nevertheless, Figure 5.7

demonstrates that the pulse signal introduces sufficient energy over a broad range of frequencies including the experimental flutter frequencies ($0.140 \leq k_{red} \leq 0.414$). Besides, the Nyquist frequency can be determined as $k_{red,Nyq} = 70.1$. Hence, also the sampling frequency does not represent a limitation for the intended simulations up to a reduced frequency of $k_{red} = 1.0$.

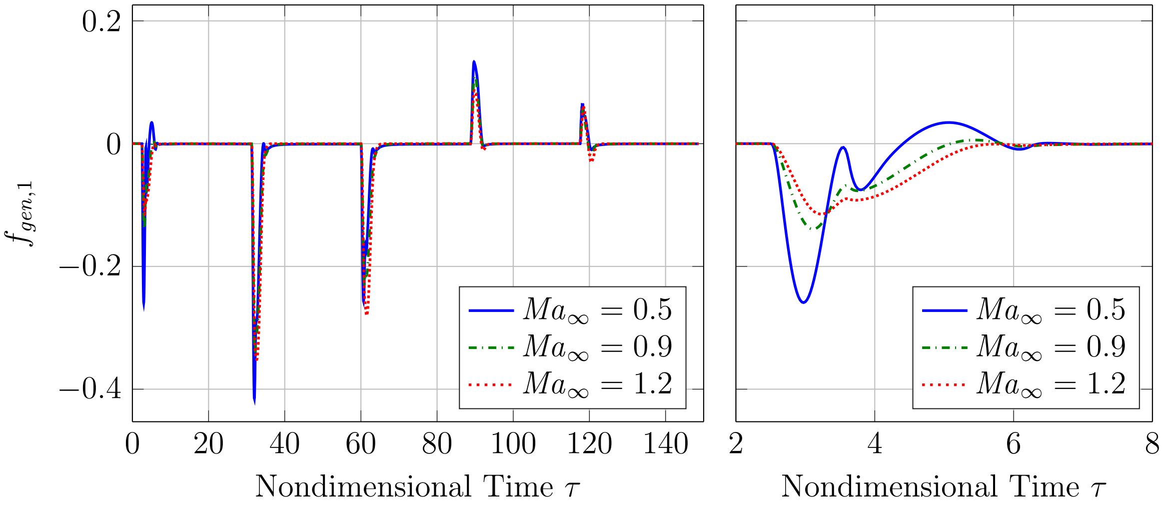

a) Complete time-series of the response

b) Detail around the first pulse

Figure 5.8: The CFD-based time-domain generalized aerodynamic forces response induced by the pulse excitation is shown for three freestream Mach numbers (AGARD 445.6 configuration, $\alpha = 0°$, $T_\infty = 270\ K$, $Re_{c_r} = 10^6$, AER-NS).

During the URANS computations for the six training freestream conditions, the instantaneous pressure- and viscosity-based forces are integrated over the surface of the investigated body and weighted with the considered mode shapes to obtain the time-discrete generalized aerodynamic force (GAF) coefficients; see Equations (2.54)-(2.56). For reasons of consistency with respect to the structural dynamics model, each vector element of $\mathbf{f}_{gen}$ has to be multiplied by the inverse of the respective scaling factor depicted in Table 5.2. This re-scaling procedure is justified by the assumed dynamic linearity due to the small-amplitude deflections. The first GAF vector element $f_{gen,1}$ caused by the prescribed pulse excitation is visualized exemplarily in Figure 5.8 for three training Mach numbers as a function of the nondimensional time τ. The nonlinear influence of Ma_∞ on the aerodynamic response is clearly visible in Figure 5.8b.

After the CFD-based input-output relationship concerning the structural excitations and the GAF responses has been obtained for the chosen training freestream conditions, the available dataset can be used for the nonlinear system identification process discussed in Chapter 3. With respect to the recurrence framework, the maximum dynamic delay-orders have been optimized yielding $m = 8$ and $n = 8$ for the inputs and outputs, respectively. Subsequently, the Monte-Carlo training methodology is applied according to Section 3.6. Therefore, $N_{MC} = 25$ neuro-fuzzy models have been trained in parallel, while the data samples have been randomly distributed for each NFM into training, validation, and test data maintaining the proportion of 70%, 15%, and 15%, respectively. The training of the local linear neuro-fuzzy models is realized by means of the LOLIMOT algorithm. In this regard, the termination criterion described in Section 3.4.2.2 is utilized. It is worth to emphasize that the neuro-fuzzy model constitutes a MISO model. As a consequence, for each of the $n_f = 5$ outputs an individual model must be trained.

For one of the 25 Monte-Carlo-based ROMs, Figure 5.9 illustrates the evolution of the one-step prediction error e_i over the number of iterations M for the first three GAF vector elements. It is interesting to note that the LOLIMOT structure selection only split the input dimension that corresponds to the freestream Mach number. In this way, two of the previously made assumptions are validated: On the one hand, the dynamic linearity for small perturbations is confirmed. On the other hand, it is demonstrated that the freestream condition exhibits a nonlinear influence on the overall system behavior, which is not captured by an ARX model or the local linear neuro-fuzzy model with $M = 1$. This insight may also allow the user to influence the local linear model partitioning process via the specification of constraints to include some prior knowledge about the underlying system.

Henceforth, the N_{MC} ROMs are considered as given and inalterable. Therefore, they can be employed for efficiently performing the simulations of interest.

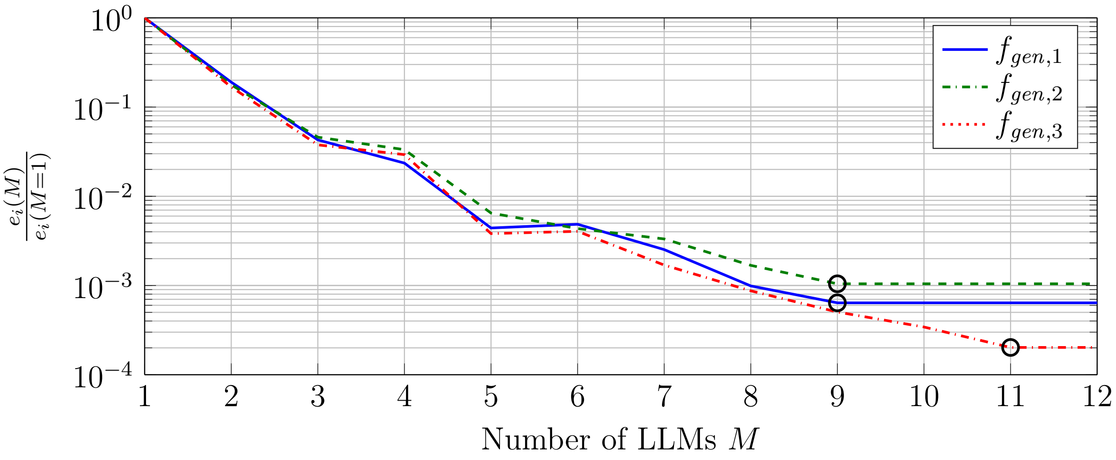

Figure 5.9: Development of the normalized one-step prediction error e_i with respect to the number of local linear models M for the first three GAF vector elements. The circle marks the further considered optimum model complexity for the given neuro-fuzzy model.

5.3 Unsteady Results - Time Domain

The trained reduced-order model is employed in this section to simulate the time-domain response induced by harmonic excitations in each of the generalized coordinates q_i. For this task, 20 freestream conditions are taken into account in order to demonstrate the capabilities of the parameter-adaptive neuro-fuzzy model. For clarification, not only the six freestream Mach numbers known from the training process but also 14 additional Ma_∞, which are not contained explicitly in the training dataset, are considered. In Table 5.4, the complete list of simulated Mach numbers $Ma_{\infty,Sim}$ is presented.

Table 5.4: Overview of the freestream Mach numbers which have been computed with the ROM and AER-NS. The cases incorporated within the training dataset are underlined.

$Ma_{\infty,Sim}$	0.499	$\underline{0.500}$	0.550	0.600	0.650	0.678	$\underline{0.700}$	0.750	0.800	0.850
	$\underline{0.900}$	0.901	0.954	$\underline{1.000}$	1.050	1.072	$\underline{1.100}$	1.141	1.150	$\underline{1.200}$

The modus operandi for each unsteady simulation is as follows: A single structural mode is excited based on a sinusoidal signal with defined reduced frequency and amplitude, whereas the inputs referring to the other modes are assigned to zero. The maximum amplitude for the excitation in mode i is chosen to be identical with the corresponding scaling factor SF_i given in Table 5.2. Hence, the time-varying excitation amplitude can be described by the following relation, taking the nondimensional formulation of the CFD framework into account:

$$q_i(\tau) = SF_i \cdot \Theta(\omega,\tau) = SF_i \cdot \sin(\omega \cdot \tau) = SF_i \cdot \sin\left(\frac{k_{red} \cdot l_{ref} \cdot Ma_\infty \cdot \sqrt{\gamma}}{c_{ref}} \cdot \tau\right) \tag{5.3}$$

In Equation (5.3), $\Theta(\omega,\tau)$ denotes the nondimensional excitation amplitude, ω is the circular frequency, and l_{ref} refers to the grid reference length for the nondimensional flow solver formulation. Furthermore, γ is the ratio of specific heats, which has the value $\gamma = 1.4$ for air as the fluid medium. For the present computational grid, $l_{ref} = 1$ applies. Moreover, the reference length for evaluating the reduced frequency has been defined to $c_{ref} = c_r = 0.558\ m$.

In order to achieve periodicity with respect to the aerodynamic response, three oscillation cycles have been computed using both the ROM and the AER-NS solver. Considering the CFD reference solution, each cycle is resolved with $N_\tau = 100$ discrete time steps. Hence, the nondimensional time step size $\Delta\tau$ corresponding to the considered freestream Mach number and reduced frequency is case-dependent and can be calculated by means of Equation 5.4.

$$\Delta\tau = \frac{2\pi \cdot c_{ref}}{(N_\tau - 1) \cdot k_{red} \cdot l_{ref} \cdot Ma_\infty \cdot \sqrt{\gamma}} \tag{5.4}$$

In contrast, the ROM is always applied with the identical time step size resulting from the training dataset (here: $\Delta\tau = 0.025$). As a consequence, a different cycle discretization is obtained for each combination of Ma_∞ and k_{red}.

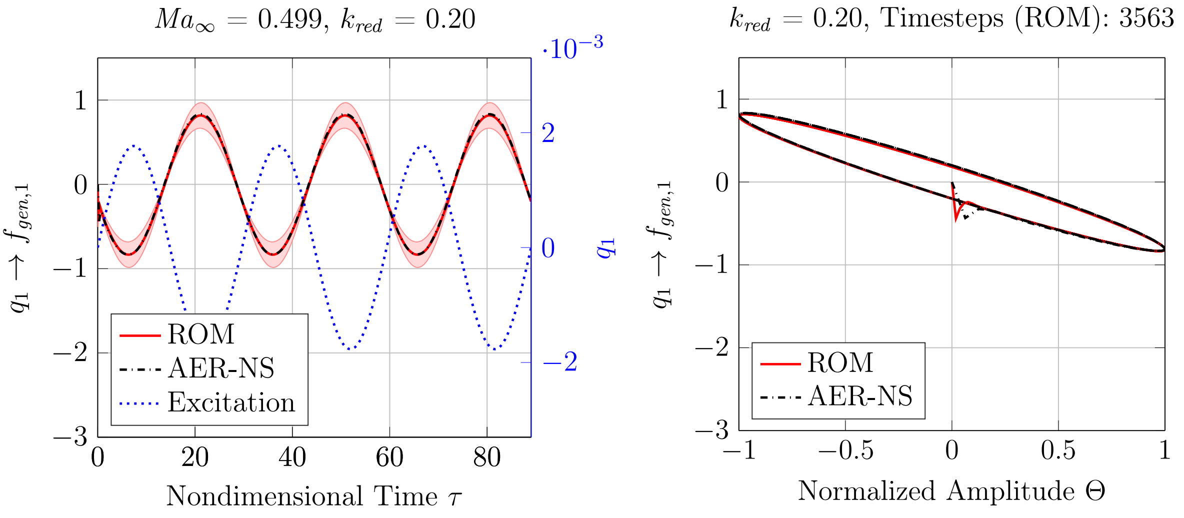

Figure 5.10: Time-domain response and Lissajous figure showing $f_{gen,1}$ caused by three harmonic excitation cycles of q_1 with $k_{red} = 0.20$. AGARD 445.6, $Ma_\infty = 0.499$, $\alpha = 0°$, $T_\infty = 270\ K$, $Re_{c_r} = 10^6$.

Concerning the eigenmode-based harmonic deflections, various reduced frequencies have been simulated to evaluate the effect of the excitation frequency on the ROM performance. An overview of the considered reduced frequencies is provided in Table 5.5. Taking into account the 20 freestream conditions, 12 reduced frequencies, and 5 structural modes, in total 1,200 unsteady cases have been simulated for the AGARD 445.6 wing with the neuro-fuzzy-based ROM and AER-NS.

Table 5.5: Overview of the reduced frequencies which have been computed with the ROM and the AER-NS solver.

k_{red}	0.01	0.02	0.05	0.10	0.20	0.30	0.40	0.50	0.60	0.70	0.80	1.00

In Figures 5.10-5.12, the time-domain response of the AGARD 445.6 wing is shown exemplarily for three freestream conditions in terms of the first GAF vector element $f_{gen,1}(\tau)$ excited by a sinusoidal deflection of the first mode shape. Therefore, representative freestream Mach numbers have been selected from the subsonic, transonic, and supersonic flight regime. According to Section 5.2, $N_{MC} = 25$ independent models have been obtained based on the Monte-Carlo training strategy. Hence, all available models can be applied to each simulation case resulting in 25 responses that can be statistically processed. Owing to this fact, all diagrams in the following display the mean response as the main line, whereas the standard deviation σ of the response is visualized by a shaded area around the main curve unless otherwise specified. Furthermore, the respective Lissajous figures are plotted on the right hand side of Figures 5.10-5.12 showing the ROM and the CFD solver output time-series as a function of the normalized amplitude Θ. For the Lissajous plots, the standard deviation of the ROM output is omitted for the sake of a clear representation.

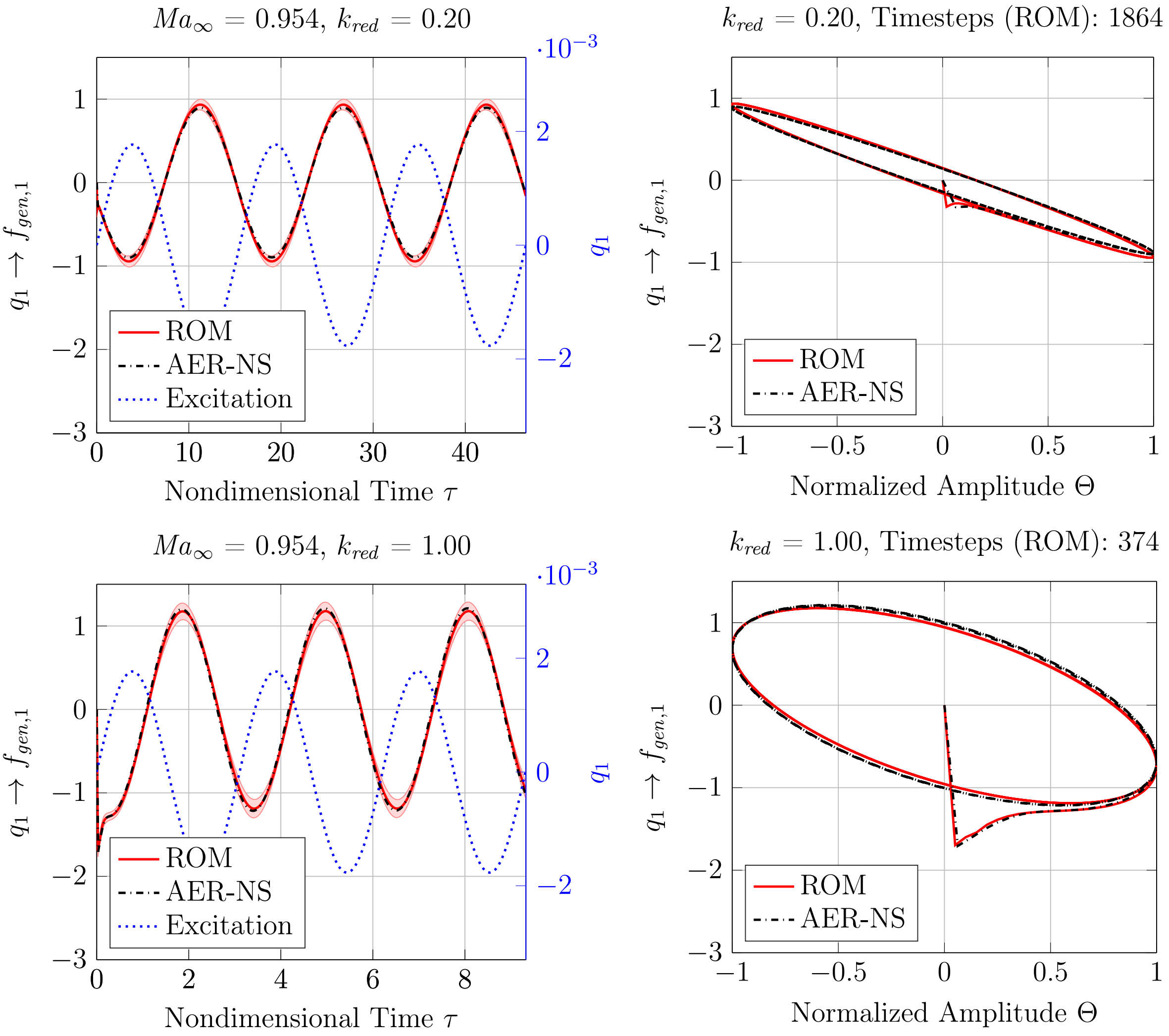

Figure 5.11: Time-domain response and Lissajous figure showing $f_{gen,1}$ caused by three harmonic excitation cycles of q_1 with $k_{red} = [0.20,\ 1.00]$. AGARD 445.6, $Ma_\infty = 0.954$, $\alpha = 0°$, $T_\infty = 270\ K$, $Re_{c_r} = 10^6$.

The $Ma_\infty = 0.499$ case depicted in Figure 5.10 indicates a very good correlation between the mean ROM result and the AER-NS reference solution since this condition corresponds almost to $Ma_{\infty,Trn} = 0.5$ incorporated within the training freestream Mach number set. Hence, it is verified that the ROM is capable of reproducing the trained system behavior with sufficient accuracy. Nonetheless, the standard deviation exhibits a larger magnitude near the extrema of the $f_{gen,1}$ response. Consequently, individual models may not always provide the correct amplitude characteristic of the motion-induced generalized aerodynamic force for this case. This is one of the reasons why the use of the Monte-Carlo-based reduced-order modeling strategy is recommended.

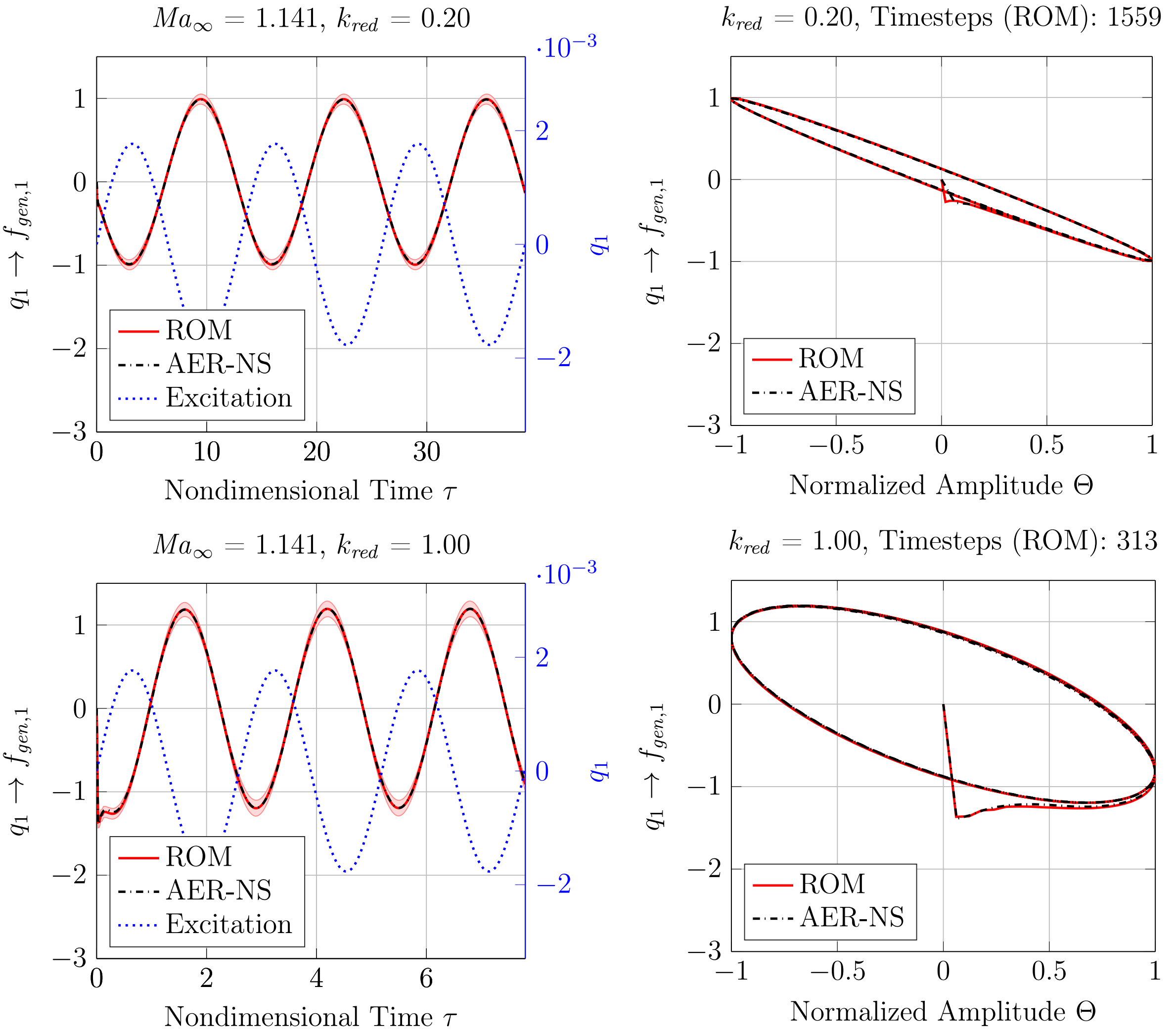

Figure 5.12: Time-domain response and Lissajous figure showing $f_{gen,1}$ caused by three harmonic excitation cycles of q_1 with $k_{red} = [0.20, 1.00]$. AGARD 445.6, $Ma_\infty = 1.141$, $\alpha = 0°$, $T_\infty = 270\ K$, $Re_{c_r} = 10^6$.

The cases in Figures 5.11 and 5.12 can be considered as an *interpolation* with respect to the trained freestream Mach number range. For $Ma_\infty = 0.954$, the ROM results deviate slightly from the reference in terms of the phase and amplitude of the response. Nonetheless, the general characteristics are reflected well for the considered examples, which is underpinned by the results at $Ma_\infty = 1.141$. The standard deviations observed in Figures 5.11 and 5.12 are comparatively small which indicates the good reproducibility of the ROM solution.

However, larger discrepancies are discovered for certain excitation mode – GAF vector element combinations. For example, Figure 5.13 shows the $f_{gen,1}$ time-series due to an excitation of the second structural mode as well as the $f_{gen,2}$ response induced by a harmonic excitation of mode 1 for $Ma_\infty = 0.954$. While the phase of the response is well represented, there is a noticeable amplitude offset for the $q_1 \rightarrow f_{gen,2}$ case.

A similar deviation between the mean ROM solution and the AER-NS reference result is ascertained for the $q_2 \rightarrow f_{gen,2}$ case at a freestream Mach number of $Ma_\infty = 1.072$ shown in Figure 5.14. It is worth to note that the CFD reference is not within the range spanned by the standard deviation of the ROM result. Therefore, it must be followed that training data are missing for this case to better resolve the amplitude characteristic of the aerodynamic system. At this point, the question arises why some combinations fit better than others. The answer is that some transfer functions between the excitation mode and the GAF response element are more nonlinear than others. This is illustrated in the following section.

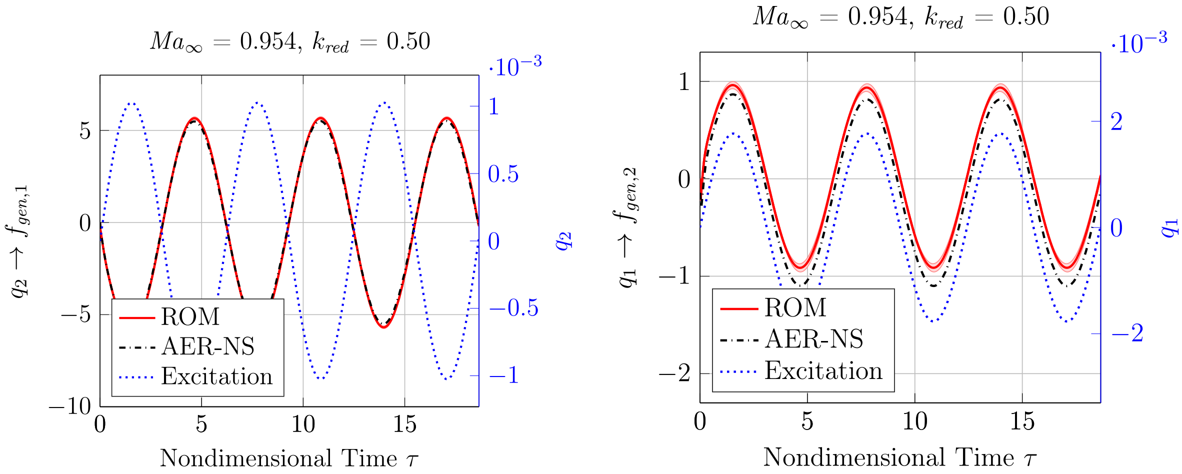

Figure 5.13: Left: Time-domain response of $f_{gen,1}$ caused by three harmonic excitation cycles of q_2 with $k_{red} = 0.50$. Right: Time-domain response of $f_{gen,2}$ caused by three harmonic excitation cycles of q_1 with $k_{red} = 0.50$. AGARD 445.6, $Ma_\infty = 0.954$, $\alpha = 0°$, $T_\infty = 270\ K$, $Re_{c_r} = 10^6$.

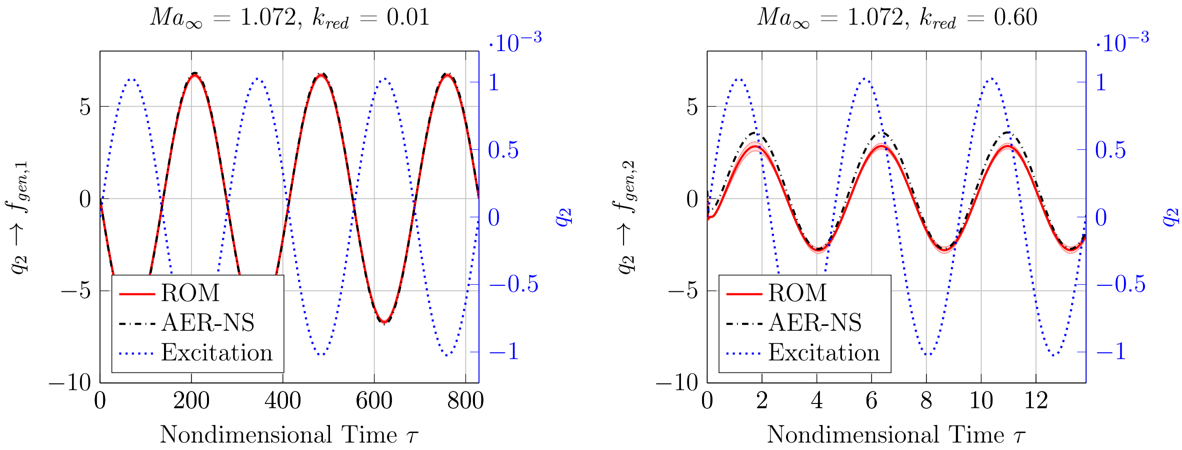

Figure 5.14: Left: Time-domain response of $f_{gen,1}$ caused by three harmonic excitation cycles of q_2 with $k_{red} = 0.01$. Right: Time-domain response of $f_{gen,2}$ caused by three harmonic excitation cycles of q_2 with $k_{red} = 0.60$. AGARD 445.6, $Ma_\infty = 1.072$, $\alpha = 0°$, $T_\infty = 270\ K$, $Re_{c_r} = 10^6$.

5.4 Unsteady Results - Frequency Domain

For a more compact representation, the computed time-domain results discussed in Section 5.3 can be transformed into the frequency domain via Fourier analysis. Therefore, only the third oscillation cycle is taken into account. Details regarding the aforementioned transformation are discussed, for instance, in the work of Fleischer [38].

As a further motivation for the frequency-domain consideration, the resulting transfer function, namely the **GAF** matrix, can be utilized to conduct a numerical flutter analysis, which is outlined in Section 5.5. Because of the assumed dynamic linearity around a chosen reference state, i.e., for fixed freestream conditions, the real and imaginary parts of the first harmonic load are sufficient to describe the aerodynamic response [128, 192]. Thus, the **GAF** matrix is computed for each combination of k_{red} and Ma_∞ using the ROM as well as the AER-NS solver. The complex-valued matrix element $GAF_{ij}(k_{red})$ can be interpreted as the first harmonic of the ith generalized aerodynamic force response that is caused by an excitation of the jth generalized coordinate with frequency k_{red} and unit amplitude.

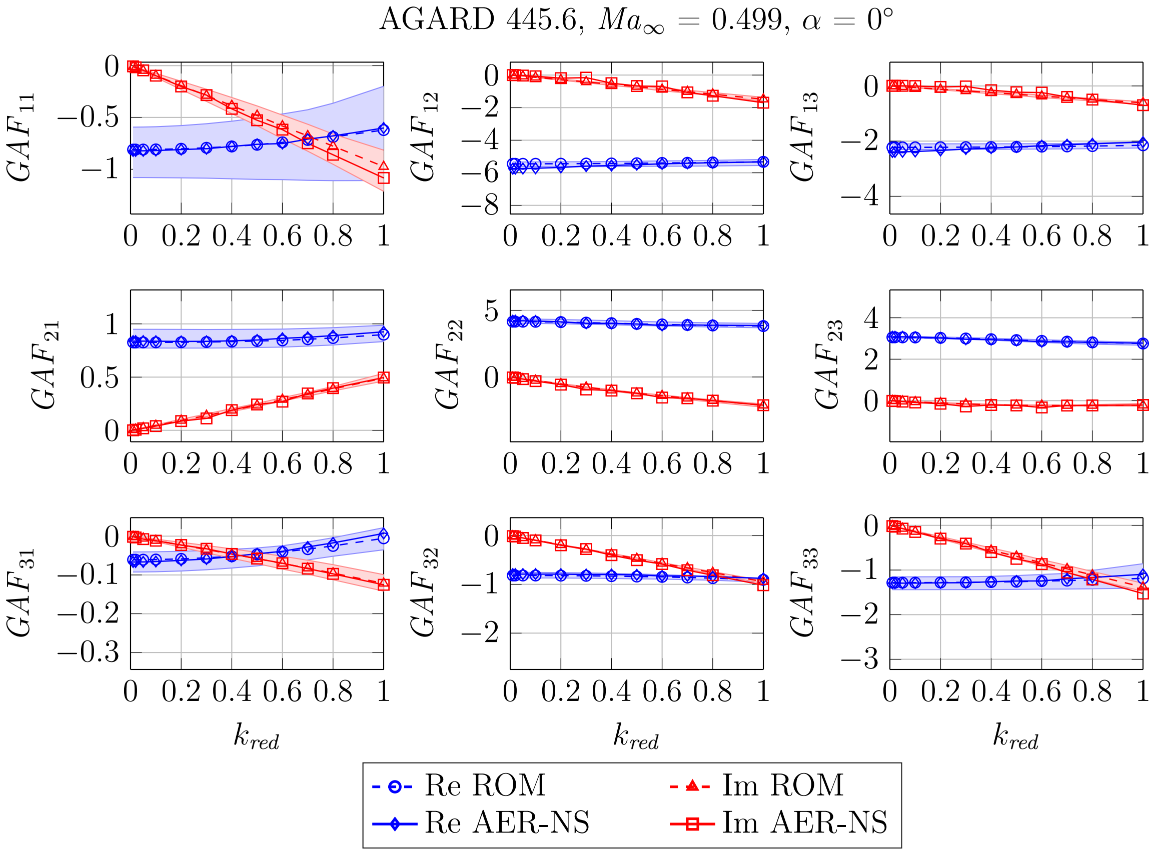

Figure 5.15: Real and imaginary parts of the frequency-domain **GAF** matrix elements plotted as a function of the reduced frequency for $Ma_\infty = 0.499$. The shaded area is spanned between the respective minimum and maximum values resulting from the $N_{MC} = 25$ models. AGARD 445.6, $\alpha = 0°$, $T_\infty = 270\ K$, $Re_{c_r} = 10^6$.

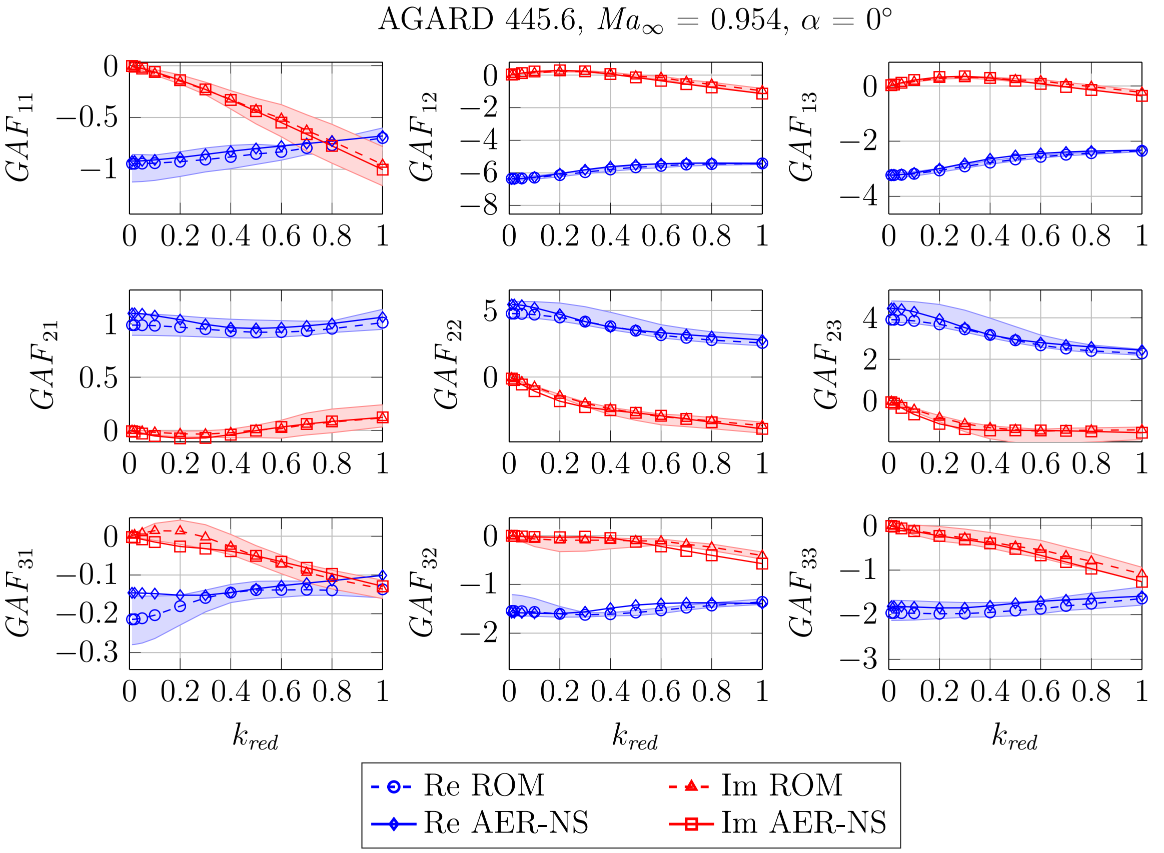

Figure 5.16: Real and imaginary parts of the frequency-domain **GAF** matrix elements plotted as a function of the reduced frequency for $Ma_\infty = 0.954$. The shaded area is spanned between the respective minimum and maximum values resulting from the $N_{MC} = 25$ models. AGARD 445.6, $\alpha = 0°$, $T_\infty = 270\ K$, $Re_{c_r} = 10^6$.

For further insights regarding the variation of the model outputs, the $N_{MC} = 25$ ROMs (see Section 5.2) have been applied for computing the **GAF** matrix with respect to all cases described by Tables 5.4 and 5.5. In contrast to the standard deviation that has been considered beforehand, the minimum and maximum of the occurring GAF values are shown in the following figures by means of the shaded area. In this way, the reproducibility and significance of the results is made assessable.

In Figures 5.15-5.17, the frequency domain **GAF** matrix elements are shown as a function of the reduced frequency for the first three eigenmodes and three selected freestream Mach numbers. Thereby, the real part of the complex value is marked with *Re*, while the imaginary part is denoted with *Im*. Similar to the observations for the time domain responses, very good agreement is ascertained for the subsonic case at $Ma_\infty = 0.499$. This is not surprising as this freestream condition is almost exactly included within the training data. Only for higher excitation frequencies, some deviations are detectable. The reason for this frequency-dependent error behavior is the fixed time step size of the discrete model that results in a coarser cycle discretization for higher k_{red}. For this reason, reduced frequencies of $k_{red} > 1.0$ have not been considered in this chapter.

The frequency domain transfer function for $Ma_\infty = 0.954$ depicted in Figure 5.16 can be considered as the most critical benchmark case for two reasons: First, this freestream Mach number exhibits the most dominant transonic aerodynamic effects from all considered flight conditions ($Ma_{\infty,Sim}$). Second, the adjacent training Mach numbers $Ma_{\infty,Trn} = [0.9,\, 1.0]$ have been chosen in a comparatively coarse way, despite the dominant nonlinearities in this challenging flow regime. Nevertheless, satisfying to good conformity between the ROM result and the CFD reference can be observed depending on the matrix element. Most important, the general characteristics of the aerodynamic system are captured by the neuro-fuzzy model. Keeping in mind that the approach is employed for unsteady aerodynamic computations across subsonic, transonic, and supersonic flow regimes, the overall solution quality is remarkable.

Moreover, also the cases with supersonic inflow conditions show a good agreement of the ROM results with the corresponding AER-NS solution. Here, the $Ma_\infty = 1.141$ case is exemplary shown in Figure 5.17 to underpin this statement.

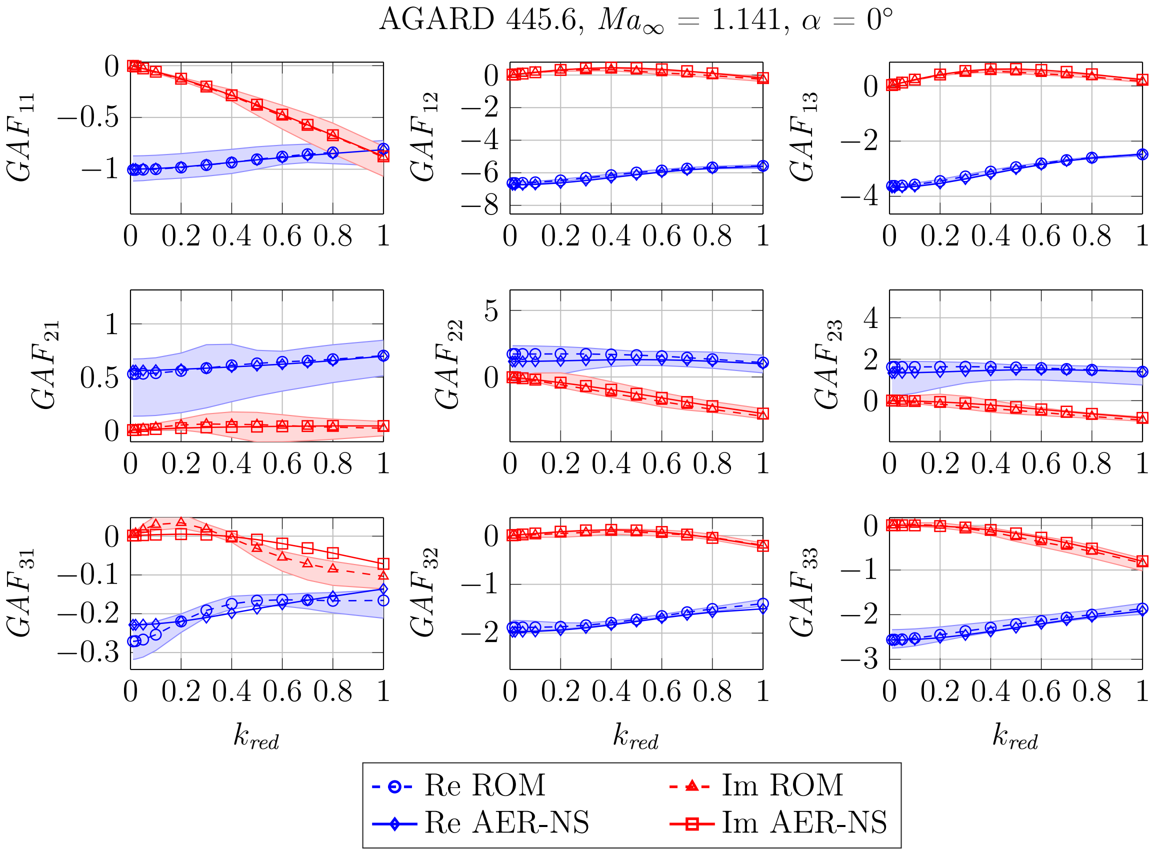

Figure 5.17: Real and imaginary parts of the frequency-domain **GAF** matrix elements plotted as a function of the reduced frequency for $Ma_\infty = 1.141$. The shaded area is spanned between the respective minimum and maximum values resulting from the $N_{MC} = 25$ models. AGARD 445.6, $\alpha = 0°$, $T_\infty = 270\ K$, $Re_{c_r} = 10^6$.

Comparing individual matrix elements for different freestream conditions, it becomes evident that some $\mathbf{GAF}_{ij}$ are more difficult to predict than others. Especially, the matrix elements GAF_{31} and GAF_{23} seem to be challenging for the ROM. This can be traced back to their distinct nonlinear dependence on the freestream Mach number.

In order to visualize this characteristic, the **GAF** matrix elements have been plotted in Figures 5.18 and 5.19 for fixed reduced frequencies as a function of selected freestream Mach numbers. For a clear presentation, only the first three modes are illustrated. Considering the matrix entries with observable discrepancies between the ROM and the reference solution, a comparatively large variation in the model output is encountered in most instances. Hence, for a more accurate resolution of the aerodynamics, further training data in terms of additional freestream parameters are required. If the $k_{red} = 0.20$ case shown in Figure 5.18 is juxtaposed to the $k_{red} = 1.00$ case depicted in Figure 5.19, it can be stated that the deviations between the ROM and the CFD solver do not exhibit a pronounced frequency-dependent behavior. Nevertheless, the unsteady aerodynamic characteristics are strongly affected by the change of the excitation frequency.

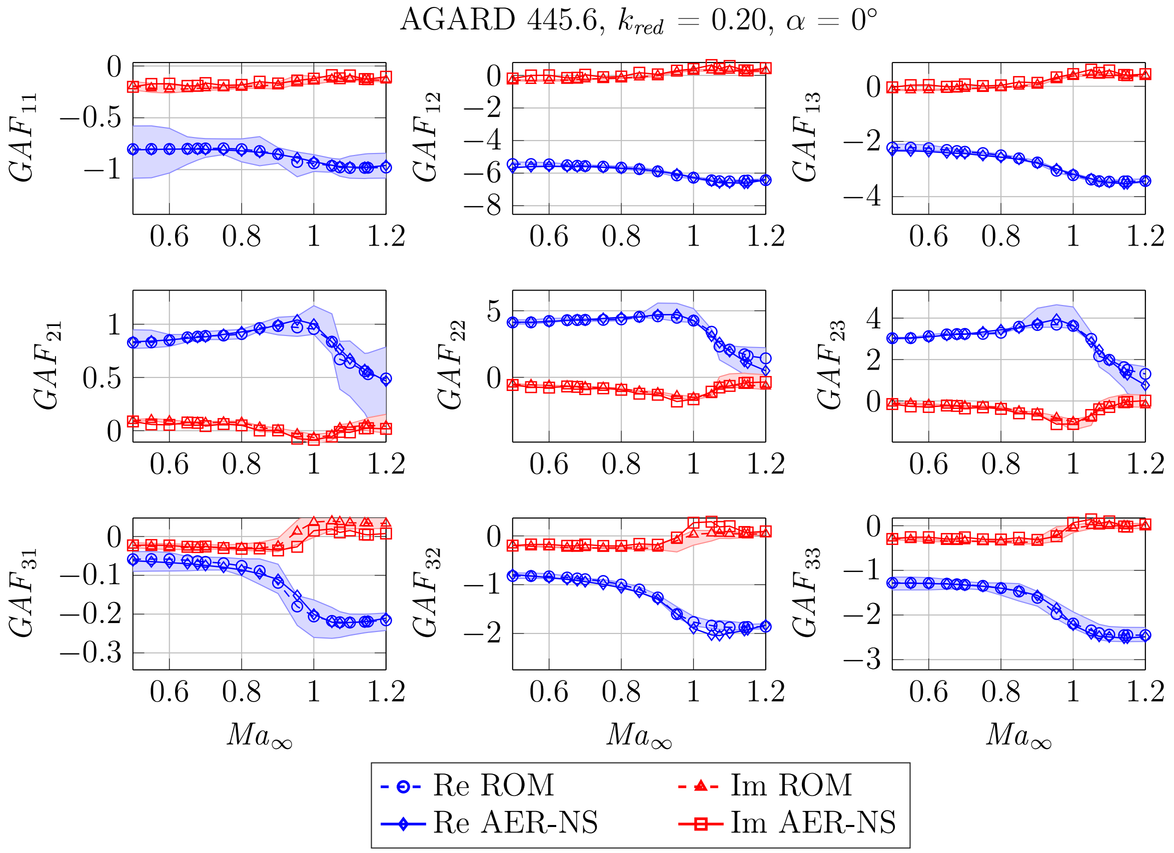

Figure 5.18: Real and imaginary parts of the frequency-domain **GAF** matrix elements plotted as a function of the freestream Mach number for $k_{red} = 0.20$. The shaded area is spanned between the respective minimum and maximum values resulting from the $N_{MC} = 25$ models. AGARD 445.6, $\alpha = 0°$, $T_\infty = 270\ K$, $Re_{c_r} = 10^6$.

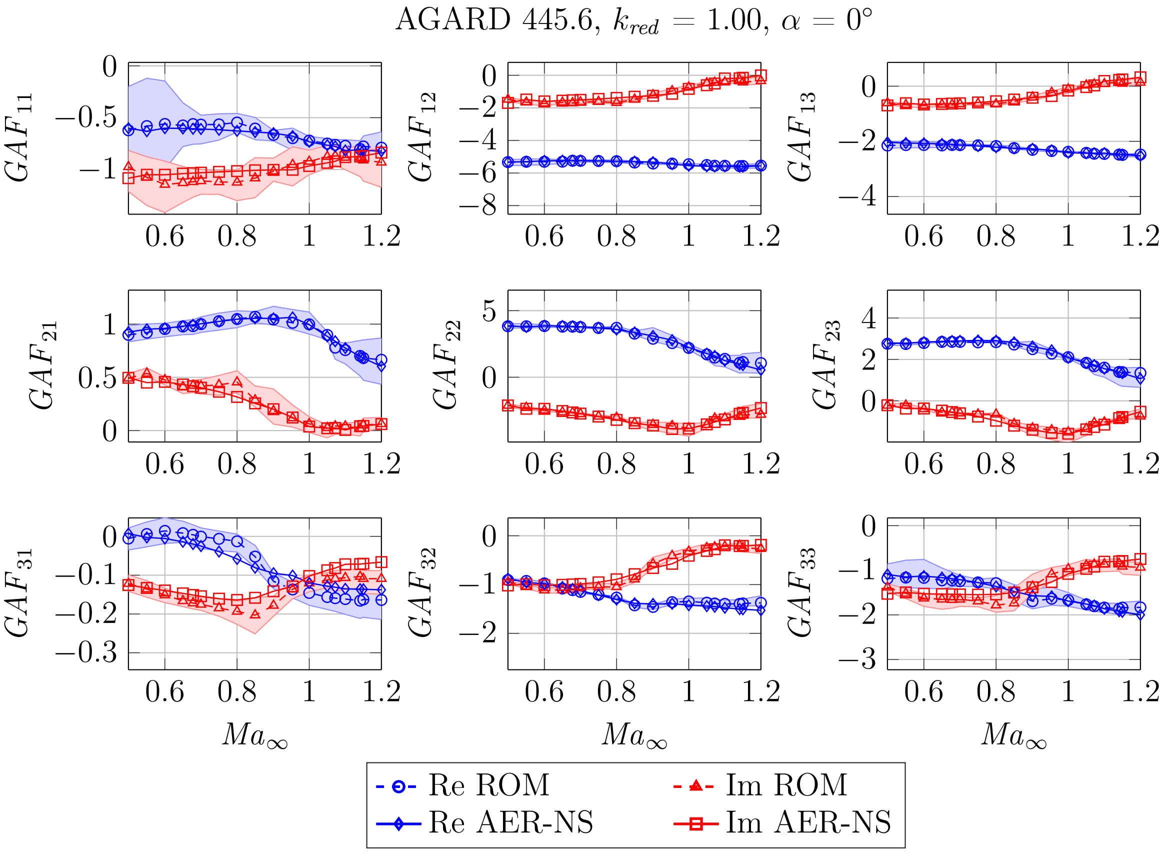

Figure 5.19: Real and imaginary parts of the frequency-domain **GAF** matrix elements plotted as a function of the freestream Mach number for $k_{red} = 1.00$. The shaded area is spanned between the respective minimum and maximum values resulting from the $N_{MC} = 25$ models. AGARD 445.6, $\alpha = 0°$, $T_\infty = 270\ K$, $Re_{c_r} = 10^6$.

Finally, an overview of the frequency-domain datasets is presented for all computed Ma_∞-k_{red} combinations. In Figures 5.20 and 5.21, the respective real and imaginary parts of the **GAF** matrix are shown for the first two modal degrees of freedom. Thereby, the mean ROM output is denoted by the colored surface, whereas the AER-NS result is depicted with the mesh in combination with the inked points. This representation is well suited to highlight the nonlinearity caused by the freestream Mach number variation. From the 3D plots it becomes evident that the general characteristics are reproduced well by the presented ROM approach. Noticeable deviations of the ROM solution relative to the URANS result can be observed at $Ma_\infty = 0.954$ due to the limited training data within this flight regime. Between the trained conditions at $Ma_{\infty,Trn} = 0.9$ and $Ma_{\infty,Trn} = 1.0$, a shock evolves from the inboard region of the AGARD 445.6 wing, which has an influence on the global aerodynamic characteristics. The latter effect is not fully captured by the training data and, therefore, can not be predicted accurately by the ROM. Besides, there are some discrepancies at the edges and corners of the considered

k_{red}-Ma_∞ space, e.g., for large Mach numbers and low reduced frequencies. In conclusion, however, it can be stated that the NFM-based ROM reproduces the nonlinearities with respect to the AGARD 445.6 wing unsteady aerodynamics.

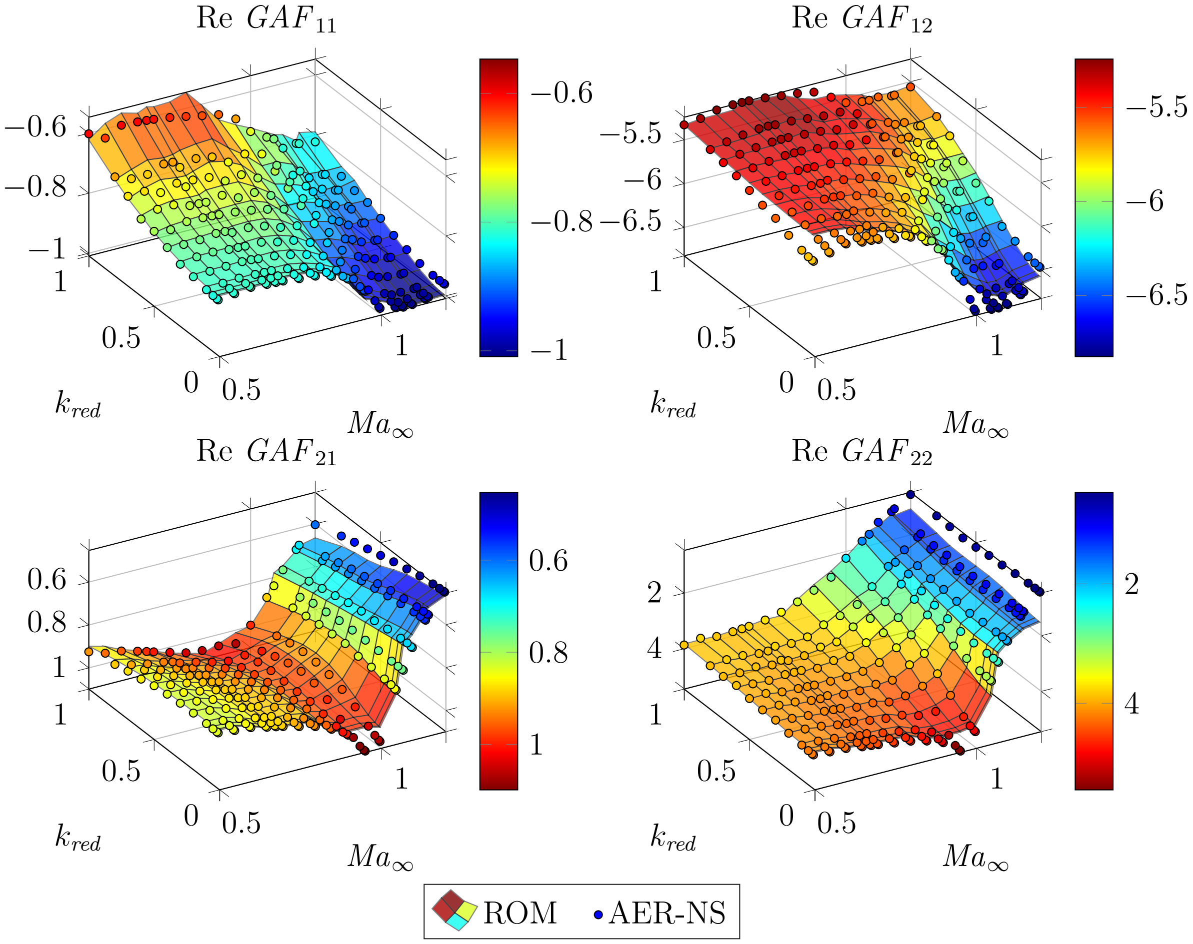

Figure 5.20: Real part of the frequency-domain **GAF** matrix as a function of reduced frequency and freestream Mach number. The ROM solution (mean of $N_{MC} = 25$ responses) is visualized by the surface plot, whereas the AER-NS result is represented by the mesh with colored points. AGARD 445.6, $\alpha = 0°$, $T_\infty = 270\ K$, $Re_{c_r} = 10^6$.

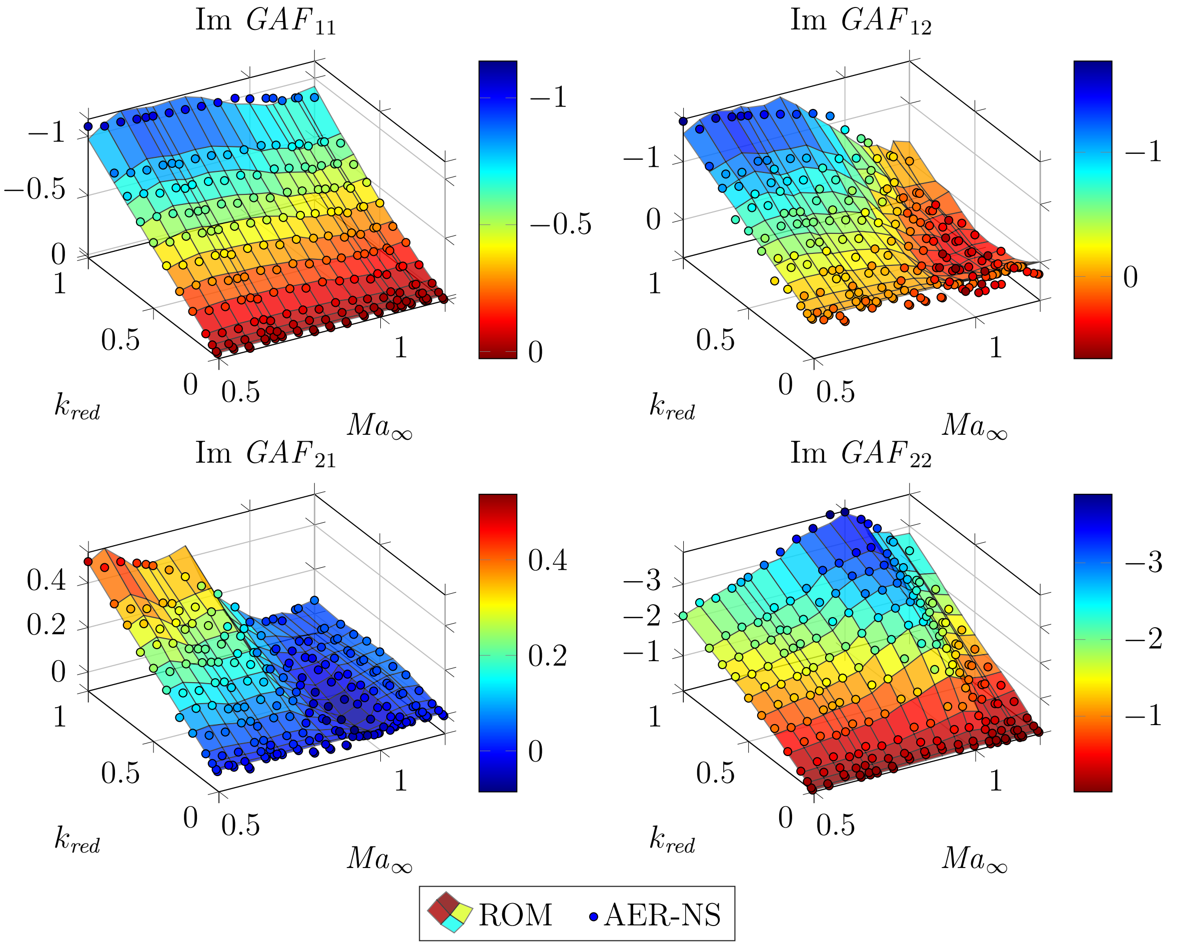

Figure 5.21: Imaginary part of the frequency-domain **GAF** matrix as a function of reduced frequency and freestream Mach number. The ROM solution (mean of $N_{MC} = 25$ responses) is visualized by the surface plot, whereas the AER-NS result is represented by the mesh with colored points. AGARD 445.6, $\alpha = 0°$, $T_\infty = 270\ K$, $Re_{c_r} = 10^6$.

5.5 Numerical Flutter Analysis

Additionally, a linear stability analysis has been conducted using both the ROM- and the CFD-based unsteady aerodynamic forces. Since the associated procedure involves also structural modeling aspects as well as the interaction between the inertial, elastic, and aerodynamic forces, the findings of this section should not be considered as a model verification but as a general feasibility demonstration.

The flutter analysis has been performed by means of the pk-method [56, 68] under consideration of the first five structural eigenmodes. Therefore, the frequency-domain **GAF** matrices discussed in the previous section have been utilized. In Table 5.5, the respective reduced frequencies are listed, whereas the following freestream Mach numbers are taken into account: $Ma_\infty = [0.499,\ 0.678,\ 0.901,\ 0.954,\ 1.072,\ 1.141]$. For verification purposes, the **GAF** matrices resulting from the ROM procedure as well as the CFD methodology are considered for the studies presented below.

Besides the aerodynamic and structural modeling discussed in Section 5.1.1, further inputs are required for the investigation of aeroelastic stability. In particular, the generalized mass matrix $\mathbf{M}_{gen}$ is defined by an identity matrix (mass normalized form), whereas all elements of the generalized damping matrix $\mathbf{C}_{gen}$ have been set to zero. Furthermore, the diagonal of the generalized stiffness matrix $\mathbf{K}_{gen}$ is composed of the squared angular frequencies: $K_{gen,ii} = (2\pi \cdot f_i)^2$. The corresponding natural frequencies f_i can be extracted from Figure 5.2.

Hereinafter, only normalized quantities are considered as the output of the pk-method-based flutter simulation. The nondimensional indicators for comparative purposes are the flutter speed index *FSI* and the frequency ratio *FR*. According to Yates [194], they are defined as:

$$FSI = \frac{2V_f}{c_{ref} \cdot \omega_\alpha \cdot \sqrt{\overline{\mu}}}, \qquad \overline{\mu} = \frac{m}{\rho_\infty \cdot V} \quad \text{with } V = \frac{s \cdot \pi}{3}\left(\frac{c_r^2}{4} + \frac{c_r \cdot c_t}{4} + \frac{c_t^2}{4}\right) \tag{5.5}$$

$$FR = \frac{\omega_f}{\omega_\alpha} \tag{5.6}$$

Based on Equation (5.5), the *FSI* relates the flutter speed V_f to the freestream density ρ_∞, which is included within the mass ratio $\overline{\mu}$. Moreover, c_t refers to the tip chord, whereas s and c_r denote the semi-span and the root chord, respectively. With the mass of the wing of $m = 1.86\ kg$, the mass ratio can be calculated for each freestream condition using the freestream densities provided by Table 5.3. The resulting values for $\overline{\mu}$ are given in Table 5.6 as a function of Ma_∞. Furthermore, the angular frequency of the first uncoupled torsion mode is regarded with $\omega_\alpha = 239.3\ rad/s$.

Originating from the previously outlined modeling framework, the computed *FSI* and *FR* values are plotted across the freestream Mach number in Figure 5.22 for both the ROM- and the CFD-based aerodynamics. Besides the URANS results (AER-NS),

Table 5.6: Mass ratio for the considered freestream Mach number range [194].

Freestream Mach number Ma_∞	0.499	0.678	0.901	0.954	1.072	1.141
Mass ratio $\overline{\mu}$	33.465	68.753	143.92	225.82	259.59	182.74

Euler-equation-based flutter speed indices and frequency ratios extracted from Reference [185] are shown (AER-Eu). At this point, it is worth mentioning again that the freestream conditions investigated by the ROM and the AER-NS solver are not strictly consistent with the experiment; see the discussion about the fixed Reynolds number and freestream temperature in Section 5.2. Hence, the only reference solution for the ROM is the AER-NS result. The other data sources have been added for classification purposes only.

Concerning the ROM result, the **GAF** matrices obtained by the $N_{MC} = 25$ models have been independently utilized in terms of the pk-method flutter analyses. The plots in Figure 5.22 therefore show the mean of the ROM-generated *FSI* and *FR* data, whereas the shaded area is spanned between the encountered minimum and maximum values. An overview of the flutter speed indices and frequency ratios is also given in Table 5.7.

Table 5.7: Flutter speed indices and frequency ratios obtained by the ROM (averaged) and the AER-NS solver at six freestream conditions. For classification purposes, Euler-CFD and experimental results are also included. AGARD 445.6, $\alpha = 0°$, $T_\infty = 270\ K$, $Re_{c_r} = 10^6$.

Ma_∞	0.499	0.678	0.901	0.954	1.072	1.141
FSI (ROM)	0.4390	0.4225	0.3692	0.3415	0.4817	0.5102
FSI (AER-NS)	0.4311	0.4169	0.3430	0.2724	0.4067	0.5635
FSI (AER-Eu)	0.4197	0.4044	0.3270	0.2201	0.1785	0.1517
FSI (Yates [194])	0.4459	0.4174	0.3700	0.3059	0.3201	0.4031
FR (ROM)	0.6044	0.5470	0.4416	0.4086	0.7683	0.9210
FR (AER-NS)	0.5593	0.5235	0.4070	0.3422	0.4656	0.6576
FR (AER-Eu)	0.5449	0.5052	0.3940	0.3092	1.2880	1.2841
FR (Yates [194])	0.5350	0.4722	0.4220	0.3810	0.3620	0.4593

Based on Figure 5.22, it can be observed that the ROM results correlate generally with the trend of the reference CFD approach (AER-NS). Starting with the subsonic flight conditions ($Ma_\infty \leq 0.93$), a good agreement between the ROM and the AER-NS solutions is obtained. The neuro-fuzzy approach slightly overpredicts the *FSI* as well as

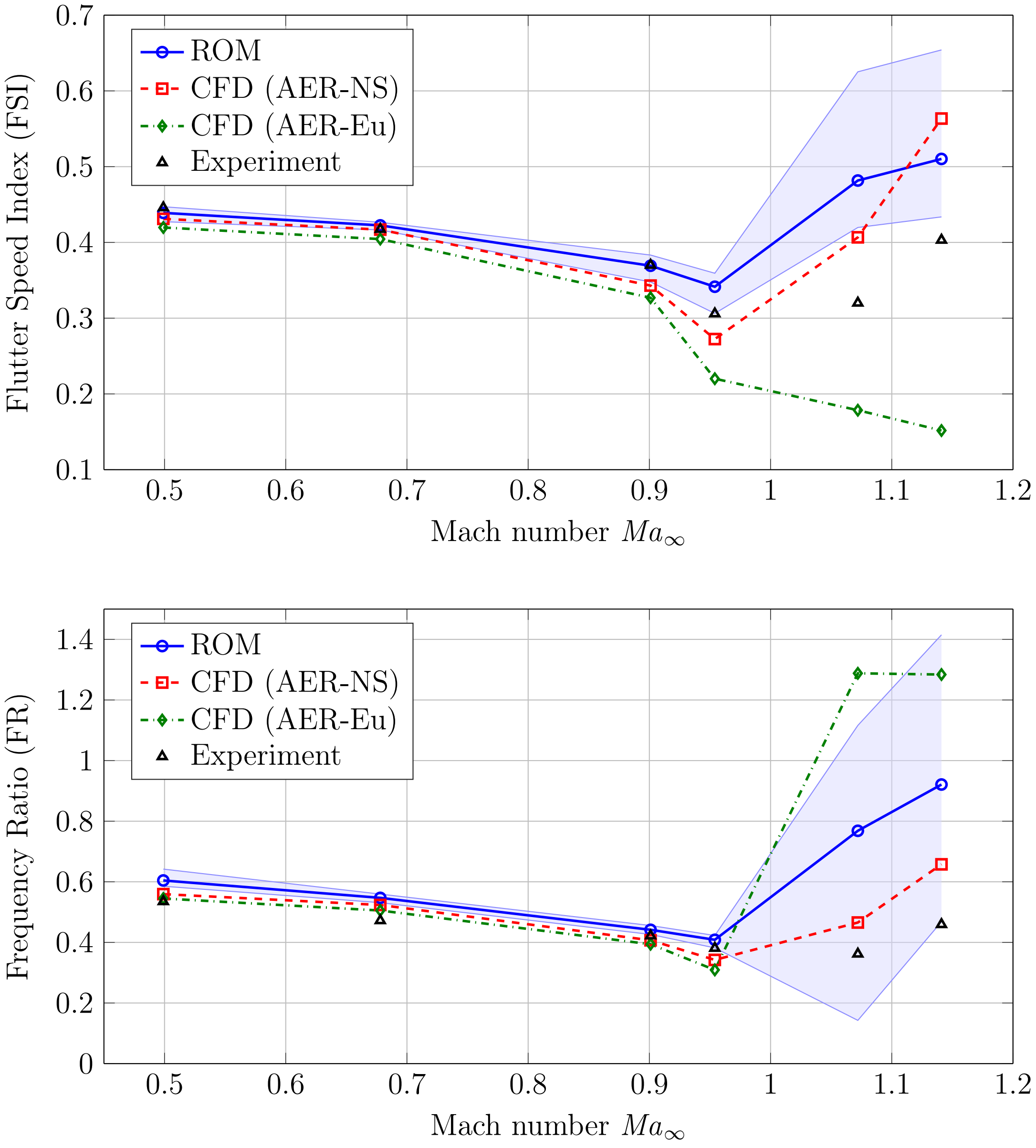

Figure 5.22: Flutter speed indices and frequency ratios obtained with the ROM- and the AER-NS-based aerodynamics as a function of the freestream Mach number (AGARD 445.6, $\alpha = 0°$, $T_\infty = 270\ K$, $Re_{c_r} = 10^6$). The ROM result represents the mean solution of the $N_{MC} = 25$ computations. In contrast, the shaded area is spanned between the encountered minimum and maximum FSI and FR values. For classification purposes, the AER-Eu solution as well as the experimental result has been added to the diagrams.

the *FR*, while the fluctuation range due to different model training processes is comparatively small for both quantities. Hence, the uncertainties regarding the prediction of the flutter speed and flutter frequency are small for the considered subsonic conditions. Besides, the results also agree well with the experimental findings and the inviscid aerodynamic modeling.

Although no training data have been provided between $0.9 < Ma_\infty < 1.0$, the transonic dip in the flutter boundary, that is mainly caused by the compressibility of the flow, can be predicted to some extent by the freestream-parameter-adaptive ROM methodology. However, as a result of the discrepancies in the frequency-domain **GAF** matrices explained in Section 5.4, a larger deviation between the ROM- and AER-NS-generated *FSI* and *FR* can be detected at $Ma_\infty = 0.954$. This error can be traced back directly to the limited training data for transonic conditions. Moreover, the range between the minimum and the maximum of the model-predicted *FSI* and *FR* values increases slightly in comparison to the subsonic flight regime. As the AER-NS solution at $Ma_\infty = 0.954$ is not covered within the fluctuation range of the $N_{MC} = 25$ ROMs, also individual neuro-fuzzy models have not been able to correctly predict the reference values. This confirms again that relevant information is missing in the training data from which the ROM has been constructed. Nevertheless, the difference between the mean ROM result and the AER-NS result is of the same order of magnitude compared with the deviation due to the Euler- and URANS-based aerodynamic modeling.

If the inflow becomes supersonic ($Ma_\infty \geq 1.07$), the flutter speed index and the frequency ratio increase with larger freestream Mach numbers. While the deviations between the ROM and the AER-NS solution with respect to the *FSI* remain as large as for transonic inflow conditions, the range of variation for different neuro-fuzzy model simulations increases considerably. Hence, the ROM prediction becomes less trustworthy for $Ma_\infty = [1.072, 1.141]$. Furthermore, the frequency ratio is discernibly overpredicted by the mean ROM solution in contrast to the URANS result. However, it should be noted that the correct flutter mechanism is captured for the ROM-based aerodynamics in contrast to the inviscid AER-Eu solution. As it has been described by Silva et al. [153], the generalized aerodynamic forces computed by an Euler-equation solver lead to instabilities in the third mode, which are observed neither in the experiment nor with URANS methods. As a consequence, the *FSI* and *FR* stemming from the AER-Eu solution deviate strongly from all other results. The discrepancy between the ROM results and the AER-NS reference can be explained on the basis of the **GAF** matrix shown in Figure 5.17. Although the mean ROM-based generalized aerodynamic forces show a good agreement with the CFD result, the fluctuation of the model-based responses in some of the matrix entries is very pronounced. In particular the off-diagonal matrix elements can have a crucial influence on the flutter characteristic. Accordingly, strongly varying flutter speeds and flutter frequencies are ascertained. By adding more training information, the model-based uncertainties can be reduced.

Despite the satisfactory performance of the ROM for the supersonic inflow conditions, the general characteristic of the flutter envelope is reproduced by the ROM. It should be pointed out again that for academic reasons very few freestream Mach numbers have been selected with respect to the training dataset. If more training states are chosen for practical applications, the reasonable application of the proposed neuro-fuzzy model for aeroelastic problems is out of question.

5.6 Efficiency Considerations

In this section, the efficiency of the freestream-parameter-adaptive neuro-fuzzy modeling framework is examined. To ensure comparability, all computations have been performed on the Linux cluster of the Leibniz Supercomputing Center (LRZ) utilizing multiple Intel Xeon E5-2697 v3 2.6 GHz processors in serial operation (serial/parallel farming). As the initial steady-state simulations are the basis for the ROM as well as the full-order unsteady CFD computations, they contribute in the same way to the numerical costs. Hence, they are neglected for the following comparison.

First, the costs for the ROM procedure are analyzed: Generating the CFD-based training dataset has required about 23.29 CPU days for the $N_{FC} = 6$ forced-motion URANS simulations. Therefore, adding another freestream Mach number to the training dataset would cost in average 3.88 CPU days. Remarkable is the fact that the fastest simulation has taken 1.93 CPU days ($Ma_{\infty,Trn} = 0.5$), whereas the slowest needed 5.29 CPU days to converge ($Ma_{\infty,Trn} = 1.0$). The LOLIMOT-based training of the $N_{MC} = 25$ ROMs has been performed in merely 0.14 CPU days. In this way, the training of an individual ROM requires less than 0.01 CPU days. Moreover, the application of all 25 models to the prediction of the generalized aerodynamic force responses required 0.09 CPU days. The aforementioned cost evaluation incorporates the computation of three oscillation cycles with respect to the five considered structural modes for 12 reduced frequencies and 20 freestream Mach numbers. Hence, in total 1,200 simulation cases have been treated by the 25 individually trained ROMs. Consequently, the average computation cost for a single model is approximately 0.26 CPU seconds per case, whereas the total numerical effort for obtaining the ROM results is about 23.52 CPU days. It becomes evident that almost only the training CFD simulations have a noteworthy contribution to the overall reduced-order modeling cost, whereas the training and application of the neuro-fuzzy model requires less than 1% of the total effort.

Second, the computational cost for obtaining the reference CFD results is investigated: With respect to the 1,200 unsteady simulation cases (20 Mach numbers, 12 reduced frequencies, and 5 eigenmodes), the simulation of three oscillation cycles needed 2950.97 CPU days using the AER-NS solver. Consequently, the average simulation time is about 2.46 CPU days per simulation case.

Regarding the full-order CFD runs, the minimum time for simulating a case is 1.15 CPU days ($Ma_\infty = 1.0$, $k_{red} = 1.0$, excitation of mode 1), whereas a maximum of 5.21 CPU days is observed ($Ma_\infty = 1.1$, $k_{red} = 0.01$, excitation of mode 2).

Comparing the aforementioned computational efforts of the unsteady aerodynamic simulations, an acceleration by the factor of 125.5 is realized by the ROM in contrast to the full-order CFD solver. Keeping in mind that the ROM can be further used for efficient predictions at other freestream Mach numbers and different excitation signals, the computational advantage increases supplementary. Once the ROM is available, the resulting speed-up factor for each individual simulation is of the order of five magnitudes.

5.7 Summary

In this chapter, it was shown that the reduced-order modeling procedure discussed in Section 4.1 can be successfully applied for the prediction of motion-induced (generalized) aerodynamic forces under variable freestream conditions. Therefore, the AGARD 445.6 wing subject to subsonic, transonic, and supersonic inflow conditions was investigated, while structural mode-shape-based deflections have been prescribed. By means of the aforementioned test case, the training procedure of the neuro-fuzzy model based on nonlinear system identification methods was demonstrated. Subsequently, time-domain aerodynamic responses were computed for structural oscillations with varying frequencies at different freestream Mach numbers to assess the accuracy and numerical efficiency of the approach in comparison to the full-order CFD result. Since the time and frequency-domain results indicated a good agreement with the reference solution for most of the considered cases, it was pointed out that the method can adequately predict aerodynamic forces induced by structural excitations. Additionally, a classical linear flutter analysis based on the obtained frequency-domain aerodynamic transfer functions was carried out. It was indicated that the methodology could predict the flutter boundary with reasonable accuracy. In addition, the importance of adequate training data was emphasized. A detailed analysis of the computational costs revealed that the overall effort was substantially reduced in comparison to the fully CFD-based aeroelastic analysis process. For the studied test cases, the necessary CPU time was decreased by a factor of 125.5. Moreover, once the ROM is available, a speed-up of about five orders of magnitude relative to the CFD solver can be achieved.

6 Modeling of Unsteady Surface Pressure Distributions

In this chapter, the surrogate modeling approach presented in Section 4.2, which is based on the combination of recurrent neuro-fuzzy models and the proper orthogonal decomposition dimensionality reduction procedure, is applied to efficiently simulate motion-induced unsteady surface pressure fluctuations. For this purpose, the LANN wing configuration undergoing a pitching motion is investigated at high subsonic and transonic flow conditions. The main objective is to evaluate the accuracy and efficiency of the ROM methodology rather than undertaking detailed flow-physical analyses for the test case under consideration. Therefore, the outputs of the POD-ROM simulations are always compared with corresponding steady and unsteady CFD results. The following content is mainly derived from a pre-publication of the author, Reference [184].

For demonstration of the ROM fidelity, the chapter is structured as follows: First, the LANN wing configuration is introduced in Section 6.1, whereas selected steady-state CFD results are presented in Section 6.2. Concerning the training of the surrogate model, the acquisition of the CFD-based dataset containing the flow response due to forced pitching motions is outlined in Section 6.3. Given the aforementioned unsteady aerodynamic data, the POD is applied to extract the dominant modes of the flow. Subsequently, the recurrent neuro-fuzzy model is used to train the dynamic mapping between the rigid body excitation and the corresponding POD coefficients. In Section 6.5, the application of the previously obtained POD-ROM to the simulation of harmonically excited pitching oscillations is shown. In this regard, the quality of the ROM results is compared against corresponding time-accurate CFD solutions, which are provided by the AER-Eu solver in the present context. Additionally, the obtained responses are analyzed in the frequency domain in Section 6.6 to highlight further potentials of the approach concerning fluid-structure interaction and loads computations. A comparison related to the integral aerodynamic coefficients, which are derived from the ROM-based surface pressure data, is given in Section 6.7. Finally, the numerical efficiency of the methodology is inspected in Section 6.8, while the ROM training and application effort is juxtaposed to the respective CFD costs.

6.1 Test Case: LANN Wing

Within the unsteady aerodynamics community, the LANN wing is a well-known test configuration of a transport-type wing equipped with a supercritical airfoil. According to the technical report of Zwaan [205], the name of the configuration is deduced from the partners of a cooperative programme consisting of Lockheed-Georgia, Air Force Flight

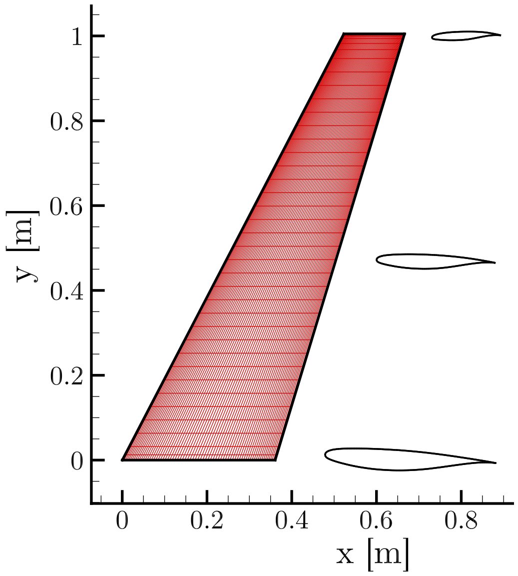

Figure 6.1: Planform of the LANN wing configuration along with cross-sections showing the supercritical airfoil. The CFD surface grid is shown in red.

Dynamics Laboratory, NASA-Langley, and NLR. The aim of the conducted experiments was to provide a database in order to validate steady and unsteady aerodynamic solvers at transonic flow conditions. Since the LANN wing is governed by a λ-shock system on the suction side of the wing at a freestream Mach number of $Ma_\infty = 0.82$ and an angle of incidence of $\alpha = 0.6°$, this challenging test case is predestined for testing the POD-ROM approach.

Table 6.1: Geometric properties of the LANN wing [205].

Quantity	**Symbol**	**Value**
Root chord	c_r	0.361 m
Reference area	S_{ref}	0.253 m^2
Semi-span	s	1.0 m
Aspect ratio	AR	7.92
Taper ratio	λ	0.4
Leading edge sweep angle	φ_{LE}	27.49°
Trailing edge sweep angle	φ_{TE}	16.91°
Reference length (k_{red})	c_{ref}	0.361 m

The LANN configuration shown in Figure 6.1 is geometrically represented by a swept and tapered semi-span wing. The model exhibits a leading-edge sweep angle of $\varphi_{LE} = 27.49°$, a trailing-edge sweep angle of $\varphi_{TE} = 16.91°$, a taper ratio of $\lambda = 0.4$, and a semi-span of $s = 1.0\ m$. The wing's cross-section is characterized by a supercritical airfoil with a relative thickness of $t/c = 12\%$. Detailed coordinates of the airfoil as well as the twist distribution can be taken from Reference [205]. Moreover, the root chord of the LANN wing is given as $c_r = 0.361\ m$, whereas the pitching axis for the considered rigid body motion is placed at 62.1% of the root chord. Within the experiments, the semi-span model was attached directly to the wind tunnel wall, while forced sinusoidal pitching excitations were applied by means of a hydraulic actuation. Since static aeroelastic deformations have not been measured during the wind tunnel tests, they are also neglected within the scope of this work. The relevant geometric properties are further summarized in Table 6.1.

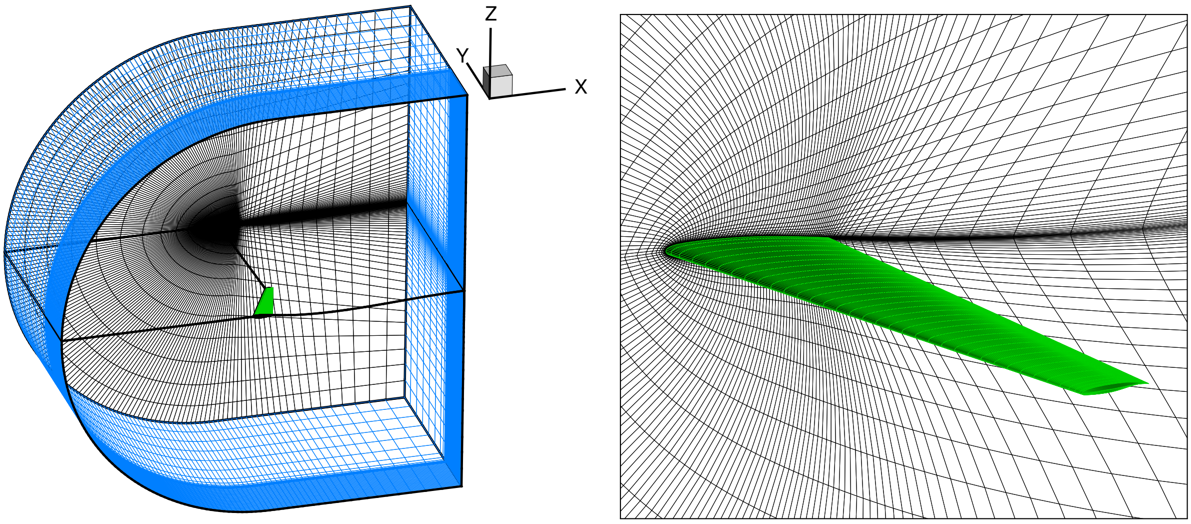

(a) Computational grid (b) Wing discretization

Figure 6.2: Grid topology and discretization of the structured reference CFD grid for the LANN wing. The wing is shown in green, whereas the blue and black faces mark the farfield and symmetry boundary conditions, respectively.

Regarding the steady and unsteady CFD computations, a structured two-block C-H topology grid with 368,640 cells is employed, which has been generated on the basis of a grid provided by Kreiselmaier and Laschka [87] using ANSYS ICEM CFD [2]. In Figure 6.2, the CFD grid topology is visualized along with a detail cutout showing the mesh refinement in the vicinity of the wing. Each of the upper and the lower wing surfaces is discretized by 72 × 35 cells. Consequently, $N_{SE} = 5{,}040$ surface elements are available for the POD-based modeling. With respect to the forced-motion unsteady aerodynamic simulations, the deformed grid representing the pitching deflection has been generated via a rigid body rotation of the grid points around the defined pitching axis.

6.2 Steady Results and Flow Topology

Within the scope of this chapter, two freestream conditions are considered: On the one hand, the steady-state conditions of the AGARD CT1 test case [205] are taken into account, which are characterized by a freestream Mach number of $Ma_\infty = 0.62$ and an angle of attack of $\alpha = 0.6°$. Although the maximum occurring Mach number in the flow domain is $Ma = 0.91$ based on the steady inviscid CFD simulation, the pressure coefficient falls below its critical value of $C_p^* = -1.17$ in terms of the intended unsteady simulations. However, the aerodynamic characteristics are dominated by subsonic flow, since no strong transonic effects are encountered. Therefore, this case is referred to as the high subsonic case.

On the other hand, the freestream Mach number and the incidence angle associated to the AGARD CT4/CT5 tests [205] have been selected for further investigations. The corresponding freestream parameters are $Ma_\infty = 0.82$ and $\alpha = 0.6°$. Related to the distinct λ-shock system on the suction side of the wing, strong nonlinear effects can be observed, especially, if the wing is undergoing a pitching motion. Consequently, this case is termed the transonic test condition.

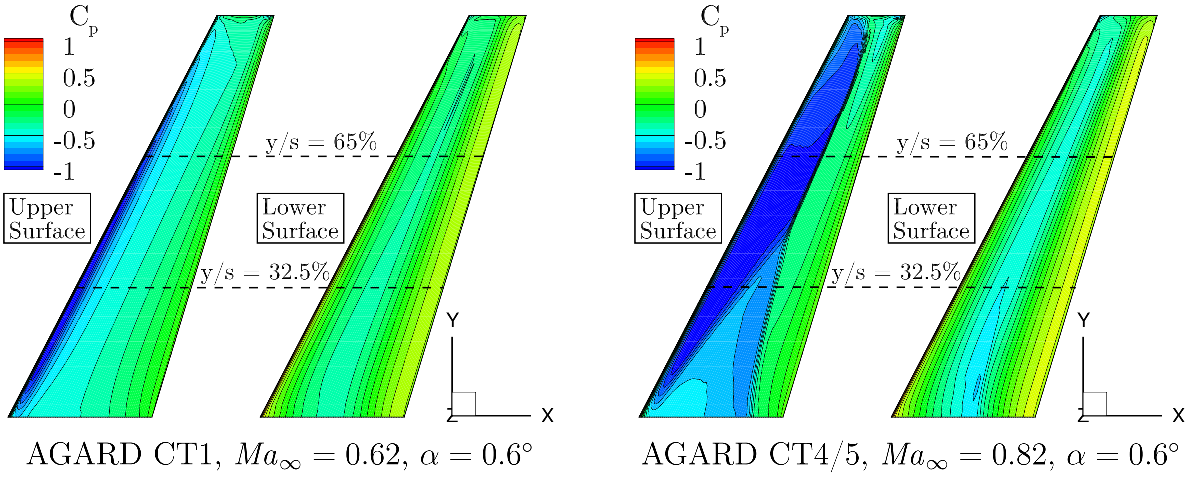

AGARD CT1, $Ma_\infty = 0.62$, $\alpha = 0.6°$ AGARD CT4/5, $Ma_\infty = 0.82$, $\alpha = 0.6°$

Figure 6.3: Steady-state pressure coefficient contours depicted for the upper and lower LANN wing surface at two selected freestream conditions (AER-Eu).

In Figure 6.3, the steady-state pressure coefficient distribution with respect to the upper and lower wing surface is shown for the aforementioned freestream conditions related to the AGARD CT1 and CT4/CT5 test cases. Considering the C_p surface contours, the AGARD CT1-related flow condition yields a pressure distribution which is representative for subsonic flight. In contrast, the AGARD CT4/CT5-deduced freestream condition leads to a clearly transonic C_p distribution. Focusing on the λ-shock system on the upper wing surface, two shocks emanate from the inboard wing. Near the geometric center of the wing, the aforementioned separate shocks unite such that the outboard wing is dominated by a single shock. In Figure 6.3 and also throughout this chapter, the flow is modeled as inviscid by employing the AER-Eu solver. As the main objective is the demonstration of the ROM methodology rather than performing detailed flow-physical analyses, the Euler-equations-based solver has been chosen for the sake of a significantly increased efficiency compared to the AER-NS counterpart. Nonetheless, it is well-known that the viscosity of the flow exhibits a non-negligible impact on the aerodynamic characteristics of the LANN wing. This can be proven by Figure 6.4 showing the AER-Eu result in contrast to the RANS-CFD solution (AER-NS) and the experimental data taken from Reference [205]. It becomes apparent that both the intensity of the shock and its chordwise position are overestimated by AER-Eu relative to the experimental result. The RANS solver captures the relevant flow physics considerably better, especially, for the $\eta = 65\%$ section. However, also the Euler solution contains the characteristic pressure trend and incorporates the dominant nonlinear mechanisms for the underlying test case. Therefore, the AER-Eu solver is used for the CFD computations presented in this chapter. Due to the lack of comparability between the inviscid and viscous aerodynamic modeling approaches, the experimental results are omitted for clarity with the exception of Figure 6.4. Nevertheless, it should be emphasized again that the employed CFD solver is always decisive for the ROM method and represents the only legitimate reference result.

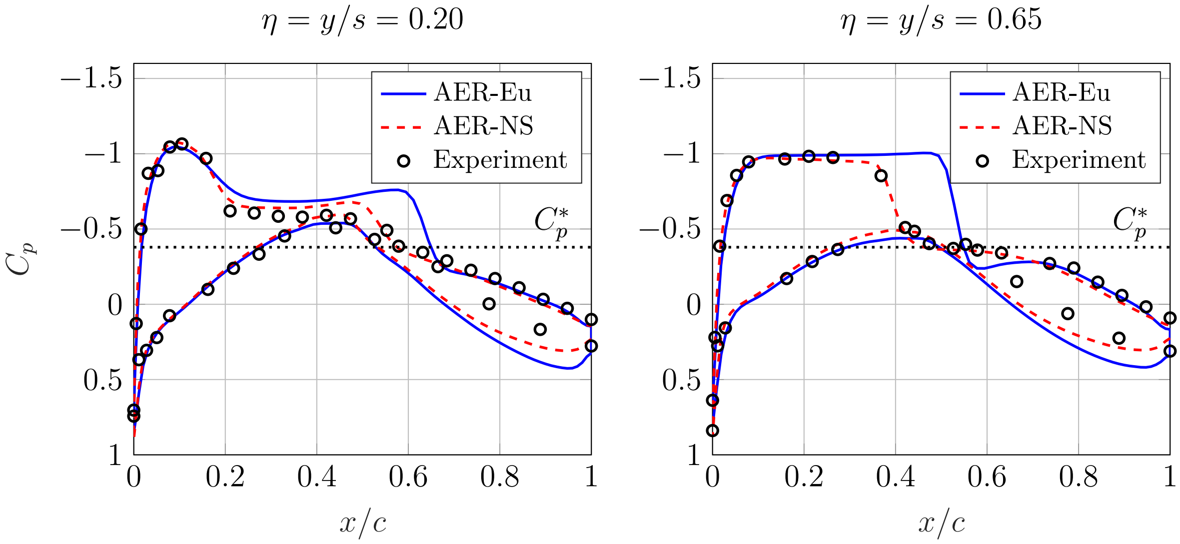

Figure 6.4: Steady-state C_p distribution of the LANN wing for $Ma_\infty = 0.82$ and $\alpha = 0.6°$. The results from the AER-Eu and the AER-NS solver as well as the experimental test data are shown for two sections. Concerning the AER-NS solution, the Reynolds number is set to $Re_{l_\mu} = 5.43 \cdot 10^6$ (with $l_\mu = 0.268\ m$), whereas the freestream temperature is chosen as $T_\infty = 299.15\ K$ in accordance with the experimental conditions.

6.3 Surface Data Processing via the POD and ROM Training

Based on the POD-ROM procedure explained in Section 4.2, unsteady forced-motion CFD simulations have been computed for both freestream conditions (high subsonic and transonic case) in order to obtain the training data for the reduced-order model. In this regard, pitching oscillations around the fixed angle of attack of $\alpha = 0.6°$ are considered. The maximum pitch amplitude $\theta_1 = \max\ \theta(t) = 0.25°$ investigated in terms of the AGARD CT1, CT4, and CT5 test cases, however, has been increased to $\theta_1 = 2°$ in order to obtain a stronger nonlinear characteristic due to the intensified shock motion. Nevertheless, the nonlinear ROM trained with a higher excitation amplitude can be also generalized to smaller amplitudes, which will be demonstrated in Section 6.7. Hence, the considered setup is well-suited to assess the robustness of the POD-based surrogate model against multiple excitation amplitudes.

According to the system identification approach outlined in Chapter 3, problem-dependent inputs and outputs must be initially defined. Considering the LANN wing undergoing a pitching motion, only a single degree of freedom is excited. Hence, the pitch angle θ can be considered as the system input. The system output, however, is formed by the POD coefficients that can be computed once the unsteady CFD solution is available. As a consequence, the system inputs and outputs are defined as:

$$u(t) = \theta(t) \in \mathbb{R}, \qquad \mathbf{y}(t) = \begin{pmatrix} b_1(t) \\ b_2(t) \\ \vdots \\ b_{M_{POD}}(t) \end{pmatrix} \in \mathbb{R}^{M_{POD}}, \qquad \Xi \in \varnothing \tag{6.1}$$

In Equation (6.1), M_{POD} denotes the number of POD modes, whereas b_i refers to the POD coefficient corresponding to POD mode i. Moreover, the empty time-independent parameter vector Ξ is shown in Equation (6.1) for completeness, since no static parameter changes are taken into account by the model.

Due to the nonlinear nature of the investigated problem, an APRBS has been generated for the excitation of the pitch angle in the range of $-2° \leq \theta \leq 2°$. Thereby, a minimum hold time of 30 time steps has been specified to achieve a reasonable compromise between computing time, CFD simulation stability, and training data quality. Using the APRBS, a quasi-random pitch angle variation is enforced as it can be seen in Figure 6.5. As a consequence of the 3,401 signal samples in combination with the defined nondimensional time step size of $\Delta\tau = 0.3$, a nondimensional time interval from 0 to 1,020 is considered for the training CFD simulations.

In addition, the frequency spectrum of the APRBS-based excitation law is presented in Figure 6.6. Since the reduced frequency does not depend on the freestream Mach number due to the nondimensional time formulation of the utilized AER-Eu code, the frequency spectrum is freestream-condition-invariant. Here, the root chord serves as the reference length for calculating the reduced frequency: $k_{red} = c_{ref} \cdot \omega / U_\infty$ with $c_{ref} = c_r = 0.361\ m$. Based on Figure 6.6, it is demonstrated that the generated APRBS introduces energy at a broad frequency range. In particular, the signal excites the reduced frequencies of interest with respect the considered test cases, i.e., $k_{red} = 0.133$ for

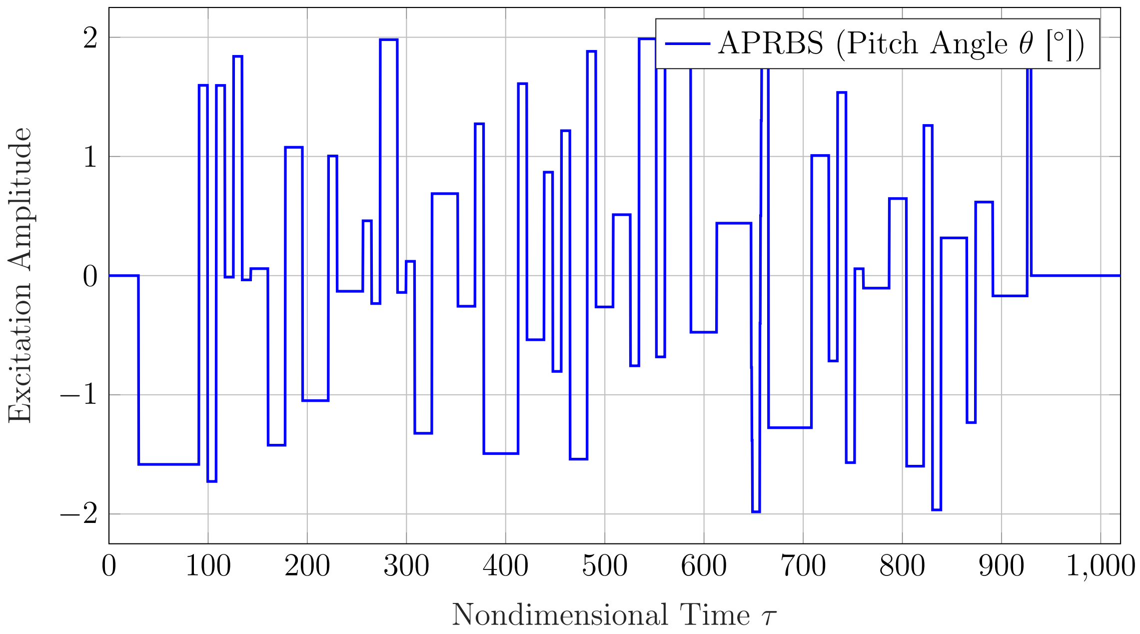

Figure 6.5: APRBS-based excitation amplitude concerning the pitch angle θ. The shown signal is used for the simulations at $Ma_\infty = 0.62$ and $Ma_\infty = 0.82$.

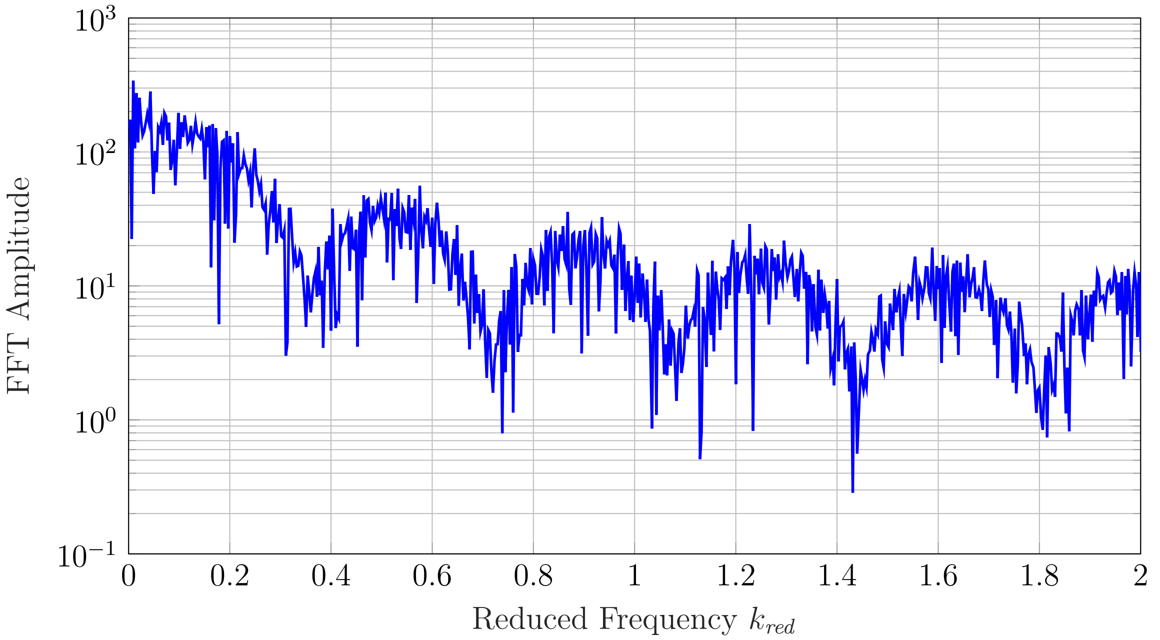

Figure 6.6: The fast Fourier transform (FFT) amplitude of the APRBS is shown as a function of the reduced frequency.

the AGARD CT1 test and $k_{red} = [0.051, 0.102]$ for the respective CT4 and CT5 tests. Furthermore, the Nyquist frequency of $k_{red,Nyq} = 5.23$ does not represent a limitation for the intended POD-ROM simulations.

Based on the time-varying surface pressure distributions provided by the unsteady CFD computations for $Ma_\infty = 0.62$ and $Ma_\infty = 0.82$, the POD procedure discussed in Section 4.2.1 has been carried out yielding the POD modes as well as the corresponding POD coefficients. To achieve a *RIC* value larger than 99% throughout the following comparisons, $M_{POD} = 40$ modes are considered for the high subsonic case, whereas $M_{POD} = 363$ modes are necessary under the same *RIC* constraint for the transonic case. The aforementioned observation indicates that the flow at $Ma_\infty = 0.82$ is governed by more complex flow structures with respect to the pressure fluctuations. In Figure 6.7, the first five out of the 363 POD modes are visualized for the transonic case. Comparing the mean surface pressure distribution, which is also shown in Figure 6.7 along with the POD modes, it becomes evident that the dominant structures arising within the POD

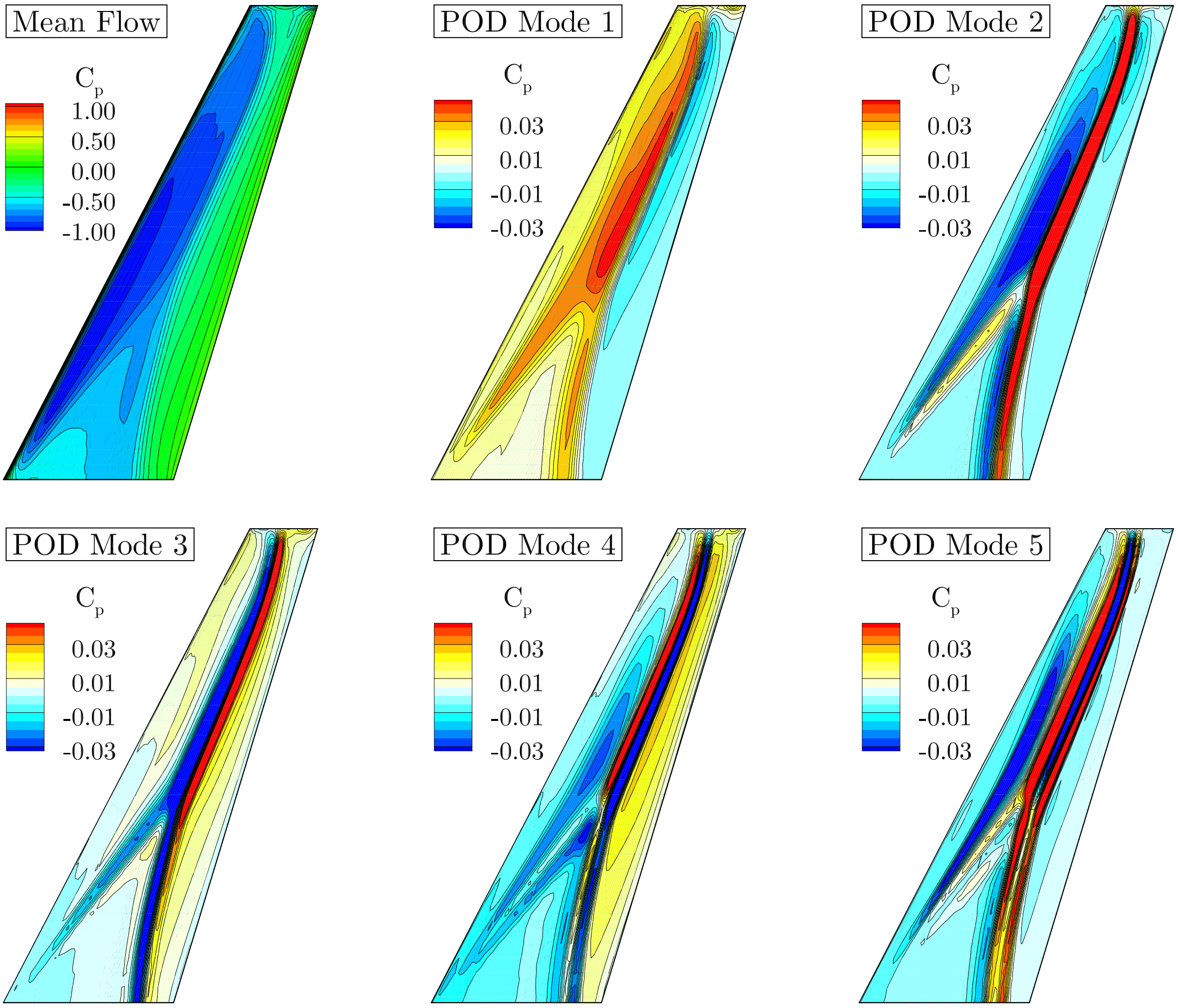

Figure 6.7: Time-averaged pressure coefficient distribution along with the first five POD modes computed from the unsteady CFD result. The upper surface of the LANN wing is shown for the $Ma_\infty = 0.82$ case ($\alpha = 0.6°$, AER-Eu).

modes can be traced back to the discontinuities of the λ-shock system. In addition, the POD coefficient time series for the $Ma_\infty = 0.82$ case are shown exemplarily in Figure 6.8 for the first three POD modes, i.e., $b_1(\tau), b_2(\tau), b_3(\tau)$.

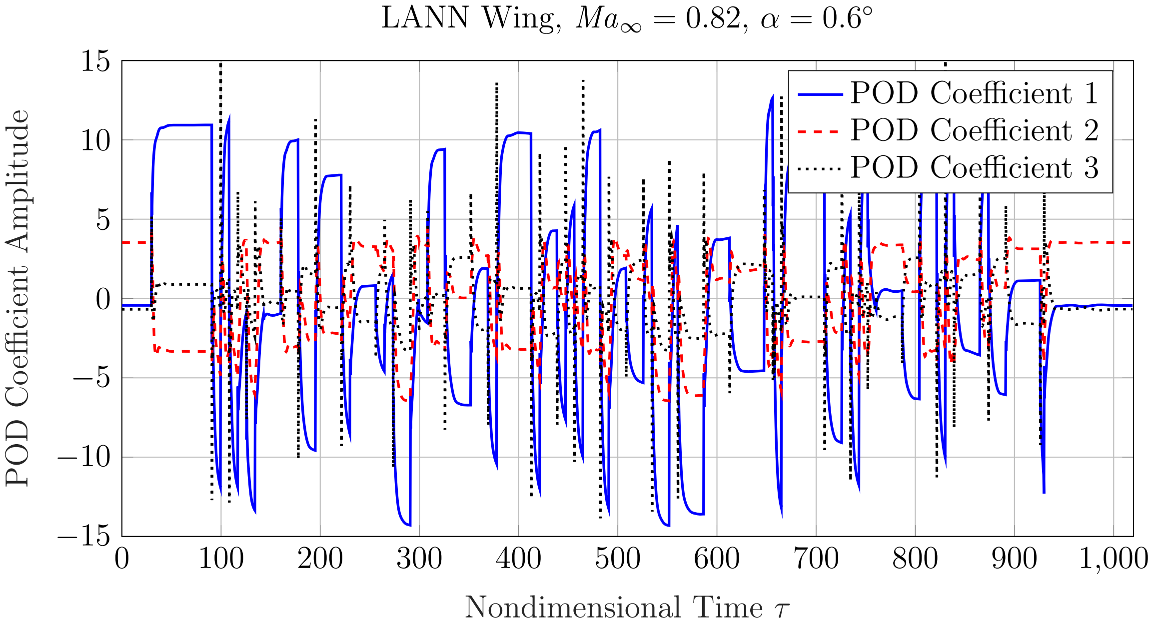

Figure 6.8: POD coefficient response due to the APRBS-based pitching excitation. The coefficients corresponding to the first three POD modes are shown. LANN wing, $Ma_\infty = 0.82$, $\alpha = 0.6°$, AER-Eu.

Provided by the unsteady AER-Eu simulations and the subsequent POD-based post-processing, the respective 40×3401 and 363×3401 POD coefficient response matrices $\mathbf{B}$ become available for the high subsonic and the transonic test case. Thus, the APRBS input can be linked to the POD coefficient matrix to form the input/output relationship of the underlying aerodynamic system.

In accordance with the procedure discussed in Section 4.2, the aforementioned input/output datasets must be pre-processed prior to the neuro-fuzzy model training process. Associated to this step, also the dynamic delay-orders for the external dynamics approach have to be determined. In this regard, the optimization procedure discussed in Section 3.3.3 has been applied resulting in the maximum dynamic delay-orders of $m = 3$, $n = 6$ ($Ma_\infty = 0.62$) and $m = 0$, $n = 11$ ($Ma_\infty = 0.82$) for the respective inputs and outputs. After concluding the preprocessing steps, the local linear neuro-fuzzy model has been trained using the LOLIMOT algorithm. Thereby, the learning procedure has been terminated if the one-step prediction error improvement was less than 3%; see Section 3.4.2.2. For a clearer discussion of the results, the Monte-Carlo methodology outlined in Section 3.6 has not been employed within the scope of this chapter. Consequently, the results of a single model are presented below. Once the data acquisition and neuro-fuzzy model training process is completed, the POD-ROMs for both freestream conditions are available and, therefore, can be used for performing quasi-steady and unsteady aerodynamic computations.

6.4 Quasi-Steady ROM Application

In the following, the trained surrogate model is used to simulate quasi-steady and unsteady aerodynamic responses induced by user-defined excitations. For performance and accuracy classification, the ROM result is therefore compared to the respective full-order CFD solution generated by AER-Eu. It should be emphasized that the POD-ROM can be only applied in a reasonable way if the system under investigation can be considered identical to the system that has been used to provide the training data. Thus, the configuration, freestream Mach number, and nondimensional time step size cannot be changed for the present set-up. Consequently, the POD-ROM trained for the high subsonic case cannot be used for the transonic case and vice versa.

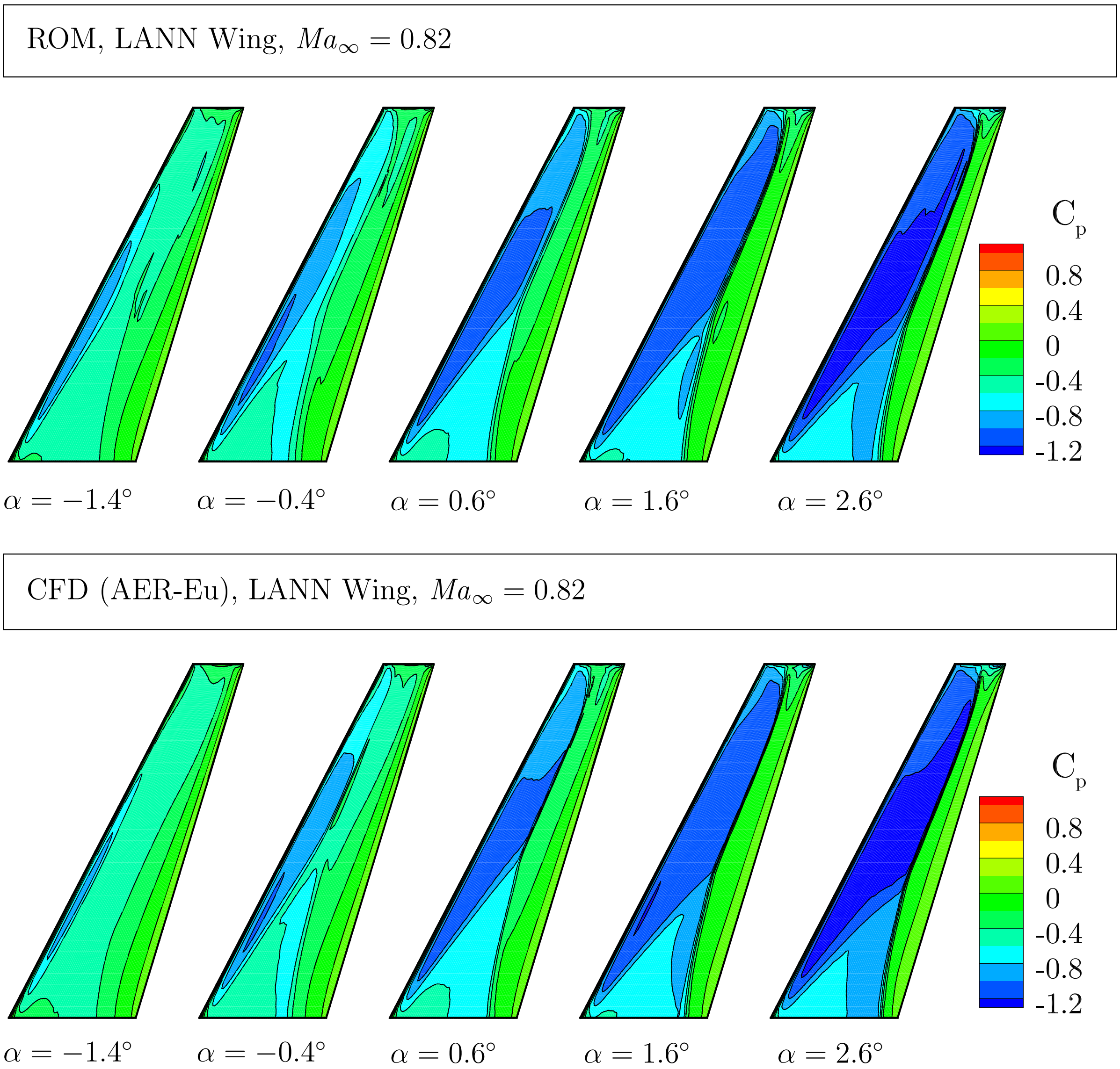

Figure 6.9: Steady-state C_p distribution of the upper LANN wing surface provided by the POD-ROM and the CFD reference (AER-Eu) for various incidence angles.

Firstly, the surrogate model is applied to compute the steady surface pressure distribution for different incidence angles $\alpha = [-1.4°, -0.4°, 0.6°, 1.6°, 2.6°]$ at $Ma_\infty = 0.82$.

Although no varying angles of attack have been trained, a change in α can be mimicked by considering different static pitch angles. Thus, the flow at the aforementioned incidence angles is obtained for $\theta = [-2^\circ, -1^\circ, 0^\circ, 1^\circ, 2^\circ]$ keeping in mind the initial angle of attack of $\alpha = 0.6^\circ$. However, since the surrogate model is formulated for time-varying quantities, a ramp function must be deployed to increase or decrease the pitch angle θ continuously to the target value. For this reason, the present investigation is termed *quasi-steady* to characterize this simulation modus operandi. The resulting steady pressure coefficient distributions are depicted in Figure 6.9 for the upper LANN wing surface, while the POD-ROM outputs are presented above of the corresponding AER-Eu reference solutions. Although the direct comparison of the ROM and CFD contour plots exhibits some minor discrepancies, the general C_p distribution is reproduced well by the surrogate model. The same applies to the high subsonic case, which is not displayed here for briefness. Furthermore, it can be seen that the POD-ROM is capable of modeling the development and regeneration of the complex shock system with respect to static analyses.

The generally good agreement between the ROM and the CFD results is underlined by the lift (C_L) and pitching moment (C_{M_y}) coefficient polars visualized in Figure 6.10. With respect to the calculation of C_{M_y}, the reference point has been defined as the quarter-chord of the wing root. In contrast to the direct modeling of integral quantities (see for example Chapters 5 and 7), the lift and pitching moment coefficients of the ROM shown in Figure 6.9 are computed on the basis of the reconstructed POD-based surface pressure distribution. In conclusion, the prediction quality concerning static analyses can be considered as sufficient for rapid aerodynamic assessments.

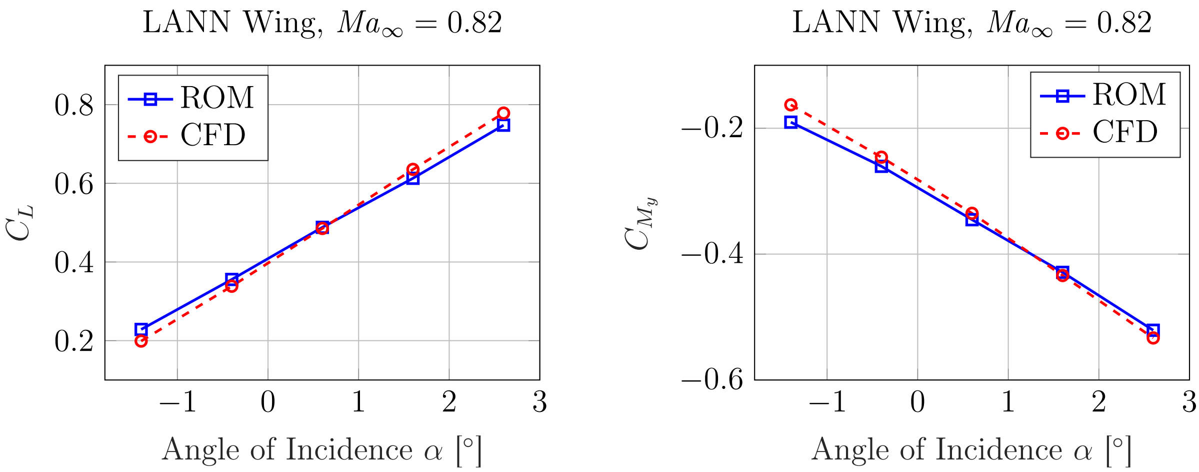

Figure 6.10: Lift and pitching moment coefficient polars computed from the POD-ROM- and CFD-based surface pressure distributions. LANN wing, $Ma_\infty = 0.82$, $\alpha = [-1.4^\circ, -0.4^\circ, 0.6^\circ, 1.6^\circ, 2.6^\circ]$.

6.5 Unsteady Results - Time Domain

Henceforth, analog to the experimental investigations summarized in Reference [205], the unsteady aerodynamic loads due to harmonic pitching oscillations are analyzed for demonstration and validation purposes. In accordance with the trained system characteristics, the surrogate model is applied to compute the time-domain response due to sinusoidal excitations with a maximum pitching amplitude of $\theta_1 = 2°$. The limited excitation range regarded in the AGARD CT1, CT4, and CT5 experiments ($-0.25° \leq \theta \leq 0.25°$) is not further considered in this section in order to focus on the distinctly nonlinear aerodynamic cases. However, the cases with $\theta_1 = 0.25°$ are taken into account in Section 6.7. For all unsteady simulations presented in this chapter, three oscillation cycles have been computed using both the POD-ROM as well as the AER-Eu solver in order to achieve load periodicity. As it has been discussed in further detail in Section 5.3, the ROM must be applied using the constant nondimensional time step size embedded within the training dataset, resulting in a frequency-dependent cycle discretization. In contrast, for generating the AER-Eu reference solution, each excitation period is resolved with 100 time steps.

The motion-induced unsteady aerodynamics for the high subsonic case, i.e., for $Ma_\infty = 0.62$, is presented for the single reduced frequency of $k_{red} = c_r \cdot 2\pi f / U_\infty = 0.133$. Concerning the transonic case, the two reduced frequencies $k_{red} = [0.051, 0.102]$ are taken into account for the excitation of the pitching motion. In this way, the frequency-dependent performance of the methodology can be assessed. Based on the POD-ROM application procedure shown in Figure 4.2, the sinusoidal time laws related to the pitching angle θ are fed into the neuro-fuzzy model, leading to the corresponding time-discrete POD coefficients $\tilde{\mathbf{b}}(\tau)$. Thereby, the tilde denotes a quantity that has been generated by means of the neuro-fuzzy model. In Figures 6.11 and 6.12, the output of the ROM is shown for the harmonic excitation with $k_{red} = 0.133$ at $Ma_\infty = 0.62$ and $k_{red} = 0.051$ at $Ma_\infty = 0.82$, respectively. It is apparent that for the second and third POD coefficient, a nonlinear dependency with respect to the input is ascertained, justifying the use of the employed neuro-fuzzy model approach. Nonetheless, whereas the high subsonic case exhibits only weak nonlinearities concerning the higher-order POD coefficients, for the transonic case most of the $\tilde{\mathbf{b}}$ coefficients depend nonlinearly on the pitch amplitude as it can be seen from the corresponding Lissajous figures.

On the basis of the stored POD modes in combination with the previously discussed POD coefficients produced by the neuro-fuzzy model, the unknown pressure coefficient distribution can be computed via weighted superposition according to Equation (4.4). Introducing T as the nondimensional period length with respect to the third excitation cycle, the POD-ROM outputs can be compared to the corresponding full-order CFD results. In Figure 6.13, the C_p distribution originating from the surrogate modeling approach is visualized in contrast to the AER-Eu solution for $Ma_\infty = 0.62$ and $k_{red} = 0.133$.

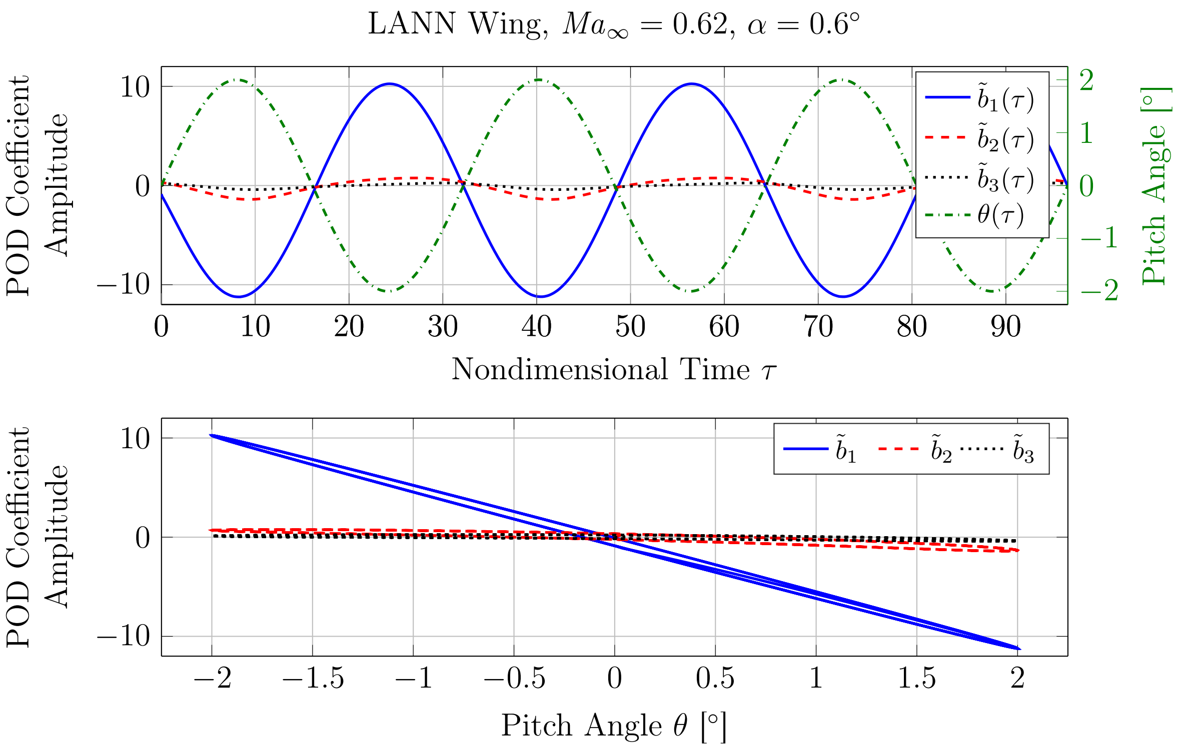

Figure 6.11: First three NFM-based POD coefficients caused by a harmonic excitation with $k_{red} = 0.133$ (LANN wing, $Ma_\infty = 0.62$, $\alpha = 0.6°$).

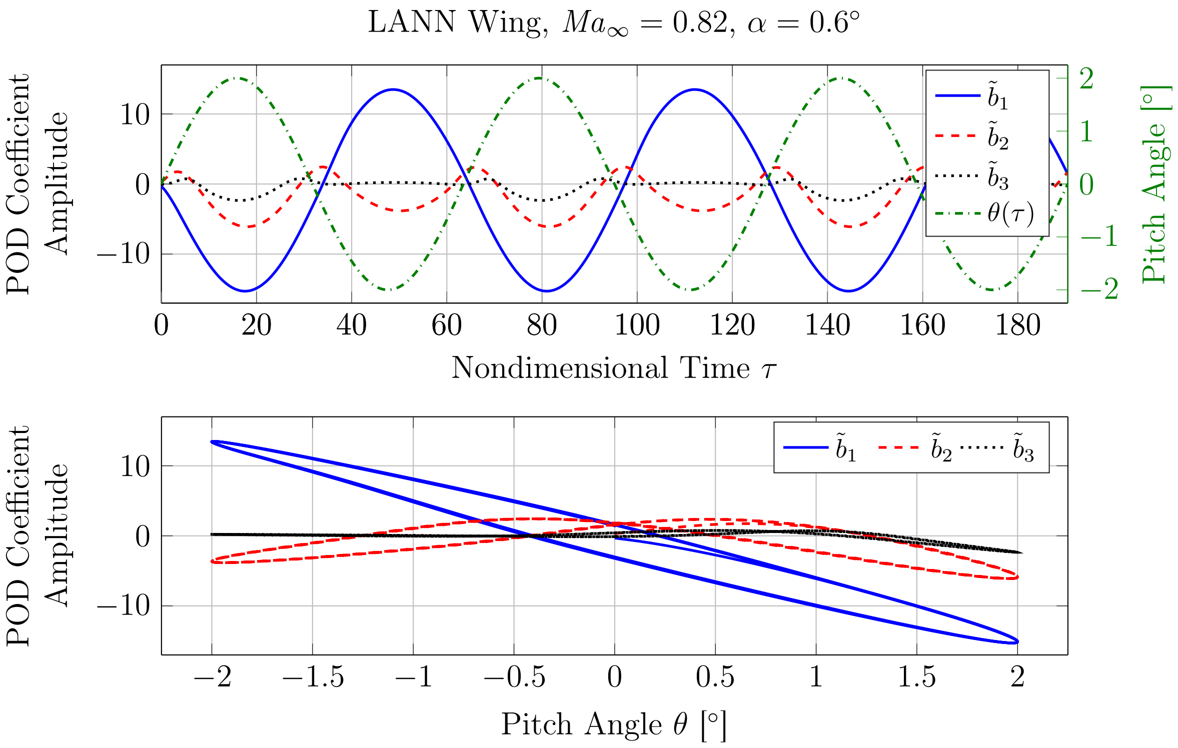

Figure 6.12: First three NFM-based POD coefficients caused by a harmonic excitation with $k_{red} = 0.051$ (LANN wing, $Ma_\infty = 0.82$, $\alpha = 0.6°$). The Lissajous figure underpins the nonlinear behavior of the second and third POD coefficient.

Comparing the results at the two time steps $t_2 = 0.25\ T$ and $t_4 = 0.75\ T$, a very good agreement can be identified. The high conformity between the POD-ROM and the CFD solution for the $Ma_\infty = 0.62$ case also applies to other time steps that are not shown for briefness.

Analogously, the pressure coefficient distribution induced by a harmonic excitation with $k_{red} = 0.102$ is shown at four discrete time steps in Figure 6.14 for $Ma_\infty = 0.82$. The associated contour plots illustrate a generally good correlation between the POD-ROM and the reference results, although the discontinuity caused by the shock is not predicted as sharp by the ROM as with the AER-Eu solver. Moreover, some minor superposition artifacts exist within the surface distribution. Nonetheless, the overall POD-ROM-based solution quality regarding the motion-induced aerodynamic loads is good for both the high subsonic and the transonic freestream conditions.

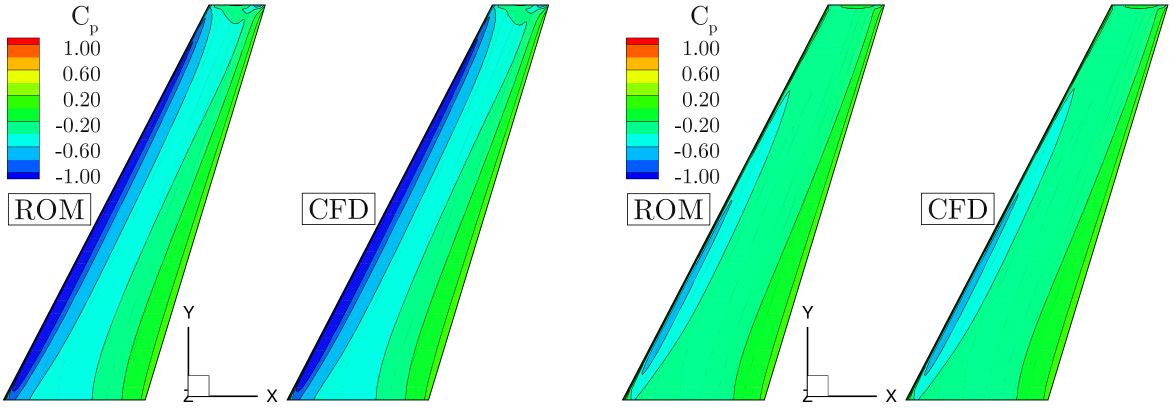

(a) $t_2 = 0.25\ T$, $\theta(t_2) = 2°$ (b) $t_4 = 0.75\ T$, $\theta(t_4) = -2°$

Figure 6.13: ROM- and CFD-based pressure coefficient distribution due to a harmonic pitching motion with $k_{red} = 0.133$. The upper LANN wing surface is shown for two time steps within the third excitation cycle. The CFD reference solution is provided by the AER-Eu solver. $Ma_\infty = 0.62$, $\alpha = 0.6°$, $\theta_1 = 2°$.

Besides considering the pressure distribution on the upper LANN wing surface, a further comparative analysis is conducted to focus on the local accuracy of the ROM approach. For that purpose, the streamwise cross-sections at 32.5% and 65% of the semi-span measured from the wing root are investigated in detail; see Figure 6.3 for a visualization of the respective cross-sections. Figures 6.15-6.17 show the chordwise C_p characteristics that result from harmonic pitching excitations, while four time steps associated to the third excitation cycle are plotted. As it can be seen from the figures, a good concordance between the ROM and the full-order CFD solution is observed in general. In particular, an almost perfect agreement can be noticed with respect to the high subsonic case. Moreover, the distribution of the pressure coefficient on the lower wing surface is predicted with high accuracy using the POD-ROM, which applies to both the high subsonic and the transonic freestream conditions. In contrast, the precise unsteady aerodynamic modeling regarding the upper surface, which is dominated by the formation of the λ-shock topology for the LANN wing at $Ma_\infty = 0.82$, is challenging for the POD-ROM as

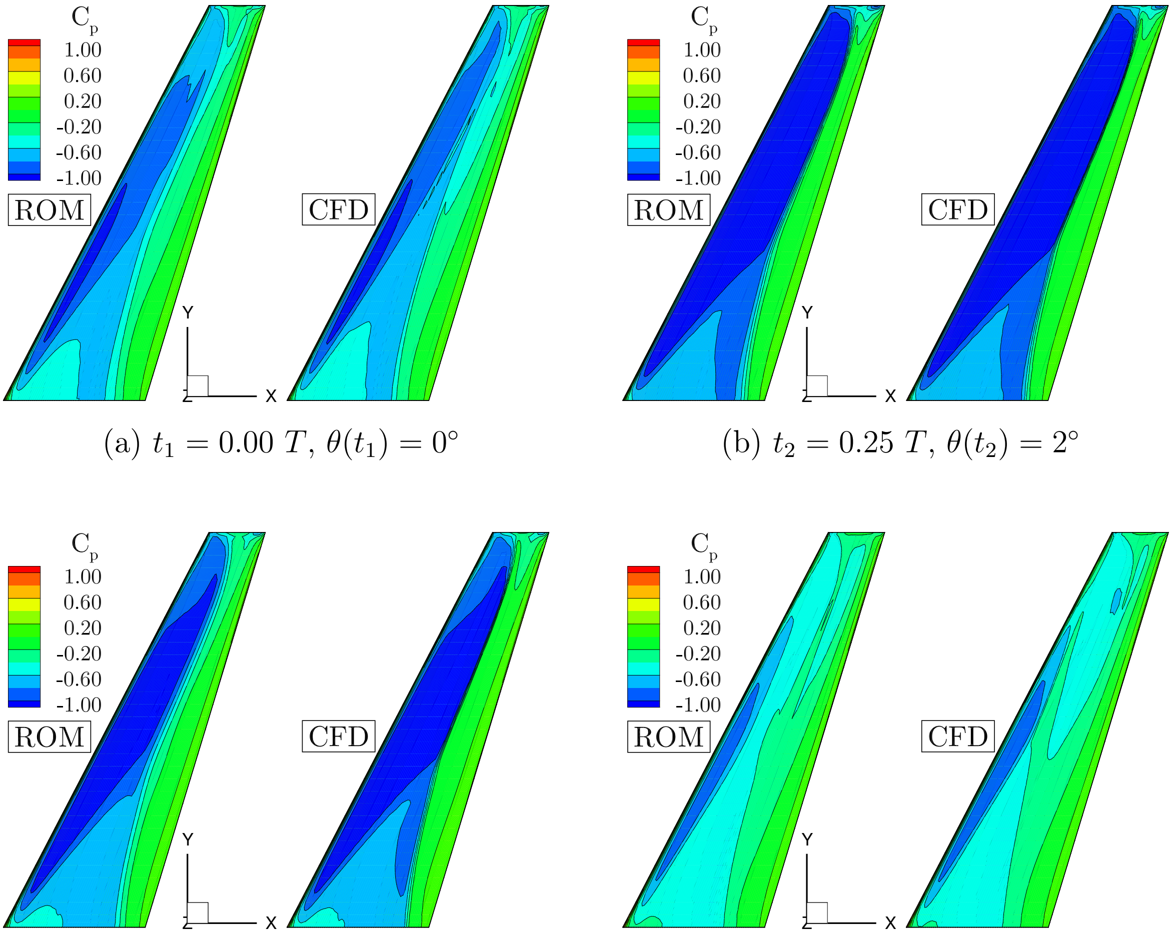

(a) $t_1 = 0.00\ T$, $\theta(t_1) = 0°$ (b) $t_2 = 0.25\ T$, $\theta(t_2) = 2°$

(c) $t_3 = 0.50\ T$, $\theta(t_3) = 0°$ (d) $t_4 = 0.75\ T$, $\theta(t_4) = -2°$

Figure 6.14: ROM- and CFD-based pressure coefficient distribution due to a harmonic pitching motion with $k_{red} = 0.102$. The upper LANN wing surface is shown for four time steps within the third excitation cycle. The CFD reference solution is provided by the AER-Eu solver. $Ma_\infty = 0.82$, $\alpha = 0.6°$, $\theta_1 = 2°$.

it can be inferred from Figures 6.16 and 6.17. Specifically, the chordwise position of the shock(s) as well as the pressure gradient is not always captured accurately. Thus, the local accuracy is slightly deteriorated due to the discrepancies with respect to the shock resolution. The aforementioned phenomenon, that pronounced discontinuities are not well resolved using the POD's linear superposition principle, was also noted by other researchers concerning POD-based static approximation problems [70, 104]. Nevertheless, the transient development and regeneration of the complex shock system is principally reproduced by the reduced-order model.

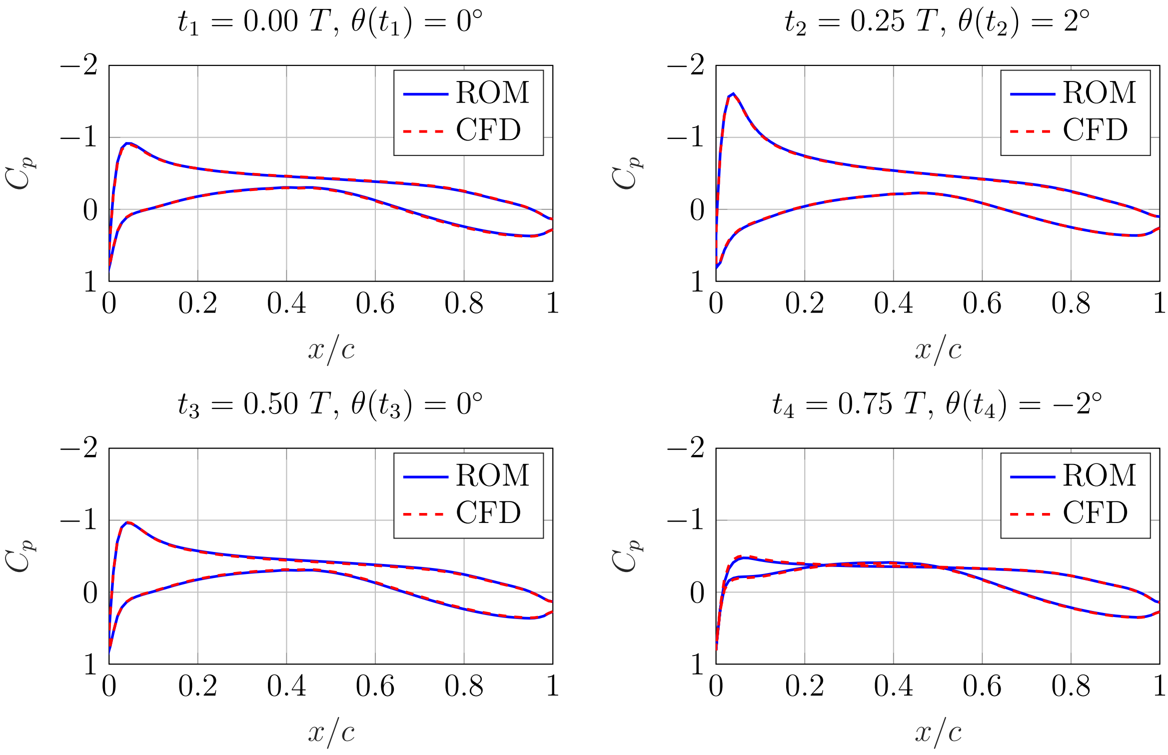

Figure 6.15: Evolution of the chordwise C_p distribution at $\eta = y/s = 32.5\%$ caused by a harmonic pitching motion with $k_{red} = 0.133$. LANN wing, $Ma_\infty = 0.62$, $\alpha = 0.6°$, $\theta_1 = 2°$, POD-ROM and AER-Eu results are shown.

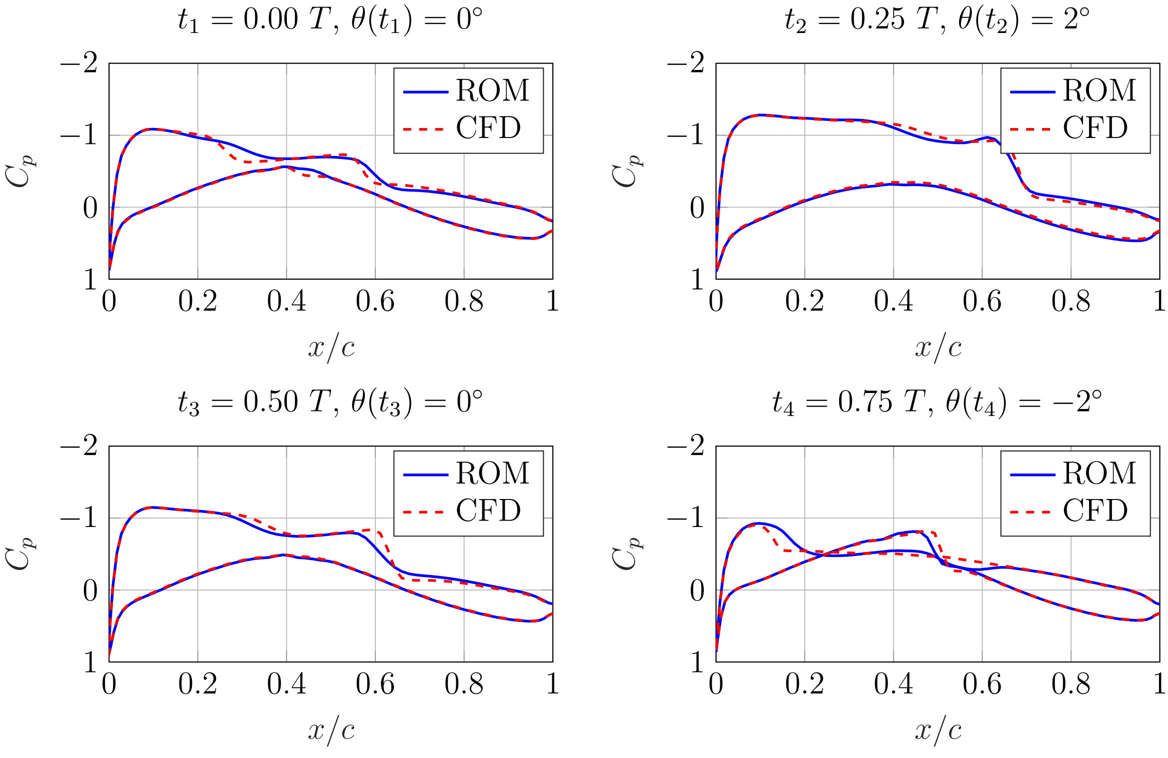

Figure 6.16: Evolution of the chordwise C_p distribution at $\eta = y/s = 32.5\%$ caused by a harmonic pitching motion with $k_{red} = 0.102$. LANN wing, $Ma_\infty = 0.82$, $\alpha = 0.6°$, $\theta_1 = 2°$, POD-ROM and AER-Eu results are shown.

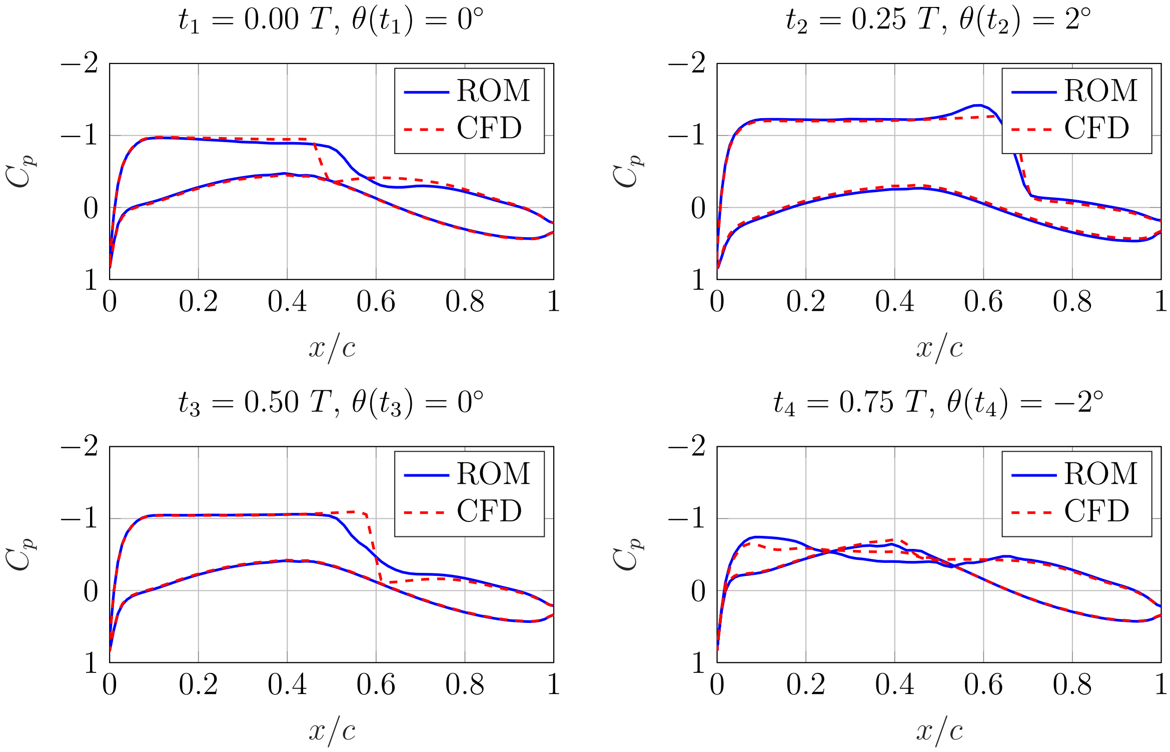

Figure 6.17: Evolution of the chordwise C_p distribution at $\eta = y/s = 65\%$ caused by a harmonic pitching motion with $k_{red} = 0.102$. LANN wing, $Ma_\infty = 0.82$, $\alpha = 0.6°$, $\theta_1 = 2°$, POD-ROM and AER-Eu results are shown.

6.6 Unsteady Results - Frequency Domain

For aeroelastic applications, the frequency-domain formulation of the unsteady aerodynamic loads is of paramount importance [192]. In this regard, complex-valued force and load amplitudes are considered that represent the magnitude and phase of the response. Due to the high practical significance of those considerations, the time-domain results presented in Section 6.5 are transformed into the frequency domain via Fourier analysis to gather further insights. For comparative purposes, not only the POD-ROM-based C_p distribution but also the respective AER-Eu result is transformed and taken into account within the following discussions.

Figure 6.18 presents the real and imaginary parts of the first harmonics with respect to the surface pressure coefficient amplitude that is caused by a pitching motion with $k_{red} = 0.133$ at $Ma_\infty = 0.62$. As it can be expected from the time-domain results shown in the previous section, also in the frequency domain a very good agreement between the ROM and the CFD result can be stated for the high subsonic case. Furthermore, Figures 6.19 and 6.20 depict the complex-valued first and second harmonics related to the C_p distribution that is induced by pitching motions with the respective reduced frequencies of $k_{red} = 0.051$ and $k_{red} = 0.102$ for the transonic freestream condition case.

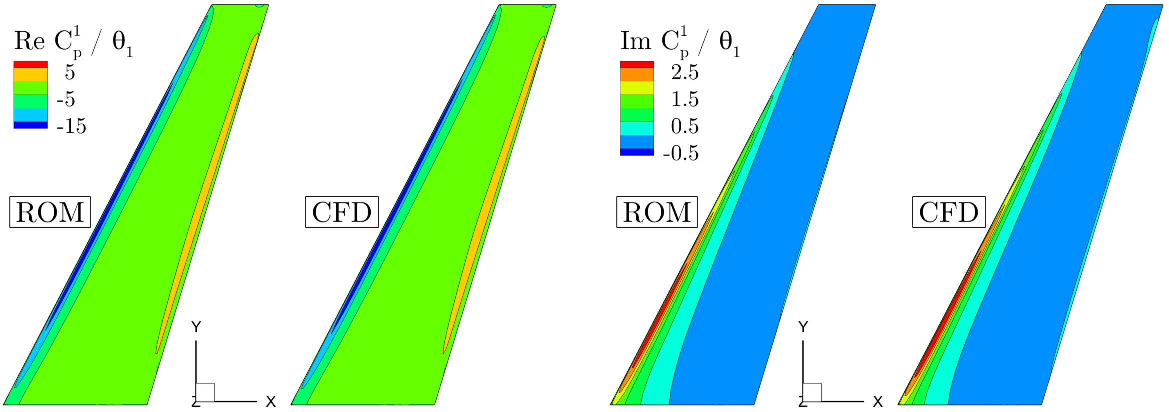

Figure 6.18: Real and imaginary part regarding the first harmonics of the C_p response shown for the upper LANN wing surface. The frequency-domain unsteady aerodynamic result shown for the POD-ROM and the AER-Eu solver is caused by a harmonic pitching motion with $k_{red} = 0.133$. $Ma_\infty = 0.62$, $\alpha = 0.6°$, $\theta_1 = 2°$.

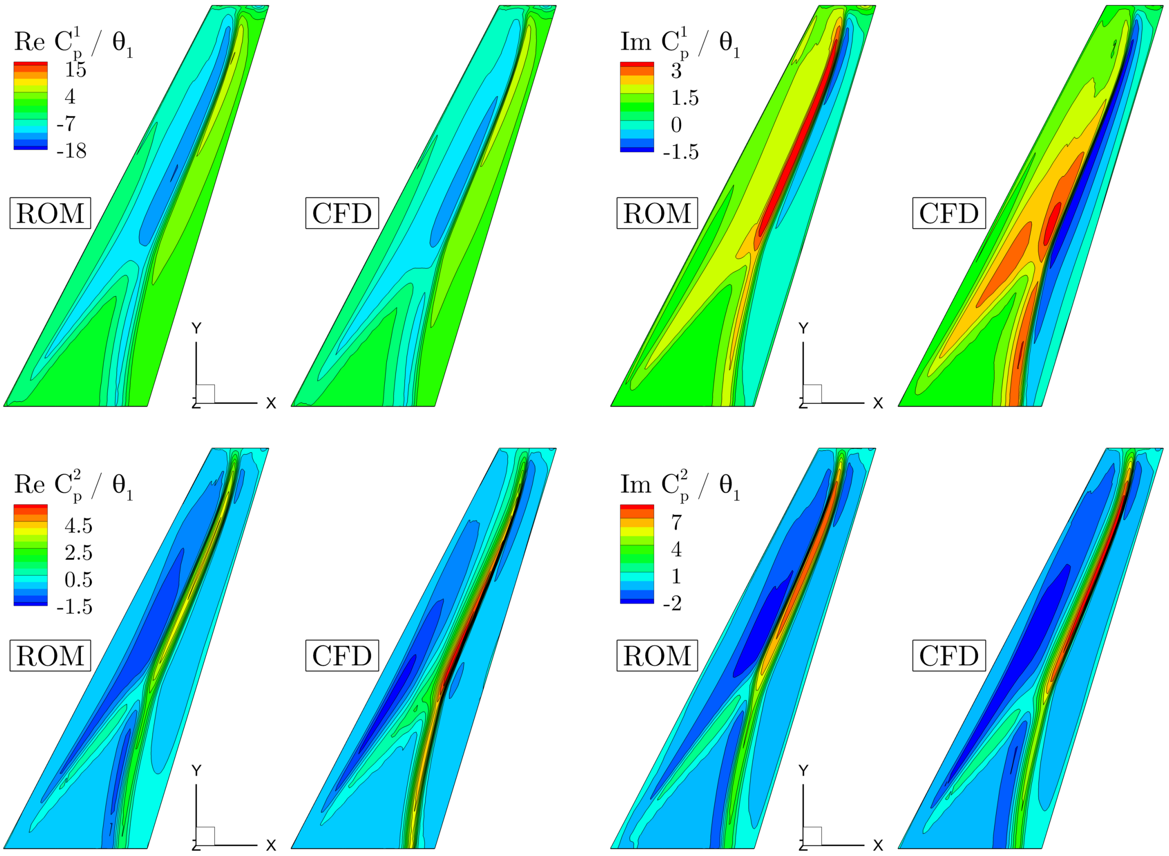

Figure 6.19: Real and imaginary part regarding the first and second harmonics of the C_p response shown for the upper LANN wing surface. The frequency-domain unsteady aerodynamic result shown for the POD-ROM and the AER-Eu solver is caused by a harmonic pitching motion with $k_{red} = 0.051$. $Ma_\infty = 0.82$, $\alpha = 0.6°$, $\theta_1 = 2°$.

As it can be seen from Figures 6.19 and 6.20, the surrogate model is generally able to capture the second harmonics of the aerodynamic response constituted by Re C_p^2 and

Im C_p^2. The same holds true for higher harmonics of the response amplitude not displayed in this work. This property underlines the nonlinear nature of the investigated problem as well as the capability of the POD-ROM approach to reproduce nonlinear aerodynamic effects. At this point it is worth to note that a linear aerodynamic model would only provide the first harmonics of the response.

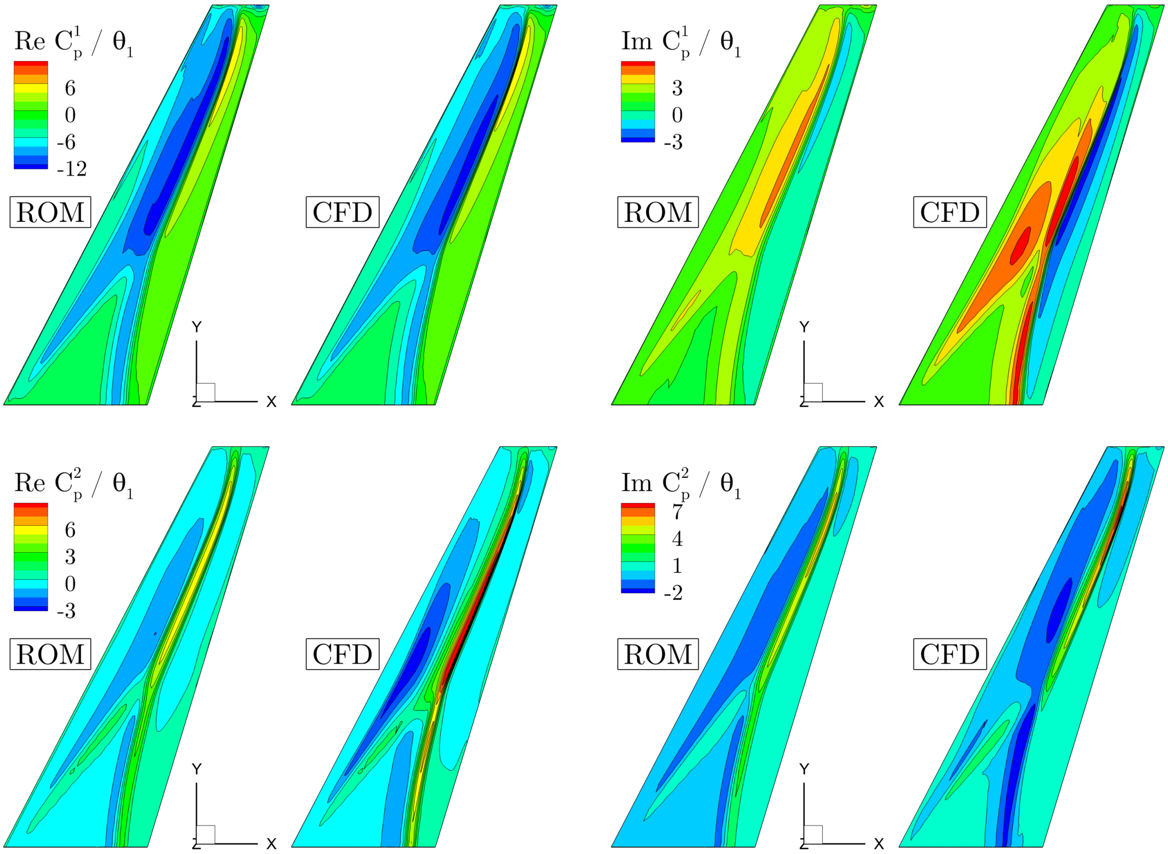

Figure 6.20: Real and imaginary part regarding the first and second harmonics of the C_p response shown for the upper LANN wing surface. The frequency-domain unsteady aerodynamic result shown for the POD-ROM and the AER-Eu solver is caused by a harmonic pitching motion with $k_{red} = 0.102$. $Ma_\infty = 0.82$, $\alpha = 0.6°$, $\theta_1 = 2°$.

Considering Figures 6.19 and 6.20, the real part of the first harmonics with respect to the C_p distribution, which is referred to as Re C_p^1, correlates well with the reference for both considered excitation frequencies. In contrast, the imaginary part of the first harmonic load denoted by Im C_p^1 as well as the higher harmonics of the C_p amplitude show a satisfying agreement with the AER-Eu reference solution. The present deviations can be traced back to the limited prediction quality regarding the shock system. Nonetheless, the characteristic patterns in terms of the frequency-domain pressure distribution are qualitatively reproduced by the POD-ROM approach.

In order to allow a more detailed interpretation of the results, three additional plots are introduced showing the local distribution of the complex-valued C_p response amplitude.

In this regard, the Figures 6.21-6.23 provide the chordwise Re C_p^1 and Im C_p^1 characteristics at the two cross-sections defined by 32.5% and 65% of the semi-span. The high subsonic test case ($Ma_\infty = 0.62$, $k_{red} = 0.133$) is shown in Figure 6.21, whereas the transonic freestream condition specified by $Ma_\infty = 0.82$ is plotted for $k_{red} = [0.051, 0.102]$ in Figures 6.22 and 6.23, respectively. Analog to the results analyzed beforehand, the chordwise pressure distribution for the high subsonic case exhibits an almost exact agreement.

Related to the $Ma_\infty = 0.82$ test cases, the POD-ROM-based chordwise Re C_p^1 and Im C_p^1 distributions shown in Figures 6.22 and 6.23 exhibit certain deviations with respect to the full-order CFD solution. In contrast to the time-domain considerations shown in Figures 6.16 and 6.17, the discrepancies in the frequency domain are not strictly limited to the direct neighborhood of the discontinuity. Nevertheless, the characteristic trends of the reference CFD result are also captured by the ROM. Unless a highly accurate result is needed, the POD-ROM procedure can yield satisfying results within a fraction of the time compared to the underlying CFD system; see the discussion in Section 6.8.

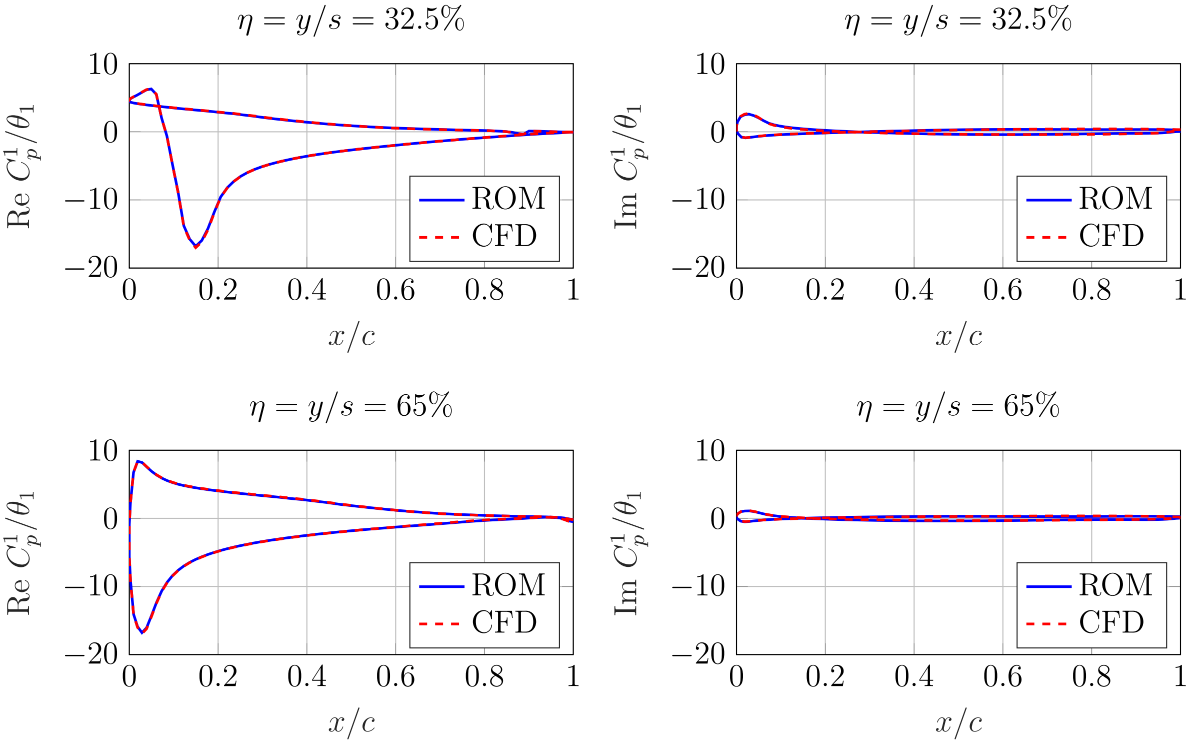

Figure 6.21: Real and imaginary part of the first harmonics with respect to the chordwise C_p distribution plotted at $\eta = 32.5\%$ and $\eta = 65\%$. The response is enforced by a harmonic pitching motion with $k_{red} = 0.133$. $Ma_\infty = 0.62$, $\alpha = 0.6°$, $\theta_1 = 2°$, POD-ROM and AER-Eu results are shown.

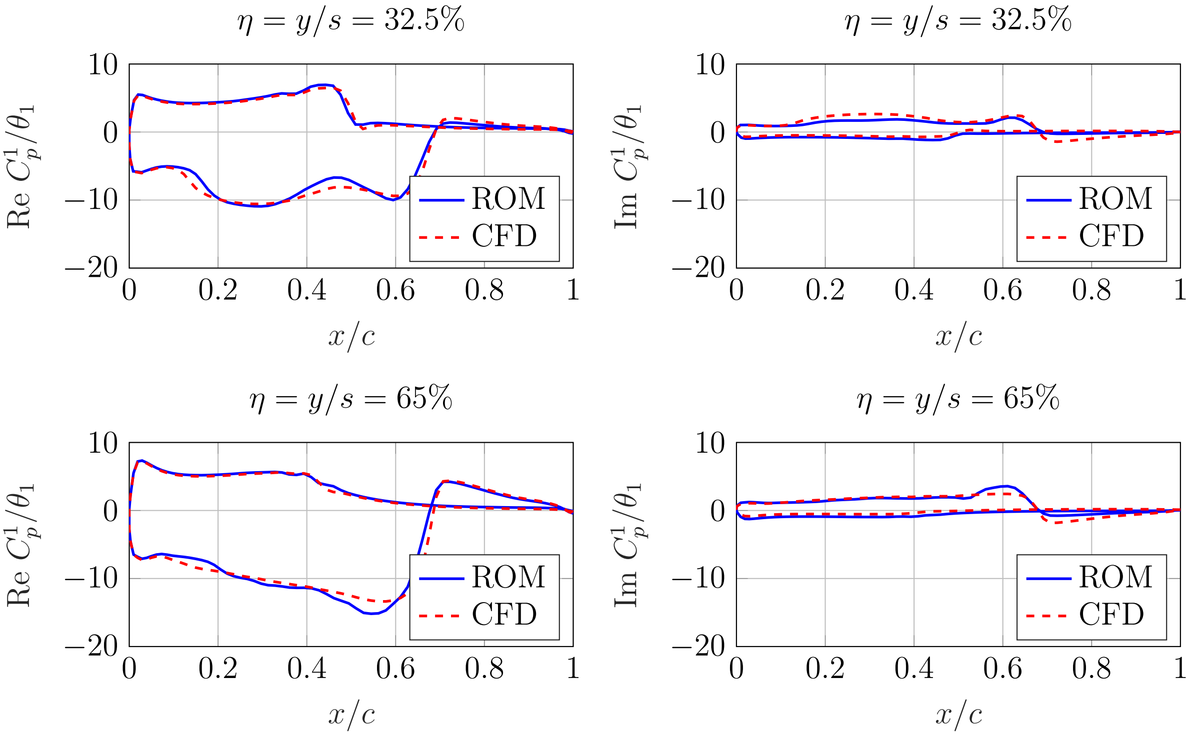

Figure 6.22: Real and imaginary part of the first harmonics with respect to the chordwise C_p distribution plotted at $\eta = 32.5\%$ and $\eta = 65\%$. The response is enforced by a harmonic pitching motion with $k_{red} = 0.051$. $Ma_\infty = 0.82$, $\alpha = 0.6°$, $\theta_1 = 2°$, POD-ROM and AER-Eu results are shown.

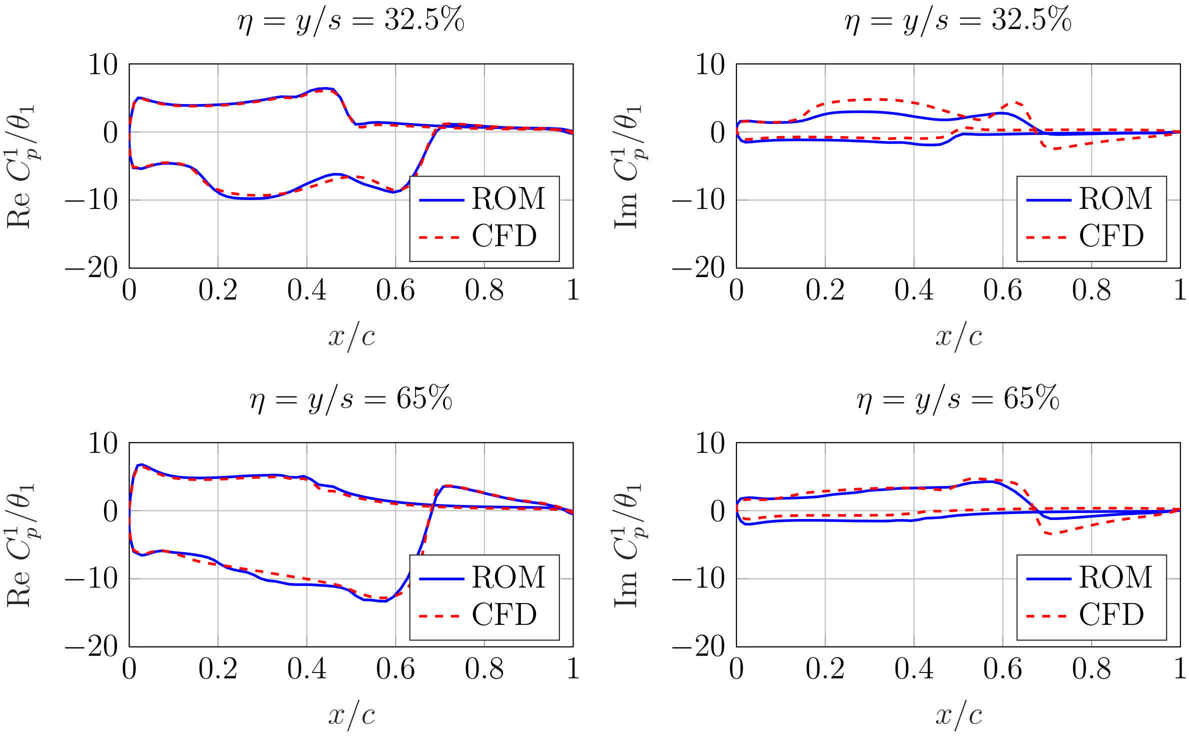

Figure 6.23: Real and imaginary part of the first harmonics with respect to the chordwise C_p distribution plotted at $\eta = 32.5\%$ and $\eta = 65\%$. The response is enforced by a harmonic pitching motion with $k_{red} = 0.102$. $Ma_\infty = 0.82$, $\alpha = 0.6°$, $\theta_1 = 2°$, POD-ROM and AER-Eu results are shown.

6.7 Integral Quantities

Analog to the quasi-steady investigation outlined in Section 6.4, the lift and pitching moment coefficients have been calculated from the unsteady surface pressure distributions in order to analyze the solution quality concerning the integral quantities. With respect to the lift coefficient C_L, the results are depicted in Figure 6.24 for all considered test cases. Thereby, not only the two freestream conditions in combination with the variable excitation frequencies are considered ($Ma_\infty = 0.62$, $k_{red} = 0.133$ and $Ma_\infty = 0.82$, $k_{red} = [0.051, 0.102]$), but also the two different pitching angle amplitudes of $\theta_1 = [0.25°, 2°]$. The sinusoidal pitching excitation with $\theta_1 = 0.25°$ has been chosen in accordance with the wind tunnel experiments [205]. It is important to emphasize that the same POD-ROM trained by the APRBS shown in Figure 6.5 is employed to predict the small amplitude cases with $\theta_1 = 0.25°$. In this way, the robustness of the model in terms of predicting small and large amplitudes is tested. Using the same reduced-order model, virtually no additional computational effort is necessary to produce the surrogate-model-based output for $\theta_1 = 0.25°$. However, further AER-Eu simulations are required for providing the respective comparative data.

Considering Figure 6.24, it can be asserted that the lift coefficient is predicted with high accuracy. Specifically, the high subsonic case shows an excellent agreement, whereas marginal amplitude and phase shifts can be determined for the transonic cases. Moreover, the ROM is able to simulate the C_L response induced by the significantly smaller excitation amplitude given by $\theta_1 = 0.25°$. Although the relative deviations are larger for the small amplitude cases compared to the $\theta_1 = 2°$ results, the POD-ROM-based lift coefficients correlate well with the CFD reference. Interestingly, the integral response of the aerodynamic system is linear for both excitation amplitudes, although the local pressure distribution is governed by nonlinearities under certain conditions, e.g., the transonic cases with a pitching amplitude of $\theta_1 = 2°$. Nevertheless, the aforementioned characteristic is well reproduced by the POD-ROM methodology.

The pitching moment, which is related to the quarter-chord point of the wing root (undeflected state), is shown in Figure 6.25 for the same set of cases. Although some deviations exist between the ROM solution and the CFD reference, the diagrams indicate a good agreement for the prediction of C_{M_y}. Nonetheless, it becomes evident that the local deviations discussed in Section 6.5 contribute stronger to the moment coefficients due to the spatial weighting. Hence, the error between the POD-ROM and the AER-Eu result is typically larger for the pitching moment coefficient in contrast to C_L. Even though the discrepancies are slightly more pronounced for the $\theta_1 = 0.25°$ cases than for the large amplitude simulations, the prediction quality is sufficient for fast preliminary investigations. Thus, the ROM procedure described in Section 4.2 can be also employed to deduce integral aerodynamic coefficients with reasonable accuracy on the basis of the POD-based datasets.

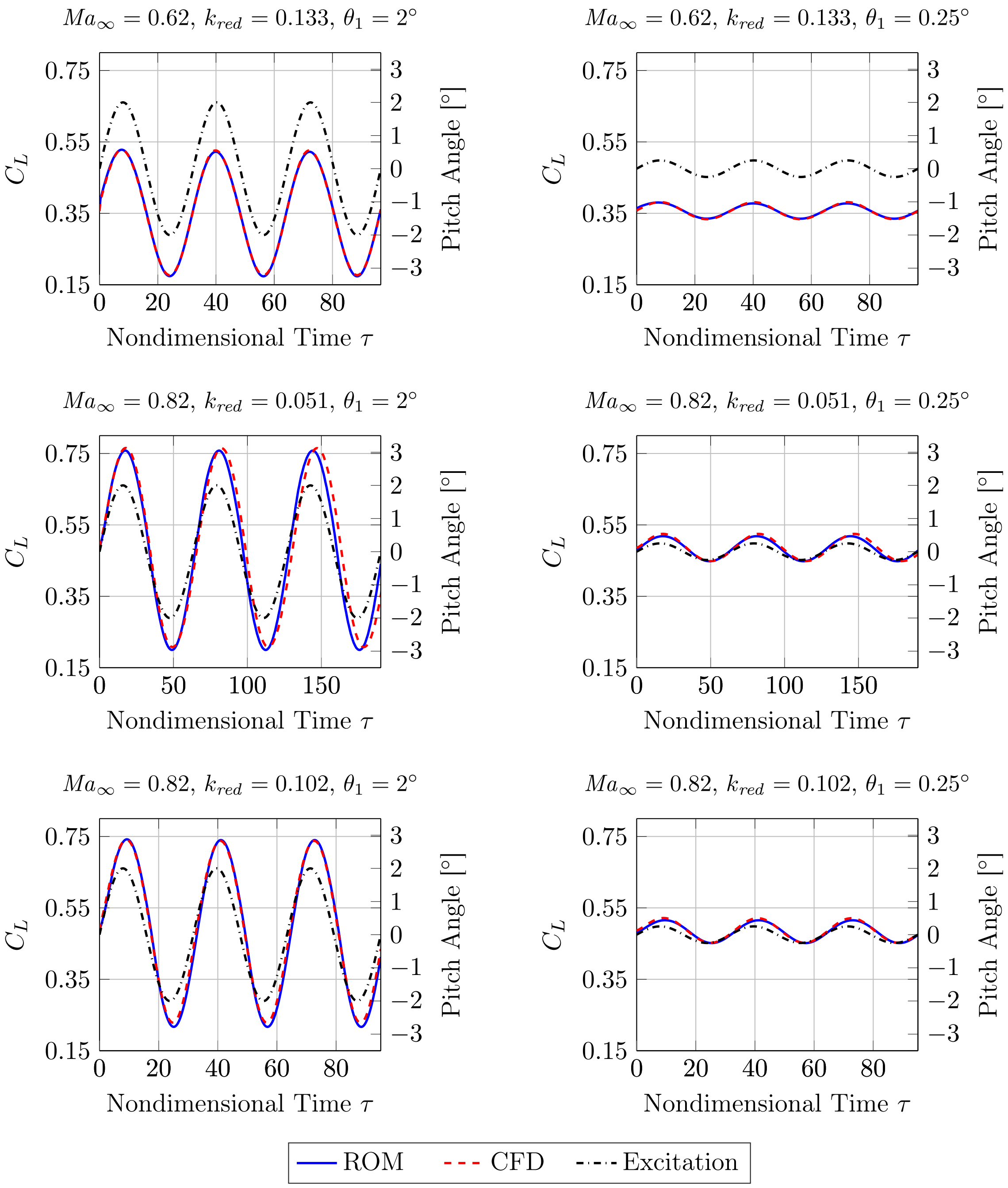

Figure 6.24: Unsteady lift coefficient time-series evaluated by means of the POD-ROM- and the CFD-based surface pressure distributions. The results are shown for all considered combinations of freestream Mach number, excitation frequency, and maximum pitch amplitude. LANN wing, $\alpha = 0.6°$.

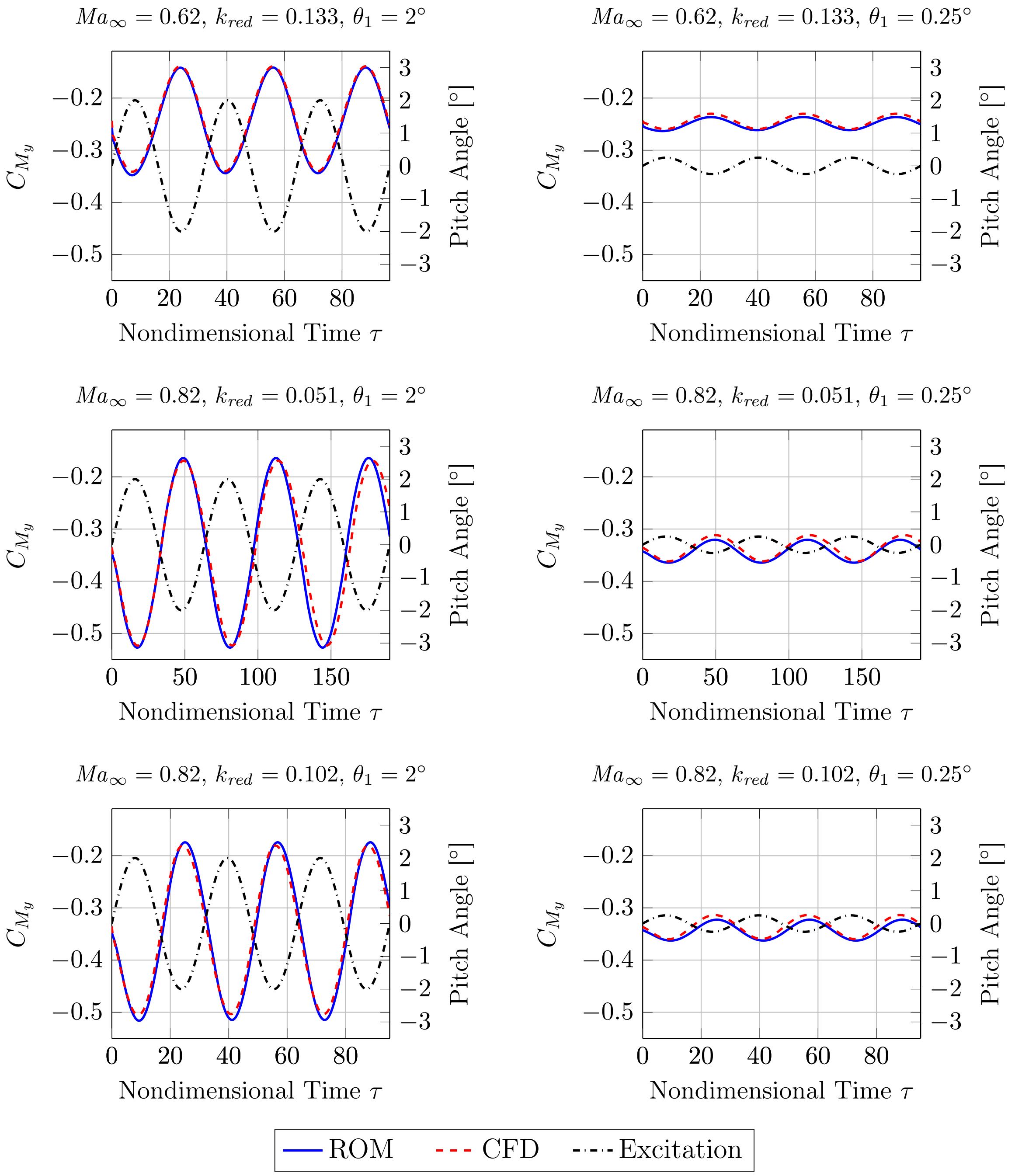

Figure 6.25: Unsteady pitching moment coefficient time-series evaluated by means of the POD-ROM- and the CFD-based surface pressure distributions. The results are shown for all considered combinations of freestream Mach number, excitation frequency, and maximum pitch amplitude. LANN wing, $\alpha = 0.6°$.

6.8 Efficiency Analysis

Finally, the computational efficiency of the POD-based reduced-order modeling framework is investigated. For classification of the simulation costs, all POD-ROM and CFD simulations presented in this chapter have been performed on a workstation equipped with an Intel Xeon 2.3 GHz processor. Thereby, a single CPU core has been utilized to ensure comparability. Analog to the considerations presented in Section 5.6, the steady computations are neglected within the total cost evaluation since they contribute to the full-order model in the same way as to the ROM construction.

Taking the numerical effort of the POD-ROM into account, the training data generation, i.e., the APRBS-based pitching-motion CFD simulation, has required 18.9 CPU hours for the high subsonic case ($Ma_\infty = 0.62$) and 37.6 CPU hours for the transonic case ($Ma_\infty = 0.82$). Moreover, the computation of the POD modes and coefficients needed about 0.01 CPU hours for each case, whereas the neuro-fuzzy model training by means of the LOLIMOT algorithm has taken 0.02 CPU hours and 0.18 CPU hours for $Ma_\infty = 0.62$ and $Ma_\infty = 0.82$, respectively. For a total cost estimation related to the ROM, the aforementioned training data acquisition, POD application, and model training must be respected. Thus, the creation of the POD-ROM for the high subsonic case required merely 18.93 CPU hours, whereas the respective model for the transonic case has been obtained in approximately 37.79 CPU hours. From the breakdown of the ROM generation costs it becomes clear that the forced-motion CFD simulation has the most severe impact on the total effort. Once the CFD-based input/output dataset is available, the remaining ROM construction effort is typically less than 1%.

Considering the application of the two POD-ROMs to the six cases that are listed for example in Figure 6.24, the computational cost for these simulations has been less than six CPU seconds. Hence, each simulation needed in average about one CPU second, including the neuro-fuzzy model application and the surface reconstruction using the POD modes. In comparison to the ROM construction effort, the application costs are virtually negligible.

In contrast, the computational costs for obtaining the reference CFD results can be summarized as follows: The AER-Eu simulations for the high subsonic freestream condition have required about 5.5 CPU hours with respect to the two harmonic excitation cases ($k_{red} = 0.133$ and $\theta_1 = [0.25°, 2°]$). Concerning the transonic case incorporating four simulation runs ($k_{red} = [0.051, 0.102]$ in combination with $\theta_1 = [0.25°, 2°]$), 18.9 CPU hours have been spend to compute the reference results. In average, the simulation of three pitching excitation periods at $Ma_\infty = 0.62$ needed about 2.3 CPU hours using the AER-Eu solver, whereas the numerical effort per case has been approximately 4.7 CPU hours for $Ma_\infty = 0.82$.

Consolidating the previously discussed computational cost analysis, it can be concluded that the ROM generation effort is about 8.2 times larger for the high subsonic case than the computation of a typical unsteady CFD run at the same freestream condition. For the transonic case, a corresponding factor of approximately 8.0 is obtained for the underlying test cases. Consequently, if more than about eight unsteady simulations are intended to be computed, the aerodynamic loads are calculated faster using the the surrogate model in comparison to the respective full-order CFD solver. Keeping in mind that an already available ROM can be employed for highly efficient simulations regarding other excitation amplitudes and frequencies within the scope of the underlying training data, the computational advantage is increased with added computation cases. By disregarding the POD-ROM generation effort, the speed-up factor for each individual simulation is of the order of four magnitudes based on the presented examples.

6.9 Summary

In the present chapter, the POD-based unsteady aerodynamic surrogate modeling approach outlined in Section 4.2 was employed to predict the surface pressure fluctuations of the LANN wing subject to pitching motions. The examples at high subsonic and transonic flow conditions demonstrated the training/application process concerning the reduced-order modeling framework and indicated the potential and fidelity of the methodology. At this point, it is worth to emphasize again that the general approach can be applied to any two- or three-dimensionally distributed, time-varying quantity under the precondition that suitable training data are provided.

Starting from the quasi-steady application example, it was shown that the proposed POD-ROM can predict the dominant unsteady aerodynamic characteristics that have been induced by multiple excitation frequencies and pitching amplitudes. In this regard, the time and frequency domain results indicated a sufficient accuracy between the ROM and the CFD reference. Nonetheless, it was also noted that the precise prediction of discontinuities such as moving shocks is still challenging. This circumstance can be interpreted as a limitation of the linear dimensionality reduction method, namely the POD, which forwards the nonlinear dynamics to the subsequently employed neuro-fuzzy model. However, taking into account the savings in computing time, the surrogate model can be easily coupled with solvers from other disciplines in terms of the model inputs and outputs. The speed-up of four orders of magnitude can be particularly interesting for computationally intensive multidisciplinary analyses such as fluid-structure-interaction problems, numerical optimization tasks, and load estimation.

7 Investigation of Strongly-Nonlinear Aerodynamic Characteristics

In this chapter, the performance of the connected neural network approach introduced in Section 4.3 is evaluated. For this purpose, the aerodynamic forces and moments acting on the NLR 7301 airfoil are investigated, while forced pitching and plunging motions are simultaneously applied. It is shown how the combined model consisting of the recurrent local linear neuro-fuzzy model and the multilayer perceptron neural network can be trained using CFD-based datasets. Moreover, the application of the novel identification-based reduced-order modeling approach is highlighted with respect to distinctly-nonlinear unsteady aerodynamic simulations. The content of this chapter is based on the author's pre-publication, Reference [189].

To test the NFM-MLP-based reduced-order model, the content of this chapter is structured in the following way: First, the NLR 7301 test case description and background information related to the associated aerodynamic modeling are given in Sections 7.1 and 7.2. Subsequently, the CFD-based training data acquisition as well as the three-stage model training process is undertaken. The main part of this chapter is formed by the model application. In this regard, the ROM is used in Section 7.5 to simulate the unsteady aerodynamic forces and moments due to harmonic motions with different frequencies and excitation amplitudes. By examining the NFM-MLP-based results in comparison to established ROM methods it is indicated that the novel approach leads to an enhanced simulation performance. In Section 7.6, the ROM fidelity is verified for a generically-defined vibration excitation. Thereby, also a variation of the static equilibrium is considered to evaluate the generalization capabilities and robustness of the model. By comparing the ROM results with the full-order CFD reference solution, it is shown that the essential linear and nonlinear aerodynamic characteristics can be accurately reproduced by the novel methodology. Finally, the analysis of the computational effort indicates the method's potential for reducing the simulation costs in the context of unsteady aerodynamic investigations.

7.1 Test Case: NLR 7301 Airfoil

For demonstrating the nonlinear ROM approach discussed in Section 4.3, the NLR 7301 airfoil has been chosen. The associated unsteady aerodynamic test cases in the transonic flight regime are well-known in the community for their strongly nonlinear characteristics [28, 162, 206]. In Figure 7.1, the CFD grid of the supercritical airfoil geometry is depicted. According to Zwaan [206], a chord length of $c_{ref} = 0.3\ m$ is specified, whereas the axis for the considered pitching motion has been defined at 40% of the chord.

In this chapter, the NLR 7301 airfoil is investigated at a freestream Mach number of $Ma_\infty = 0.753$ and an angle of attack of $\alpha = 0.6°$. According to the experimental tests described in Reference [206], the aforementioned flow condition leads to a pronounced shock on the airfoil's suction side. As it is shown in the further course of this study, the intensity and position variation of the shock becomes nonlinearly related to the displacement amplitude if the airfoil undergoes a sufficiently large pitching and plunging motion. Consequently, also the flow-induced forces and moments are affected in a nonlinear way. Due to this strongly-nonlinear relationship between the inputs and outputs of the aerodynamic system, the NLR 7301 test case has been selected to challenge the NFM-MLP-based reduced-order model.

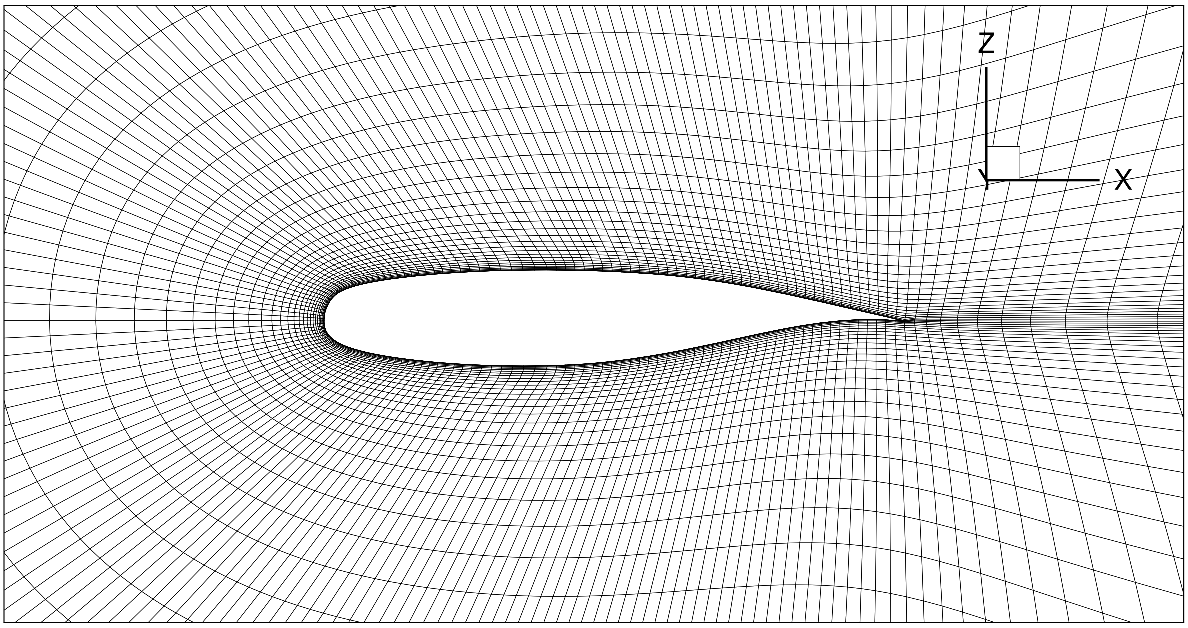

Figure 7.1: Geometry of the NLR 7301 supercritical airfoil embedded within the block-structured computational grid for the CFD-based simulations.

Consolidating the identification theory presented in Chapter 3 with the test-case-specific boundary conditions, the system input consists of the pitch and plunge excitation amplitudes, whereas the output of the system is composed of the lift and pitching moment coefficients. With $h(t)$ being the time-dependent plunge amplitude, the system inputs and outputs can be defined as:

$$\mathbf{u}(t) = \begin{pmatrix} \theta(t) \\ h(t) \end{pmatrix} \in \mathbb{R}^2, \qquad \mathbf{y}(t) = \begin{pmatrix} C_L(t) \\ C_{M_y}(t) \end{pmatrix} \in \mathbb{R}^2, \qquad \Xi \in \varnothing \tag{7.1}$$

In Equation (7.1), the empty parameter vector Ξ has been added for completeness, as no static parameter changes are taken into account by the model in contrast to the investigations presented in Chapter 5. Furthermore, the fixed reference point for the calculation of C_{M_y} is specified as the quarter-chord point of the undeflected airfoil.

7.2 Computational Set-up and Steady-State Flow

In the present investigation, the fluid dynamic modeling of the NLR 7301 test case is realized by solving the Euler equations using AER-Eu. According to the discussion in Chapter 2, the influence of the viscosity of the flow is excluded in this way. Consequently, neither shock-boundary-layer interaction effects nor flow-separation-induced phenomena are captured by the CFD solver. For a comparison with experimental data, the viscous effects must be taken into account for the present case [178]. However, the focus here is on an intermethod comparison between various ROM architectures and the CFD reference result. Since strongly nonlinear effects are encountered, the Euler-based view does not restrict the validity of the presented results.

With respect to the inviscid CFD simulations, a structured 2.5-dimensional multi-block grid has been generated using ANSYS ICEM CFD [2]. The computational grid shown in Figure 7.1 is composed of 14,396 finite volumes, while the airfoil surface is resolved with 156 cells. To obtain a body-fitted grid, the respective cells are arranged in a four-block C-type topology. Moreover, the grid is refined towards the airfoil by adjusting the off-body distance of the first cell height to $1 \cdot 10^{-3}\ c_{ref}$. Finally, the grid has been postprocessed with the in-house Poisson-equation-based mesh smoother [26].

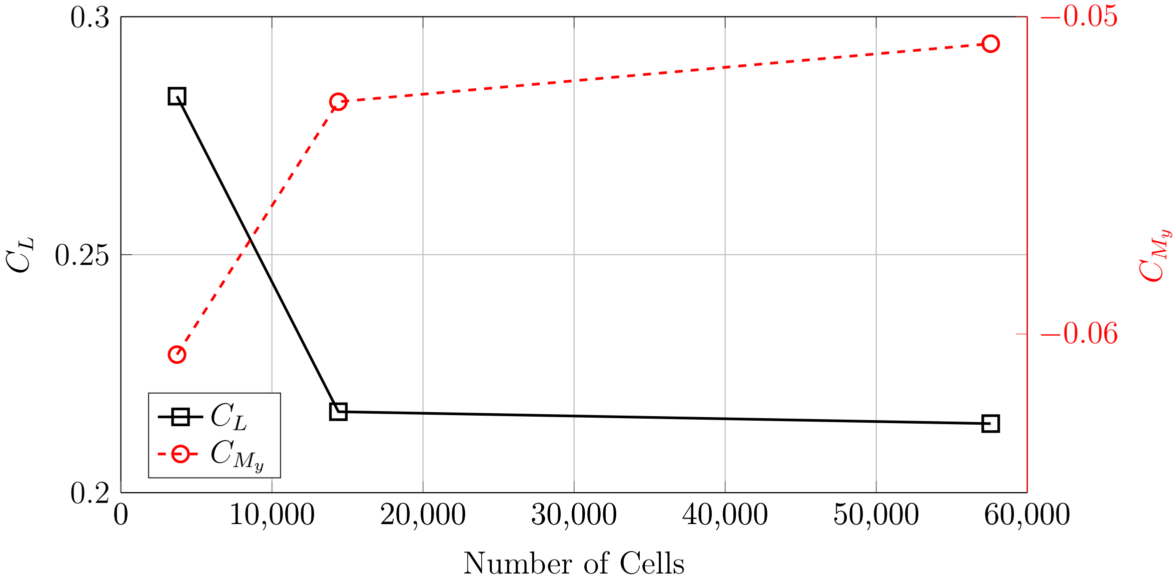

Figure 7.2: Steady-state results of the grid refinement study by example of the aerodynamic lift (C_L) and pitching moment (C_{M_y}) coefficients. NLR 7301, AER-Eu.

In order to guarantee the independence of the solution from the spatial resolution, a mesh sensitivity study has been conducted. For this purpose, a coarse, a medium and a fine grid have been created. The coarse and the fine grid are characterized by the respective halved and doubled number of edge nodes relative to the medium grid level. In Figure 7.2, the steady-state lift and pitching moment coefficients are depicted for the aforementioned grid levels. Based on the grid sensitivity plot, it becomes clear that the coarse grid leads to considerably different results compared to the other two grids. For this reason, the coarse grid is not further considered in this work. Comparing the results originating from the medium and the fine grid, the relative error is given as 1.1% with respect to C_L and 3.6% for C_{M_y}. Besides the steady-state grid sensitivity investigation displayed in Figure 7.2, an additional unsteady test campaign indicated the same trends for the three grid levels. Hence, the medium grid realizes a good compromise between the solution quality and the computational costs. It is therefore considered to be adequate for the following simulations.

In the course of this investigation, a fixed transonic flight condition characterized by a freestream Mach number of $Ma_\infty = 0.753$ and an angle of attack of $\alpha = 0.6°$ is considered. The only exception is the generalization study provided in Section 7.6, which also includes results at $\alpha = 2°$ for the same freestream Mach number. Concerning the steady and unsteady CFD results presented in this chapter, the simulations have been terminated once the Euclidean norm with respect to the density normalized with the corresponding value after the first iteration reached a value below 10^{-5}. In Figure 7.3, the steady-state AER-Eu simulation result is shown by means of the pressure coefficient contours for the selected medium grid level. As a result of the transonic freestream condition, a crisp shock is formed on the suction side of the supercritical airfoil. Referring to the ROM procedure outlined in Section 4.3.2, the steady solution forms the basis for the subsequently discussed unsteady aerodynamic analyses.

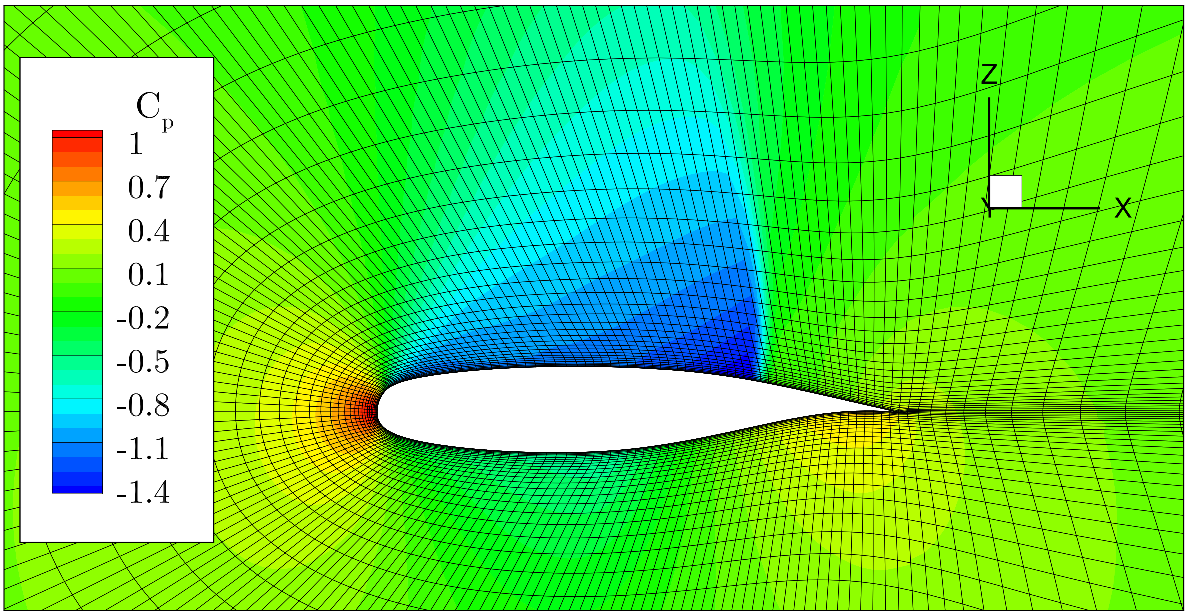

Figure 7.3: CFD-based steady-state pressure coefficient contours around the NLR 7301 airfoil at $Ma_\infty = 0.753$ and $\alpha = 0.6°$ (AER-Eu).

7.3 CFD-Based Training Data Generation

According to the training procedure discussed in Section 4.3, the aerodynamic response due to forced motions must be computed using the CFD solver to provide the training data for the reduced-order model. Here, the output of the aerodynamic system is recorded in terms of the lift and pitching moment coefficients, while the pitch and plunge deflection degrees of freedom of the NLR 7301 airfoil are taken into account. Consequently, deformed computational grids are required by the AER-Eu solver in order to conduct the intended unsteady simulations. Within the scope of this chapter, the deformed CFD grids have been generated by means of rigid body rotations/translations of the grid nodes to model the respective pitch and plunge motions.

Table 7.1: Overview of the generically defined amplitude scenarios for the ROM-based investigations.

Amplitude level		Pitch angle range	Plunge displacement range
Training		$-5.5° < \theta < 5.5°$	$-11\%\ c_{ref} < h < 11\%\ c_{ref}$
Application:	Small (SA)	$-0.1° < \theta < 0.1°$	$-0.5\%\ c_{ref} < h < 0.5\%\ c_{ref}$
	Medium (MA)	$-3° < \theta < 3°$	$-4\%\ c_{ref} < h < 4\%\ c_{ref}$
	Large (LA)	$-5° < \theta < 5°$	$-10\%\ c_{ref} < h < 10\%\ c_{ref}$

In order to assess the model performance for different input amplitude levels, three excitation scenarios have been defined for ROM application. In Table 7.1, the small, medium, and large amplitude cases are specified by means of intervals for the pitch and plunge amplitude. With respect to the underlying aerodynamic system, the large excitation amplitudes are expected to provoke the most pronounced nonlinear characteristics. This can be proven by the unsteady AER-Eu solutions depicted in Figure 7.4. The diagram shows the (normalized) lift coefficient due to a harmonic pitching motion with a reduced frequency of $k_{red} = \omega \cdot c_{ref}/U_\infty = 0.01$ for the small, medium, and large amplitude scenarios. While the C_L time-series for the maximum pitching amplitude of $\theta_{max} = 5°$ is nonlinearly related to the sinusoidal airfoil motion, the small perturbation (SA) case can be regarded as entirely linear. Furthermore, it should be noted that the pitching moment typically responds in a more nonlinear manner than the lift coefficient. As it has been discussed for instance by Kou et al. [84], it is more difficult to capture both linear and nonlinear dynamic effects with a single ROM in comparison to exclusively treating linear or nonlinear system characteristics. Hence, it is concluded based on Figure 7.4 that the defined amplitude range leads to a significant level of nonlinearity.

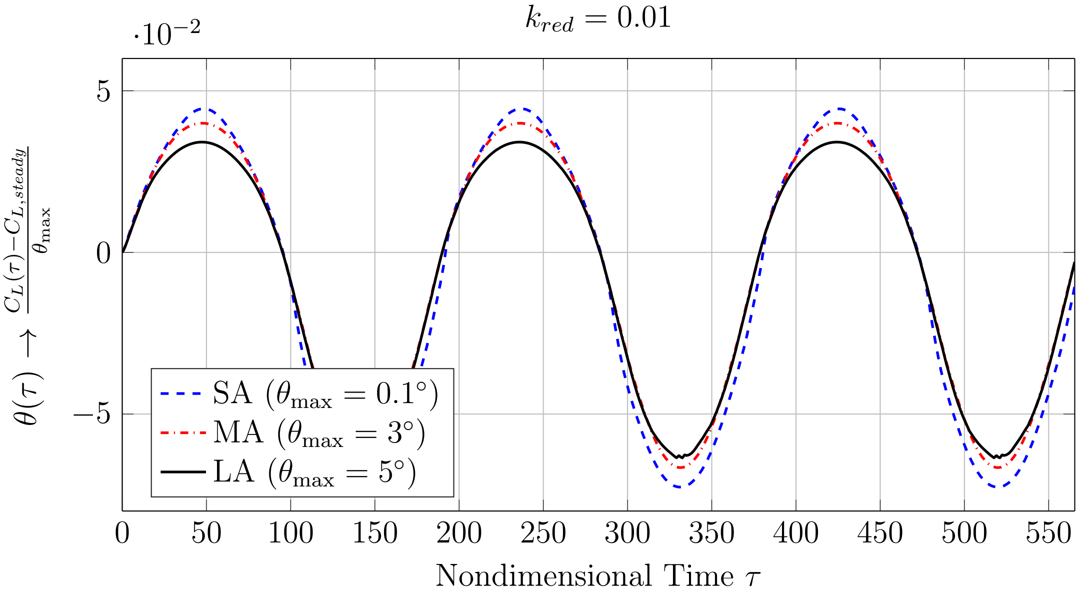

Figure 7.4: The lift coefficient normalized with the pitching amplitude is shown for three harmonic pitching cycles with $k_{red} = 0.01$. The result clearly indicates the nonlinear amplitude-dependent characteristics for the considered test case. NLR 7301, $Ma_\infty = 0.753$, $\alpha = 0.6°$, AER-Eu.

In contrast to the application-related cases summarized in Table 7.1, an excitation range of $-5.5° < \theta < 5.5°$ and $-11\%\ c_{ref} < h < 11\%\ c_{ref}$ has been chosen for the training pitch and plunge deflections. In this way, the specified amplitudes for the ROM application are covered within the trained input characteristics. On the basis of the aforementioned training amplitudes, smoothed amplitude-modulated pseudo-random binary signals (SAPRBS, see Section 3.7) have been generated for the pitch and the plunge motion as it is shown in Figure 7.5. Concerning the associated two training excitation signals, an overlap of 20% has been set to capture possible nonlinear interactions caused by the simultaneous deflection of both degrees of freedom. An a priori conducted time step sensitivity study for the present CFD set-up revealed that a nondimensional time step size of $\Delta\tau = 0.01$ must be chosen to obtain converged results. In combination with the nondimensional time interval from 0 to 820 depicted in Figure 7.5, the unsteady CFD simulation yielding the ROM training data is characterized by 82,000 time steps. Due to the anticipated strongly-nonlinear behavior of the aerodynamic system, the time interval has been chosen sufficiently large in order to ensure an adequate information content of the training data. With respect to the temporal resolution, however, the small time step size needed for the AER-Eu simulation can be increased concerning the nonlinear ROM-based prediction tasks. Hence, every 10th sample of the CFD input/output dataset is used for calibrating the model. In this way, the training and application process can be accelerated, without affecting the quality of the ROM results. Following the previous discussion, 8,200 training samples have been exploited for the present test case, while the effective discrete time step size for the identified reduced-order models becomes $\Delta\tau = 0.1$.

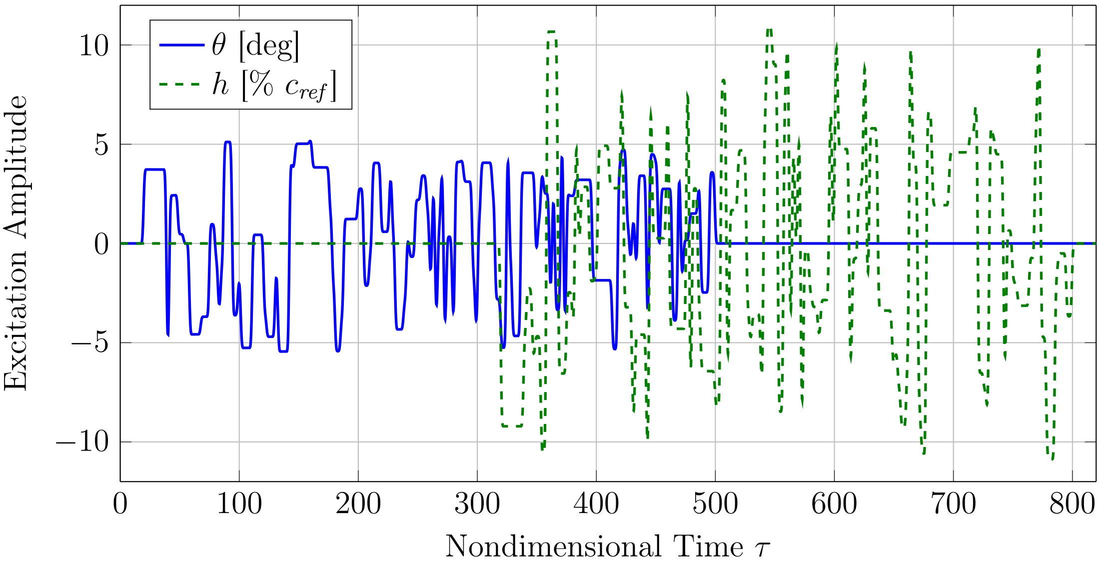

Figure 7.5: Smoothed amplitude-modulated pseudo-random binary signals for the prescribed excitation of the pitch and plunge degrees of freedom (NLR 7301, $\Delta\tau = 0.01$).

Furthermore, the SAPRBS-related plateaus have been designed such that reduced frequencies ranging from $0 < k_{red} < 0.5$ can be investigated by means of the ROM. In Figure 7.6 it is demonstrated that the generated training signals introduce sufficient energy at the aforementioned frequency interval. As a consequence, the training signals, which are simultaneously applied for both rigid body motions, are considered to be compatible with the underlying problem and the intended unsteady aerodynamic simulations.

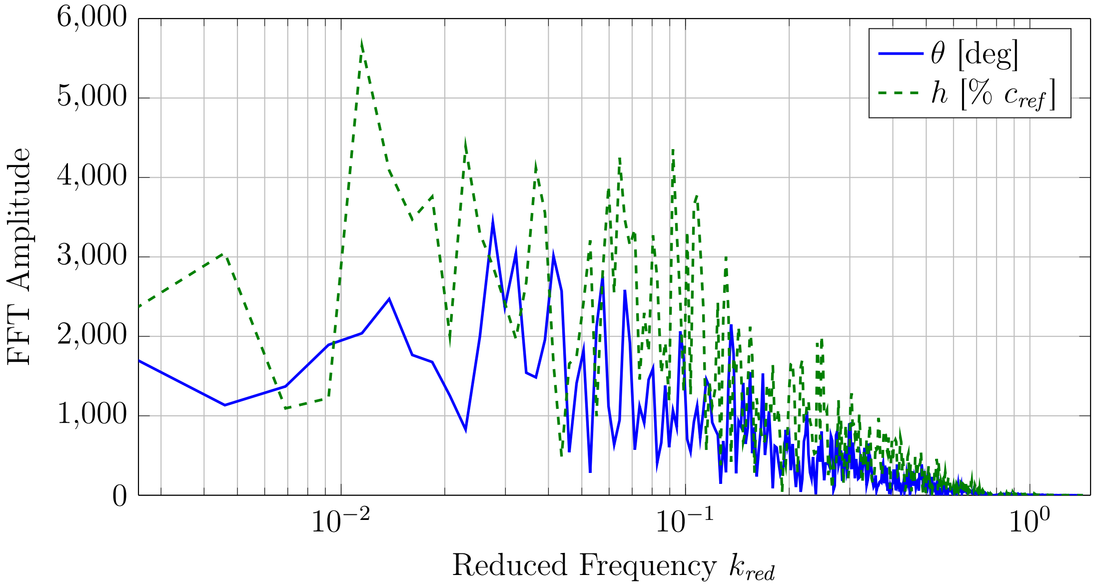

Figure 7.6: The frequency spectrum of the SAPRBS-based pitch and plunge training inputs is shown as a function of the reduced frequency k_{red}.

Proceeding from the steady-state simulation at $Ma_\infty = 0.753$ and $\alpha = 0.6°$, the unsteady aerodynamic response induced by the prescribed pitch and plunge motions has been obtained by a single AER-Eu simulation. In particular, the CFD output of interest is shown in Figure 7.7 by example of the C_L and C_{M_y} time-series. At this point, it is important to highlight that the data contained in Figures 7.5 and 7.7 constitute the full training dataset. All identification-based ROMs presented below are trained exclusively by means of the displayed information.

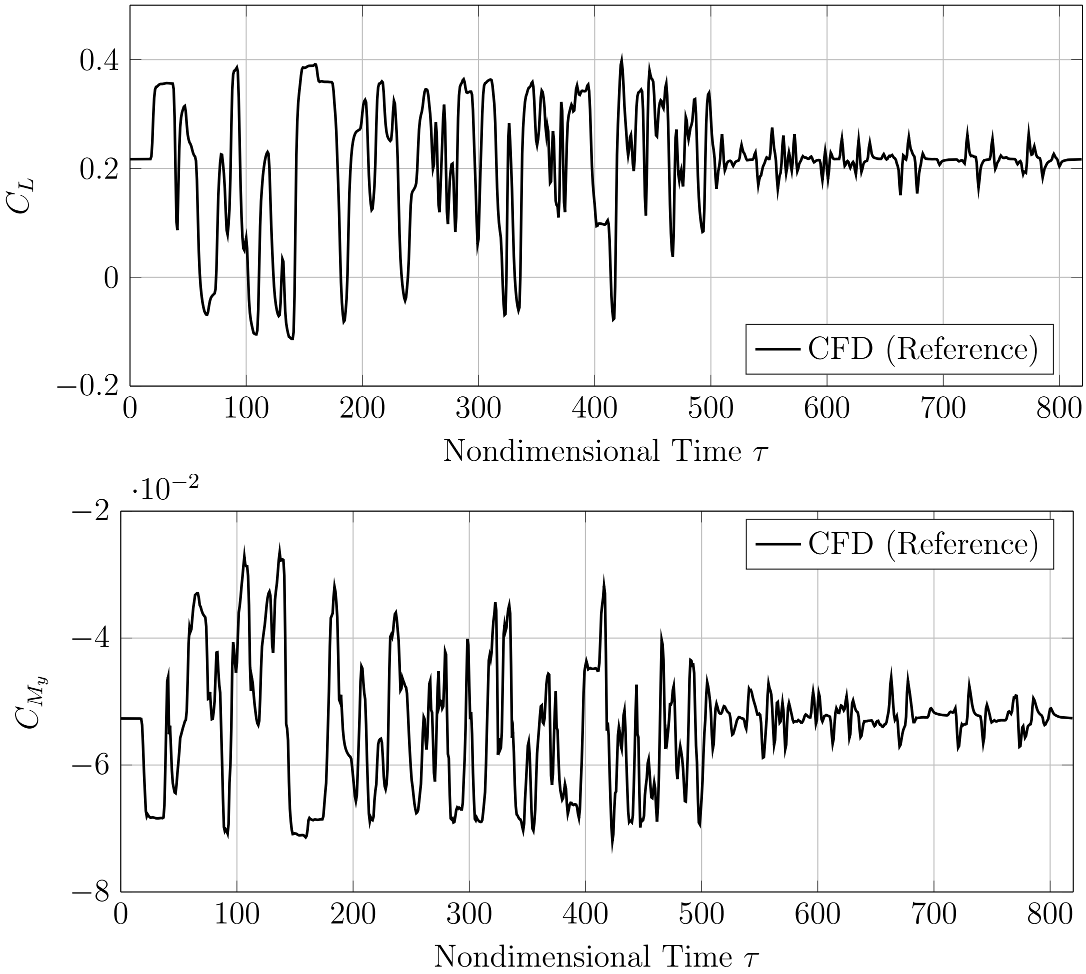

Figure 7.7: Lift and pitching moment coefficient response caused by the prescribed SAPRBS excitation of the pitch and plunge rigid body modes. NLR 7301, $Ma_\infty = 0.753$, $\alpha = 0.6°$, $\Delta\tau = 0.01$, AER-Eu.

7.4 Training of the Reduced-Order Models

Given the training data representing the aerodynamic behavior of the NLR 7301 airfoil, the identification-based ROM training has been performed. In this regard, the maximum dynamic delay-orders for the recurrence framework methodology have been specified to $m = n = 8$ for all presented models. Besides applying the developed NFM-MLP training procedure discussed in Section 4.3, three additional ROMs have been constructed within the scope of this chapter for comparative purposes:

1) ROM/ARX: First, an auto-regressive with exogenous input (ARX) model has been generated, serving as the least-sophisticated ROM for the considered problem. This globally linear model is obtained via the LOLIMOT algorithm by restricting the maximum number of local linear models to one ($M = 1$).

2) ROM/NFM: Second, the local linear neuro-fuzzy model described in Section 3.4.2 is trained by means of the LOLIMOT algorithm. In contrast to the aforementioned ROM/ARX, the number of local linear models is data-dependent and not limited to $M = 1$. Due to the nonlinear nature of the underlying test case, several partitions of the model input space are necessary to reasonably approximate the training data.

3) ROM/MLP: Third, the classical multilayer perceptron neural network outlined in Section 3.4.3 has been trained from the available unsteady aerodynamic dataset. For the intended application-related simulations, the MLP neural network must be applied in the recurrent modus operandi, i.e., exhibiting a feedback of the neural network outputs. The number of neurons for the model with two hidden layers has been specified to $M_{MLP} = [5,\ 2]$ for the respective first and second hidden layer. Due to the frequently encountered model instabilities concerning the ROM/MLP response, the respective results are not visualized except from a single diagram for the sake of a clear presentation.

4) ROM/NFM-MLP: Finally, the novel approach incorporating the recurrent NFM coupled with the MLP neural network is employed. Thereby, the same settings are applied compared to the individual ROM/MLP and ROM/NFM models to ensure comparability.

For each of the four ROM types, $N_{MC} = 25$ separate models have been trained according to the Monte-Carlo procedure discussed in Section 3.6. Hence, in total 100 models are available for conducting unsteady aerodynamic simulations, allowing conclusive comparisons for the different model architectures. As a consequence, all diagrams in this chapter display the mean of the $N_{MC} = 25$ responses as the main line, while a shaded area marks the corresponding standard deviation unless otherwise specified. Based on the statistical information about a particular ROM output, the following conclusions can be derived: If the standard deviation spans a comparatively small range around the main line, the likelihood is high that also individual ROMs provide the mean response. Furthermore, small standard deviations σ can be an indicator that sufficient training data are available in the associated amplitude and frequency regimes to capture the prevailing effects. A small σ value, however, does not guarantee a certain level of accuracy. In contrast, large standard deviations are typically connected with a lack of training data or, alternatively, possible model instabilities. Thus, inaccurate model outputs are indicated by high σ values. These general remarks are further refined in the following.

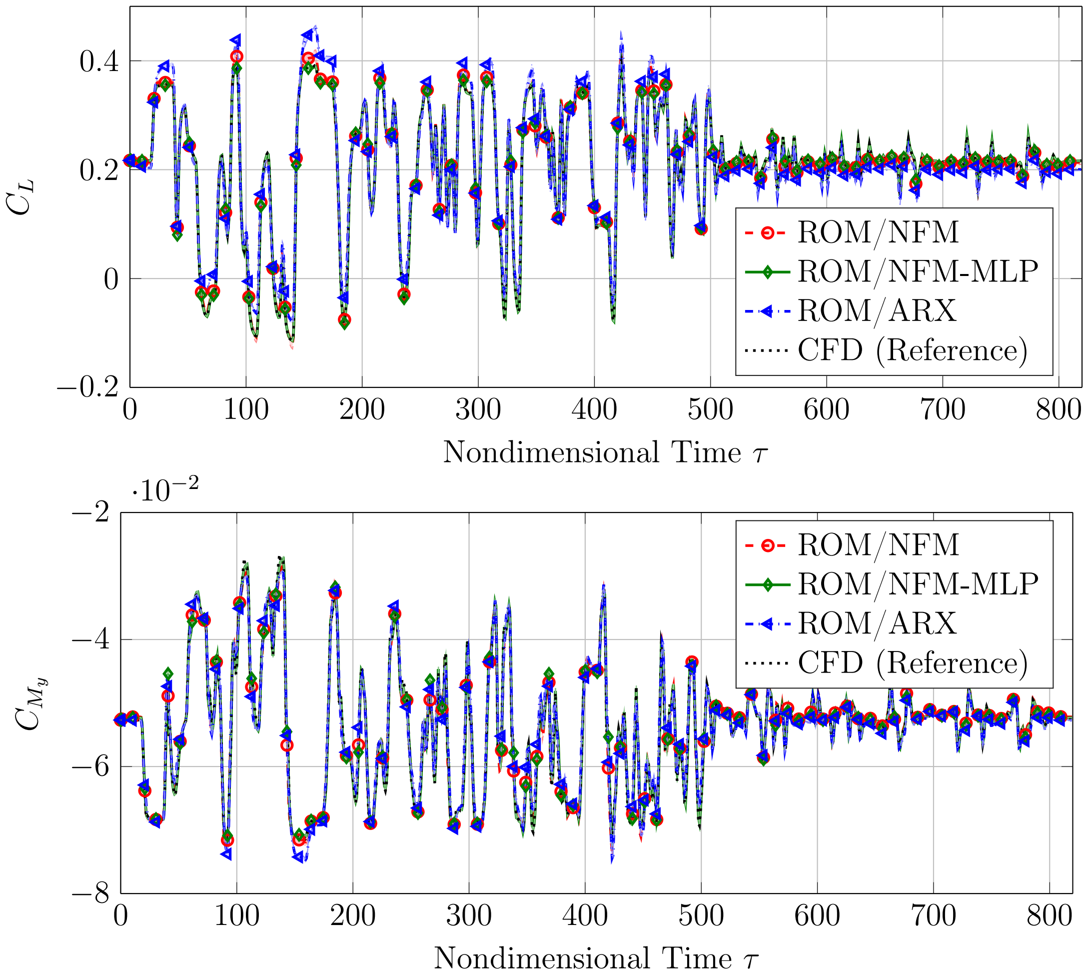

Figure 7.8: C_L and C_{M_y} response induced by the SAPRBS excitation shown in Figure 7.5. The simulation results of three ROM approaches are juxtaposed to the respective training solution provided by the CFD solver. NLR 7301, $Ma_\infty = 0.753$, $\alpha = 0.6°$.

Prior to the application studies presented in Sections 7.5 and 7.6, the ROM performance is evaluated based on the training data itself. Therefore, multi-step ahead predictions are computed using the considered ROM approaches to gain a basic impression of the fidelity of the methods. If a certain model is not able to reproduce the training data sufficiently well, a deteriorated accuracy can be expected also for the application cases. In Figure 7.8, the ROM outputs are shown along with the AER-Eu reference data, from which the models have been trained. In order to provide a quantitative measure of the ROM-related errors, the fit factor Q is introduced in Equation (7.2) according to Ljung [102]:

$$Q = 100\% \cdot \left[1 - \frac{\sqrt{\sum_{s=1}^{N_S} \Big(y(s) - \hat{y}(s) \Big)^2}}{\sqrt{\sum_{s=1}^{N_S} \Big(y(s) - \overline{y} \Big)^2}} \right] \tag{7.2}$$

$$\overline{y} = \frac{1}{N_S} \sum_{s=1}^{N_S} y(s) \tag{7.3}$$

The fit factor for a specific case is computed by inserting the mean ROM response as the model output $\hat{y}$. Moreover, the CFD-based reference result enters Equations (7.2)-(7.3) by means of $y(s)$, whereas N_S denotes the number of signal samples. As a fit factor of 100% indicates an exact agreement, the criterion can be employed to assess the quality of the model outputs. Concerning the results depicted in Figure 7.8, the fit factors are summarized in Table 7.2.

Table 7.2: Fit factors evaluated for the training dataset.

Fit factor Q	C_L	C_{M_y}
ROM/ARX	80.88%	85.06%
ROM/NFM	95.40%	91.32%
ROM/MLP	85.69%	32.74%
ROM/NFM-MLP	96.53%	94.43%

By analyzing Table 7.2 and Figure 7.8, it is apparent that the ROM/ARX solution fairly approximates the global trend of the training data. Nevertheless, a more detailed consideration illustrates the shortcomings of the linear model, especially, in contrast to the results of the ROM/NFM and ROM/NFM-MLP approaches. The MLP neural network result, which is not displayed in Figure 7.8, becomes unstable with respect to the pitching moment. Consequently, a poor fit factor Q arises for the ROM/MLP regarding C_{M_y}. In contrast, the methods that are based on the neuro-fuzzy model, namely ROM/NFM and ROM/NFM-MLP, reproduce the training data in an accurate manner. The novel NFM-MLP approach yields the highest fit factors, which can be underlined by the frequency spectrum of the lift coefficient shown in Figure 7.9. The high precision exhibited by the ROM/NFM-MLP result, however, is not surprising for the training case since the a posteriori employed MLP neural network statically reduces the error between the CFD output and the NFM solution.

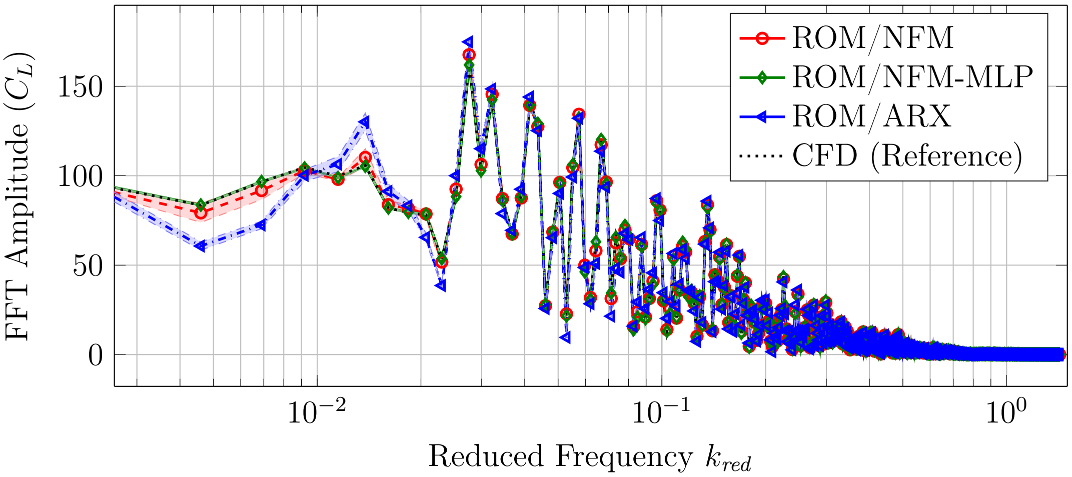

Figure 7.9: Fast Fourier transform amplitude regarding the lift coefficient response for the training dataset plotted as a function of the reduced frequency. NLR 7301, $Ma_\infty = 0.753$, $\alpha = 0.6°$.

7.5 Unsteady Results: Sinusoidal Excitation

Henceforth, the ROM approaches are used to compute the aerodynamic responses for a priori unknown excitation patterns. The first test consists of the simulation of sinusoidal excitations due to their paramount importance for unsteady aerodynamic and aeroelastic applications. In this regard, a single degree of freedom of the NLR 7301 airfoil, e.g., either the pitch angle or the plunge displacement, is harmonically varied, whereas the other input is held constant at its respective static equilibrium position. Within the scope of this study, the excitation reduced frequencies of $k_{red} = [0.01, 0.05, 0.1, 0.2, 0.3, 0.4]$ are taken into account to evaluate the performance of the reduced-order models. Besides the frequency variation, also the different amplitude scenarios introduced in Table 7.1 are considered. For example, the pitch angle θ undergoes a sinusoidal motion in the range of $-0.1° < \theta < 0.1°$ if the small amplitude (SA) case is investigated.

Analogously to the application tests outlined in Chapters 5 and 6, three oscillation cycles have been simulated to eliminate the influence of initial transients. On the one hand, each cycle computed by the AER-Eu solver is discretized with 500 time steps to obtain the reference data for comparative purposes. On the other hand, the ROMs are applied using the constant time step size of $\Delta\tau = 0.1$ from the underlying resampled training dataset. Consequently, a frequency-dependent cycle resolution must be respected for ROM utilization. Nevertheless, on the basis of a sensitivity study it has been ensured that the temporal discretization is adequate for the ROM- as well as the CFD-based modeling. Given the $N_{MC} = 25$ models for each of the four considered ROM approaches, the Monte-Carlo-based application strategy discussed in Section 3.6 has been followed to obtain the statistically-processed results presented below.

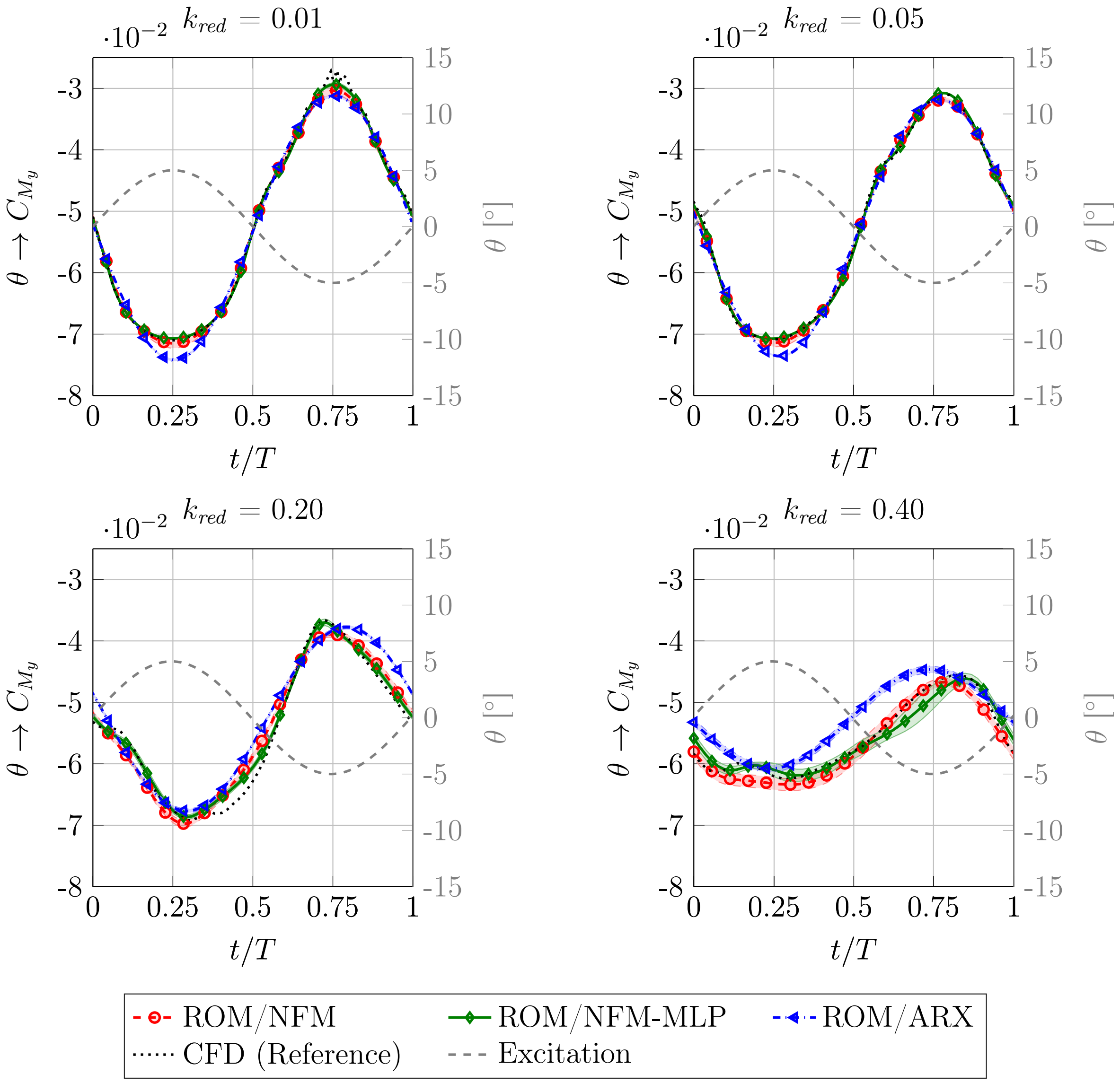

Figure 7.10: Pitching moment coefficient response induced by pitching oscillations at selected reduced frequencies (LA case). The response is shown for the third excitation cycle, while T denotes the period length. NLR 7301, $Ma_\infty = 0.753$, $\alpha = 0.6°$.

In Figures 7.10-7.13, the response of the aerodynamic system due to harmonic pitch and plunge deflections is presented for exemplary cases. In particular, the results generated by the ROM/ARX, ROM/NFM, and ROM/NFM-MLP models are plotted along with the AER-Eu reference. Therefore, both the time-domain response (Figures 7.10 and 7.13) and the Lissajous figure representation are utilized to enable a suitable illustration of the results. Concerning the Lissajous plots shown in Figures 7.11 and 7.12, the normalized excitation amplitude Θ is utilized, which covers the range of values between $-1 \leq \Theta \leq 1$.

As it can be stated from Figures 7.10-7.13, the linear ROM/ARX is generally able to predict the trend of the input/output relationship for the large amplitude (LA) cases. This can be confirmed especially for the lower excitation frequencies, i.e., $k_{red} < 0.1$.

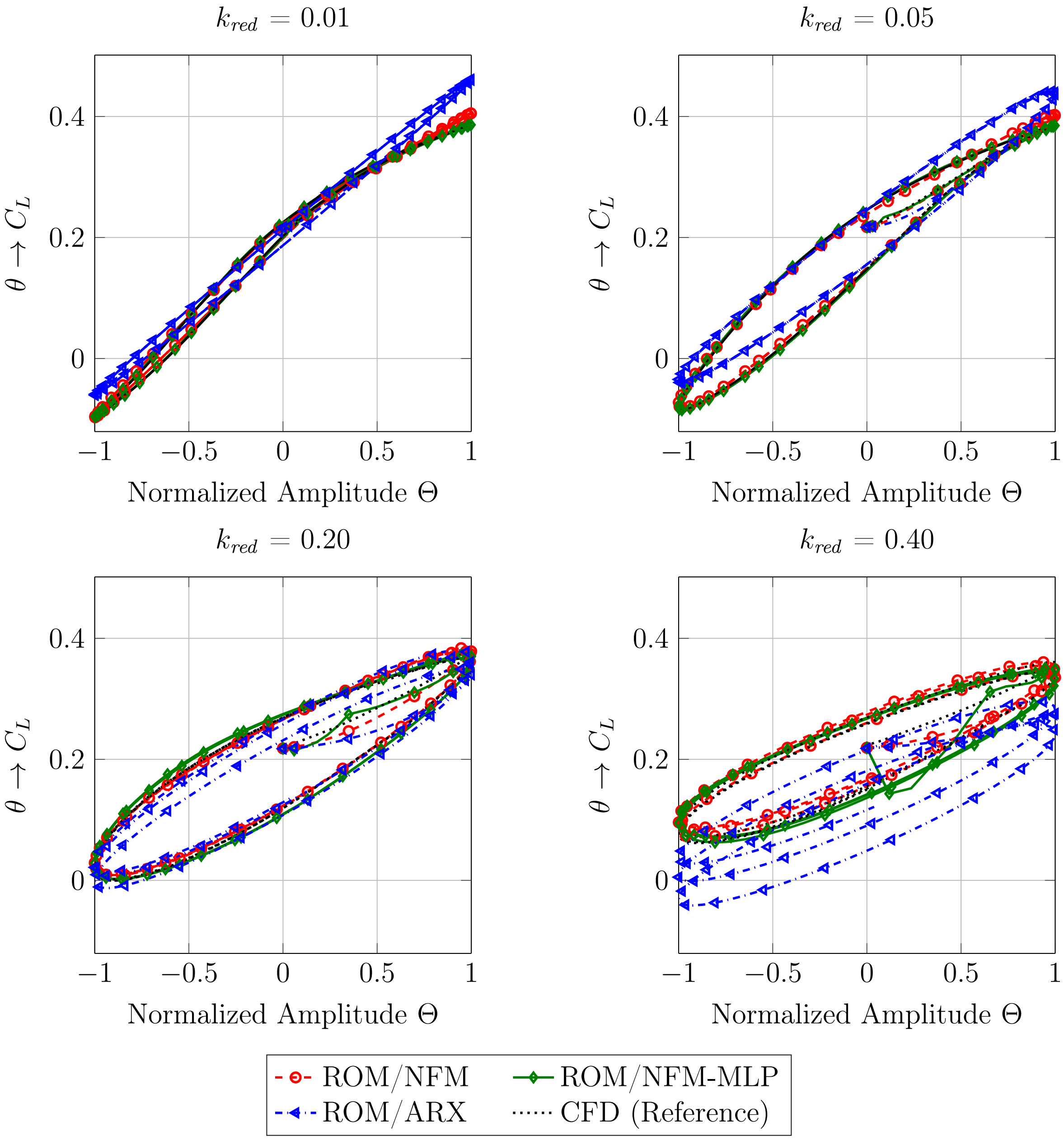

Figure 7.11: Lissajous figures of the lift coefficient response due to pitching oscillations at selected reduced frequencies (LA case). For clarity, the standard deviation is not shown in this figure. NLR 7301, $Ma_\infty = 0.753$, $\alpha = 0.6°$.

Nevertheless, it is self-explanatory that a linear model cannot predict any nonlinear dependencies. For this reason, the Lissajous figures associated to the ROM/ARX response become elliptic. Hence, a linear ROM approach is an inappropriate choice regarding the given test case set-up.

Comparing the stand-alone ROM/NFM-based results with the CFD reference, a good correlation is ascertained for the LA cases. Moreover, the novel system identification technique (ROM/NFM-MLP) is shown to be well-suited for describing the nonlinear aerodynamics of the NLR 7301 test case as it can be seen from Figures 7.10-7.12. In particular, larger excitation frequencies and stronger nonlinear characteristics are more accurately resolved by the ROM/NFM-MLP methodology in comparison to the competing methods. Summarizing the results for the large amplitude case, it becomes apparent that the amplitude range of the aerodynamic response as well as the associated phase lag is well captured by the nonlinear-identification-based models, which is particularly valid for the ROM/NFM-MLP method.

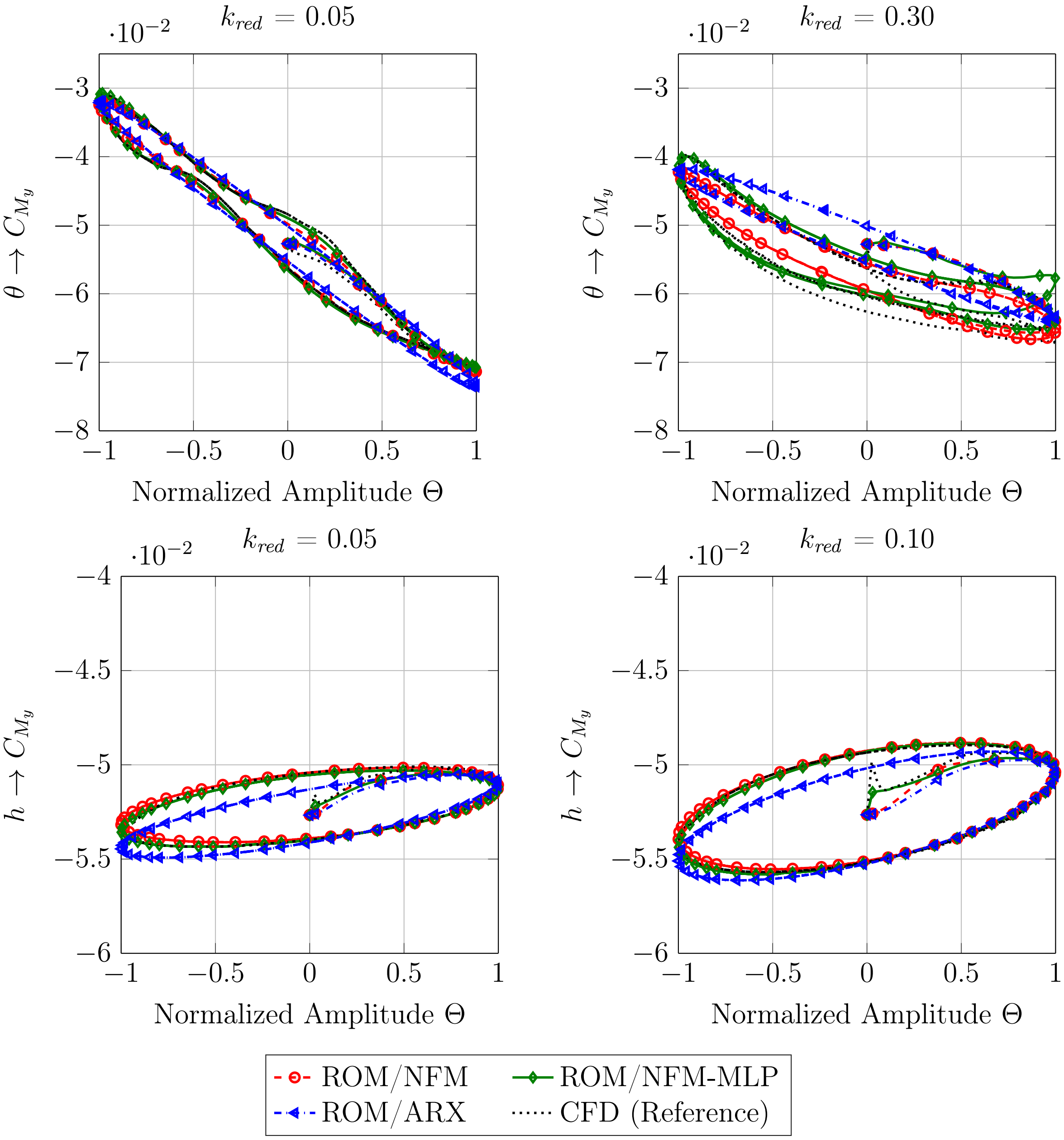

Figure 7.12: Lissajous figures of the pitching moment coefficient response caused by pitch and plunge oscillations at selected reduced frequencies (LA case). For clarity, the standard deviation is not shown in this figure. NLR 7301, $Ma_\infty = 0.753$, $\alpha = 0.6°$.

The aforementioned observation of a generally good conformity between the nonlinear-ROM-based results cannot be extrapolated to the small amplitude (SA) case. As it can be seen in Figure 7.13, severe discrepancies are encountered for small excitation amplitudes. Based on the depicted results, neither the ROM/ARX nor the ROM/NFM are suited to simulate the aerodynamic response due to the small excitation amplitudes regarded in terms of the SA cases. Thus, the established methods presented herein fail to generalize towards small amplitude motions associated with an essentially linear system behavior. In contrast, the novel model not only outperforms the conventional ROM approaches in terms of predicting strongly-nonlinear characteristics but also reproduces the regimes that are governed by a linear behavior in a precise manner. Except from the initial errors that can be traced back to the simulation initialization (see Section 3.3), the ROM/NFM-MLP results exhibit a very good agreement with the respective AER-Eu reference solutions, while also the range of fluctuation between different models (expressed by the standard deviation) is comparatively small. It should be emphasized again that all ROMs have been trained by the same dataset. Hence, it is shown for the conducted tests that the novel approach clearly outperforms the established modeling techniques.

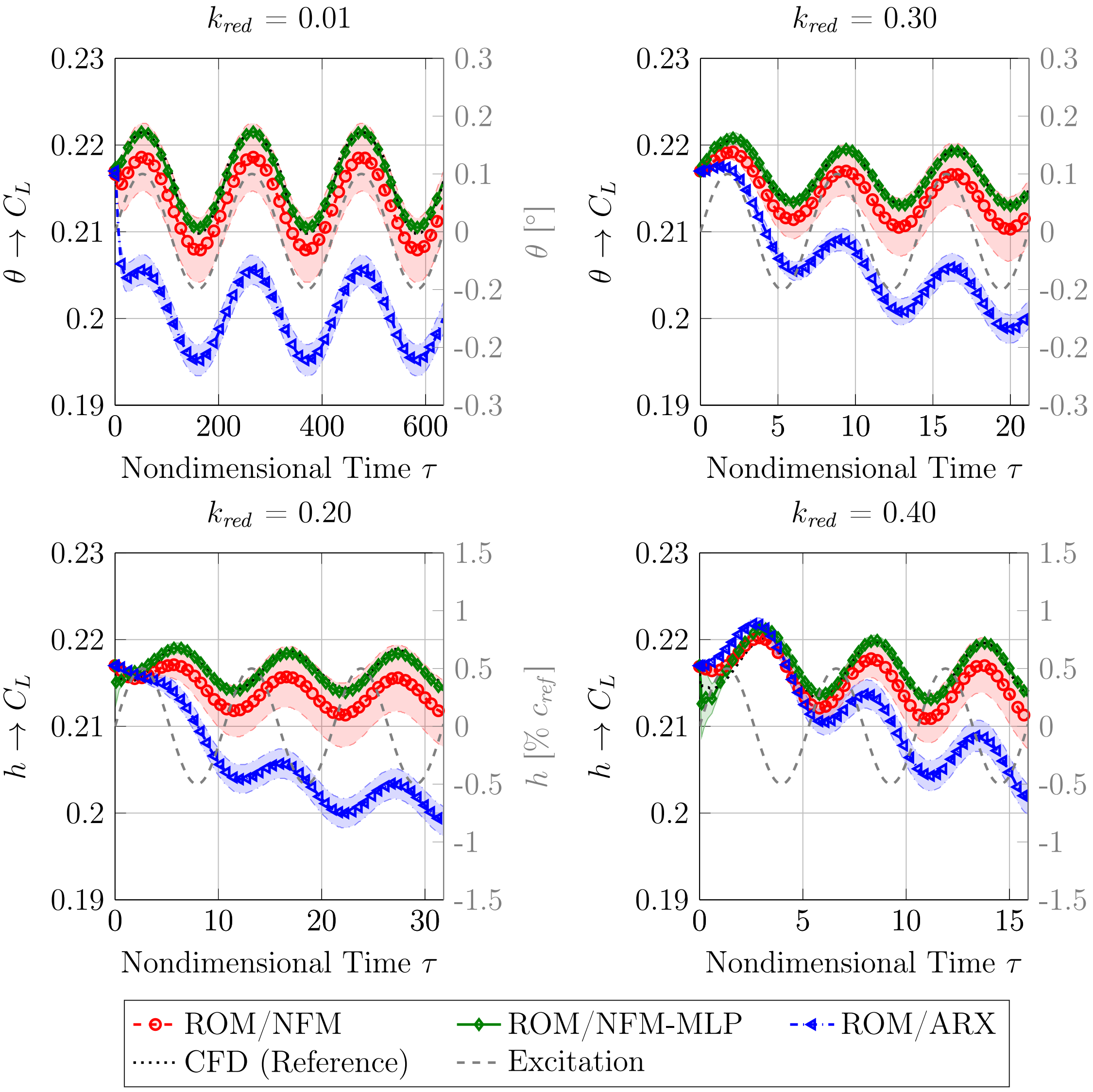

Figure 7.13: Lift coefficient response induced by pitch and plunge oscillations at selected reduced frequencies (SA case). NLR 7301, $Ma_\infty = 0.753$, $\alpha = 0.6°$.

7.6 Unsteady Results: Generic Vibration Excitation

Besides the consideration of purely sinusoidal motions discussed in Section 7.5, a set of amplified, frequency-modulated vibration signals has been generated for ROM demonstration purposes. In Figure 7.14, two signals associated to the simultaneously enforced pitch and plunge motion are shown for the large amplitude case introduced in Table 7.1. The frequency spectrum that is excited by the generically constructed signals is also depicted in Figure 7.14. The defined test scenario, which is referred to as the generic vibration case in the following, offers an increased challenge for the reduced-order models compared to the harmonic excitation study due to the necessity of predicting multiple amplitude and frequency regimes within a single simulation.

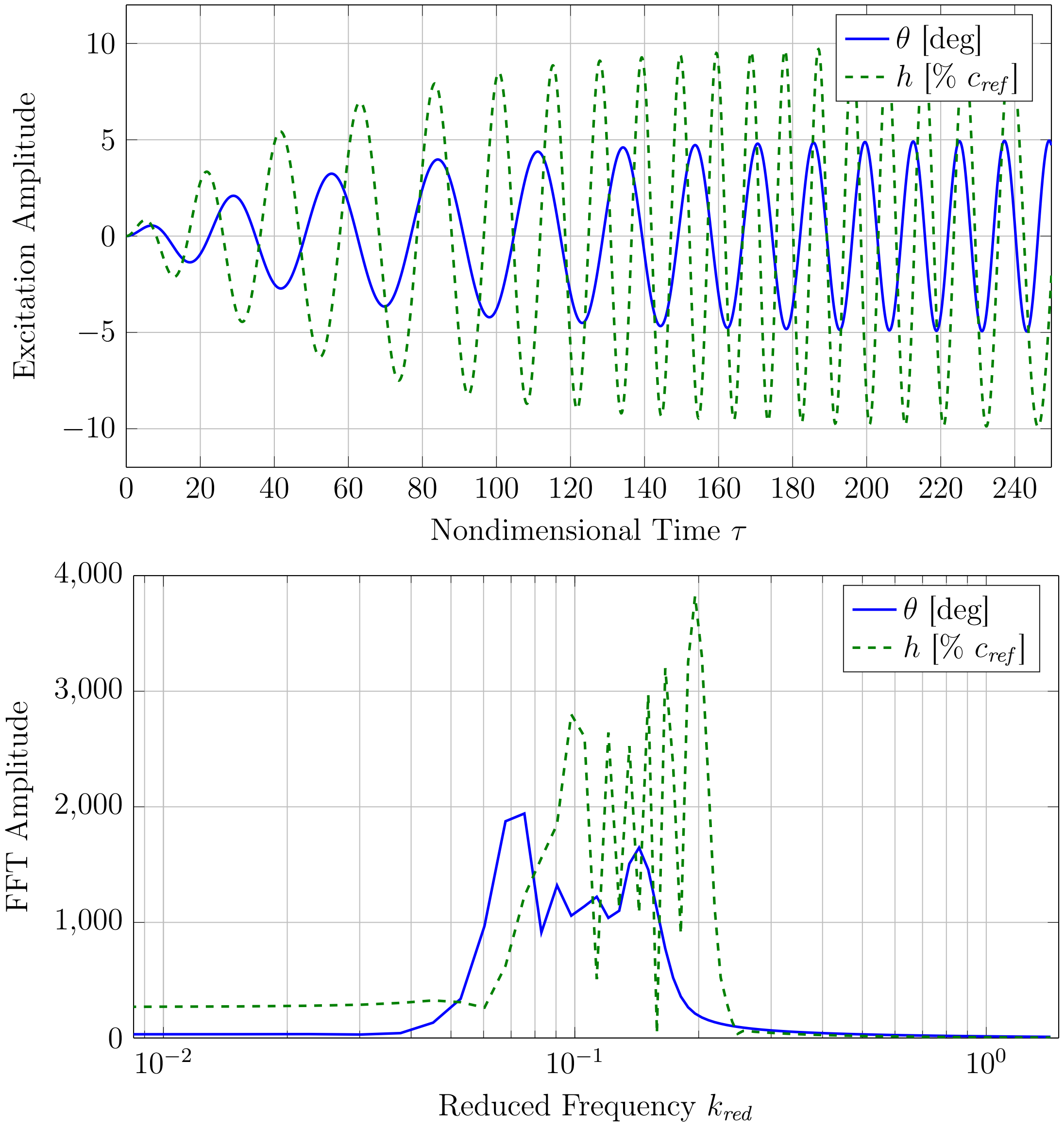

Figure 7.14: The generic vibration signals for the pitch and plunge excitation (top) are shown along with the corresponding frequency spectrum (bottom). Exemplarily, the large amplitude (LA) case is depicted.

Similar to the procedure followed in Section 7.5, the four ROM approaches (ARX, NFM, MLP, NFM-MLP) have been employed to simulate the aerodynamic responses caused by the prescribed generic vibration inputs for the SA, MA, and LA cases. In this regard, also the Monte-Carlo application methodology has been carried out yielding the mean and the standard deviation of the respective ROM outputs. Additionally, the aerodynamic force and moment coefficients have been computed with the AER-Eu solver for the same excitation inputs to provide the reference results.

Figure 7.15 depicts the aerodynamic response in terms of the lift coefficient due to the large-amplitude generic vibration excitation, while the results originating from the ROM/ARX, ROM/NFM, and ROM/NFM-MLP approaches are juxtaposed to the respective CFD-based reference solution. Aside from the time-domain response, also the frequency spectrum with respect to C_L is presented in Figure 7.15. For the same case, Figure 7.16 displays the pitching moment coefficient response. Based on these graphs it becomes evident that the global linear model (ROM/ARX) features the largest discrepancies relative to the CFD reference. While the aerodynamic response computed by the ROM/NFM approach deviates slightly from the AER-NS solution, the mean ROM/NFM-MLP output matches the reference almost perfectly. The visually obtained impressions can be underpinned by the fit factors Q which are listed in Table 7.3 for the LA generic vibration case.

Table 7.3: Fit factors evaluated for the large-amplitude generic vibration test.

Fit factor Q	C_L	C_{M_y}
ROM/ARX	85.74%	81.17%
ROM/NFM	95.80%	88.04%
ROM/MLP	80.05%	30.56%
ROM/NFM-MLP	96.13%	92.81%

In contrast to the three ROM approaches shown in Figures 7.15 and 7.16, the recurrent MLP neural network leads to an unstable model behavior concerning C_{M_y}. The instability, which is indicated by means of Figure 7.17 for the large amplitude case, manifests itself by an abruptly increased standard deviation. Aggravating is the fact that the higher output variance also deteriorates the accuracy of the mean response as it can be seen in Figure 7.17. Hence, the reliability and precision of individual ROM/MLP models is low for the present case. This characteristic cannot be improved by a Monte-Carlo-based averaging over several model outputs. Nevertheless, the fit factors for the medium-amplitude generic vibration case given in Table 7.4 indicate that a good agreement might be obtained by the ROM/MLP for certain cases.

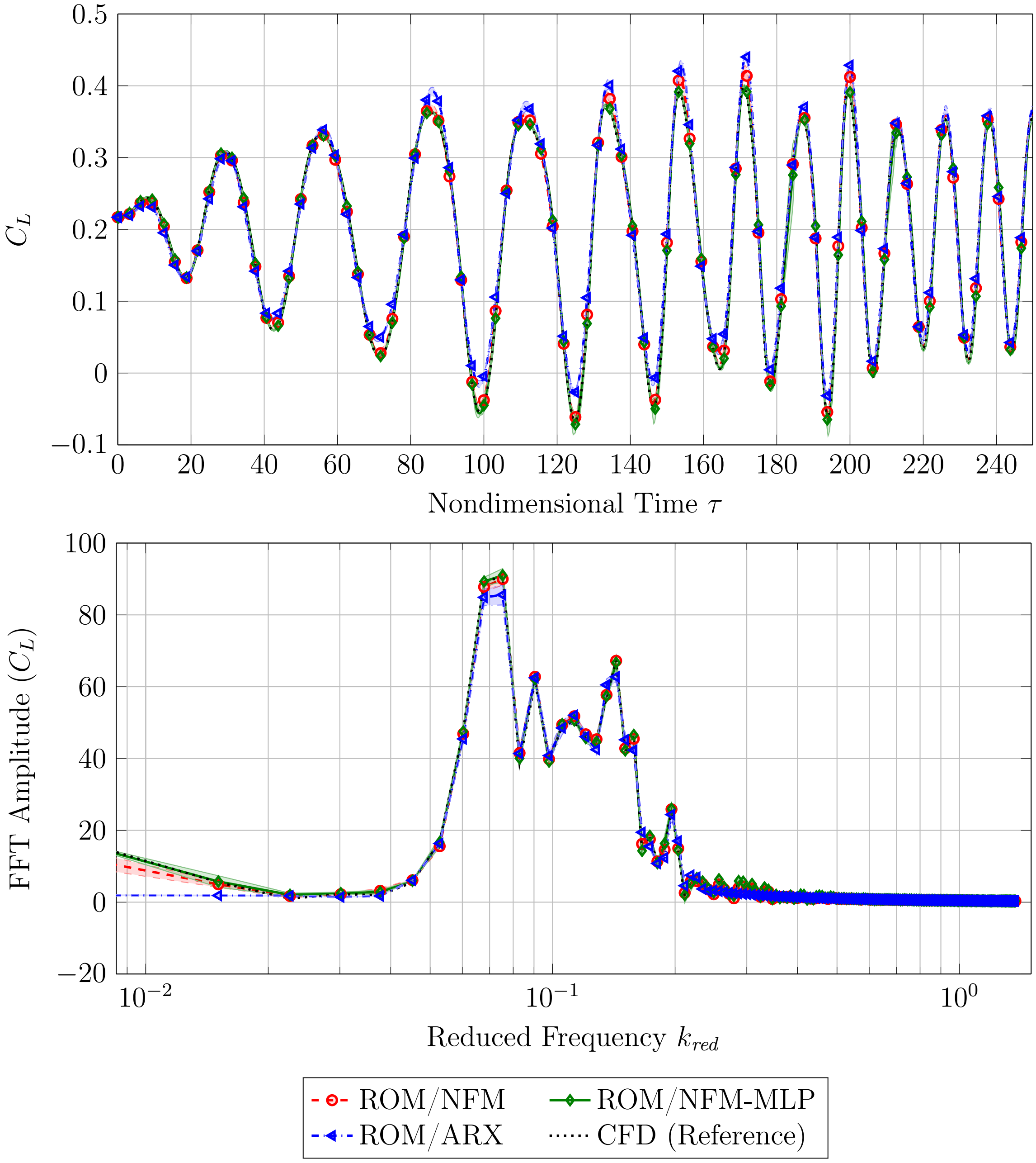

Figure 7.15: The lift coefficient response (top) and the associated fast Fourier transform amplitude of C_L (bottom) is shown for the large-amplitude generic vibration excitation. NLR 7301, $Ma_\infty = 0.753$, $\alpha = 0.6°$.

Considering the ROM-based C_L responses for the small-amplitude generic vibration case presented in Figure 7.18, equivalent conclusions can be drawn relative to the small-amplitude harmonic excitation tests examined in Section 7.5. Based on the SA case results, it is clearly shown that the proposed ROM/NFM-MLP methodology provides a significantly better solution quality in contrast to the established reduced-order models. This statement can be substantiated by the fit factors for the small-amplitude generic vibration test given in Table 7.5. Besides the superior accuracy of the mean ROM results, the responses predicted by the ROM/NFM-MLP models are characterized by a considerably smaller variance in contrast to the outputs computed by the ROM/NFM models.

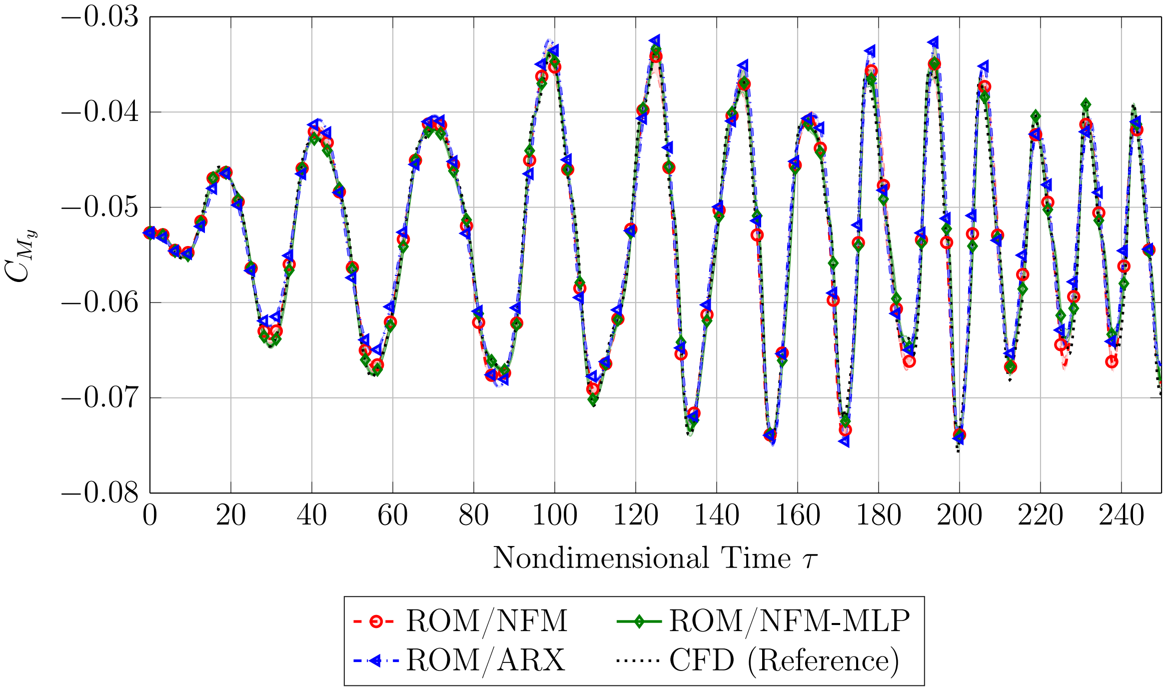

Figure 7.16: The pitching moment coefficient response is presented for the large-amplitude generic vibration excitation. NLR 7301, $Ma_\infty = 0.753$, $\alpha = 0.6°$.

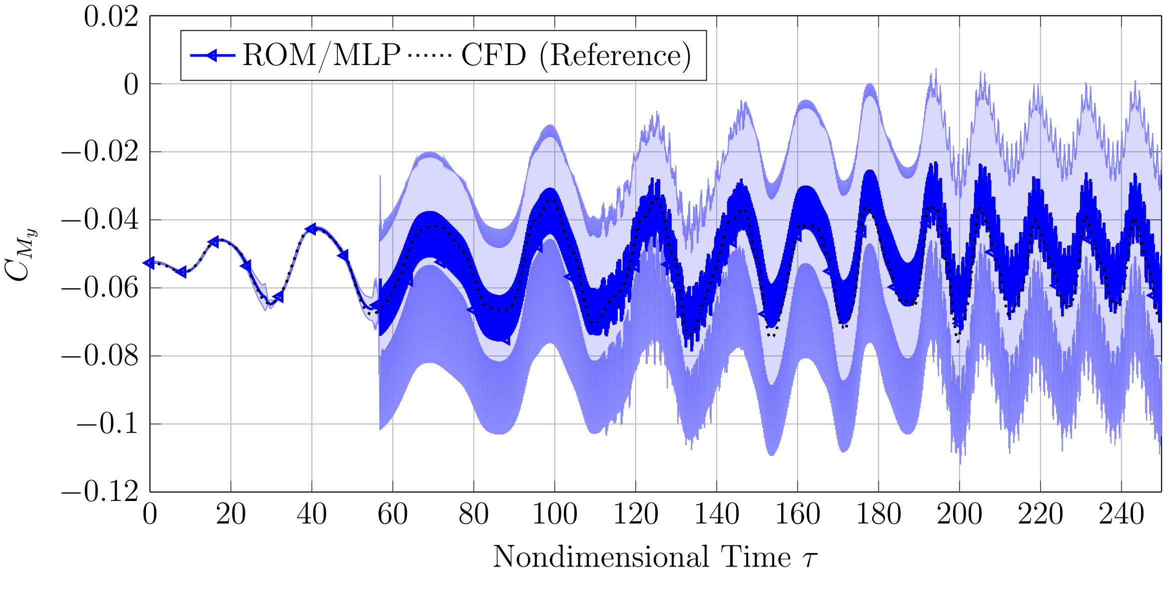

Figure 7.17: Exemplary results of unstable ROM/MLP models by means of the C_{M_y} response induced by the large-amplitude generic vibration test. NLR 7301, $Ma_\infty = 0.753$, $\alpha = 0.6°$.

From the discussed observations, it can be stated that the robustness and reliability is drastically increased by the novel connected neural network approach.

In order to conclude these investigations, the effect of a static equilibrium variation is taken into account. In this regard, the initial angle of attack, which has been fixed to $\alpha = 0.6°$ for all previous considerations, is increased to $\alpha = 2°$ for demonstrative purposes. This can be geometrically realized by adding a constant offset of $\Delta\theta = 1.4°$ to the

Table 7.4: Fit factors evaluated for the medium-amplitude generic vibration test.

Fit factor Q	C_L	C_{M_y}
ROM/ARX	88.82%	79.88%
ROM/NFM	95.99%	91.21%
ROM/MLP	88.71%	93.95%
ROM/NFM-MLP	96.08%	93.86%

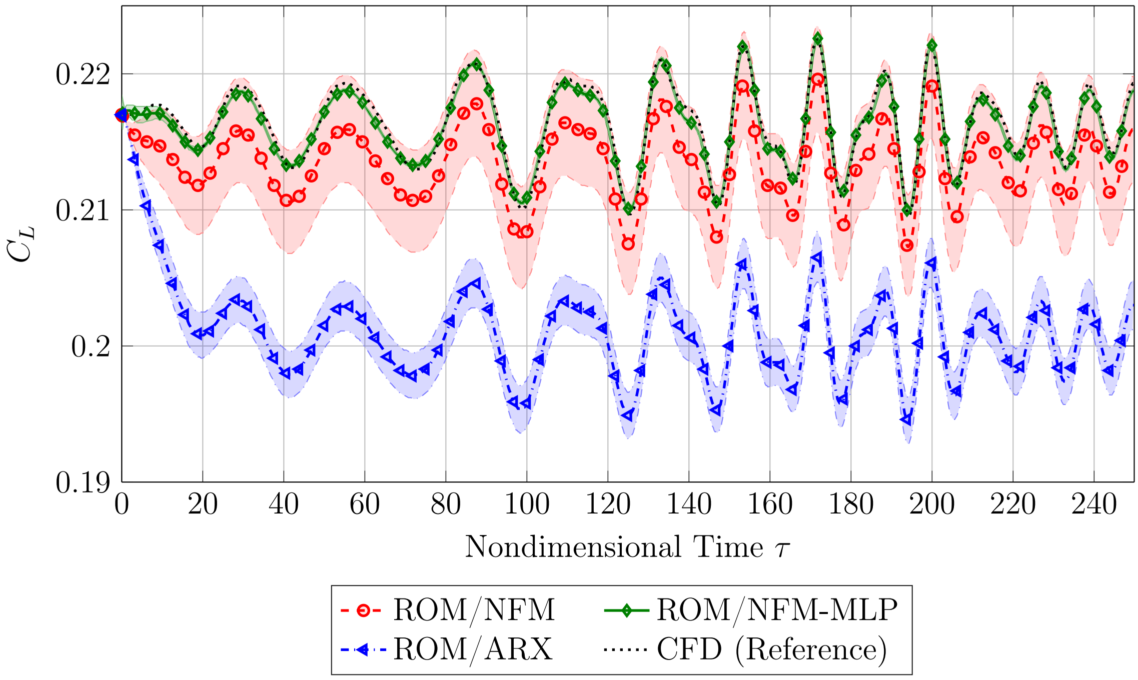

Figure 7.18: The lift coefficient response is plotted for the small-amplitude generic vibration excitation. NLR 7301, $Ma_\infty = 0.753$, $\alpha = 0.6°$.

pitch excitation signals. Consequently, the extrapolation behavior of the reduced-order models can be assessed since the involved maximum pitch amplitude ($\theta_{max} = 6.4°$) clearly exceeds the input range defined by the training data ($-5.5° \leq \theta \leq 5.5°$). Nonetheless, it is worth to highlight that the already available ROMs described by Section 7.4 are used for this additional study. Hence, no further model training effort is necessary for investigating the changed static equilibrium. In contrast, additional AER-Eu reference computations have been undertaken to provide the respective verification results.

In Figure 7.19, the lift coefficient response induced by the medium-amplitude generic vibration excitation is shown for the angle of attack of $\alpha = 2°$. For all ROM simulations presented in this chapter, the starting values needed for the recurrence framework initialization have been taken from the known steady-state at $\alpha = 0.6°$. Thus, the lift coefficient has been initialized with $C_L = 0.22$, whereas the pitching moment has been set to $C_{M_y} = -0.053$. As a consequence, the ROM results at $\alpha = 2°$ exhibit an initialization error. Nevertheless, as it can be seen by the graphs in Figure 7.19, the initial error does

Table 7.5: Fit factors evaluated for the small-amplitude generic vibration test.

Fit factor Q	C_L	C_{M_y}
ROM/ARX	N/A	15.55%
ROM/NFM	N/A	21.72%
ROM/MLP	82.78%	23.67%
ROM/NFM-MLP	84.82%	48.11%

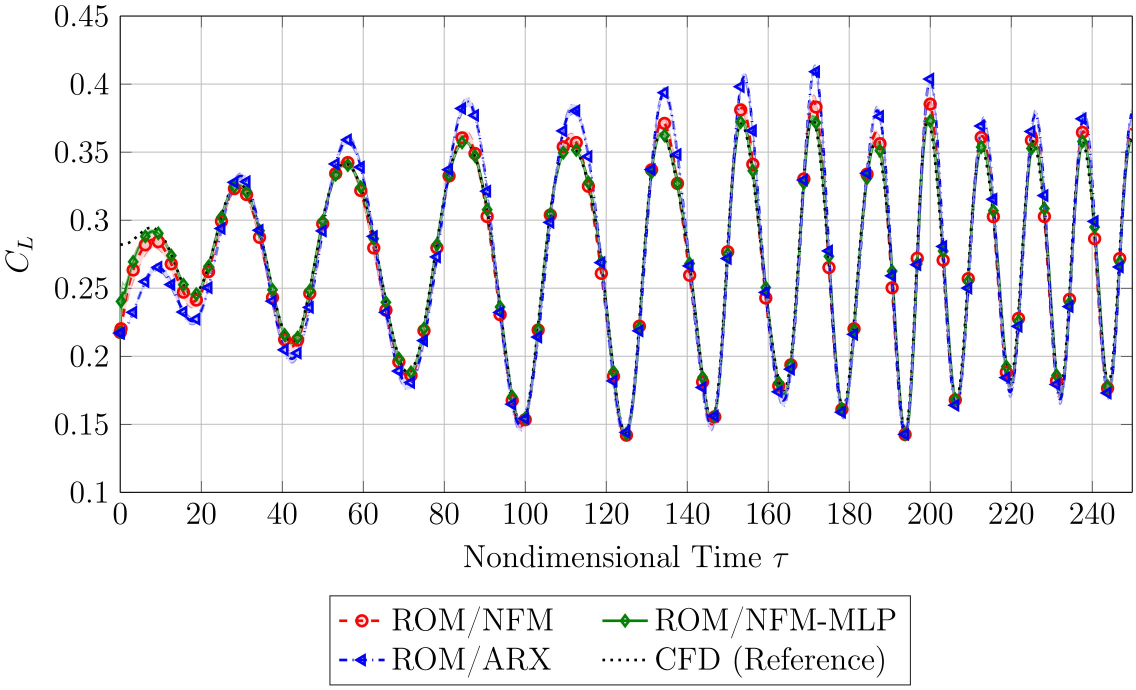

Figure 7.19: The lift coefficient response is presented for the medium-amplitude generic vibration excitation. The initial angle of attack is increased to $\alpha = 2°$ to investigate the generalization capabilities of the ROMs. NLR 7301, $Ma_\infty = 0.753$, $\alpha = 2°$.

not affect the long-term simulation quality. Whereas the ROM/MLP (not represented in Figure 7.19) yields an unstable response for the MA generic vibration case at $\alpha = 2°$, the respective ROM/ARX and ROM/NFM results exhibit a satisfying and good accordance with the CFD solution. Except from the discrepancies due to the inconsistent simulation start, the ROM-NFM-MLP result agrees very well with the AER-Eu solution.

Finally, focusing on the large amplitude generic vibration case at $\alpha = 2°$, the aforementioned trend can be confirmed by means of the fit factors that are summarized in Table 7.6. Although the occurring maximum pitch angle of $\theta_{max} = 6.4°$ is well beyond the trained pitch angle regime, the ROMs show a remarkably well performance as it can be proven by Figure 7.20. Apart from the justified initialization errors and an increased standard deviation related to the generalization operation, the responses provided by

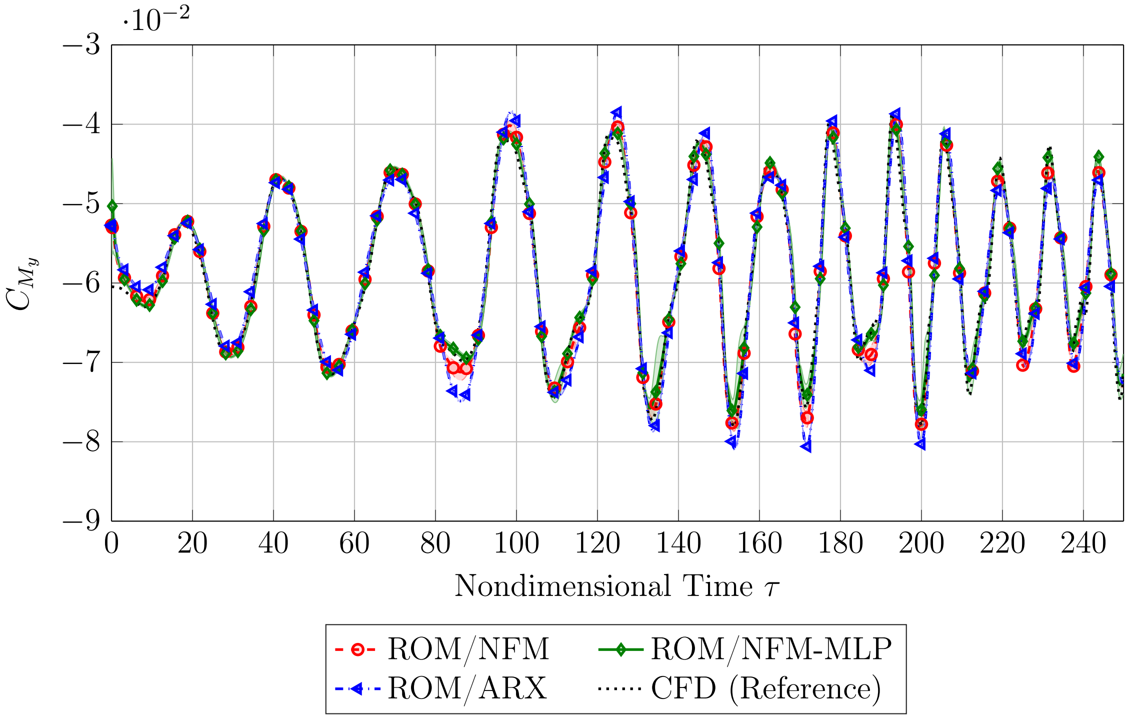

Figure 7.20: The pitching moment coefficient response is shown for the large-amplitude generic vibration excitation. The initial angle of attack is increased to $\alpha = 2°$ to investigate the extrapolation capabilities of the ROMs. NLR 7301, $Ma_\infty = 0.753$, $\alpha = 2°$.

the ROM/NFM-MLP method reflect the behavior of the underlying aerodynamic system very well. By performing a cumulative analysis incorporating all conducted tests and ROM approaches, the superior agreement of the ROM/NFM-MLP results with the CFD reference is clearly confirmed. By means of the given examples, it has been shown that the new identification strategy leads to a significantly increased simulation fidelity and reliability concerning the prediction of strongly nonlinear aerodynamic characteristics.

Table 7.6: Fit factors evaluated for the large-amplitude generic vibration test with modified static equilibrium conditions ($\alpha = 2°$).

Fit factor Q	C_L	C_{M_y}
ROM/ARX	70.00%	76.18%
ROM/NFM	86.90%	85.60%
ROM/MLP	73.70%	55.26%
ROM/NFM-MLP	94.16%	88.73%

7.7 Efficiency Evaluation

Last but not least, the computational advantage of the connected-neural-network-based reduced-order modeling approach is analyzed. To ensure comparability, the ROM training and application procedures as well as the AER-Eu computations presented in this chapter have been carried out on a workstation equipped with an Intel Xeon 2.3 GHz processor using a single CPU core.

First, the numerical effort related to the ROM methodologies is outlined. In this regard, the CFD-based training data generation has required 26.6 CPU hours for the computation of the SAPRBS-forced pitch and plunge motions. Keeping in mind the 82,000 time steps of the signals depicted in Figure 7.5, an average cost of 1.17 CPU seconds per physical time step is determined.

Furthermore, the training effort for the different ROM architectures is summarized below. On the one hand, the training-related computation times for all $N_{MC} = 25$ models are given in Table 7.7. On the other hand, the averaged training time for each individual model is additionally shown due to its practical significance.

Table 7.7: Breakdown of the training costs for the considered reduced-order models.

Training effort	Total time ($N_{MC} = 25$ models) [CPU seconds]	Average time per model [CPU seconds]
ROM/ARX	1.52	0.06
ROM/NFM	3,260.92	130.44
ROM/MLP	385.33	15.41
ROM/NFM-MLP	3,753.75	150.15

A graphical representation of the ROM generation costs is provided by Figure 7.21. It should be emphasized that the ordinate in Figure 7.21 is logarithmically plotted to cover the different time scales arising for the CFD simulation and the ROM training procedures. Similar to the conclusions that have been drawn in the previous chapters, the CFD-based training simulation constitutes the main cost driver in terms of the overall ROM generation effort.

Besides the ROM-related training computations, the costs for applying the models towards the simulation of the harmonic oscillation and generic vibration cases must be respected as well. For the sinusoidal pitch and plunge motions, in total 36 simulation cases have been computed. The aforementioned number of simulations is based on two excitation degrees of freedom in combination with three amplitude levels (SA, MA, LA) as well as six reduced frequencies. Additionally, the generic vibration test comprises six simulations due to the consideration of three amplitude scenarios at two different incidence angles. Taking the $N_{MC} = 25$ models for each ROM type into account, the averaged application effort for a single reduced-order model is presented in Table 7.8:

Table 7.8: Averaged computational resources for applying the ROM and CFD approaches to the investigated unsteady aerodynamic test cases.

Application case	Approach	Computation time [CPU seconds]	Effort per time step [CPU seconds]
Harmonic excitations	ROM/ARX	0.30	$1.12 \cdot 10^{-5}$
(3 amplitude scenarios	ROM/NFM	0.99	$3.64 \cdot 10^{-5}$
2 degrees of freedom	ROM/MLP	0.96	$3.60 \cdot 10^{-5}$
6 reduced frequencies)	ROM/NFM-MLP	1.20	$4.48 \cdot 10^{-5}$
	CFD (AER-Eu)	$1.90 \cdot 10^{5}$	3.53
	ROM/ARX	0.17	$1.12 \cdot 10^{-5}$
Generic vibrations	ROM/NFM	0.55	$3.64 \cdot 10^{-5}$
(3 amplitude scenarios	ROM/MLP	0.54	$3.60 \cdot 10^{-5}$
2 angles of attack)	ROM/NFM-MLP	0.67	$4.48 \cdot 10^{-5}$
	CFD (AER-Eu)	$1.77 \cdot 10^{5}$	1.18

For a particular ROM approach, Table 7.8 indicates that the respective computational effort per time step is identical regardless of the considered example. Consequently, the CPU seconds per time step are a suitable measure to assess and compare the ROM performance. For this reason, the application effort per time step has been plotted in Figure 7.22 for the four ROM approaches relative to the ROM/NFM costs. As it can be seen, the ROM/ARX needs about 31% of the computational resources compared to the ROM/NFM model. Although it is more efficient, the ROM/ARX accuracy is only satisfactory for the present nonlinear test cases according to the discussions in Sections 7.5 and 7.6. In comparison to the ROM/NFM approach, the ROM/NFM-MLP model requires only 23% more computation time, while the fidelity and robustness is significantly increased. Since the ROM application is performed within a few seconds for typical application cases, the slightly increased ROM effort per time step does not represent a veritable restriction for the connected neural network methodology.

In contrast to the ROM costs discussed beforehand, the numerical effort for computing the CFD reference results is also depicted in Table 7.8 with respect to the identical test cases. It becomes evident that the AER-Eu solver requires approximately 10^5 times more CPU resources compared to the available reduced-order models. Consequently, once the ROMs are already trained, they can clearly demonstrate their efficiency advantage.

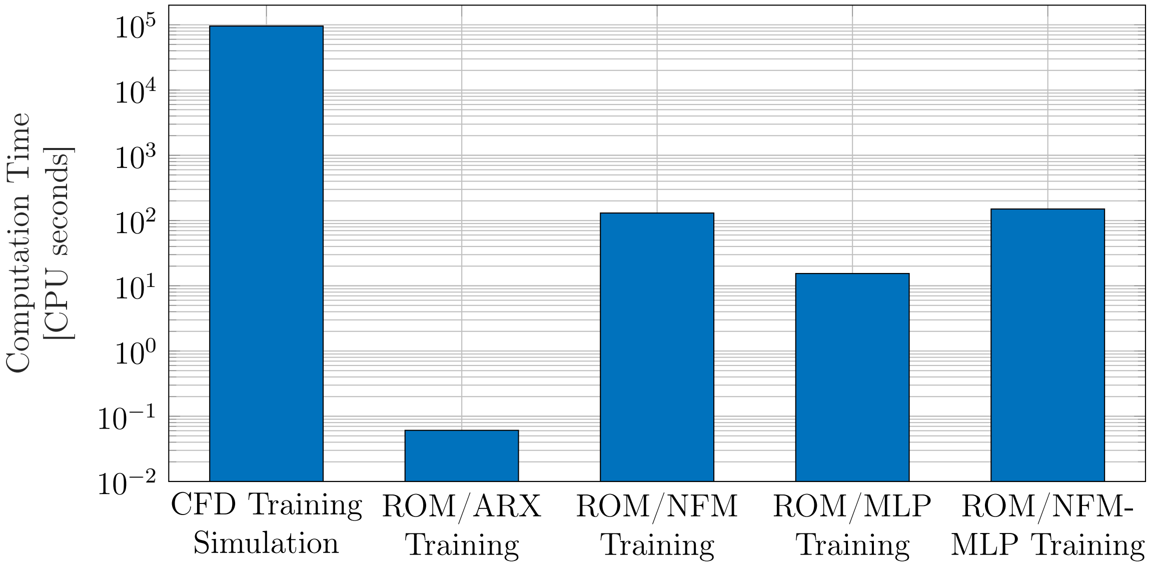

Figure 7.21: Overview of the required computational effort to obtain, on the one hand, the CFD-based training dataset and, on the other hand, the reduced-order models based on given training data. The ROM training effort is shown as the averaged training time for a single model.

Based on the presented efficiency data, the following conclusions can be derived: Taking the total ROM generation and application costs into account, i.e., the CFD training simulation, the model training, and the model application, the following speed-up relative to the underlying CFD solver is achieved for the exemplarily shown cases:

Table 7.9: ROM-based speed-up for the studied unsteady aerodynamic test cases. The Monte-Carlo training and application costs are included. For the single model performance, the application-only speed-up must be multiplied by $N_{MC} = 25$.

	Speed-up (total effort)	Speed-up (application only)
ROM/ARX	3.84	$3.13 \cdot 10^4$
ROM/NFM	3.71	$0.96 \cdot 10^4$
ROM/MLP	3.83	$0.98 \cdot 10^4$
ROM/NFM-MLP	3.70	$0.79 \cdot 10^4$

Keeping in mind that an existing ROM can be used for additional simulations regarding different excitation amplitudes and frequencies, the computational advantage is further increased with each added computation case. In summary, it can be stated that the very high prediction quality and generalization capability of the ROM/NFM-MLP approach in combination with the achieved simulation speed-ups demonstrates the enormous potential of the methodology for accelerating CFD-based aerodynamic analyses.

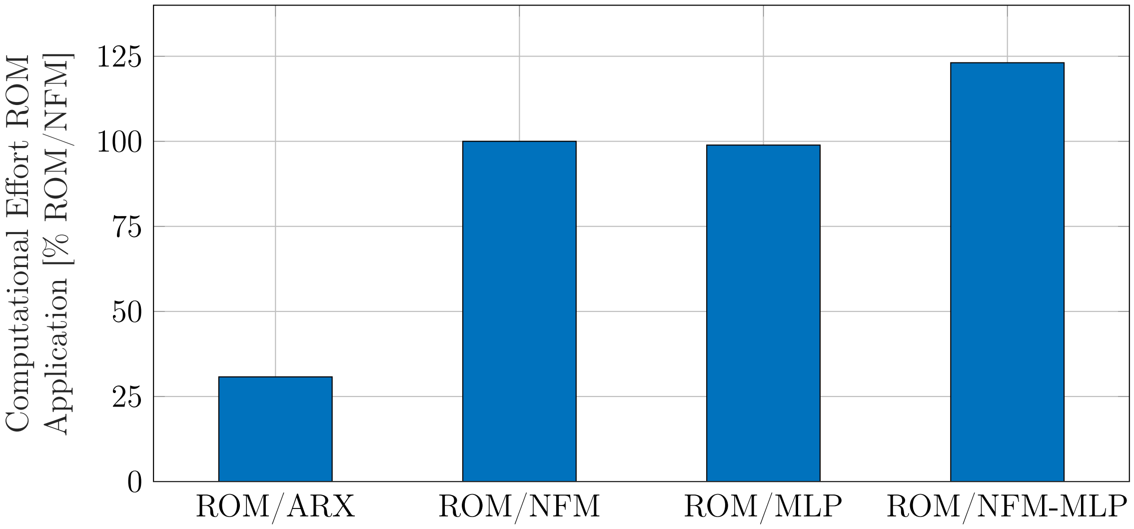

Figure 7.22: Comparison of the computational costs for the application of different reduced-order modeling approaches. The numerical effort is given in percent relative to the ROM/NFM cost. The training data acquisition and ROM calibration is not included in this consideration.

7.8 Summary

For validation purposes, the ROM framework introduced in Section 4.3, which has been developed to model strongly-nonlinear system characteristics, was applied in this chapter to simulate the pitch and plunge induced aerodynamic responses of the NLR 7301 airfoil. The methodology was based on the series connection of a recurrent local linear NFM and a MLP neural network in order to achieve advantageous simulation and generalization properties. Based on test cases at transonic flight conditions, it was pointed out that the forces and moments caused by prescribed motions can be accurately predicted by the ROM/NFM-MLP. Moreover, it was shown that the connected neural network is well-suited for reflecting both linear and nonlinear system dynamics using a single model, which is a known challenge for established reduced-order models. Finally, by considering model inputs beyond the regime from which the ROM has been trained, the results indicated the improved generalization capabilities related to multi-step ahead time series predictions. A comparison with other ROMs clearly underpinned the superior agreement of the ROM/NFM-MLP solutions with respect to the CFD reference. Besides the overall very good prediction quality, the developed methodology was demonstrated to achieve significant numerical cost savings as well. Consequently, an overall robust and accurate unsteady aerodynamic modeling framework is available for multidisciplinary operation and computationally demanding applications.

8 ROM Application Towards Realistic Aircraft Configurations

In the preceding chapters, the developed reduced-order modeling approaches have been applied to exemplary test cases to verify the function and effectiveness of the neuro-fuzzy-model-based methodologies. The test cases, however, have been chosen to exhibit a simple to moderate level of complexity in order to allow a clear and focused investigation of the ROM capabilities. Nonetheless, the application of the ROM procedures to problems with a considerably increased number of degrees of freedom cannot a priori be considered as straightforward without further verification. The proposed techniques are therefore applied in this chapter to a complex aircraft configuration test case to indicate their potential for industrial purposes. In particular, the neuro-fuzzy-model-based ROM approach applicable to freestream parameter variations discussed in Section 4.1 and the POD-ROM procedure outlined in Section 4.2 are employed to simulate the unsteady aerodynamics of the common research model (CRM) configuration. At this point it should be emphasized that the following results represent a feasibility study with regard to future practical applications of the developed ROM procedures. For this reason, the considered number of structural and aerodynamic degrees of freedom is significantly increased, whereas the degree of nonlinearity is concurrently decreased by taking small perturbation amplitudes into account. The latter measure has been taken in order to limit the overall computational effort. Hence, this chapter is intended to provide an outlook to what extent the neuro-fuzzy model-based ROMs can be generalized to aerospace-industry-relevant scales. The content presented below is based on the pre-publication of the author, Reference [186].

With respect to the presentation of the test case, the numerical set-up, and the results, the chapter is organized as follows: Initially, the common research model configuration is introduced in Section 8.1, while both the aerodynamic and the structural modeling strategies are highlighted. Subsequently, Section 8.2 discusses selected steady-state CFD results at the investigated transonic freestream conditions. The application of the freestream-parameter-adaptive neuro-fuzzy model is undertaken in Section 8.3, while aerodynamic responses due to small-amplitude structural motions are predicted across a variable angle of attack. Furthermore, the POD-ROM approach is employed in Section 8.4 to simulate unsteady surface pressure variations due to eigenmode-based structural excitations. For classification of the ROM accuracy, a comparison with the full-order CFD solution is conducted. Finally, the chapter is concluded by an assessment of the computational efficiency.

8.1 Test Case: Common Research Model (CRM) Configuration

In this section, NASA's common research model configuration is introduced in terms of a description of the main geometric properties as well as the aerodynamic and structural modeling set-up. The CRM configuration, which represents a modern commercial transport aircraft, fulfills the requirement of a considerably increased geometrical complexity compared to the test cases presented in Chapters 5-7. The research model developed by NASA's subsonic fixed wing aerodynamics technical working group in collaboration with the drag prediction workshop (DPW) organizing committee [137, 170, 171] was designed for a transonic cruise condition at $Ma_\infty = 0.85$ in combination with a target lift coefficient of $C_L = 0.5$. The CRM variant investigated in this chapter is the wing/body/horizontal-tail (WBT0) configuration with supercritical wing design that has been in the focus during the fourth AIAA CFD drag prediction workshop [171]. In particular, the horizontal tail with an installation angle of 0° is considered, which leads to the designation WBT0. The important geometrical and reference properties of the CRM configuration are summarized in Table 8.1.

The geometry of the CRM configuration is visualized in Figure 8.1 by means of an isometric view as well as a three-side view. In contrast to the fourth AIAA CFD drag prediction workshop set-up, which focuses on the half model of the configuration, the full-span geometry is investigated in this work to allow time-marching aerodynamic simulations of both symmetric and antisymmetric deflections; see also Section 8.1.2.

Quantity	**Symbol**	**Value**
Reference area	S_{ref}	$383.69\ m^2$
Wing span	b	$58.763\ m$
Wing reference chord	c_{ref}	$7.0053\ m$
Aspect ratio	AR	9.0
Quarter chord sweep angle	$\varphi_{0.25}$	35°
Taper ratio	λ	0.275
Reference point	x_{ref}	$33.68\ m$
	y_{ref}	$0\ m$
	z_{ref}	$4.52\ m$

Table 8.1: Geometric properties of the CRM configuration according to Vassberg et al. [170].

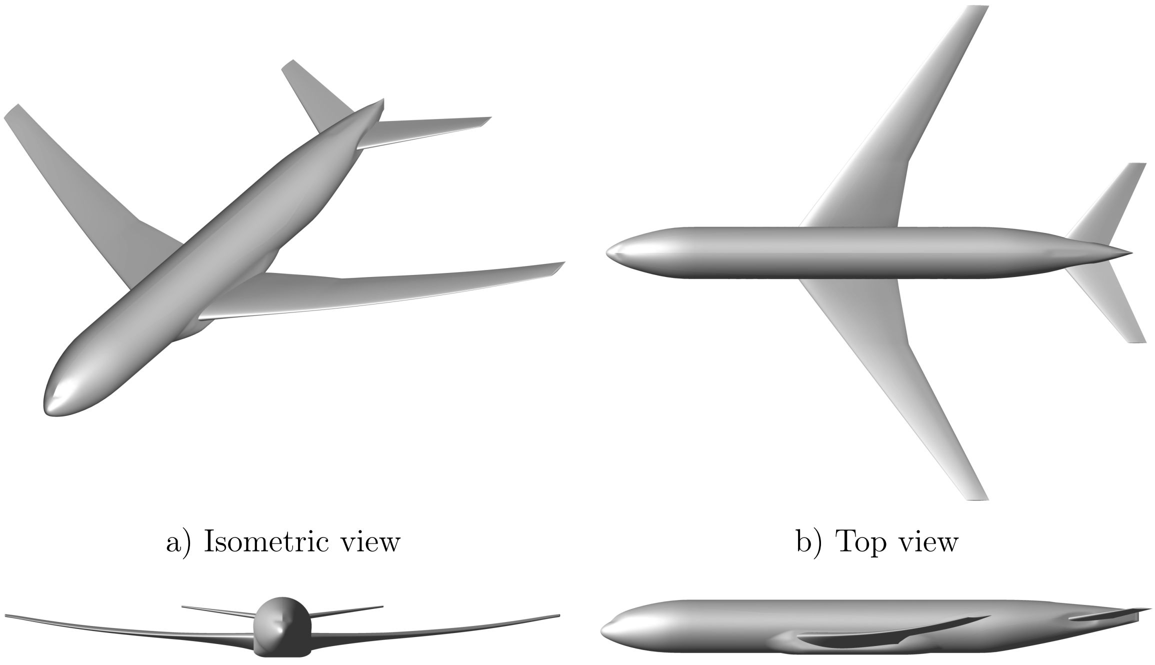
a) Isometric view
b) Top view
c) Front view
d) Side view

Figure 8.1: Geometry of the common research model (WBT0 configuration). In contrast to the DPW4 set-up, a full-span model is investigated in this work to take both symmetric and antisymmetric mode shapes into account.

8.1.1 Aerodynamic Modeling and Grid Sensitivity Analysis

As a prerequisite for the CFD computations, a structured multi-block grid has been generated using the commercial meshing software ANSYS ICEMCFD [2]. For simulating free-flight flow conditions, the aircraft has been embedded within a spherical domain with a radius of twenty semi-spans to prevent non-physical interactions between the farfield boundary and the nearfield flow around the aircraft. For the reasoning of a manageable computing effort, the Euler-equations-based AER-Eu solver is used in this chapter. Associated to the inviscid modeling, the grid has been refined towards the wall with an off-body distance of the first cell height of $5 \cdot 10^{-4}\ c_{ref}$. Moreover, a grid sensitivity study has been conducted to guarantee the solutions' independence from the spatial resolution. For this purpose, however, not the full-span aircraft but the half-model of the CRM configuration is taken into account since no lateral motion sensitivities are analyzed within the grid study. Starting from a baseline/medium grid level containing 2,932,376 finite volume cells, the number of cells has been reduced and increased by a factor of 2 yielding the respective coarse and fine grid refinement levels. In Figure 8.2, the coarse and the fine half-model grids are represented by the CRM surface and symmetry plane mesh.

In Figure 8.3, the lift and pitching moment coefficients obtained by steady AER-Eu simulations are depicted for the coarse, medium, and fine grid refinement levels. In this regard, a freestream condition characterized by $Ma_\infty = 0.85$ and $\alpha = 1°$ is taken into

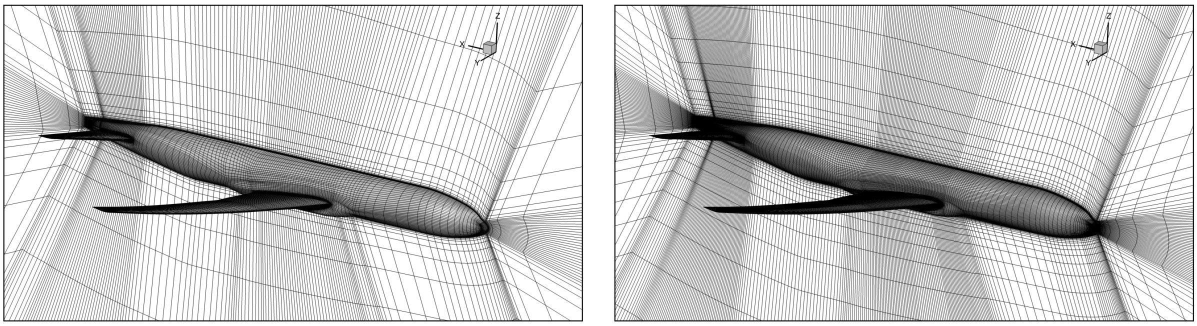

a) Coarse grid (1,425,880 cells) b) Fine grid (5,834,046 cells)

Figure 8.2: Structured surface discretization visualizing the coarse and fine grid refinement levels of the semi-span CRM configuration (WBT0).

account, which leads to a lift coefficient close to the design C_L using the inviscid CFD solver. Relative to the medium grid level, the CFD result obtained from the coarse grid yields a difference in the lift coefficient of -2.9%, whereas a discrepancy of +10.3% is ascertained for C_{M_y}. In contrast, the deviation of C_L between the fine grid and the medium grid is merely +0.8%, while the pitching moment deviates by -3.3%. On the basis of the mesh sensitivity analysis, it is concluded that the medium grid realizes an adequate compromise between the quality of the aerodynamic solution and the anticipated computational costs.

The aforementioned medium-level semi-span grid of the CRM configuration (2,932,376 finite-volume cells) has been used, on the one hand, by Rozov et al. [139] in order to validate the novel antisymmetric boundary condition for small disturbance CFD solvers. On the other hand, the semi-span grid has been mirrored around the aircraft's symmetry plane ($y = 0$) to obtain the full-span grid for the present investigations.

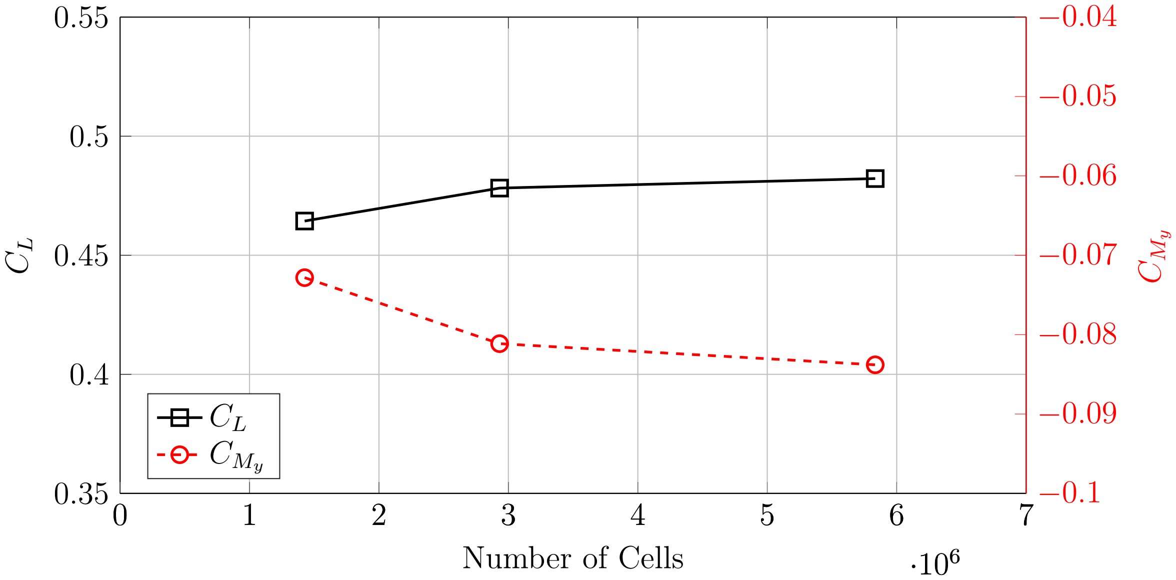

Figure 8.3: The steady-state lift (C_L) and pitching moment (C_{M_y}) coefficients are shown as a function of the computational grid resolution for the CRM semi-span model. $Ma_\infty = 0.85$, $\alpha = 1°$, AER-Eu.

The full-span reference grid of the CRM configuration, which is employed for all further CFD simulations discussed in this chapter, is shown in Figure 8.4 by means of the surface mesh as well as the blocking concept. The grid contains a total of 5,864,752 finite volume cells, whereas the aircraft's surface is resolved by $N_{SE} = 67{,}856$ elements.

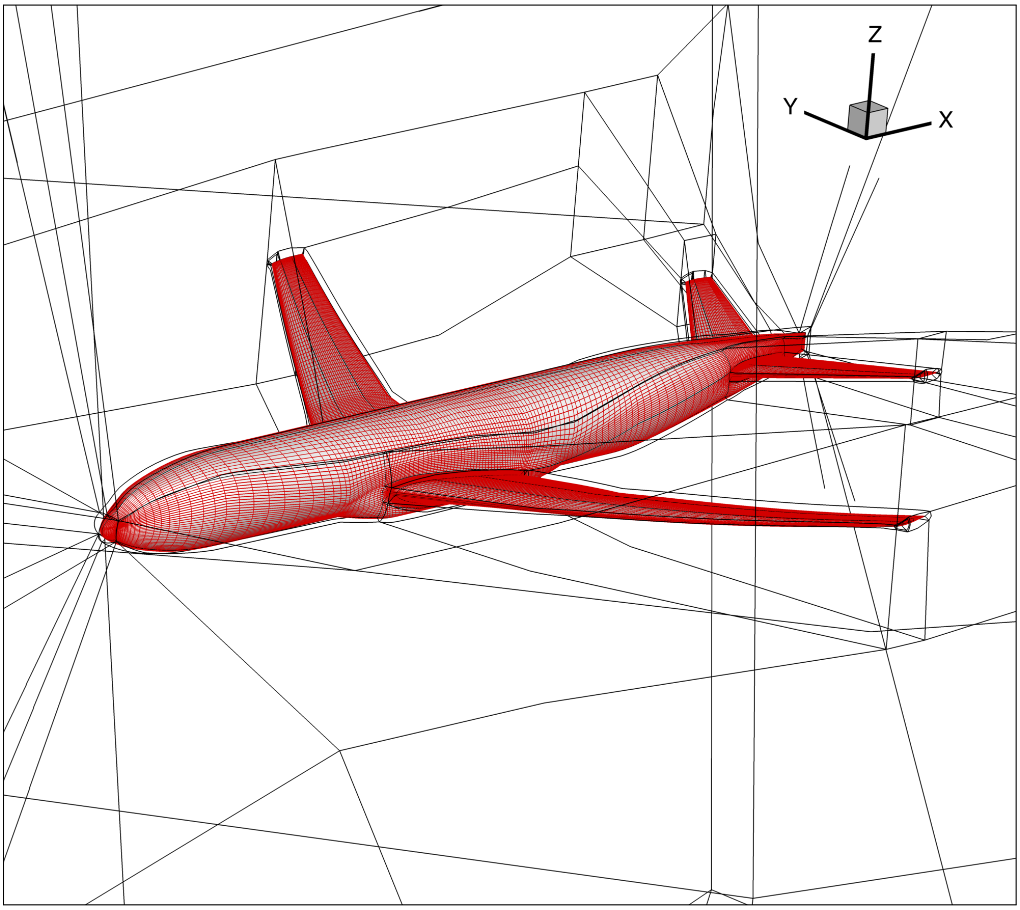

Figure 8.4: The block-structured grid of the full-span CRM configuration involves 5,864,752 cells, while the surface is resolved by 67,856 surface elements.

8.1.2 FERMAT Structural Model

For the structural modeling, the FERMAT configuration introduced by Klimmek [79] is utilized. The associated parametric finite element model was developed to obtain an academic test case on the basis of the CRM geometry for performing static and dynamic aeroelastic investigations. With respect to unsteady aerodynamic and aeroelastic tool chain validation purposes, the generic CRM-FERMAT test case was already suggested by Voss and Thormann [175]. The FERMAT model was configured for two mass set-ups, namely the C1 case representing the maximum zero fuel weight (MZFW) configuration as well as the C2 case typifying the maximum take-off weight (MTOW) with 100% fuel. Within the scope of this work, only the C2 mass configuration is taken into account.

The condensed finite element model of the FERMAT configuration is visualized in Figure 8.5a. However, by confronting the structural model with the aerodynamic model

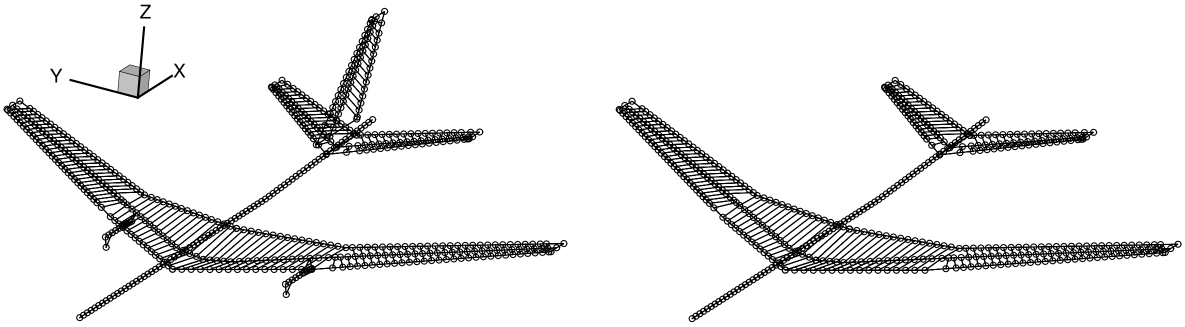

a) FERMAT finite-element model [79] b) FE nodes for surface interpolation

Figure 8.5: Condensed structural model of the FERMAT configuration. The C2 mass case is considered in this work.

discussed in the previous section, it becomes evident that the FE model includes nodes for the vertical tail (VT), pylons, and engines, whereas these components are not present within the CFD mesh. Consequently, the finite element model nodes associated to the VT, pylons, and engines are not considered for the surface interpolation between the structural grid and the aerodynamic surface grid; see Figure 8.5b for clarification.

In the course of this chapter, neither static aeroelastic deformations nor trimming is taken into account. Although the consideration of the aforementioned effects leads to a more realistic modeling of the overall aircraft and is necessary within an industrial context, they are not important for the anticipated ROM validity studies. In this way, a generic ROM test case is obtained, whereas the modeling strategy is kept as simple as possible. For clarification, the aim followed here is not the comparison between different CFD solvers, aeroelastic modeling approaches, or a fit evaluation exploiting experimental data but to provide a clean reduced-order model testing framework. Therefore, many challenging aspects have been incorporated within this generic test case, e.g., the presence of realistic structural eigenmodes, the necessity to model a wide range of excitation frequencies, the consideration of both symmetric and antisymmetric motions, and the occurrence of aerodynamic nonlinearities in terms of pronounced shocks along the wingspan.

Given the baseline CFD grid of the CRM configuration shown in Figure 8.4 as well as the FERMAT database including the non-deformed structural model and the elastic mode shapes, the interpolation of the modal deflections onto the surface grid has been achieved via the TPS method. Moreover, the arc-length-based TFI has been applied to adapt the block-internal grid points to the updated surface geometry [41]. Regarding the FERMAT C2 configuration, in total 56 modes have been provided including six rigid body and 50 elastic eigenmodes [79]. For ROM demonstration purposes, however, a subset of the entire dataset is defined consisting of six elastic modes. Thereby, the focus has been put on the consideration of dominant symmetric and antisymmetric wing and/or horizontal tail modes as well as fuselage modes, whereas mode shapes with dominant

VT or nacelle deflections have been excluded. In Figure 8.6, the six considered mode shapes are shown by means of TPS-deformed surfaces.

Elastic mode 1, $f = 1.057\ Hz$,
Symmetric wing bending

Elastic mode 2, $f = 1.455\ Hz$,
Antisymmetric wing bending

Elastic mode 11, $f = 3.603\ Hz$,
Symmetric wing/htp bending

Elastic mode 13, $f = 4.930\ Hz$,
Antisymmetric wing fore/aft

Elastic mode 19, $f = 7.342\ Hz$,
Antisymmetric wing/htp bending

Elastic mode 24, $f = 10.602\ Hz$,
Symmetric wing torsion

Figure 8.6: The selected structural-eigenmode-based surface deformations of the FERMAT-C2 configuration (red) are presented relative to the non-deformed aircraft geometry (grey). For a clearer presentation, exaggerated deflections are shown.

In contrast to the exaggerated deflections visualized in Figure 8.6, the actual deformations have been scaled to small perturbation amplitudes for the intended numerical computations. With the definition of $\Delta x = x_{def} - x_{ref}$, $\Delta y = y_{def} - y_{ref}$, and $\Delta z = z_{def} - z_{ref}$ between the deformed grid and the reference grid coordinates, the requirement $\max(\sqrt{\Delta x^2 + \Delta y^2 + \Delta z^2})_{x,y,z} = 0.1\%\ c_{ref}$ has been verified for the present case to yield a dynamically linear behavior between the deflections and the aerodynamic response in the context of the unsteady CFD modeling. The restriction to small disturbances has been necessary, on the one hand, to limit the computational costs of the time-marching CFD simulations and, on the other hand, to demonstrate the application of both the freestream-adaptive ROM and the POD-ROM using the same modeling set-up. Analogously to the discussion in Section 5.1.2, the amplitude scaling of the mode-shape-related deflections requires the consideration of scaling factors SF to ensure consistency between the structural and the aerodynamic model. In Table 8.2, the resulting scaling factors are summarized.

Table 8.2: Scaling factors for the elastic mode shapes of the FERMAT configuration to ensure $\max(\sqrt{\Delta x^2 + \Delta y^2 + \Delta z^2})_{x,y,z} = 0.1\%\ c_{ref}$.

	Mode 1	Mode 2	Mode 11	Mode 13	Mode 19	Mode 24
Scaling factor SF $[10^{-3}]$	6.616	6.386	6.104	15.736	5.030	2.995

8.2 Steady CFD Results: Basis for ROM Training

According to the parameter-adaptive reduced-order modeling procedure outlined in Section 4.1, steady CFD simulations have been carried out with respect to the training freestream conditions. In the context of this chapter, it is defined that the unsteady aerodynamic loads are to be determined for the design lift coefficient of $C_L = 0.5$ at $Ma_\infty = 0.85$. Therefore, the training dataset incorporates the generalized aerodynamic forces time-series for various angles of attack, whereas the freestream Mach number is kept constant. Thus, not Ma_∞ but the angle of attack is the variable freestream parameter within the present investigation in contrast to the studies discussed in Chapter 5. Specifically, the following angles of attack are taken into account for the training dataset: $\alpha_{Trn} = [0.5°, 1.0°, 1.5°, 2.0°]$. For completeness, it should be noted that no sideslip angle has been considered, i.e., $\beta = 0°$.

A priori conducted numerical investigations using the Euler-based aerodynamic modeling showed that an angle of attack of $\alpha_{Sim} = 1.13°$ yields the target lift for the WBT0 configuration. Hence, the angle of attack designated for ROM application is covered by the training conditions spanned by α_{Trn}. In Figure 8.7, the AER-Eu-based steady-state surface pressure coefficient distributions are shown for the $N_{FC} = 4$ training freestream conditions in terms of the upper side of the CRM configuration. Figure 8.7 highlights the increased shock intensity with enlarged angles of attack. Moreover, the transonic nature of the flow at the given freestream conditions is clearly indicated by the C_p distribution.

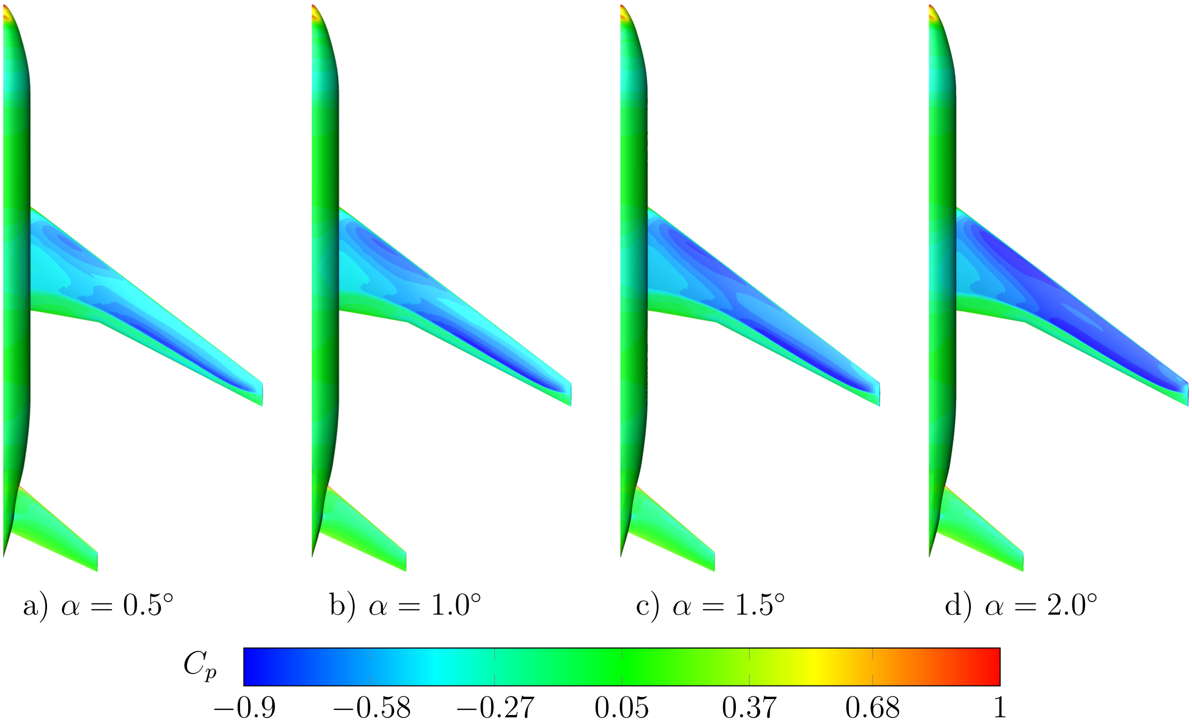
a) $\alpha = 0.5°$ b) $\alpha = 1.0°$ c) $\alpha = 1.5°$ d) $\alpha = 2.0°$

Figure 8.7: The steady-state pressure coefficient contours are depicted for α_{Trn}. For reasons of symmetry, only the starboard side is shown, although the CFD computations have been carried out using the full-span model. CRM configuration (top view), $Ma_\infty = 0.85$, AER-Eu.

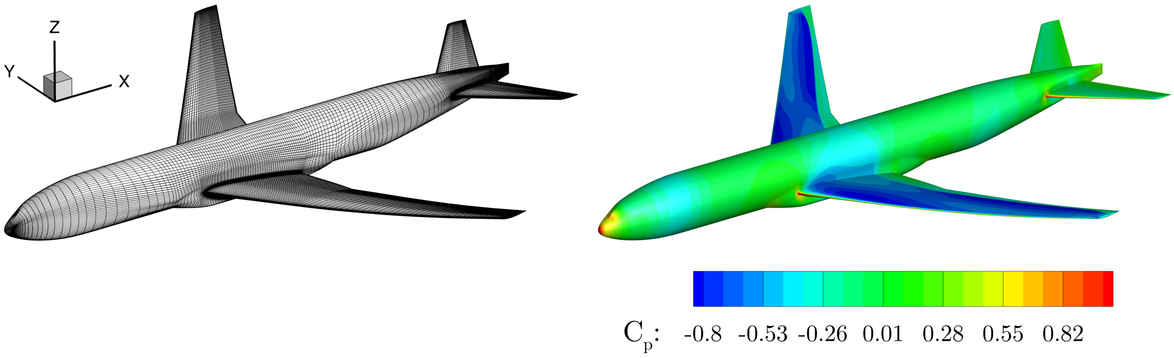

Figure 8.8: Left: Structured surface grid of the CRM-WBT0 configuration. Right: Steady-state C_p distribution at $Ma_\infty = 0.85$ and $C_L = 0.5$ (AER-Eu).

Concerning the application of the POD-ROM methodology at the design freestream condition of the CRM configuration ($Ma_\infty = 0.85$, $C_L = 0.5$), a further AER-Eu simulation at $\alpha = 1.13°$ is required to provide the steady reference state. Figure 8.8 shows the aerodynamic surface grid along with the pressure coefficient distribution for the aforementioned freestream condition. The steady result depicted in Figure 8.8 is the starting point for the unsteady training simulations related to the POD-ROM calibration. Furthermore, the steady AER-Eu solution forms the basis for the comparative CFD simulations, which are needed to assess the accuracy and efficiency of the ROM approaches.

In the subsequent section, the training and application of the freestream-parameter-adaptive neuro-fuzzy model is outlined. The respective discussion related to the POD-ROM procedure is given in Section 8.4.

8.3 Unsteady Results: ROM Valid Across Freestream Parameter Variations

In order to obtain the training data for calibrating the α-adaptive neuro-fuzzy model, forced-motion CFD computations have been carried out for each of the $N_{FC} = 4$ training angles of attack to provide the aerodynamic responses induced by structural-eigenmode-based deflections. For that purpose, the steady AER-Eu simulations presented in the previous section as well as the mode shapes from the FERMAT configuration, which are visualized in Figure 8.6, are adopted. The problem-dependent system inputs and outputs for the underlying test case can be summarized as:

$$\mathbf{u}(t) = \begin{pmatrix} q_1(t) \\ q_2(t) \\ q_{11}(t) \\ q_{13}(t) \\ q_{19}(t) \\ q_{24}(t) \end{pmatrix} \in \mathbb{R}^{n_q}, \qquad \mathbf{y}(t) = \begin{pmatrix} f_{gen,1}(t) \\ f_{gen,2}(t) \\ f_{gen,11}(t) \\ f_{gen,13}(t) \\ f_{gen,19}(t) \\ f_{gen,24}(t) \end{pmatrix} \in \mathbb{R}^{n_f}, \qquad \Xi = (\alpha) \in \mathbb{R} \tag{8.1}$$

In Equation (8.1), q_i symbolizes the ith modal coordinate, whereas $f_{gen,j}$ denotes the time-domain GAF vector element j; see Section 2.2 for further details regarding the structural dynamic and aeroelastic modeling. Based on the discussion in Section 8.1.2, six elastic mode shapes have been exemplarily selected in order to model the structural behavior of the CRM configuration. As a consequence, the dimension of the vectors $\mathbf{u}$ and $\mathbf{y}$ is $n_q = n_f = 6$. Besides, the angle of attack serves as the scalar, time-invariant parameter Ξ.

Concerning the excitation of each mode shape, the smoothed amplitude-modulated pseudo-random binary signal (SAPRBS) depicted in Figure 8.9 has been chosen as the training signal; see Section 3.7 for an overview of several excitation signal types. Although a signal for linear identification purposes would be sufficient for the given small excitation amplitudes, the SAPRBS has been selected in order to facilitate a general demonstration of the methodology. The SAPRBS displayed in Figure 8.9 has been normalized within the range of $[-1, 1]$. However, similar to the approach outlined in Chapter 5, the maximum deflection amplitude for each modal coordinate coincides with the respective scaling factor SF presented in Table 8.2.

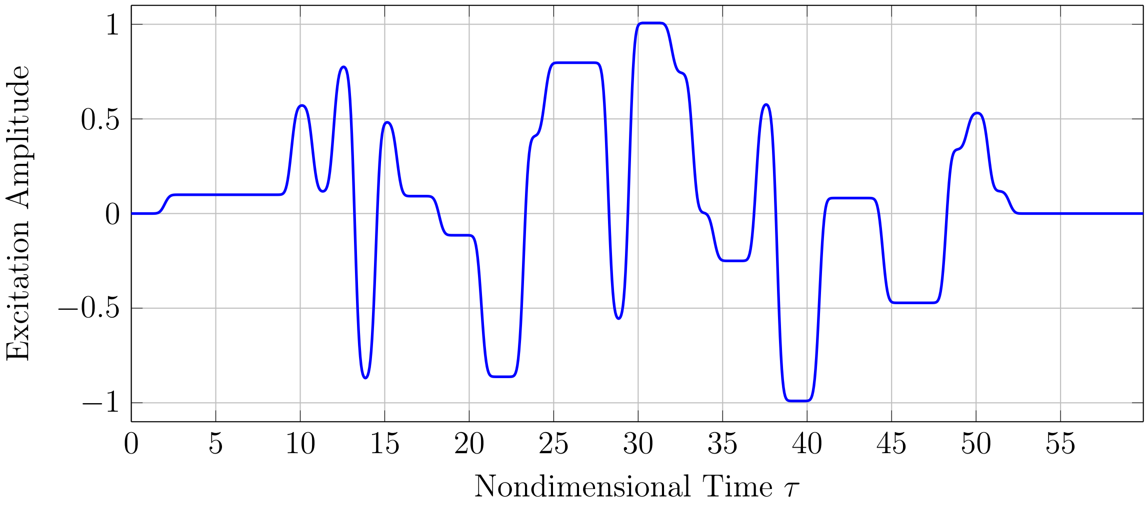

Figure 8.9: SAPRBS containing 1,200 samples for the forced-motion excitation of the structural degrees of freedom of the CRM-FERMAT configuration. The shown signal is normalized in the interval $[-1, 1]$, whereas a nondimensional time step size of $\Delta\tau = 0.05$ is prescribed.

Due to encountered random-access memory overflows in terms of the POD-based post-processing, each mode shape has been excited within a separate AER-Eu simulation in order to limit the amount of data prior to the singular value decomposition. This modus operandi is also followed here for convenience, although the generalized aerodynamic forces are not processed by the POD.

Within the 24 unsteady CFD simulations[1], the instantaneous pressure-based forces are integrated over the aircraft's surface and weighted with the considered mode shapes to obtain the time-discrete generalized aerodynamic force coefficients. Nevertheless, for consistency reasons, each vector element of $\mathbf{f}_{gen}$ is further multiplied by the inverse of the corresponding scaling factor SF; cf. Table 8.2. Due to the consideration of small-amplitude deflections, this re-scaling procedure is mathematically justified. Originating from the discrete time step size of $\Delta\tau = 0.05$ for the signal shown in Figure 8.9, 1,200 training samples are obtained for each combination of α_{Trn} and q_i.

---

[1] The total number of AER-Eu training simulations results from the six structural degrees of freedom in combination with the four training freestream conditions.

Following the nonlinear identification procedure discussed in Chapter 3, the local linear model tree algorithm has been executed to calibrate the freestream-condition-adaptive ROM on the basis of the available training data. Prior to this step, the dynamic delay-orders have been optimized yielding $m = 8$ and $n = 3$ for the respective generalized coordinate inputs and GAF outputs. For the sake of a simplified presentation, the Monte-Carlo procedure is not applied within the scope of this chapter.

Finally, the neuro-fuzzy model trained for $\alpha_{Trn} = [0.5°, 1.0°, 1.5°, 2.0°]$ is employed to simulate the motion-induced aerodynamic responses at $\alpha_{Sim} = 1.13°$. In Reference [185], for instance, it has been shown that the $\mathbf{GAF}$ matrix known from the classical frequency-domain flutter equation can be constructed by applying harmonic excitations in each generalized coordinate. Exemplarily, this application scenario is adopted here, although the focus in this chapter is exclusively on the unsteady aerodynamics.

It should be noted that the angle of attack associated to the design lift coefficient of the CRM configuration is not explicitly included in the training dataset. Therefore, the adaption capabilities of the neuro-fuzzy model to predict "unknown" freestream parameters can be evaluated. Due to the enormous computational effort that is required for further CFD validation simulations, however, the investigations are limited to a single freestream condition. Nevertheless, the ROM is deemed valid for providing unsteady aerodynamic responses at any angle of attack within the training data range.

Table 8.3: Overview of the reduced frequencies that have been considered with the ROM and the CFD solver for simulating the harmonic responses of the CRM configuration (FERMAT structural model).

k_{red} (ROM/NFM)	0.5	1.0	2.0	3.0	4.0	5.0
k_{red} (AER-Eu)	0.5	1.0	2.0			5.0

In order to demonstrate the ROM's ability to capture a broad range of excitation frequencies, the reduced frequencies listed in Table 8.3 have been taken into consideration for the sinusoidal excitation of the the mode-shape-based deflections. As it is indicated in Table 8.3, six k_{red} have been simulated by the neuro-fuzzy model, whereas a subset of four reduced frequencies has been additionally computed with the AER-Eu solver for validation purposes. To eliminate the influence of the initial transient response on the final aerodynamic solution, three oscillation cycles have been simulated with the ROM as well as the AER-Eu solver. Subsequently, the computed responses have been analyzed exclusively on the basis of the last excitation period.

For allowing a compressed overview of the numerous unsteady results, i.e., the 36 ROM as well as the 24 CFD solutions, the **GAF** matrix representation is chosen here. Therefore, the time-domain generalized aerodynamic force responses have been transferred into the frequency domain by means of a Fourier analysis yielding the complex-valued coefficients GAF_{ij}. For clarification, the matrix element GAF_{ij} symbolizes the first harmonic of the ith generalized aerodynamic force response that is induced by an excitation of the jth modal coordinate. In the following, the real part of the **GAF** matrix is denoted by *Re*, whereas the respective imaginary part is indicated with *Im*.

In Figure 8.10, the complex-valued **GAF** matrix resulting from the discussed modeling approach is visualized for the investigated excitation and generalization degrees of freedom as a function of the reduced frequency. As it can be seen from Figure 8.10, a generally good agreement between the ROM-based solution and the AER-Eu reference is ascertained. The trend of the GAFs across the different excitation frequencies is captured correctly for all mode shapes. In this regard, it is worth to emphasize that the unsteady aerodynamic characteristics caused by the symmetric and antisymmetric deflections as well as bending and torsion mode shapes are adequately reproduced. The good accordance of the responses' magnitude and phase applies, especially, to the diagonal of the GAF matrix. Except from some discrepancies at low excitation frequencies, which can be observed for the real and imaginary parts of $GAF_{24,11}$ and $GAF_{24,19}$ for instance, the neuro-fuzzy model achieves a high accuracy for the underlying aerodynamic simulations. It is important to keep in mind that the Ma_∞-α combination, for which the **GAF** matrix depicted in Figure 8.10 has been evaluated, is not explicitly included in the training data. Subject to this circumstance, the quality of the ROM/NFM results is highly satisfactory.

At this point, it must be recapitulated that the investigations conducted within the scope of Chapter 8 represent a feasibility study aiming at the demonstration of the developed nonlinear ROM approaches towards complex, industry-relevant aerospace problems. For a comprehensive analysis of the underlying test case, however, further training signal variations, additional mode shapes, and other freestream conditions should be taken into account. Moreover, from the limited validation data, neither the degree of nonlinearity nor the detailed influence of α variations on the unsteady aerodynamics is further identified. Despite the aforementioned remarks, the angle-of-attack-adaptive neuro-fuzzy model results indicate that the methodology outlined in Section 4.1 can yield very promising results even for full-size aircraft configurations involving realistic structural eigenmodes and an increased geometrical complexity.

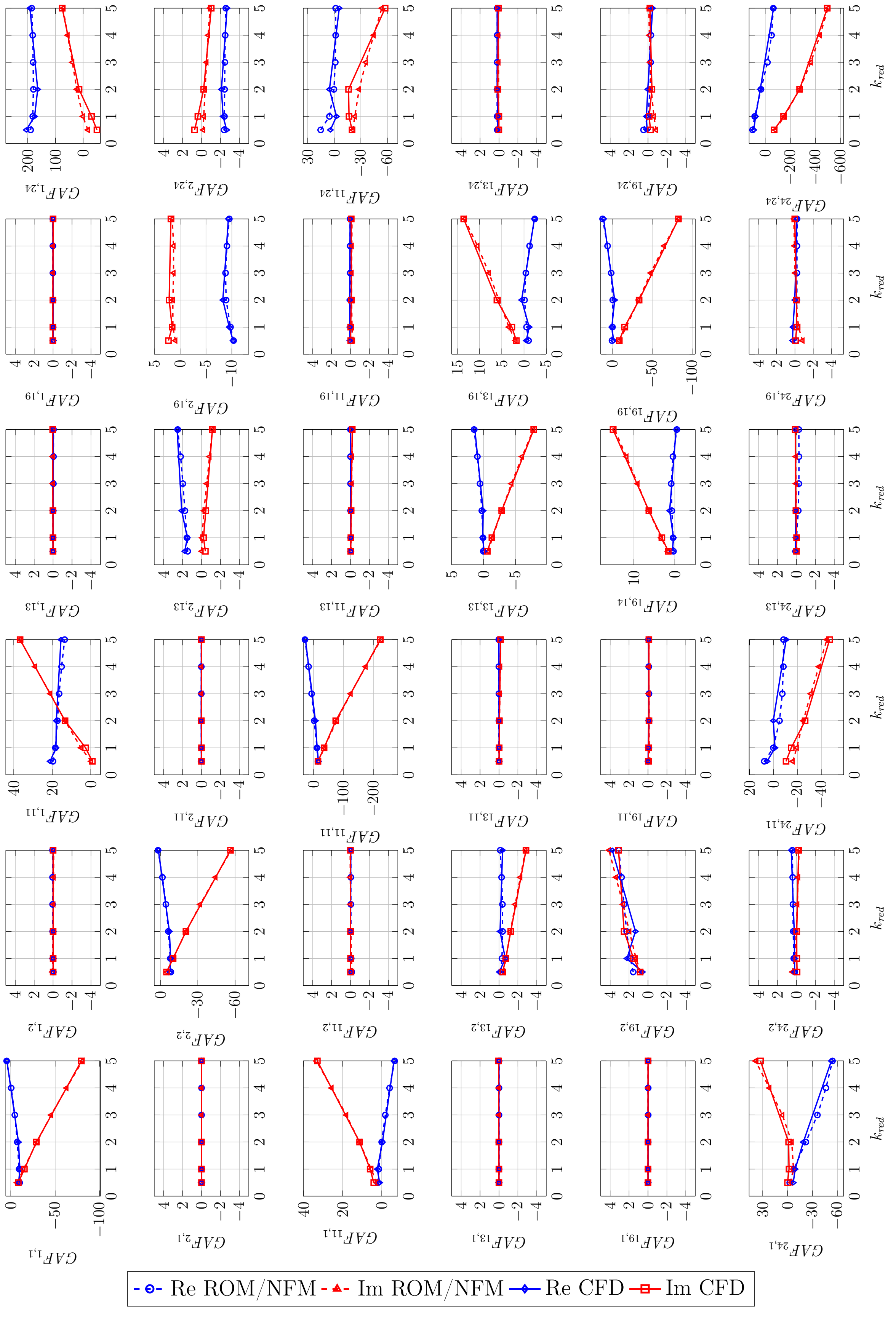

Figure 8.10: The real and imaginary parts of the frequency-domain **GAF** matrix are presented for the ROM- and the AER-Eu-based modeling. $Ma_\infty = 0.85$, $\alpha_{Sim} = 1.13°$, CRM-WBT0 configuration, FERMAT structural model.

8.4 Unsteady Results: POD-ROM for Surface Pressure Distribution Modeling

In contrast to the parameter-adaptive ROM procedure applied in the previous section, the freestream condition specified by $Ma_\infty = 0.85$ and $\alpha = 1.13°$ is not only taken into account for the application of the POD-ROM approach but also during the training process. In this regard, additional unsteady forced-motion CFD simulations have been performed at $\alpha = 1.13°$ for each considered excitation degree of freedom q_i utilizing the same SAPRBS that has been employed to construct the α-adaptive neuro-fuzzy model. Consequently, also the POD-ROM is based on a nondimensional time step size of $\Delta\tau = 0.05$ according to the excitation signal shown in Figure 8.9.

Once the $n_q = 6$ unsteady forced-motion CFD results are available for $\alpha = 1.13°$, the resulting surface pressure distributions can be exploited by means of the proper orthogonal decomposition to provide the POD modes as well as the corresponding POD coefficients. For a specific excitation mode q_i, the POD snapshot matrix $\mathbf{Y}_i \in \mathbb{R}^{N_{SE} \times N_S}$ comprises the pressure coefficients related to $N_{SE} = 67{,}856$ surface elements in combination with $N_S = 1{,}200$ temporal samples. Under the constraint that a relative information content criterion of $RIC > 0.95$ is fulfilled, the number of POD modes has been identified in the range between $M_{POD,i} = 34$ and $M_{POD,i} = 42$, depending on the considered excitation mode. In Figure 8.11, selected POD modes originating from the unsteady C_p surface solutions are shown. After the POD modes and POD coefficients have been obtained, the LOLIMOT-algorithm-based identification has been carried out. The system inputs and outputs for the underlying identification problem have been formulated according to Equation (8.2) with respect to the excitation degree of freedom q_i, $i \in [1, 2, 11, 13, 19, 24]$:

$$u_i(t) = q_i(t) \in \mathbb{R}, \qquad \mathbf{y}_i(t) = \begin{pmatrix} b_{1,i}(t) \\ b_{2,i}(t) \\ \vdots \\ b_{M_{POD},i}(t) \end{pmatrix} \in \mathbb{R}^{M_{POD,i}}, \qquad \Xi_i \in \varnothing \tag{8.2}$$

In Equation (8.2), $b_{j,i}$ denotes the time-variant POD coefficient that is linked to the jth time-invariant POD mode $\boldsymbol{\varphi}_{j,i}$. Regarding the recurrence framework of the neuro-fuzzy model, the dynamic delay orders have been optimized to $m = 25$ and $n = 10$ using the mapping $u_1(t) \rightarrow \mathbf{y}_1(t)$; see Section 3.3.3 for further details.

After finishing the POD-ROM training process, the obtained model can be employed to conduct the unsteady aerodynamic simulations of interest. In the course of this investigation, again harmonic motions are prescribed with respect to the excitation of the modal coordinates, while several reduced frequencies ($k_{red,ROM} = [0.5, 1.0, 2.0, 5.0]$) are taken into account for each degree of freedom. Therefore, three oscillation cycles have

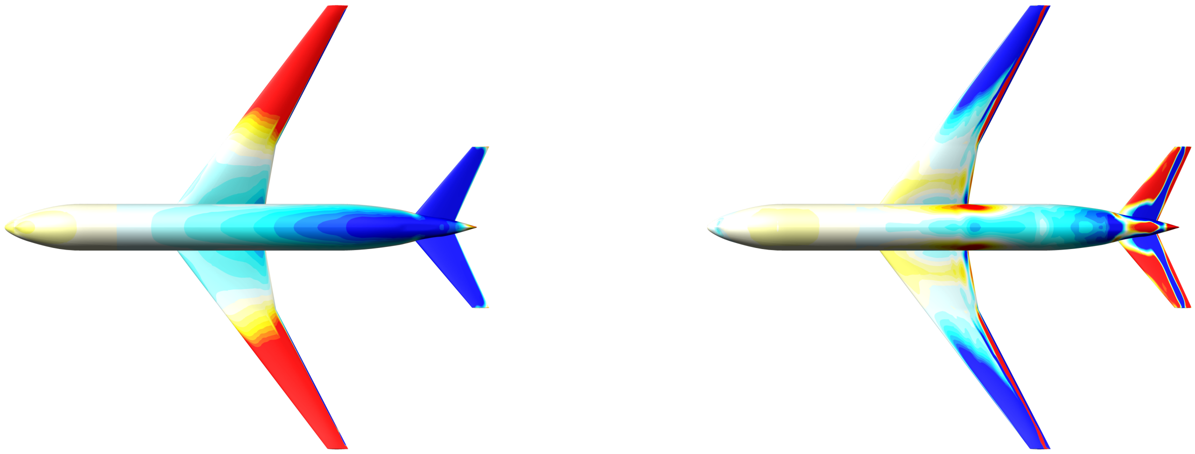

POD mode 1 (excitation of elastic mode 1) POD mode 4 (excitation of elastic mode 1)

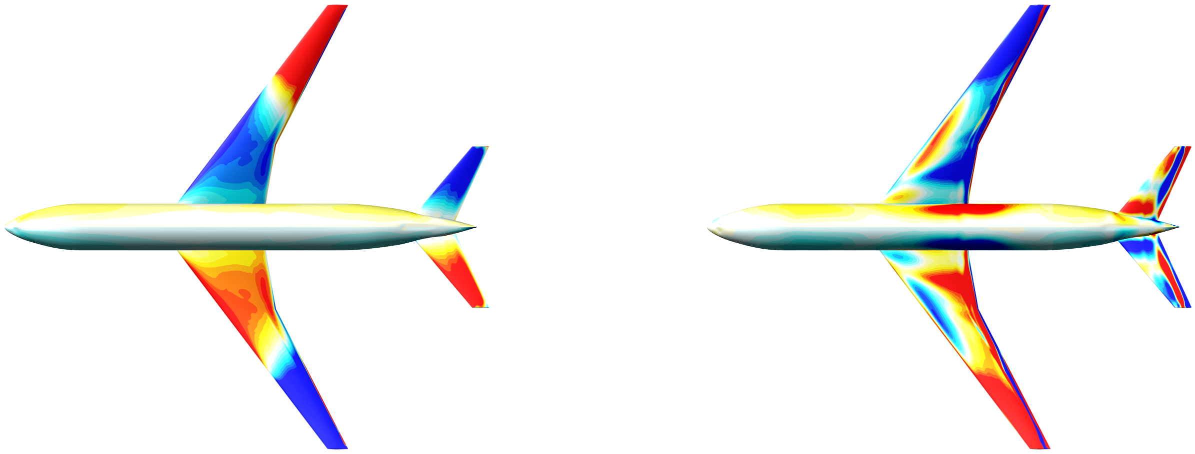

POD mode 1 (excitation of elastic mode 2) POD mode 4 (excitation of elastic mode 2)

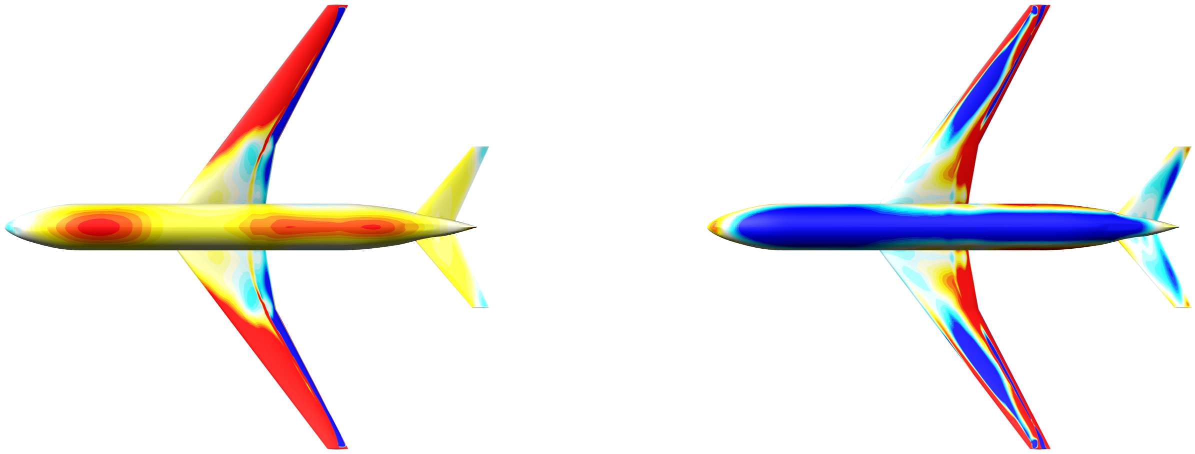

POD mode 1 (excitation of elastic mode 24) POD mode 4 (excitation of elastic mode 24)

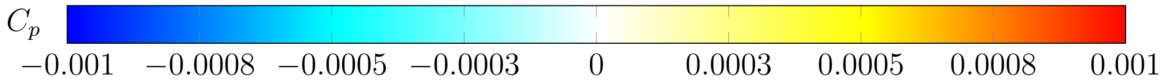

Figure 8.11: Visualization of selected POD modes that have been extracted from forced-motion unsteady CFD simulations. The excitation degree of freedom leading to the POD mode is specified within the parenthesis. AER-Eu, $Ma_\infty = 0.85$, $\alpha = 1.13°$, CRM configuration, FERMAT structural model.

been computed with the POD-based ROM, whereas the CFD reference solutions are already available on the basis of the investigations outlined in Section 8.3. For a more compact representation of the results, a Fourier analysis of the time-domain information has been performed yielding the real and imaginary parts of the first harmonic surface C_p distribution; see also Section 6.6.

In Figures 8.12-8.16, the surface pressure coefficient response caused by the excitation of representative symmetric eigenmodes is visualized for selected reduced frequencies. Due to the symmetry of the elastic mode shapes with respect to the $y = 0$ plane for the generalized coordinates q_1, q_{11}, and q_{24}, the POD-ROM solutions are shown for the starboard side, whereas the respective AER-Eu results are depicted for the port side. The top view contour plots indicate a generally good agreement between the POD-ROM and the AER-Eu reference. However, as it has been already noted for the LANN wing in Chapter 6, regions with a dominant shock influence are not accurately reproduced by the ROM. The associated discrepancies become visible for example at the wing root. Further deviations between the POD-ROM and the reference solutions emerge at the horizontal tail. The reason for the latter errors is not a flow nonlinearity but the order of magnitude of the pressure variations in the tail region. As a consequence of the proper orthogonal decomposition, greater importance is attributed to globally-occurring, high-energy structures compared to locally pronounced effects of smaller magnitude. This effect is amplified by the a posteriori employed neural network, which also minimizes globally-defined cost functions. Nonetheless, besides the local, small-scale mismatches in the pressure distribution the overall pressure patterns are in good accordance.

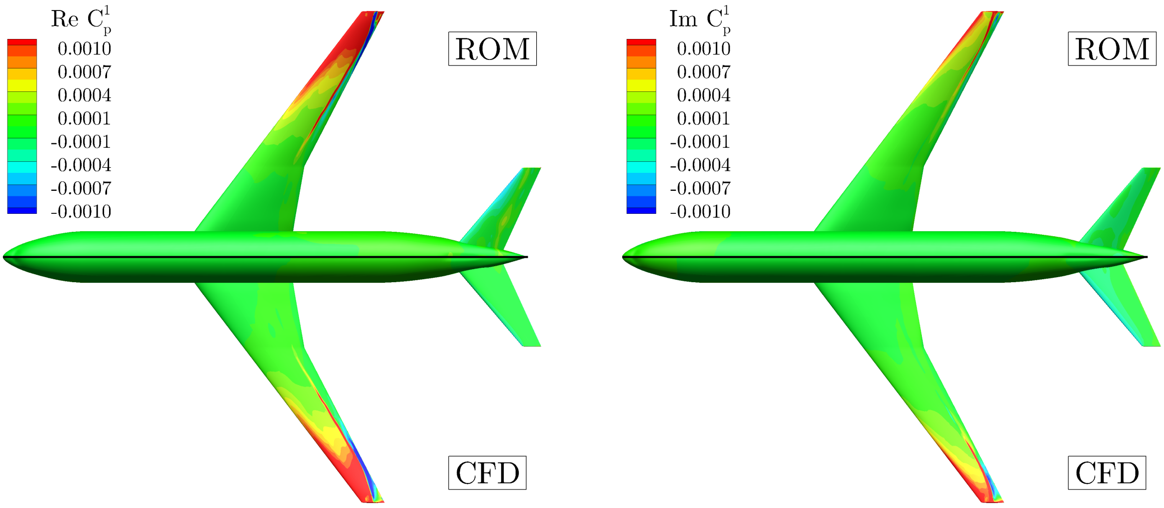

Real part (elastic mode 1, $k_{red} = 0.5$) Imaginary part (elastic mode 1, $k_{red} = 0.5$)

Figure 8.12: First harmonic of the C_p response induced by a sinusoidal excitation of elastic mode 1 with $k_{red} = 0.5$. Due to the $y = 0$ symmetry of the mode shape, the ROM result is shown for the upper surface of the starboard side, whereas the AER-Eu result is depicted for the port side. $Ma_\infty = 0.85$, $\alpha = 1.13°$, CRM configuration, FERMAT structural model.

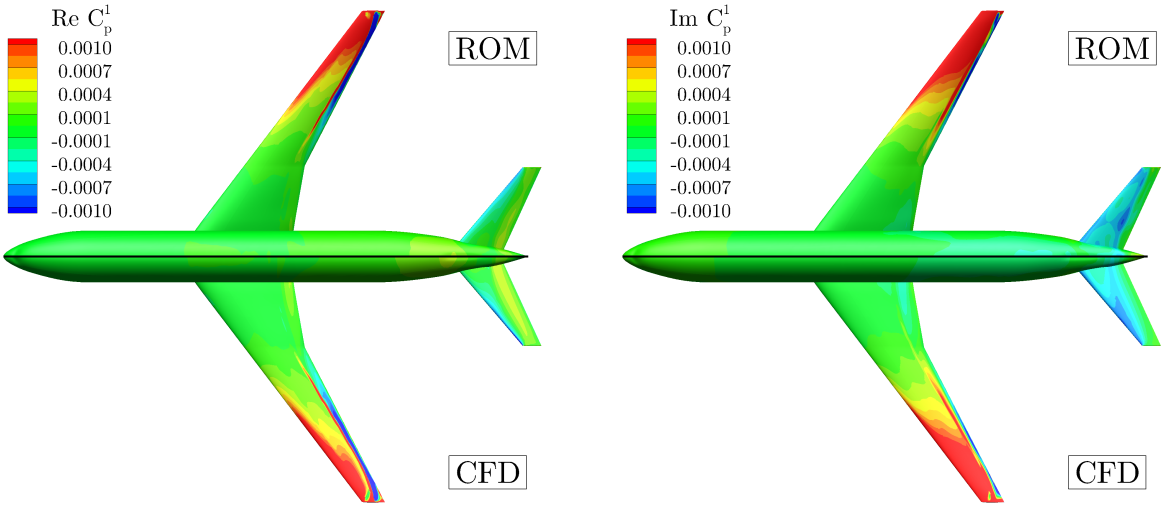

Real part (elastic mode 1, $k_{red} = 2.0$) Imaginary part (elastic mode 1, $k_{red} = 2.0$)

Figure 8.13: First harmonic of the C_p response induced by a sinusoidal excitation of elastic mode 1 with $k_{red} = 2.0$. Due to the $y = 0$ symmetry of the mode shape, the ROM result is shown for the upper surface of the starboard side, whereas the AER-Eu result is depicted for the port side. $Ma_\infty = 0.85$, $\alpha = 1.13°$, CRM configuration, FERMAT structural model.

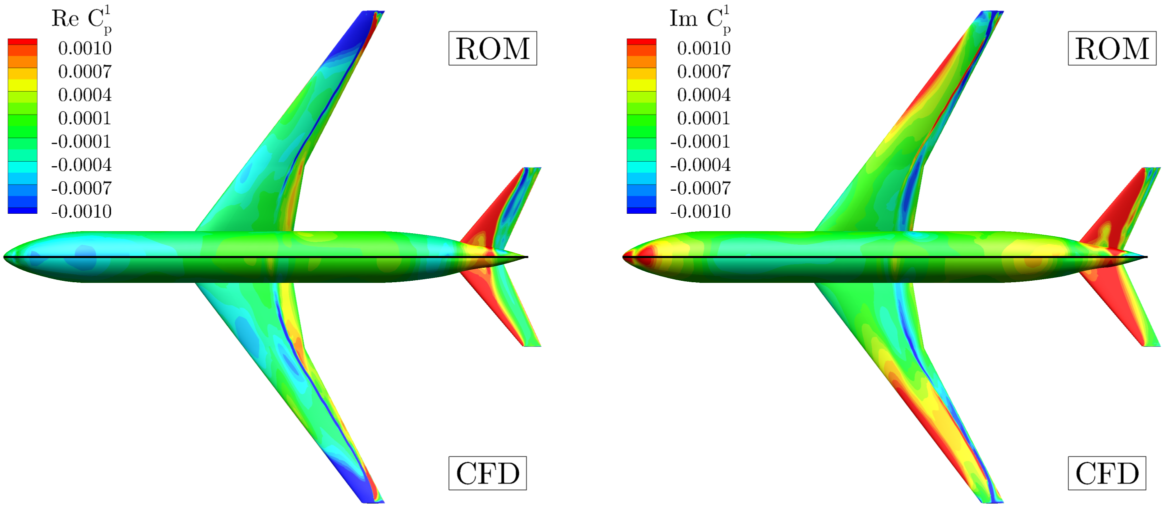

Real part (elastic mode 11, $k_{red} = 1.0$) Imaginary part (elastic mode 11, $k_{red} = 1.0$)

Figure 8.14: First harmonic of the C_p response induced by a sinusoidal excitation of elastic mode 11 with $k_{red} = 1.0$. Due to the $y = 0$ symmetry of the mode shape, the ROM result is shown for the upper surface of the starboard side, whereas the AER-Eu result is depicted for the port side. $Ma_\infty = 0.85$, $\alpha = 1.13°$, CRM configuration, FERMAT structural model.

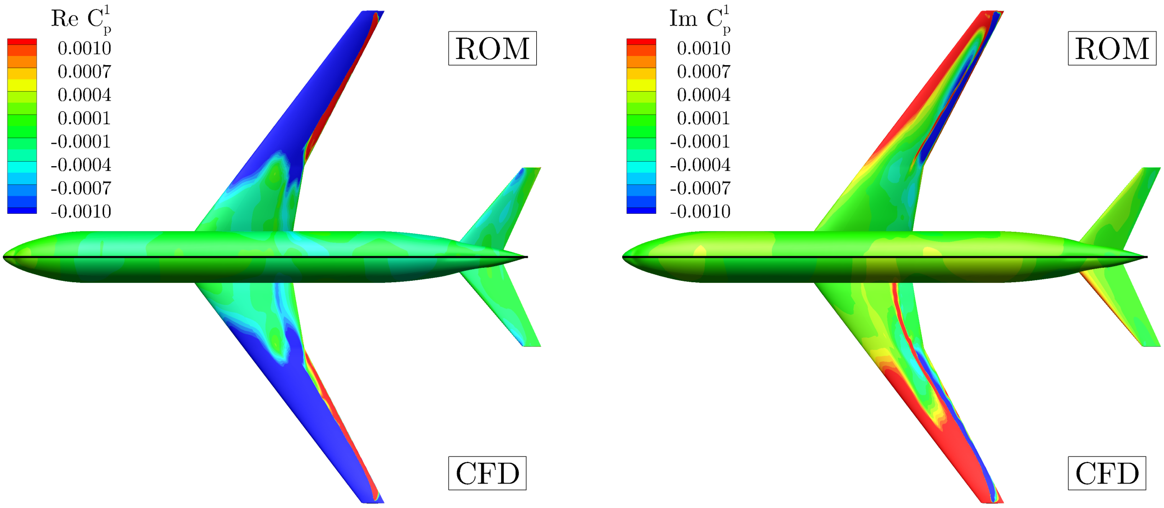

Real part (elastic mode 24, $k_{red} = 0.5$) Imaginary part (elastic mode 24, $k_{red} = 0.5$)

Figure 8.15: First harmonic of the C_p response induced by a sinusoidal excitation of elastic mode 24 with $k_{red} = 0.5$. Due to the $y = 0$ symmetry of the mode shape, the ROM result is shown for the upper surface of the starboard side, whereas the AER-Eu result is depicted for the port side. $Ma_\infty = 0.85$, $\alpha = 1.13°$, CRM configuration, FERMAT structural model.

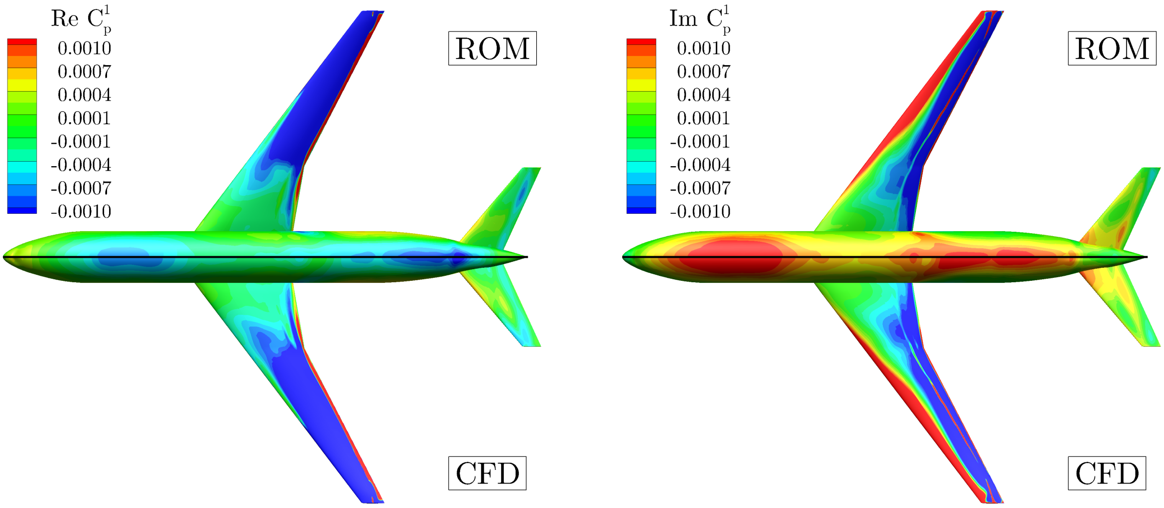

Real part (elastic mode 24, $k_{red} = 5.0$) Imaginary part (elastic mode 24, $k_{red} = 5.0$)

Figure 8.16: First harmonic of the C_p response induced by a sinusoidal excitation of elastic mode 24 with $k_{red} = 5.0$. Due to the $y = 0$ symmetry of the mode shape, the ROM result is shown for the upper surface of the starboard side, whereas the AER-Eu result is depicted for the port side. $Ma_\infty = 0.85$, $\alpha = 1.13°$, CRM configuration, FERMAT structural model.

Furthermore, also unsteady aerodynamic responses that are induced by the excitation of antisymmetric mode shapes can be adequately reproduced by the POD-ROM as it can be seen from Figures 8.17-8.18. Based on the depicted results, it can be concluded that the ROM approach can be equivalently applied to realistic aircraft configurations compared to the less-complex case investigated in Chapter 6. However, due to the increased number of degrees of freedom, the data handling as well as the data input/output can be cumbersome and may exceed the memory/computing limits. In order to avoid locally manifested deviations, e.g. the mismatches at the horizontal tail, the POD-ROM procedure can be applied to local components of the aircraft rather than the entire configuration. Thus, the applicability of the methodology is generally not restricted by the complexity of the test case.

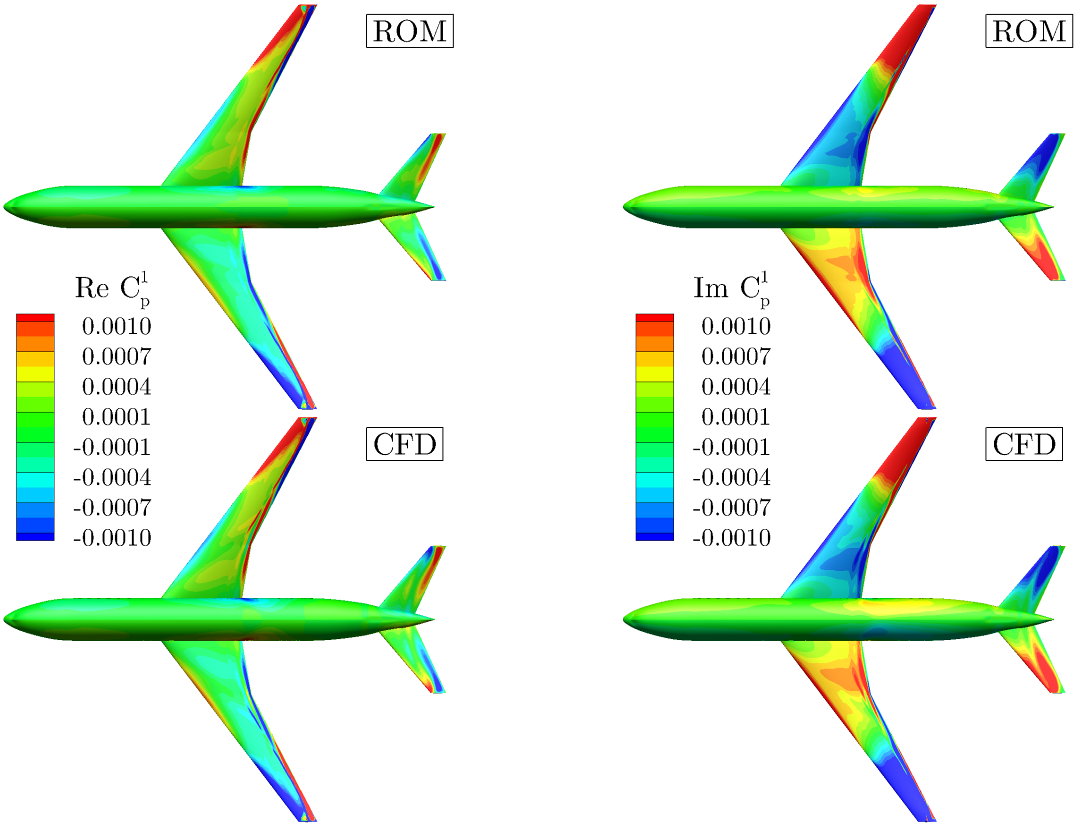

Real part (elastic mode 2, $k_{red} = 5.0$) Imaginary part (elastic mode 2, $k_{red} = 5.0$)

Figure 8.17: First harmonic of the C_p response induced by a sinusoidal excitation of elastic mode 2 with $k_{red} = 5.0$. Due to the antisymmetric characteristic of the eigenmode, the full-span configuration is displayed. The ROM result is presented at the top, whereas the AER-Eu result is shown at the bottom. $Ma_\infty = 0.85$, $\alpha = 1.13°$, CRM configuration, FERMAT structural model.

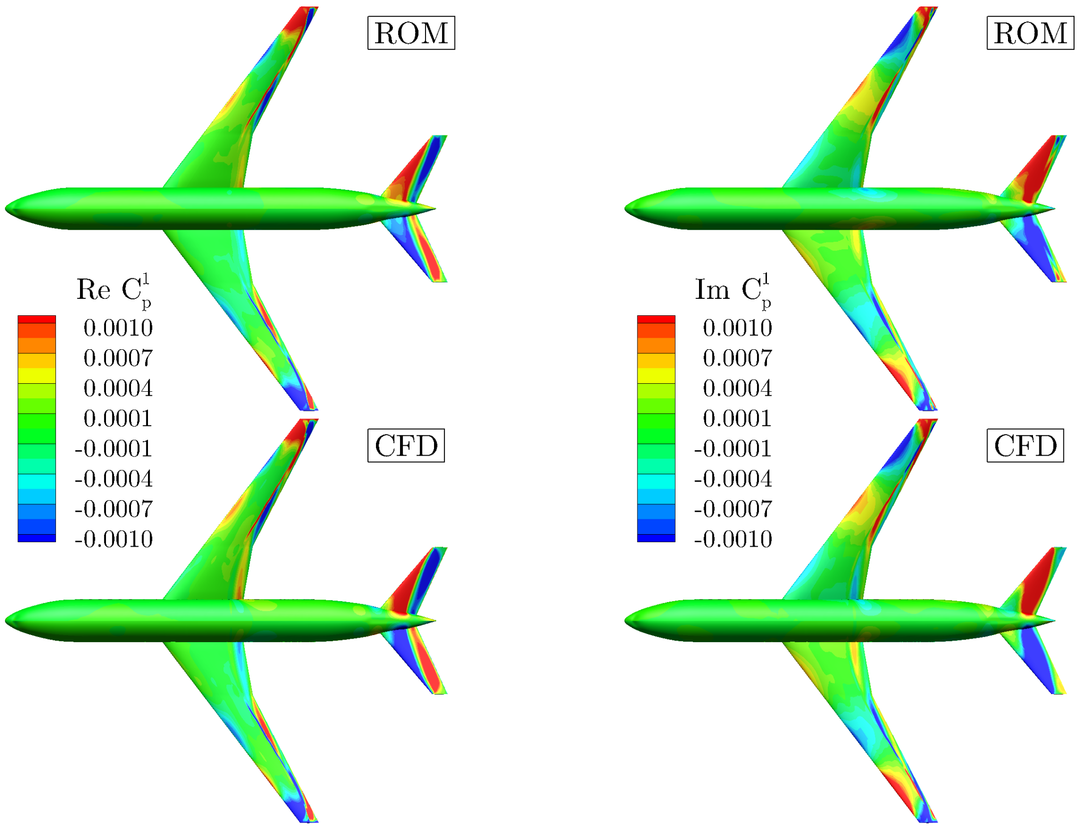

Real part (elastic mode 19, $k_{red} = 2.0$) Imaginary part (elastic mode 19, $k_{red} = 2.0$)

Figure 8.18: First harmonic of the C_p response induced by a sinusoidal excitation of elastic mode 19 with $k_{red} = 2.0$. Due to the antisymmetric characteristic of the eigenmode, the full-span configuration is displayed. The ROM result is presented at the top, whereas the AER-Eu result is shown at the bottom. $Ma_\infty = 0.85$, $\alpha = 1.13°$, CRM configuration, FERMAT structural model.

8.5 Efficiency Considerations and Résumé

Finally, the computational speed-up is investigated for the freestream-parameter-adaptive neuro-fuzzy model as well as the POD-ROM approach. The training and application of the two reduced-order models as well as the Euler-equations-based CFD simulations presented in this chapter have been carried out on the Linux cluster of the Leibniz Supercomputing Center (LRZ). For comparability, all computation jobs have been processed in serial operation (serial/parallel farming) using a single core of the Intel Xeon E5-2697 v3 2.6 GHz CPU. As a consequence, the CPU times presented below can be interpreted as wall clock times for each individual simulation.

Considering first the efficiency of the freestream-parameter-adaptive ROM, the AER-Eu simulations related to the $N_{FC} = 4$ training angles of attack and six excitation degrees of freedom have required in total 27,132 CPU hours. Thus, a computational cost of 47.1 CPU days has been necessary in average for each forced-motion training simulation. In contrast, the subsequent neuro-fuzzy model calibration has taken only 0.63 CPU hours, whereas the application of the model to the generalized aerodynamic forces computation at $\alpha_{Sim} = 1.13°$ has been performed in 15.1 CPU seconds (0.42 CPU seconds per simulation case). For comparison, the total computational cost for generating the harmonic motion reference results has been 9,953 CPU hours incorporating four reduced frequencies and six mode shapes. Thus, the average validation CFD run has required about 17.3 CPU days. Regarding the investigations presented in Section 8.3, the ROM speed-up relative to the AER-Eu solver for an already trained model is therefore about five orders of magnitude. However, the effective speed-up, which must respect the effort due to the training CFD simulations, strongly depends on the number of intended simulations and cannot be specified in a reasonable manner for this generically constructed example.

Second, the computational costs of the POD-ROM methodology are analyzed: In terms of the POD-ROM training, unsteady CFD simulations related to six modal degrees of freedom have been computed in about 6,702 CPU hours, leading to an average effort of 1,117 CPU hours for each individual AER-Eu simulation. Furthermore, the computation of the POD modes and POD coefficients has required about 4.9 CPU hours, while the neuro-fuzzy model training has been carried out in merely 1.7 CPU hours. In terms of a total cost estimation, the training data acquisition, POD application, and LOLIMOT-based model calibration must be taken into account. Thus, the total POD-ROM construction effort has been about 6,709 CPU hours. In contrast, the application of the POD-ROM to the 24 simulation cases has required approximately 37.3 CPU seconds. The aforementioned application cost already includes the neuro-fuzzy-model-based simulation, which provides the POD coefficients, as well as the reconstruction of the surface C_p distribution. Hence, each simulation has needed about 1.6 CPU seconds in average. Although the POD-ROM has been applied for the simulation of four reduced-frequencies only, the total computational effort of 6,709 CPU hours is already lower than the comparable cost required by the reference system for the present cases (9,953 CPU hours). It should be emphasized again that the efficiency advantage becomes higher with added computation cases. In the limit for an infinite number of application runs, the training effort can be neglected yielding a speed-up factor for each individual simulation of the order of five magnitudes.

In this chapter, the freestream-parameter-adaptive ROM and the POD-ROM methodology were applied to the CRM configuration in combination with the FERMAT structural model in order to assess their performance and efficiency related to unsteady aerodynamic problems with a considerably increased number of degrees of freedom. For this purpose, the neuro-fuzzy model ROM was employed to compute harmonic aerodynamic responses due to different elastic-mode-shape-related excitations, while the angle of attack served as an additional input parameter to the model. Moreover, unsteady surface pressure fluctuations induced by modal deformations were predicted by the POD-based ROM approach. The results obtained from both approaches demonstrated that the developed ROM methodologies are generally applicable to complex, industry-relevant problems. Due to the fact that the CFD simulations become more involved for test cases of increased complexity, the computational cost saving potential due to the use of reduced-order models is also increased.

9 Conclusions and Outlook

Related to aircraft aeroelastic investigations, the aim of this work was the efficient modeling of unsteady aerodynamic forces and moments as well as load distributions that are caused by structural excitations or rigid body motions. In particular, the focus was laid on the prediction of prevailing nonlinearities in the transonic flow regime induced by distinct shock motions, large deflection amplitudes, and pronounced freestream parameter variations. Since the aforementioned effects cannot be reproduced accurately using linear aerodynamic methods, the herein developed model-order reduction approaches were based on the full-order Euler and Reynolds-averaged Navier-Stokes CFD solvers. To achieve a tradeoff between the quality of the results and the associated computational costs, the neuro-fuzzy-model-based reduced-order models were trained on the basis of selected time-domain CFD solutions by exploiting nonlinear system identification methodologies. The proposed ROM procedures encompassed the entire modeling process chain, starting from the required CFD solver interfaces, the excitation signal design, the model structure determination and parameter optimization, up to the realization of efficient and accurate simulations. Compared to established aerodynamic reduced-order modeling concepts, significant progress was made regarding the prediction accuracy of nonlinear characteristics and the robustness of the training and application process. Validated by selected application examples, the models were capable of representing the essential linear and nonlinear dynamics of the underlying flow problems. Consequently, the ROM approaches devised in this thesis led to a considerable acceleration of numerical unsteady aerodynamic analyses, which may allow the assessment of the aeroelastic behavior at an earlier stage in the aircraft development process.

With respect to a comprehensive evaluation of the approaches, four unsteady aerodynamic validation cases were thoroughly taken into account. First, it was highlighted that the developed reduced-order modeling procedure can be applied for the prediction of motion-induced integral aerodynamic loads across variable freestream conditions. Specifically, structural deflections were prescribed on the AGARD 445.6 wing at subsonic, transonic, and supersonic inflow conditions, while a monolithic neuro-fuzzy model was used to compute the respective aerodynamic responses. The ROM-based time-domain results as well as the derived frequency domain solutions showed a good agreement with the CFD reference simulations. Besides, the suggested Monte-Carlo training and application process ensured that initialization influences have a negligible impact on the ROM result. Nevertheless, it was also indicated that the quality of the training data has a decisive influence on the attainable model fidelity. Additionally, a linear flutter analysis was performed for both the ROM- and the CFD-based generalized aerodynamic forces dataset. It was pointed out that the accuracy of the neuro-fuzzy model is sufficient enough for preliminary aeroelastic considerations. A detailed analysis of the computational costs showed that the overall effort was considerably reduced in comparison to a thorough CFD-based aeroelastic analysis.

Furthermore, the POD-ROM methodology, which combines the recurrent neuro-fuzzy model and the proper orthogonal decomposition technique, was tested to simulate unsteady surface pressure distributions. The example of the LANN wing undergoing a pitching motion showed that the dominant steady and unsteady aerodynamic load characteristic caused by multiple excitation frequencies and amplitudes could be reproduced. Nevertheless, it was identified that the precise prediction of discontinuities such as crisp shocks is associated to notable superposition errors. However, taking into account the achieved cost savings of about four orders of magnitude once the surrogate model is available, the POD-ROM can be particularly interesting for computationally demanding multidisciplinary analyses such as fluid-structure-interaction problems and numerical optimizations.

Subsequently, the connected neural network methodology, involving the recurrent local linear neuro-fuzzy model and the MLP neural network, was applied to predict the pitch and plunge induced aerodynamic responses of the NLR 7301 airfoil. Based on validation cases at transonic inflow conditions, it was outlined that both the linear and the nonlinear system dynamics were modeled very accurate by the novel method. Moreover, by considering model inputs beyond the regime from which the ROM has been trained, the results underpinned the improved generalization capabilities. A comparison between different model-order reduction techniques and the CFD reference clearly showed the superior simulation quality of the NFM-MLP approach. Despite the high fidelity, the developed modeling procedure still achieved a significant computational cost reduction.

Finally, the freestream-parameter-adaptive ROM and the POD-ROM methodology were applied to the CRM configuration in combination with the FERMAT structural model in order to assess their performance and efficiency related to a significantly more complex test case. The results indicated that the novel class of neuro-fuzzy-model-based model-order reduction techniques is applicable to industry-scale problems.

On the basis of the previously outlined results, the key achievements and findings of this thesis can be summarized as follows:

- In the present work, a novel neuro-fuzzy-model-based unsteady aerodynamic ROM framework has been developed. The proposed system identification methodology encloses the entire process chain, starting from the required CFD solver interfaces, the excitation signal definition, the model structure optimization and parameter training, up to the realization of efficient and accurate aerodynamic simulations.

- Due to the underlying local linear sub-models, the neuro-fuzzy approach is able to reproduce an exclusively linear dynamic system behavior at given operating points while being able to capture nonlinearities across variable freestream conditions.

- With respect to the excitation of the degrees of freedom of the aerodynamic system, (smoothed) amplitude-modulated pseudo-random binary signals have been suggested for applications with distinct nonlinearities. As a consequence, the training data is characterized by a large spectrum of excited amplitudes and frequencies in combination with a high information content per signal length.

- Despite the active output feedback that allows the precise modeling of memory effects and dynamic nonlinearities, the recurrent neuro-fuzzy ROM has proven to be robust.

- For enhancing the generalization capabilities of the model, the CFD-generated dataset has been randomly split into training, validation, and test data prior to the ROM calibration. In this way, aerodynamic responses can be computed for unknown excitation signals in an accurate and reliable manner.

- In order to avoid random-initialization-related influences on the final ROM solution, the Monte-Carlo training and application procedure has been implemented to enable statistical analyses with respect to the model outputs. Hence, the reproducibility and fidelity of different ROM approaches or training settings becomes comparable.

- Two powerful extensions of the basic neuro-fuzzy model framework have been developed and applied: First, by combining the neuro-fuzzy model with the POD, motion-induced unsteady load distributions can be efficiently predicted. Second, the combined NFM-MLP network allows the consideration of strongly-nonlinear aerodynamic characteristics.

- The application to a test case of significantly increased complexity demonstrated the potential of the developed approaches for industry-scale problems.

- A detailed analysis regarding the efficiency of the ROM approaches relative to the full-order CFD procedure has shown that accelerations of two to five orders of magnitude can be achieved. However, it has been also highlighted that the speed-up factor is strongly case-dependent. Once the training expenses have been amortized, which is the case for a sufficiently large number of intended simulations or if the ROM is acting as a surrogate model that is directly coupled within a multidisciplinary environment, the usage of the neuro-fuzzy methods becomes profitable.

- Finally, it has to be emphasized that the methodologies can be generalized to additional problem classes by means of an adapted formulation of the input/output interfaces. Thus, the modular model-order reduction framework can be universally applied to substitute the CFD solver with respect to computationally costly interdisciplinary simulations.

During the research activities leading to this thesis, further potentially-promising ROM approaches have been revealed in addition to the presented work. The associated insights are briefly highlighted in the following outlook.

Driven by the enormous progress in high-performance and cloud computing capabilities as well as artificial intelligence algorithms, groundbreaking developments have taken place over the last years, which have led to a multitude of new machine learning and deep learning concepts. An increasingly popular approach from this branch is the long short-term memory (LSTM) neural network. The LSTM approach could be especially interesting for describing nonlinear aerodynamic phenomena such as buffet or buzz, which are characterized by a strong feedback mechanism. Since both shock-boundary-layer interactions and flow separations already cause a time-varying load response without the presence of any structural excitation, the ROM must be capable of providing an unsteady response for fixed system inputs. According to the literature, this is a key strength of the LSTM neural network. Furthermore, the coupling of the derived aerodynamic ROMs with structural dynamics and/or flight mechanics models represents an extension of the existing process that allows the simulation of aeroelastic and aeroservoelastic characteristics beyond the flutter problem. However, this step drastically increases the validation effort due to the required computationally-intensive multidisciplinary simulations.

Besides, the interaction between the excitation signal design and the CFD-based training data generation offers potential for reducing the total computational cost and, at the same time, improving the quality of the ROM results. However, this idea requires either modifications in the employed CFD solver or many simulation restarts, since parts of the identification process must be already carried out at runtime of the flow solver. For example, the algorithm must detect whether a certain amplitude, frequency, or operating regime is sufficiently resolved or not. Depending on the outcome of this analysis, the excitation signal can be directly adapted for the subsequent time steps. Consequently, this measure can further increase the information density of the training data and decrease the training data acquisition effort.

Finally, an improvement of the POD-ROM method for predicting surface or field distributions could be achieved by using recently devised machine learning approaches. Exemplarily, the convolutional neural network (CNN), the auto-encoder network, or the conditional generative adversarial network (CGAN) are promising approaches in order to enhance the nonlinear mapping with respect to unsteady surface or field solutions.

Last but not least, the relevance of keeping an eye on the developments of other disciplines and fostering out-of-the-box thinking cannot be overemphasized. Many modern innovations are the result of smartly linking already existing concepts and approaches to different research fields. It is therefore of particular importance to understand the procedures and problems of various disciplines in order to generalize and combine them towards novel applications.

Bibliography

[1] E. Albano and W. P. Rodden, "A Doublet-Lattice Method for Calculating Lift Distributions on Oscillating Surfaces in Subsonic Flows," *AIAA Journal*, Vol. 7 (2), pp. 279–285, 1969.

[2] ANSYS Inc., Canonsburg, PA, USA, ANSYS ICEM CFD User Manual, Version 14.5, 2012.

[3] J. S. R. Anttonen, P. I. King, and P. S. Beran, "POD-Based Reduced-Order Models with Deforming Grids," *Mathematical and Computer Modelling*, Vol. 38, pp. 41–62, 2003.

[4] K. J. Badcock, S. Timme, S. Marques, H. Khodaparast, M. Prandina, J. E. Mottershead, A. Swift, A. D. Ronch, and M. A. Woodgate, "Transonic Aeroelastic Simulation for Instability Searches and Uncertainty Analysis," *Progress in Aerospace Sciences*, Vol. 47 (5), pp. 392–423, 2011.

[5] A. V. Balakrishnan, "Transonic Small Disturbance Potential Equation," *AIAA Journal*, Vol. 42 (6), pp. 1081–1088, 2004.

[6] W. F. Ballhaus and P. M. Goorjian, "Computation of Unsteady Transonic Flows by the Indicial Method," *AIAA Journal*, Vol. 16 (2), pp. 117–124, 1978.

[7] J. Becker, Bewegungsinduzierte Luftkräfte bei abgelöster Strömung und ihre Übertragung auf die Ermittlung der Strukturresponse, Dissertation, Technische Universität Braunschweig, Braunschweig, Germany, 1983.

[8] O. O. Bendiksen, "Review of Unsteady Transonic Aerodynamics: Theory and Applications," *Progress in Aerospace Sciences*, Vol. 47 (2), pp. 135–167, 2011.

[9] S. A. Billings, Nonlinear System Identification: NARMAX Methods in the Time, Frequency, and Spatio-Temporal Domains, John Wiley & Sons, 1st Edition, Chichester, West Sussex, U.K., ISBN 978-1-1185-3555-4, 2013.

[10] C. M. Bishop, Pattern Recognition and Machine Learning, Springer-Verlag, 1st Edition, New York, ISBN 978-0-387-31073-2, 2006.

[11] R. L. Bisplinghoff, H. Ashley, and R. L. Halfman, Aeroelasticity, Dover Publications, 1st Edition, Mineola, NY, USA, ISBN 978-0-4866-9189-3, 1996.

[12] J. Blazek, "Investigations of the Implicit LU-SSOR Scheme," Technical report, DLR-FB 93-51, Deutsches Zentrum für Luft- und Raumfahrt, 1993.

[13] J. Blazek, Computational Fluid Dynamics: Principles and Applications, Elsevier, 3rd Edition, Amsterdam, The Netherlands, ISBN 978-0-0809-9995-1, 2015.

[14] H.-H. Bothe, Fuzzy Logic: Einführung in Theorie und Anwendungen, Springer-Verlag, 1st Edition, Berlin, Heidelberg, ISBN 978-3-662-21929-4, 1993.

[15] C. Breitsamter, Instationäre Aerodynamik 1, Lecture notes, WS 2017/2018, Lehrstuhl für Aerodynamik und Strömungsmechanik, Technische Universität München, 2017.

[16] D. S. Broomhead and D. Lowe, "Multivariable Functional Interpolation and Adaptive Networks," *Complex Systems*, Vol. 2, pp. 321–355, 1988.

[17] M. Brown and C. J. Harris, Neurofuzzy Adaptive Modelling and Control, Prentice Hall PTR, 1st Edition, Englewood Cliffs, NJ, USA, ISBN 978-0-1313-4453-2, 1994.

[18] S. R. Chakravarthy, "High Resolution Upwind Formulations for the Navier-Stokes Equations," In: Von Karman Institute Lecture Series on Computational Fluid Dynamics, VKI 1988-05, pp. 1–105, 1988.

[19] S. Chen, S. A. Billings, and P. M. Grant, "Nonlinear System Identification Using Neural Networks," *International Journal of Control*, Vol. 51 (6), pp. 1191–1214, 1990.

[20] S. Chen, S. A. Billings, and P. M. Grant, "Recursive Hybrid Algorithm for Nonlinear System Identification Using Radial Basis Function Networks," *International Journal of Control*, Vol. 55 (5), pp. 1051–1070, 1992.

[21] S. Chen, C. F. N. Cowan, and P. M. Grant, "Orthogonal Least Squares Learning Algorithm for Radial Basis Function Networks," *IEEE Transactions on Neural Networks*, Vol. 2 (2), pp. 302–309, 1991.

[22] T. J. Cowan, A. S. Arena, and K. K. Gupta, "Accelerating Computational Fluid Dynamics Based Aeroelastic Predictions Using System Identification," *Journal of Aircraft*, Vol. 38 (1), pp. 81–87, 2001.

[23] H. J. Cunningham, J. T. Batina, and R. M. Bennett, "Modern Wing Flutter Analysis by Computational Fluid Dynamics Methods," *Journal of Aircraft*, Vol. 25 (10), pp. 962–968, 1988.

[24] N. C. G. de Paula, F. D. Marques, and W. A. Silva, "Volterra Kernels Assessment via Time-Delay Neural Networks for Nonlinear Unsteady Aerodynamic Loading Identification," *AIAA Journal*, Vol. 57 (4), pp. 1725–1735, 2019.

[25] C. W. de Silva, Vibration: Fundamentals and Practice, CRC Press, 2nd Edition, Boca Raton, FL, USA, ISBN 978-0-8493-1987-7, 2006.

[26] K. Decker, “Glätten von strukturierten Multiblocknetzen über Blockgrenzen,” Technical report, TUM-FLM-99/02, Technische Universität München, Garching, Germany, 1999.

[27] C. M. Denegri and M. R. Johnson, “Limit Cycle Oscillation Prediction Using Artificial Neural Networks,” *Journal of Guidance, Control, and Dynamics*, Vol. 24 (5), pp. 887–895, 2001.

[28] G. Dietz, G. Schewe, and H. Mai, “Experiments on Heave/Pitch Limit-Cycle Oscillations of a Supercritical Airfoil Close to the Transonic Dip,” *Journal of Fluids and Structures*, Vol. 19, pp. 1–16, 2004.

[29] E. H. Dowell, A Modern Course in Aeroelasticity, Springer-Verlag, 5th Edition, Cham, ISBN 978-3-319-09453-3, 2015.

[30] E. H. Dowell, J. Edwards, and T. Strganac, “Nonlinear Aeroelasticity,” *Journal of Aircraft*, Vol. 40 (5), pp. 857–874, 2003.

[31] E. H. Dowell and K. C. Hall, “Modeling of Fluid-Structure Interaction,” *Annual Review of Fluid Mechanics*, Vol. 33 (1), pp. 445–490, 2001.

[32] J. Duchon, “Splines Minimizing Rotation-Invariant Semi-Norms in Sobolev Spaces,” In: Constructive Theory of Functions of Several Variables, edited by W. Schempp and K. Zeller, Lecture notes in Mathematics 571, Springer-Verlag, Berlin, Heidelberg, pp. 85–100, 1976.

[33] J. D. Faires and R. L. Burden, Numerische Methoden - Näherungsverfahren und ihre praktische Anwendung, Spektrum, Akademischer Verlag, 1st Edition, Heidelberg, Germany, ISBN 978-3-8274-0596-8, 1994.

[34] W. E. Faller and S. J. Schreck, “Neural Networks: Applications and Opportunities in Aeronautics,” *Progress in Aerospace Sciences*, Vol. 32 (5), pp. 433–456, 1996.

[35] W. E. Faller and S. J. Schreck, “Unsteady Fluid Mechanics Applications of Neural Networks,” *Journal of Aircraft*, Vol. 34 (1), pp. 48–55, 1997.

[36] C. Farhat and D. Amsallem, “Recent Advances in Reduced-Order Modeling and Application to Nonlinear Computational Aeroelasticity,” In: 46th AIAA Aerospace Sciences Meeting and Exhibit, Reno, NV, USA, AIAA Paper 2008-0562, pp. 1–28, 2008.

[37] J. H. Ferziger and M. Perić, Computational Methods for Fluid Dynamics, Springer-Verlag, 3rd Edition, Berlin, Heidelberg, New York, ISBN 978-3-642-56026-2, 2002.

[38] D. Fleischer, Verfahren reduzierter Ordnung zur Ermittlung instationärer Luftkräfte, Dissertation, Technische Universität München, Garching, Germany, 2014.

[39] D. Fleischer and C. Breitsamter, "Efficient Computation of Unsteady Aerodynamic Loads using Computational-Fluid-Dynamics Linearized Methods," *Journal of Aircraft*, Vol. 50 (2), pp. 425–440, 2013.

[40] H. W. Föersching, Grundlagen der Aeroelastik, Springer-Verlag, 1st Edition, Berlin, Heidelberg, New York, ISBN 978-3-642-48285-4, 1974.

[41] M. Förster, Aeroelastische Stabilitäts- und Antwortanalyse auf Basis numerischer Strömungssimulation, Dissertation, Technische Universität München, Garching, Germany, 2016.

[42] M. Förster and C. Breitsamter, "Aeroelastic Prediction of Discrete Gust Loads Using Nonlinear and Time-Linearized CFD-Methods," *Journal of Aeroelasticity and Structural Dynamics*, Vol. 3 (3), pp. 19–38, 2015.

[43] C. Gao, W. Zhang, J. Kou, Y. Liu, and Z. Ye, "Active Control of Transonic Buffet Flow," *Journal of Fluid Mechanics*, Vol. 824, pp. 312–351, 2017.

[44] R. Gasch, K. Knothe, and R. Liebich, Strukturdynamik: Diskrete Systeme und Kontinua, Springer-Verlag, 2nd Edition, Berlin, Heidelberg, New York, ISBN 978-3-540-88977-9, 2012.

[45] M. Ghoreyshi, A. Jirásek, and R. M. Cummings, "Reduced Order Unsteady Aerodynamic Modeling for Stability and Control Analysis Using Computational Fluid Dynamics," *Progress in Aerospace Sciences*, Vol. 71, pp. 167–217, 2014.

[46] B. Glaz, P. P. Friedmann, L. Liu, J. G. Cajigas, J. Bain, and L. N. Sankar, "Reduced-Order Dynamic Stall Modeling with Swept Flow Effects Using a Surrogate-Based Recurrence Framework," *AIAA Journal*, Vol. 51 (4), pp. 910–921, 2013.

[47] B. Glaz, L. Liu, and P. P. Friedmann, "Reduced-Order Nonlinear Unsteady Aerodynamic Modeling Using a Surrogate-Based Recurrence Framework," *AIAA Journal*, Vol. 48 (10), pp. 2418–2429, 2010.

[48] I. Goodfellow, Y. Bengio, and A. Courville, Deep Learning, MIT Press, 1st Edition, ISBN 978-0-2620-3561-3, 2016.

[49] W. J. Gordon and C. A. Hall, "Construction of Curvilinear Coordinate Systems and Application to Mesh Generation," *International Journal for Numerical Methods in Engineering*, Vol. 7 (4), pp. 461–477, 1973.

[50] J. Grus, Data Science from Scratch: First Principles with Python, O'Reilly Media, 1st Edition, ISBN 978-1-4919-0142-7, 2015.

[51] R. Haber, "Nonlinearity Tests for Dynamic Processes," *IFAC Proceedings Volumes*, Vol. 18 (5), pp. 409–414, 1985.

[52] K. C. Hall and E. F. Crawley, "Calculation of Unsteady Flows in Turbomachinery Using the Linearized Euler Equations," *AIAA Journal*, Vol. 27 (6), pp. 777–787, 1989.

[53] K. C. Hall, J. P. Thomas, and W. S. Clark, "Computation of Unsteady Nonlinear Flows in Cascades Using a Harmonic Balance Technique," *AIAA Journal*, Vol. 40 (5), pp. 879–886, 2002.

[54] K. C. Hall, J. P. Thomas, and E. H. Dowell, "Proper Orthogonal Decomposition Technique for Transonic Unsteady Aerodynamic Flows," *AIAA Journal*, Vol. 38 (10), pp. 1853–1862, 2000.

[55] G. Hardier, J.-M. Biannic, C. Roos, C. Seren, and L. Verdier, "Surrogate Models for Aircraft Flight Control. Some Off-Line and Embedded Applications," *AerospaceLab Journal*, Vol. 12, pp. 1–21, 2016.

[56] H. J. Hassig, "An Approximate True Damping Solution of the Flutter Equation by Determinant Iteration," *Journal of Aircraft*, Vol. 8 (11), pp. 885–889, 1971.

[57] S. Haykin, Neural Networks: A Comprehensive Foundation, Prentice Hall PTR, 2nd Edition, Upper Saddle River, NJ, USA, ISBN 978-0-1390-8385-3, 1999.

[58] X. He and H. Asada, "A New Method for Identifying Orders of Input-Output Models for Nonlinear Dynamic Systems," In: American Control Conference, San Francisco, CA, USA, pp. 2520–2524, 1993.

[59] C. Hirsch, Numerical Computation of Internal and External Flows: The Fundamentals of Computational Fluid Dynamics, Elsevier, 2nd Edition, Amsterdam, The Netherlands, ISBN 978-0-7506-6594-0, 2007.

[60] K. A. Hoffmann and S. T. Chiang, Computational Fluid Dynamics for Engineers - Volume I, Engineering Education System, 4th Edition, Wichita, KS, USA, ISBN 0-9623731-0-9, 1995.

[61] K. A. Hoffmann and S. T. Chiang, Computational Fluid Dynamics for Engineers - Volume II, Engineering Education System, 4th Edition, Wichita, KS, USA, ISBN 0-9623731-3-3, 2000.

[62] K. A. Hoffmann and S. T. Chiang, Computational Fluid Dynamics for Engineers - Volume III, Engineering Education System, 4th Edition, Wichita, KS, USA, ISBN 0-9623731-6-8, 2000.

[63] C.-H. Huang, C.-L. Lin, and M.-J. Chao, "FERA in Parameter Identification with Application in Low Speed Wind Tunnel Test," *Aerospace Science and Technology*, Vol. 15 (6), pp. 495–509, 2011.

[64] R. Huang, H. Hu, and Y. Zhao, "Nonlinear Reduced-Order Modeling for Multiple-Input/Multiple-Output Aerodynamic Systems," *AIAA Journal*, Vol. 52 (6), pp. 1219–1231, 2014.

[65] T. J. R. Hughes, The Finite Elemente Method - Linear Static and Dynamic Finite Element Analysis, Dover Publications, 1st Edition, Mineola, NY, USA, ISBN 978-0-4864-1181-1, 2000.

[66] M. Iatrou, Ein Navier-Stokes-Verfahren kleiner Störungen für instationäre Vorgänge - Anwendung auf Transportflugzeuge, Dissertation, Technische Universität München, Garching, Germany, 2009.

[67] M. Iovnovich and D. E. Raveh, "Numerical Study of Shock Buffet on Three-Dimensional Wings," *AIAA Journal*, Vol. 53 (2), pp. 449–463, 2015.

[68] C. A. Irwin and P. R. Guyett, "The Subcritical Response and Flutter of a Swept Wing Model," Technical report, TR 65186, Royal Aircraft Establishment, Farnborough, England, U.K., 1965.

[69] R. Isermann, Identifikation dynamischer Systeme 1: Grundlegende Methoden, Springer-Verlag, 2nd Edition, Berlin, Heidelberg, ISBN 978-3-642-84679-3, 1992.

[70] E. Iuliano and D. Quagliarella, "Proper Orthogonal Decomposition, Surrogate Modelling and Evolutionary Optimization in Aerodynamic Design," *Computers & Fluids*, Vol. 84, pp. 327–350, 2013.

[71] S. B. Jaensch, On the Efficient Numerical Modeling of Nonlinear Self-Excited Thermoacoustic Oscillations, Dissertation, Technische Universität München, Garching, Germany, 2017.

[72] A. Jameson and E. Turkel, "Implicit Schemes and LU-Decompositions," *Mathematics of Computation*, Vol. 37 (156), pp. 385–397, 1981.

[73] J.-S. R. Jang, "ANFIS: Adaptive-Network-Based Fuzzy Inference System," *IEEE Transactions on Systems, Man, and Cybernetics*, Vol. 23 (3), pp. 665–685, 1993.

[74] J.-N. Juang and R. S. Pappa, "An Eigensystem Realization Algorithm for Modal Parameter Identification and Model Reduction," *Journal of Guidance*, Vol. 8 (5), pp. 620–627, 1984.

[75] C. Kaiser, R. Thormann, D. Dimitrov, and J. Nitzsche, "Time-Linearized Analysis of Motion-Induced and Gust-Induced Airloads with the DLR TAU Code,"

In: 64. Deutscher Luft- und Raumfahrtkongress, Rostock, Germany, DGLR Paper 2015-370189, pp. 1–9, Deutsche Gesellschaft für Luft- und Raumfahrt - Lilienthal-Oberth e.V., 2015.

[76] T. Kim, "Frequency-Domain Karhunen-Loeve Method and Its Application to Linear Dynamic Systems," *AIAA Journal*, Vol. 36 (11), pp. 2117–2123, 1998.

[77] T. Kim, "Efficient Reduced-Order System Identification for Linear Systems with Multiple Inputs," *AIAA Journal*, Vol. 43 (7), pp. 1455–1464, 2005.

[78] T. Kim and J. E. Bussoletti, "An Optimal Reduced-Order Aeroelastic Modeling Based on a Response-Based Modal Analysis of Unsteady CFD Models," In: 42nd AIAA/ASME/ASCE/AHS/ASC Structures, Structural Dynamics, and Materials Conference and Exhibit, Seattle, WA, USA, AIAA Paper 2001-1525, pp. 1–11, 2001.

[79] T. Klimmek, "Parametric Set-up of a Structural Model for FERMAT Configuration Aeroelastic and Loads Analysis," *Journal of Aeroelasticity and Structural Dynamics*, Vol. 3 (2), pp. 31–49, 2014.

[80] J. Kou and W. Zhang, "An Approach to Enhance the Generalization Capability of Nonlinear Aerodynamic Reduced-Order Models," *Aerospace Science and Technology*, Vol. 49, pp. 197–208, 2016.

[81] J. Kou and W. Zhang, "Layered Reduced-Order Models for Nonlinear Aerodynamics and Aeroelasticity," *Journal of Fluids and Structures*, Vol. 68, pp. 174–193, 2017.

[82] J. Kou and W. Zhang, "Multi-Kernel Neural Networks for Nonlinear Unsteady Aerodynamic Reduced-Order Modeling," *Aerospace Science and Technology*, Vol. 67, pp. 309–326, 2017.

[83] J. Kou and W. Zhang, "Reduced-Order Modeling for Nonlinear Aeroelasticity with Varying Mach Numbers," *Journal of Aerospace Engineering*, Vol. 31 (6), 2018.

[84] J. Kou, W. Zhang, and M. Yin, "Novel Wiener Models with a Time-Delayed Nonlinear Block and their Identification," *Nonlinear Dynamics*, Vol. 85 (4), pp. 2389–2405, 2016.

[85] G. Kouba, R. M. Botez, and N. Boely, "Fuzzy Logic Method Use in F/A-18 Aircraft Model Identification," *Journal of Aircraft*, Vol. 47 (1), pp. 10–17, 2010.

[86] E. Kreiselmaier, Berechnung instationärer Tragflügelumströmungen auf der Basis der zeitlinearisierten Eulergleichungen, Dissertation, Technische Universität München, Garching, Germany, 1998.

[87] E. Kreiselmaier and B. Laschka, “Small Disturbance Euler Equations: Efficient and Accurate Tool for Unsteady Load Prediction,” *Journal of Aircraft*, Vol. 37 (5), pp. 770–778, 2000.

[88] D. G. Krige, “A Statistical Approach to Some Basic Mine Valuation Problems on the Witwatersrand,” *Journal of the Southern African Institute of Mining and Metallurgy*, Vol. 52 (6), pp. 119–139, 1951.

[89] R. Kruse, J. Gebhardt, and F. Klawonn, Foundations of Fuzzy Systems, John Wiley & Sons, 1st Edition, Chichester, West Sussex, U.K., ISBN 978-0-4719-4243-6, 1994.

[90] M. Lakshmanan and S. Rajasekar, Nonlinear Dynamics: Integrability, Chaos and Patterns, Springer-Verlag, 1st Edition, Berlin, Heidelberg, ISBN 978-3-642-55688-3, 2003.

[91] E. M. Lee-Rausch and J. T. Batina, “Calculation of AGARD Wing 445.6 Flutter Using Navier-Stokes Aerodynamics,” In: 11th AIAA Applied Aerodynamics Conference and Exhibit, Monterey, CA, USA, AIAA Paper 1993–3476, 1993.

[92] E. M. Lee-Rausch and J. T. Batina, “Wing Flutter Boundary Prediction Using Unsteady Euler Aerodynamic Method,” *Journal of Aircraft*, Vol. 32 (2), pp. 416–422, 1995.

[93] E. M. Lee-Rausch and J. T. Batina, “Wing Flutter Computations Using an Aerodynamic Model Based on the Navier-Stokes Equations,” *Journal of Aircraft*, Vol. 33 (6), pp. 1139–1147, 1996.

[94] R. Lind, R. J. Prazenica, M. J. Brenner, and D. H. Baldelli, “Identifying Parameter-Dependent Volterra Kernels to Predict Aeroelastic Instabilities,” *AIAA Journal*, Vol. 43 (12), pp. 2496–2502, 2005.

[95] K. Lindhorst, Nichtlineare Ersatzmodellierung in transsonischer instationärer Aeroelastik, Dissertation, Technische Universität Braunschweig, Braunschweig, Germany, 2016.

[96] K. Lindhorst, M. C. Haupt, and P. Horst, “Efficient Surrogate Modelling of Nonlinear Aerodynamics in Aerostructural Coupling Schemes,” *AIAA Journal*, Vol. 52 (9), pp. 1952–1966, 2014.

[97] K. Lindhorst, M. C. Haupt, and P. Horst, “Aeroelastic Analyses of the High-Reynolds-Number-Aerostructural-Dynamics Configuration Using a Nonlinear Surrogate Model Approach,” *AIAA Journal*, Vol. 53 (9), pp. 2784–2796, 2015.

[98] K. Lindhorst, M. C. Haupt, and P. Horst, “Reduced-Order Modelling of Non-Linear, Transient Aerodynamics of the HIRENASD Wing,” *The Aeronautical Journal*, Vol. 120 (1226), pp. 601–626, 2016.

[99] H. Liu, H. Hu, Y. Zhao, and R. Huang, “Efficient Reduced-Order Modeling of Unsteady Aerodynamics Robust to Flight Parameter Variations,” *Journal of Fluids and Structures*, Vol. 49, pp. 728–741, 2014.

[100] P. Liu, G. Yu, X. Zhu, and Z. Du, “Unsteady Aerodynamic Prediction for Dynamic Stall of Wind Turbine Airfoils with the Reduced Order Modeling,” *Renewable Energy*, Vol. 69, pp. 402–409, 2014.

[101] E. Livne, “Future of Airplane Aeroelasticity,” *Journal of Aircraft*, Vol. 40 (6), pp. 1066–1092, 2003.

[102] L. Ljung, System Identification: Theory for the User, Prentice Hall PTR, 2nd Edition, Upper Saddle River, NJ, USA, ISBN 978-0-1365-6695-3, 1999.

[103] D. J. Lucia, P. S. Beran, and W. A. Silva, “Reduced-Order Modeling: New Approaches for Computational Physics,” *Progress in Aerospace Sciences*, Vol. 40 (1-2), pp. 51–117, 2004.

[104] D. J. Lucia, P. King, and P. Beran, “Reduced-Order Modeling of a Two-Dimensional Flow,” *Computers & Fluids*, Vol. 32, pp. 917–938, 2003.

[105] Luftfahrtnorm, Luftfahrtnorm DIN 9300, Normenstelle Luftfahrt (NL) im DIN Deutsches Institut für Normung e.V., 1990.

[106] J. Lunze, Regelungstechnik 1: Systemtheoretische Grundlagen, Analyse und Entwurf einschleifiger Regelungen, Springer-Verlag, 9th Edition, Berlin, Heidelberg, ISBN 978-3-642-29533-1, 2013.

[107] A. Mannarino, Nonlinear Aeroservoelasticity: Reduced Order Modeling and Active Control, Dissertation, Politecnico di Milano, Milan, Italy, 1997.

[108] A. Mannarino and E. H. Dowell, “Reduced-Order Models for Computational-Fluid-Dynamics-Based Nonlinear Aeroelastic Problems,” *AIAA Journal*, Vol. 53 (9), pp. 2671–2685, 2015.

[109] A. Mannarino and P. Mantegazza, “Nonlinear Aeroelastic Reduced Order Modeling by Recurrent Neural Networks,” *Journal of Fluids and Structures*, Vol. 48, pp. 103–121, 2014.

[110] A. Mannarino and P. Mantegazza, “Nonlinear Aerodynamic Reduced Order Modeling by Discrete Time Recurrent Neural Networks,” *Aerospace Science and Technology*, Vol. 47, pp. 406–419, 2015.

[111] D. Marquardt, “An Algorithm for Least-Squares Estimation of Nonlinear Parameters,” *SIAM Journal on Applied Mathematics*, Vol. 11 (2), pp. 431–441, 1963.

[112] F. D. Marques and J. Anderson, “Identification and Prediction of Unsteady Transonic Aerodynamic Loads by Multi-Layer Functionals,” *Journal of Fluids and Structures*, Vol. 15, pp. 83–106, 2001.

[113] The MathWorks Inc., Natick, MA, USA, MATLAB R2016b: Fuzzy Logic Toolbox User’s Guide, 2016.

[114] The MathWorks Inc., Natick, MA, USA, MATLAB R2016b: Neural Network Toolbox User’s Guide, 2016.

[115] The MathWorks Inc., Natick, MA, USA, MATLAB R2016b User’s Guide, 2016.

[116] D. D. McCracken, “The Monte Carlo Method,” *Scientific American*, Vol. 192 (5), pp. 90–96, 1955.

[117] W. Mendenhall and T. Sincich, Statistics for Engineering and the Sciences, Prentice-Hall PTR, 6th Edition, Upper Saddle River, NJ, USA, ISBN 978-1-4987-2885-0, 2016.

[118] S. A. Morton, R. B. Melville, and M. R. Visbal, “Accuracy and Coupling Issues of Aeroelastic Navier-Stokes Solutions on Deforming Meshes,” *Journal of Aircraft*, Vol. 35 (5), pp. 798–805, 1998.

[119] V. Mukhopadhyay, “Historical Perspective on Analysis and Control of Aeroelastic Responses,” *Journal of Guidance, Control and Dynamics*, Vol. 26 (5), pp. 673–684, 2003.

[120] K. S. Narendra and K. Parthasarathy, “Identification and Control of Dynamical Systems Using Neural Networks,” *IEEE Transactions on Neural Networks*, Vol. 1 (1), pp. 4–27, 1990.

[121] O. Nelles, Nonlinear System Identification: From Classical Approaches to Neural Networks and Fuzzy Models, Springer-Verlag, 1st Edition, Berlin, Heidelberg, ISBN 978-3-662-04323-3, 2001.

[122] D. Nguyen and B. Widrow, “Improving the Learning Speed of 2-Layer Neural Networks by Choosing Initial Values of the Adaptive Weights,” *International Joint Conference on Neural Networks*, Vol. 3, pp. 21–26, 1990.

[123] A. K. Omran and B. Newman, “Full Envelope Nonlinear Parameter-Varying Model Approach for Atmospheric Flight Dynamics,” *Journal of Guidance, Control, and Dynamics*, Vol. 35 (1), pp. 270–283, 2012.

[124] C. R. O'Neill and A. S. Arena, "Time Domain Training Signals Comparison for Computational Fluid Dynamics Based Aerodynamic Identification," *Journal of Aircraft*, Vol. 42 (2), pp. 421–428, 2005.

[125] P. F. Pai, Highly Flexible Structures: Modeling, Computation, and Experimentation, American Institute of Aeronautics and Astronautics, 1st Edition, Reston, VA, USA, ISBN 978-1-5634-7917-5, 2007.

[126] S. O. Park, K. H. Jun, S. M. Baek, M. H. Cho, K. J. Yee, and D. H. Lee, "Reduced-Order Model with an Artificial Neural Network for Aerostructural Design Optimization," *Journal of Aircraft*, Vol. 50 (4), pp. 1106–1116, 2013.

[127] A. N. Pechloff, Small Disturbance Navier-Stokes Predictions of Low-Aspect-Ratio Wing Harmonic Loading, Dissertation, Technische Universität München, Garching, Germany, 2018.

[128] A. N. Pechloff and B. Laschka, "Small Disturbance Navier-Stokes Method: Efficient Tool for Predicting Unsteady Air Loads," *Journal of Aircraft*, Vol. 43 (1), pp. 17–29, 2006.

[129] D. Pitt and D. Haudrich, "Artificial Neural Network for Multiple Aeroelastic Analysis," In: 45th AIAA/ASME/ASCE/AHS/ASC Structures, Structural Dynamics and Materials Conference and Exhibit, Palm Springs, CA, USA, AIAA Paper 2004-1750, pp. 1–8, American Institute of Aeronautics and Astronautics, 2004.

[130] W. Polifke, "Black-Box System Identification for Reduced Order Model Construction," *Annals of Nuclear Energy*, Vol. 67, pp. 109–128, 2014.

[131] R. J. Prazenica, P. H. Reisenthel, A. J. Kurdila, and M. J. Brenner, "Volterra Kernel Extrapolation for Modeling Nonlinear Aeroelastic Systems at Novel Flight Conditions," *Journal of Aircraft*, Vol. 44 (1), pp. 149–162, 2007.

[132] D. Quero Martin, An Aeroelastic Reduced Order Model for Dynamic Response Prediction to Gust Encounters, Dissertation, Technische Universität Berlin, Berlin, Germany, 2017.

[133] A. Rampurawala, K. Badcock, and S. Marques, "ANN Based ROM for the Prediction of Unsteady Aeroelastic Instabilities," In: 13th International Forum on Aeroelasticity and Structural Dynamics, Seattle, WA, USA, IFASD Paper 2009-032, pp. 1–14, 2009.

[134] D. E. Raveh, "Reduced-Order Models for Nonlinear Unsteady Aerodynamics," *AIAA Journal*, Vol. 39 (8), pp. 1417–1429, 2001.

[135] D. E. RAVEH, "Identification of Computational-Fluid-Dynamics Based Unsteady Aerodynamic Models for Aeroelastic Analysis," *Journal of Aircraft*, Vol. 41 (3), pp. 620–632, 2004.

[136] L. REIMER, A. BOUCKE, J. BALLMANN, and M. BEHR, "Computational Analysis of the High Reynolds Number Aero-Structural Dynamics (HIRENASD) Experiments," In: 13th International Forum on Aeroelasticity and Structural Dynamics, Seattle, WA, USA, IFASD Paper 2009-130, pp. 1–14, 2009.

[137] M. RIVERS and A. DITTBERNER, "Experimental Investigations of the NASA Common Research Model," In: 28th AIAA Applied Aerodynamics Conference and Exhibit, Chicago, IL, USA, AIAA Paper 2010-4218, pp. 1–35, 2010.

[138] P. L. ROE, "Approximate Riemann Solvers, Parameter Vectors and Difference Schemes," *Journal of Computational Physics*, Vol. 43 (2), pp. 357–372, 1981.

[139] V. ROZOV, M. WINTER, and C. BREITSAMTER, "Antisymmetric Boundary Condition for Small Disturbance CFD," *Journal of Fluids and Structures*, Vol. 85, pp. 229–248, 2019.

[140] D. E. RUMELHART, G. E. HINTON, and R. J. WILLIAMS, "Learning Representations by Back-Propagating Errors," *Nature*, Vol. 323, pp. 533–536, 1986.

[141] A. SAADAT, A. A. ALVANAGH, and H. REZAEI, "pH Control in Biological Process Using MMPC Based on Neuro-Fuzzy Model by LOLIMOT Algorithm," In: 9th Asian Control Conference, Istanbul, Turkey, pp. 1–6, 2013.

[142] G. SCHEWE, H. MAI, and G. DIETZ, "Nonlinear Effects in Transonic Flutter with Emphasis on Manifestations of Limit Cycle Oscillations," *Journal of Fluids and Structures*, Vol. 18, pp. 3–22, 2003.

[143] H. SCHLICHTING and E. TRUCKENBRODT, Aerodynamik des Flugzeuges, Erster Band, Springer-Verlag, 3rd Edition, Berlin, Heidelberg, New York, ISBN 978-3-540-67374-3, 2001.

[144] H. SCHLICHTING and E. TRUCKENBRODT, Aerodynamik des Flugzeuges, Zweiter Band, Springer-Verlag, 3rd Edition, Berlin, Heidelberg, New York, ISBN 978-3-642-56910-4, 2001.

[145] D. SCHRÖDER, Intelligente Verfahren: Identifikation und Regelung nichtlinearer Systeme, Springer-Verlag, 1st Edition, Berlin, Heidelberg, ISBN 978-3-642-11398-7, 2010.

[146] U. SICKMÜLLER, Instationäre Luftkräfte höherer Ordnung auf Basis der Eulergleichungen bei kleinen Störungen, Dissertation, Technische Universität München, Garching, Germany, 2006.

[147] W. A. Silva, "Application of Nonlinear Systems Theory to Transonic Unsteady Aerodynamic Responses," *Journal of Aircraft*, Vol. 30 (5), pp. 660–668, 1993.

[148] W. A. Silva, Discrete-Time Linear and Nonlinear Aerodynamic Impulse Responses for Efficient CFD Analyses, Dissertation, College of William and Mary, Williamsburg, VA, USA, 1997.

[149] W. A. Silva, "Identification of Nonlinear Aeroelastic Systems Based on the Volterra Theory: Progress and Opportunities," *Nonlinear Dynamics*, Vol. 39 (1), pp. 25–62, 2005.

[150] W. A. Silva, "Simultaneous Excitation of Multiple-Input/Multiple-Output CFD-Based Unsteady Aerodynamic Systems," *Journal of Aircraft*, Vol. 45 (4), pp. 1267–1274, 2008.

[151] W. A. Silva, "AEROM: NASA's Unsteady Aerodynamic and Aeroelastic Reduced-Order Modeling Software," *Aerospace*, Vol. 5 (2), 2018.

[152] W. A. Silva and R. E. Bartels, "Development of Reduced-Order Models for Aeroelastic Analysis and Flutter Prediction Using the CFL3Dv6.0 Code," *Journal of Fluids and Structures*, Vol. 19 (5), pp. 729–745, 2004.

[153] W. A. Silva, P. Chwalowski, and B. Perry III., "Evaluation of Linear, Inviscid, Viscous, and Reduced-Order Modelling Aeroelastic Solutions of the AGARD 445.6 Wing Using Root Locus Analysis," *International Journal of Computational Fluid Dynamics*, Vol. 28 (3-4), pp. 122–139, 2014.

[154] L. Sirovich, "Turbulence and the Dynamics of Coherent Structures. Part 1: Coherent Structures," *Quarterly of Applied Mathematics*, Vol. 45 (3), pp. 561–571, 1987.

[155] T. Skujins and C. E. S. Cesnik, "Reduced-Order Modeling of Unsteady Aerodynamics Across Multiple Mach Regimes," *Journal of Aircraft*, Vol. 51 (6), pp. 1681–1704, 2014.

[156] S. W. Smith, The Scientist and Engineer's Guide to Digital Signal Processing, California Technical Publications, 1st Edition, San Diego, CA, USA, ISBN 978-0-9660-1763-2, 1997.

[157] J. Sola and J. Sevilla, "Importance of Input Data Normalization for the Application of Neural Networks to Complex Industrial Problems," *IEEE Transactions on Nuclear Science*, Vol. 44 (3), pp. 1464–1468, 1997.

[158] P. R. Spalart and S. R. Allmaras, "A One-Equation Turbulence Model for Aerodynamic Flows," In: 30th Aerospace Sciences Meeting and Exhibit, Reno, NV, USA, AIAA Paper 1992-0439, pp. 1–22, 1992.

[159] J. H. Spurk, Strömungslehre - Eine Einführung in die Theorie der Strömungen, Springer-Verlag, 8th Edition, Heidelberg, Dordrecht, London, New York, ISBN 978-3-642-13143-1, 2010.

[160] J. L. Steger and H. E. Bailey, "Calculation of Transonic Aileron Buzz," *AIAA Journal*, Vol. 18 (3), pp. 249–255, 1980.

[161] T. Takagi and M. Sugeno, "Fuzzy Identification of Systems and Its Applications to Modeling and Control," *IEEE Transactions on Systems, Man, and Cybernetics*, Vol. SMC-15 (1), pp. 116–132, 1985.

[162] L. Tang, R. E. Bartels, P.-C. Chen, and D. D. Liu, "Numerical Investigation of Transonic Limit Cycle Oscillations of a Two-Dimensional Supercritical Wing," *Journal of Fluids and Structures*, Vol. 17, pp. 29–41, 2003.

[163] A. K. Tangirala, Principles of System Identification: Theory and Practice, CRC Press, 1st Edition, Boca Raton, FL, USA, ISBN 978-1-4398-9599-3, 2013.

[164] J. P. Thomas, E. H. Dowell, and K. C. Hall, "Modeling Viscous Transonic Limit-Cycle Oscillation Behavior Using a Harmonic Balance Approach," *Journal of Aircraft*, Vol. 41 (6), pp. 1266–1274, 2004.

[165] R. Thormann and M. Widhalm, "Linear Frequency Domain Prediction of Dynamic Response Data for Viscous Transonic Flows," *AIAA Journal*, Vol. 51 (11), pp. 2540–2557, 2013.

[166] L. Tichy, H. Mai, M. Fehrs, J. Nitzsche, and A. Hebler, "Risk Analysis for Flutter of Laminar Wings," In: 17th International Forum on Aeroelasticity and Structural Dynamics, Como, Italy, IFASD Paper 2017-217, pp. 1–17, 2017.

[167] E. F. Toro, Riemann Solvers and Numerical Methods for Fluid Dynamics, Springer-Verlag, 3rd Edition, Berlin, Heidelberg, New York, ISBN 978-3-540-49834-6, 2009.

[168] A. C. L. M. van Rooij, Aeroelastic Limit-Cycle Oscillations Resulting from Aerodynamic Non-Linearities, Dissertation, Delft University of Technology, Delft, The Netherlands, 2017.

[169] A. C. L. M. van Rooij, J. Nitzsche, and R. P. Dwight, "Energy Budget Analysis of Aeroelastic Limit-Cycle Oscillations," *Journal of Fluids and Structures*, Vol. 69, pp. 174–186, 2017.

[170] J. C. Vassberg, M. Dehaan, M. Rivers, and R. Wahls, "Development of a Common Research Model for Applied CFD Validation Studies," In: 26th, AIAA Applied Aerodynamics Conference and Exhibit, Honolulu, HI, USA, AIAA Paper 2008-6919, pp. 1–22, 2008.

[171] J. C. Vassberg, E. N. Tinoco, M. Mani, B. Rider, T. Zickuhr, D. W. Levy, O. P. Brodersen, B. Eisfeld, S. Crippa, R. A. Wahls, J. H. Morrison, D. J. Mavriplis, and M. Murayama, "Summary of the Fourth AIAA Computational Fluid Dynamics Drag Prediction Workshop," *Journal of Aircraft*, Vol. 51 (4), pp. 1070–1089, 2014.

[172] C. Vidy, L. Katzenmeier, M. Winter, and C. Breitsamter, "Verification of the Use of Small-Disturbance CFD in Flutter and Gust Analyses for Simple to Highly Complex Configurations," In: 16th International Forum on Aeroelasticity and Structural Dynamics, St. Petersburg, Russia, IFASD Paper 2015-066, pp. 1–25, 2015.

[173] O. Voitcu and Y. S. Wong, "Neural Network Approach for Nonlinear Aeroelastic Analysis," *Journal of Guidance, Control, and Dynamics*, Vol. 26 (1), pp. 99–105, 2003.

[174] R. Vos and S. Farokhi, Introduction to Transonic Aerodynamics, Springer-Verlag, 1st Edition, Dordrecht, ISBN 978-94-017-9747-4, 2015.

[175] R. Voss and R. Thormann, "Flutter Computations for a Generic Reference Aircraft Adopting CFD and Reduced Order Methods," In: 53rd AIAA/ASME/ASCE/AHS/ASC Structures, Structural Dynamics and Materials Conference and Exhibit, Honolulu, HI, AIAA Paper 2012-1715, pp. 1–19, American Institute of Aeronautics and Astronautics, 2012.

[176] W. A. Wall and B. Bornemann, Finite Elemente: Skriptum zur Vorlesung, Lecture notes, WS 2009/2010, Lehrstuhl für numerische Mechanik, Technische Universität München, 2009.

[177] Z. Wang, C. Lan, and J. Brandon, "Fuzzy Logic Modeling of Nonlinear Unsteady Aerodynamics," In: 23rd Atmospheric Flight Mechanics Conference, Boston, MA, USA, AIAA Paper 1998-4351, pp. 1–16, 1998.

[178] S. Weber, K. D. Jones, J. A. Ekaterinaris, and M. F. Platzer, "Transonic Flutter Computations for the NLR 7301 Supercritical Airfoil," *Aerospace Science and Technology*, Vol. 5 (4), pp. 293–304, 2001.

[179] C. Weishäupl and B. Laschka, "Small Disturbance Euler Simulations for Delta Wing Unsteady Flows due to Harmonic Oscillations," *Journal of Aircraft*, Vol. 41 (4), pp. 782–789, 2004.

[180] D. L. Whitfield and J. M. Janus, "Three-Dimensional Unsteady Euler Equations Solution Using Flux Vector Splitting," In: 17th Fluid Dynamics, Plasma Dynamics, and Lasers Conference, Snowmass, CO, USA, AIAA Paper 1984-1552, pp. 1–12, 1984.

[181] K. Willcox and J. Peraire, "Balanced Model Reduction via the Proper Orthogonal Decomposition," *AIAA Journal*, Vol. 40 (11), pp. 2323–2330, 2002.

[182] M. Winter and C. Breitsamter, "Reduced-Order Modeling of Unsteady Aerodynamic Loads Using Radial Basis Function Neural Networks," In: 63. Deutscher Luft- und Raumfahrtkongress, Augsburg, Germany, DGLR Paper 2014-340013, pp. 1–10, Deutsche Gesellschaft für Luft- und Raumfahrt - Lilienthal-Oberth e.V., 2014.

[183] M. Winter and C. Breitsamter, "Efficient Modeling of Generalized Aerodynamic Forces Across Mach Regimes Using Neuro-Fuzzy Approaches," In: *Notes on Numerical Fluid Mechanics and Multidisciplinary Design*, Vol. 132, edited by Dillmann et al., New Results in Numerical and Experimental Fluid Mechanics X, pp. 467–477, Springer-Verlag, Cham, 2016.

[184] M. Winter and C. Breitsamter, "Efficient Unsteady Aerodynamic Loads Prediction Based on Nonlinear System Identification and Proper Orthogonal Decomposition," *Journal of Fluids and Structures*, Vol. 67, pp. 1–21, 2016.

[185] M. Winter and C. Breitsamter, "Neurofuzzy-Model-Based Unsteady Aerodynamic Computations Across Varying Freestream Conditions," *AIAA Journal*, Vol. 54 (9), pp. 2705–2720, 2016.

[186] M. Winter and C. Breitsamter, "Application of Unsteady Aerodynamic Reduced-Order Modeling Techniques to a Complex Configuration," In: 17th International Forum on Aeroelasticity and Structural Dynamics, Como, Italy, IFASD Paper 2017-217, pp. 1–19, 2017.

[187] M. Winter and C. Breitsamter, "Monte-Carlo-Based Training and Application Framework for Enhanced Nonlinear Aerodynamic Reduced-Order Modeling," In: 66. Deutscher Luft- und Raumfahrtkongress, Munich, Germany, DGLR Paper 2017-450074, pp. 1–9, Deutsche Gesellschaft für Luft- und Raumfahrt - Lilienthal-Oberth e.V., 2017.

[188] M. Winter and C. Breitsamter, "Coupling of Recurrent and Static Neural Network Approaches for Improved Multi-step Ahead Time Series Prediction," In: *Notes on Numerical Fluid Mechanics and Multidisciplinary Design*, Vol. 136, edited by Dillmann et al., New Results in Numerical and Experimental Fluid Mechanics XI, pp. 433–442, Springer-Verlag, Cham, 2018.

[189] M. Winter and C. Breitsamter, "Nonlinear Identification via Connected Neural Networks for Unsteady Aerodynamic Analysis," *Aerospace Science and Technology*, Vol. 77, pp. 802–818, 2018.

[190] M. Winter, F. M. Heckmeier, and C. Breitsamter, “CFD-Based Aeroelastic Reduced-Order Modeling Robust to Structural Parameter Variations,” *Aerospace Science and Technology*, Vol. 67, pp. 13–30, 2017.

[191] K. Won, H. M. Tsai, M. Sadeghi, and F. Liu, “Non-Linear Impulse Methods for Aeroelastic Simulations,” In: 23rd AIAA Applied Aerodynamics Conference and Exhibit, Toronto, Canada, AIAA Paper 2005-4845, pp. 1–19, American Institute of Aeronautics and Astronautics, 2005.

[192] J. R. Wright and J. E. Cooper, Introduction to Aircraft Aeroelasticity and Loads, John Wiley & Sons, 2nd Edition, Chichester, West Sussex, U.K., ISBN 978-1-1187-0044-0, 2015.

[193] W. Yao and M.-S. Liou, “Reduced-Order Modeling for Limit-Cycle Oscillation Using Recurrent Artificial Neural Network,” In: 12th AIAA Aviation Technology, Integration, and Operations Conference and 14th AIAA/ISSMO Multidisciplinary Analysis and Optimization Conference, Indianapolis, IN, USA, AIAA Paper 2012-5446, pp. 1–15, 2012.

[194] E. C. Yates Jr., “AGARD Standard Aeroelastic Configurations for Dynamic Response. Candidate Configuration I.-Wing 445.6,” Technical report, NASA-TM-100492, National Aeronautics and Space Administration, 1987.

[195] L. A. Zadeh, “Fuzzy Sets,” *Information and Control*, Vol. 8, pp. 338–353, 1965.

[196] Q. Zhang, Nonlinear System Identification: An Overview of Common Approaches, pp. 1–12, Encyclopedia of Systems and Control, Springer-Verlag, London, 2013.

[197] W. Zhang, C. Gao, Y. Liu, Z. Ye, and Y. Jiang, “The Interaction Between Flutter and Buffet in Transonic Flow,” *Nonlinear Dynamics*, Vol. 82 (4), pp. 1851–1865, 2015.

[198] W. Zhang, Y. Jiang, and Z. Ye, “Two Better Loosely Coupled Solution Algorithms of CFD Based Aeroelastic Simulation,” *Engineering Applications of Computational Fluid Mechanics*, Vol. 1 (4), pp. 253–262, 2007.

[199] W. Zhang, J. Kou, and Z. Wang, “Nonlinear Aerodynamic Reduced-Order Model for Limit-Cycle Oscillation and Flutter,” *AIAA Journal*, Vol. 54 (10), pp. 3304–3311, 2016.

[200] W. Zhang, B. Wang, Z. Ye, and J. Quan, “Efficient Method for Limit Cycle Flutter Analysis by Nonlinear Aerodynamic Reduced-Order Models,” *AIAA Journal*, Vol. 50 (5), pp. 1019–1028, 2012.

[201] W. ZHANG and Z. YE, “Reduced-Order-Model-Based Flutter Analysis at High Angle of Attack,” *Journal of Aircraft*, Vol. 44 (6), pp. 2086–2089, 2007.

[202] X. ZHAO, Y. ZHU, and S. ZHANG, “Transonic Wing Flutter Predictions by a Loosely-Coupled Method,” *Computers & Fluids*, Vol. 58, pp. 45–62, 2012.

[203] R. ZIMMERMANN and S. GÖRTZ, “Non-Linear Reduced Order Models for Steady Aerodynamics,” *Procedia Computer Science*, Vol. 1 (1), pp. 165–174, 2010.

[204] ZONA Technology Inc., Scottsdale, AZ, USA, ZAERO Theoretical Manual, Version 8.5, 2011.

[205] R. ZWAAN, “LANN Wing Pitching Oscillation,” Technical report, AGARD-R-702, Compendium of Unsteady Aerodynamic Measurements, Addendum Nr. 1, Advisory Group for Aerospace Research and Development, 1982.

[206] R. J. ZWAAN, “Summary of Data Required for the AGARD SMP Activity ’Standard Aeroelastic Configurations’ - Two-Dimensional Configurations,” Technical report, NLR-MP-79015-U, Nationaal Lucht- en Ruimtevaartlaboratorium, 1979.

List of Publications

Peer-Reviewed Publications

- M. Winter and C. Breitsamter, “Reduced-Order Modeling of Transonic Buffet Aerodynamics,” In: *Notes on Numerical Fluid Mechanics and Multidisciplinary Design*, Vol. 142, edited by Dillmann et al., New Results in Numerical and Experimental Fluid Mechanics XII, pp. 511-520, Springer-Verlag, Cham, 2019.

- V. Rozov, M. Winter, and C. Breitsamter, “Antisymmetric Boundary Condition for Small Disturbance CFD,” *Journal of Fluids and Structures*, Vol. 85, pp. 229-248, 2019.

- M. Winter and C. Breitsamter, “Nonlinear Identification via Connected Neural Networks for Unsteady Aerodynamic Analysis,” *Aerospace Science and Technology*, Vol. 77, pp. 802-818, 2018.

- M. Winter and C. Breitsamter, “Coupling of Recurrent and Static Neural Network Approaches for Improved Multi-Step Ahead Time Series Prediction,” In: *Notes on Numerical Fluid Mechanics and Multidisciplinary Design*, Vol. 136, edited by Dillmann et al., New Results in Numerical and Experimental Fluid Mechanics XI, pp. 433-442, Springer-Verlag, Cham, 2017.

- M. Winter, F. M. Heckmeier, and C. Breitsamter, “CFD-Based Aeroelastic Reduced-Order Modeling Robust to Structural Parameter Variations,” *Aerospace Science and Technology*, Vol. 67, pp. 13-30, 2017.

- M. Winter and C. Breitsamter, “Efficient Unsteady Aerodynamic Loads Prediction Based on Nonlinear System Identfication and Proper Orthogonal Decomposition,” *Journal of Fluids and Structures*, Vol. 67, pp. 1-21, 2016.

- M. Winter and C. Breitsamter, “Neurofuzzy-Model-Based Unsteady Aerodynamic Computations Across Varying Freestream Conditions,” *AIAA Journal*, Vol. 54 (9), pp. 2705-2720, 2016.

- M. Winter and C. Breitsamter, “Efficient Modeling of Generalized Aerodynamic Forces Across Mach Regimes Using Neuro-Fuzzy Approaches,” In: *Notes on Numerical Fluid Mechanics and Multidisciplinary Design*, Vol. 132, edited by Dillmann et al., New Results in Numerical and Experimental Fluid Mechanics X, pp. 467-477, Springer-Verlag, Cham, 2016.

Conference Contributions

- M. Winter and C. Breitsamter, "Monte-Carlo-Based Training and Application Framework for Enhanced Nonlinear Aerodynamic Reduced-Order Modeling," In: 66. Deutscher Luft- und Raumfahrtkongress, Munich, Germany, DGLR Paper 2017-450074, pp. 1-9, Deutsche Gesellschaft für Luft- und Raumfahrt - Lilienthal-Oberth e.V., 2017.

- M. Winter and C. Breitsamter, "Application of Unsteady Aerodynamic Reduced-Order Modeling Techniques to a Complex Configuration," In: 17^{th} International Forum on Aeroelasticity and Structural Dynamics, Como, Italy, IFASD Paper 2017-217, pp. 1–19, 2017.

- C. Vidy, L. Katzenmeier, M. Winter, and C. Breitsamter, "Efficient and Accurate Aeroelastic Analyses Based on Small-Distrubance CFD in Early Aircraft Development", In: 17^{th} International Forum on Aeroelasticity and Structural Dynamics, Como, Italy, IFASD Paper 2017-205, pp. 1-16, 2017.

- M. Winter and C. Breitsamter, "Sensitivity Analysis of Unsteady Aerodynamic Reduced-Order Models Robust to Freestream Parameter Variations," In: 30^{th} Congress of the International Council of the Aeronautical Sciences, Daejeon, South Korea, pp. 1-11, 2016.

- M. Winter and C. Breitsamter, "Unsteady Aerodynamic Modeling Using Neuro-Fuzzy Approaches Combined with POD," In: 64. Deutscher Luft- und Raumfahrtkongress, Rostock, Germany, DGLR Paper 2015-370121, pp. 1-11, Deutsche Gesellschaft für Luft- und Raumfahrt - Lilienthal-Oberth e.V., 2015.

- M. Winter and C. Breitsamter, "Nonlinear Reduced-Order Modeling of Unsteady Aerodynamic Loads based on Dynamic Local Linear Neuro-Fuzzy Models," In: 16^{th} International Forum on Aeroelasticity and Structural Dynamics, St. Petersburg, Russia, IFASD Paper 2015-082, pp. 1-20, 2015.

- C. Vidy, L. Katzenmeier, M. Winter, and C. Breitsamter, "Verification of the Use of Small-Disturbance CFD Aerodynamics in Flutter and Gust Analysis for Simple to Highly Complex Configurations," In: 16^{th} International Forum on Aeroelasticity and Structural Dynamics, St. Petersburg, Russia, IFASD Paper 2015-066, pp. 1-25, 2015.

- M. Winter and C. Breitsamter, "Reduced-Order Modeling of Unsteady Aerodynamic Loads Using Radial Basis Function Neural Networks," In: 63. Deutscher Luft- und Raumfahrtkongress, Augsburg, Germany, DGLR Paper 2014-340013, pp. 1-10, Deutsche Gesellschaft für Luft- und Raumfahrt - Lilienthal-Oberth e.V., 2014.